The University of Southern Mississippi

The Aquila Digital Community

Dissertations

Spring 5-2008

Photopolymerization and Characterization of Crosslinked Thiol-ene Networks and POSS/Thiol-ene Nanocomposites

Tolecia Sharonda Shaunee Clark
University of Southern Mississippi

Follow this and additional works at: https://aquila.usm.edu/dissertations

Part of the Materials Chemistry Commons, and the Polymer Chemistry Commons

Recommended Citation

The University of Southern Mississippi

PHOTOPOLYMERIZATION AND CHARACTERIZATION OF CROSSLINKED

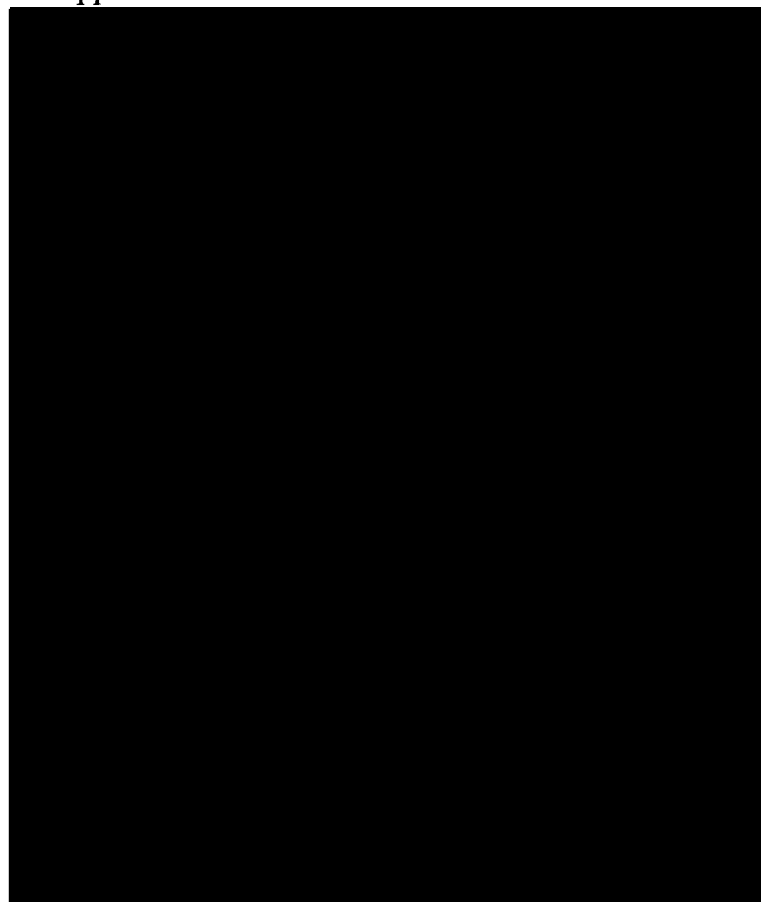# THIOL-ENE NETWORKS AND POSS/THIOL-ENE NANOCOMPOSITES

by

Tolecia Sharonda Shawnee Clark

A Dissertation
Submitted to the Graduate Studies Office
of The University of Southern Mississippi
in Partial Fulfillment of the Requirements
for the Degree of Doctor of Philosophy

Approved:

May 2008

The University of Southern Mississippi

PHOTOPOLYMERIZATION AND CHARACTERIZATION OF CROSSLINKED

THIOL-ENE NETWORKS AND POSS/THIOL-ENE NANOCOMPOSITES

by

Tolecia Sheronda Shaunee Clark

Abstract of a Dissertation
Submitted to the Graduate Studies Office
of The University of Southern Mississippi
in Partial Fulfillment of the Requirements
for the Degree of Doctor of Philosophy

May 2008

ABSTRACT

PHOTOPOLYMERIZATION AND CHARACTERIZATION OF CROSSLINKED

THIOL-ENE NETWORKS AND POSS/THIOL-ENE NANOCOMPOSITES

by Tolecia Sheronda Shaunee Clark

May 2008

Interests in the area of thiol-ene photopolymerization are rapidly expanding due to the numerous advantages over the polymers produced by traditional solvent based polymerizations. Although current research of photoinitiated thiol-ene polymerization is diverse, numerous opportunities are available for investigating structure/property and structure/reactivity relationships and novel material applications. This research in this dissertation includes a fundamental study of the effect of monomeric thiol functionality on thiol-ene polymerization kinetics and formation of the thiol-ene network structure, and an investigation of the development of novel silicate based thiol-ene nanocomposites.

The first fundamental study investigates the effect of thiol functionality on the kinetics and ensuing network structure. More specifically, the influence of thiol functionality on the polymerization rate and the thermal and mechanical behavior is described. Novel multifunctional thiol monomers having functionalities, $f = 2, 5.6, 8.1$, and 11, were synthesized via an amine-catalyzed thiol Michael addition reaction. High conversions of functional groups and marginal changes in thermal and mechanical properties for highly functional thiol monomers ($f > 6$) suggest that delayed gelation occurs, resulting in a polymer network with reduced effective crosslinked density. Also, thiol functionality has a marginal effect on polymerization rates.

The development of a novel silicate based thiol-ene nanocomposite involves an investigation of the changes in the network structure that occurs upon the inclusion of organically modified silicate nanoparticles. As for all nanocomposite materials, the prevention of aggregation is a challenge and is addressed by improving compatibility and optimizing concentration of the silicate particle within the polymer matrix. A fundamental study examines the effect of compatibility and method of incorporation (physical or chemical) of the silicate particle on the morphology and subsequent thermal, mechanical, and physical behavior by varying the type of organic substituents on the caged silicate particle and the molar concentration of silicate particle within the thiol-ene matrix. In all cases, POSS whether incorporated chemically or physically in the network reduces flame spread. Results show that compatibilization of the silicate particles has a great influence on the thermal and physical properties of the network. The influence of silicate particle inclusion is examined by analyzing thermal, mechanical, and physical properties, including enthalpic relaxation. When incorporated chemically into the network with no aggregation, POSS does not alter the thermal transitions, physical properties or mechanical transitions significantly. If hydrogen bonding chemical groups are attached to POSS, an increase in thermal and mechanical transitions as well as modulus in the rubbery region occurs. The interaction of incorporated POSS within the crosslinked thiol-ene polymer was also characterized by the changes in free volume within the network structure. This investigation includes direct analysis of free volume by positron annihilation lifetime spectroscopy (PALS) and oxygen flux measurements. Results indicate that if POSS can be connected chemically into the polymer matrix with little or no aggregation the free volume is unaffected. In addition, the oxygen

permeability is unaffected by the presence of POSS whether or not it is incorporated into

the thiol-ene network.

DEDICATION

I would like to dedicate this document to my daughters, Raven Monét and Hannah Elise, for bringing unconditional love and joy into my life, and to my mother and father, Alecia and Elvin, for giving me their love and support throughout my life and teaching me to follow God always. I would like to recognize my sister, Tomonica, who taught me to be a strong mother, and her wonderful children, Nadia, Nichele, Nicholas, Cartevion, and Alecia. Also, I would like to acknowledge my brother, Christopher Williams, for his love and support as my eldest brother. To Grace Chigwada and April Williams, you have been the best friends throughout this entire process, giving me your total support, and being the shoulders that I could cry on. But, most importantly, I would like to dedicate this document to my special friend, James Griffith, for his patience, endurance, and support through my matriculation to Ph.D.

ACKNOWLEDGEMENTS

TABLE OF CONTENTS

           Thiol-ene Photopolymerization
           Glass Transition Temperature
           Enthalpic Relaxation
           Nanocomposites
           Polyhedral Oligomeric Silsesquioxane (POSS)

           Abstract
           Introduction
           Experimental
           Results and Discussion
           Conclusions
           References

xii

LIST OF TABLES

LIST OF SCHEMES

CHAPTER I

INTRODUCTION

Photopolymerization is a process of visible or UV light-induced conversion of monomers into macromolecules by a rapid chain reaction of reactive species.[1-3] Specifically, reactive species, such as free radicals or cations, are generated upon the absorption of high energy radiation to initiate sequential chemical reactions of reactive species and monomer, which produce large molecules. Growing interest in photopolymerization for commercial applications is based upon its importance as an economical, environmentally friendly technology. Salient features, such as rapid polymerization at room temperature, low energy consumption, and selective spatial initiation and control of polymerization by shutting the light on or off, drives the growth of this technology in several types of industry, such as coatings for wood, plastic, metal substrates, optical fibers, printing inks, and adhesives.[4, 5] These features, which are cost-effective, increase productivity and reduce energy costs. Photocurable formulations require no additional organic solvents, thereby reducing emission of volatile organic solvents (VOCs) into the environment. [1-4]

Photocuring, the process of photopolymerization, involves the complete conversion of the initial liquid state of reactive species to a solid material at a fast rate, therefore going from 100% liquid to 100% solid within several seconds.[6] Generally, the components of the liquid state consist of functionalized oligomers, monomers and reactive diluents, additives and fillers, and photoinitiator. The photoinitiator upon the absorption of light generates a triplet state which produces radicals by either abstraction

(Norrish type II photoinitiator) or cleavage (Norrish type I photoinitiator) to initiate polymerization. [1-4, 7] Benzoin ethers, trimethyl benzoyl phosphine oxides and acetophenone derivatives are examples of Type 1 photoinitiators, while benzophenones, thioxanthones, camphorquinone, and ketocoumarins are Type II photoinitiators. In typical systems, acrylated oligomers with urethane, polyester, and/or epoxy backbones provide the properties such as chemical and abrasion resistance, hardness, toughness, and flexibility when mixed with multifunctional and monofunctional, low molecular weight acrylates. [1-4] Reactive diluents and monomers reduce the viscosity of high-molecular weight oligomers and additives while increasing the crosslink density, and in the case of multifunctional reactive diluents polymerization rates. [1-4] Examples of typical diluents and additives are N-vinyl pyrollidinone, stabilizers, and surfactants.

Thiol-ene Photopolymerization

Thiol-ene based systems are highly crosslinked networks produced by UV-curing of multifunctional thiols and multifunctional enes, in which the average functionality of both monomers is greater than 2. [4, 10] In general, the olefinic monomers used in these reactions are alkenes, vinyl ethers, acrylates, cyclic enes, allyl ethers, etc. Typically, any commercially available multifunctional thiol can be used as a comonomer. Polymerization in a thiol-ene system proceeds by a step-growth addition, free-radical chain-transfer mechanism. [4, 8-12] The basic thiol-ene two-step propagation step and termination steps are shown in Figure 1 along with an initial step to generate thiyl radicals.

Initiation   RSH + PI (if used) → RS• + Other Products

Propagation 1   RS• + H₂C=CHR′   →   RSH₂C-ĊHR′

Propagation 2   RSH₂C-ĊHR′ + RSH → RSH₂C-CH₂R′ + RS•

Termination   RS• + RS•   → RSSR

$$\text{RS}• + \text{RSH}_2\text{C-ĊHR}′ \rightarrow \text{RSH}_2\text{C-CHR}′\text{ with RS substituent}$$

$$\text{RSH}_2\text{C-ĊHR}′ + \text{RSH}_2\text{C-ĊHR}′ \rightarrow \text{RSH}_2\text{C-CHR}′\text{ with RSH}_2\text{C-CHR}′ \text{ substituent}$$
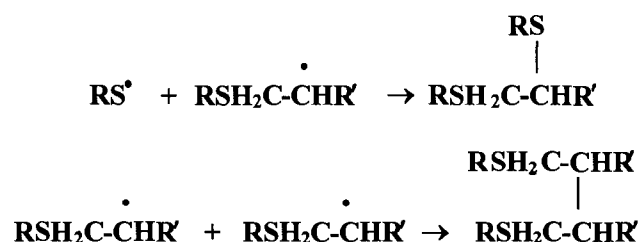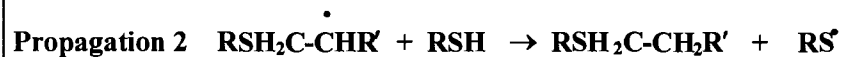
Figure 1. Step-growth, free-radical chain transfer mechanism of thiol-ene photopolymerization.

Typically, stoichiometric amounts of thiol and ene monomers are reacted. For enes that do not homopolymerize, the conversion of thiol and ene functional groups should be identical. Initiation involves the formation of thiyl radicals by a photochemical reaction with Norrish type I or Norrish type II photoinitiators. Thiyl radical production during initiation occurs differently with Norrish type I initiators and Norrish type II initiators. Norrish type I photoinitiators react by an alpha-cleavage process during UV irradiation. The thiol reacts with either one or both of the initiator fragments to form the thiyl radical (Figure 2). Norrish type II initiators such as diaryl ketones absorb UV light to form the singlet-excited state which intersystem crosses to the triplet excited state. [7] The diaryl ketone triplet state abstracts the hydrogen on the thiol to form a thiyl radical and a carbon-centered radical (See Figure 3). The thiyl radical will initiate polymerization while the ketyl radical will terminate polymerization. Alternatively, the

thiol can be directly excited to give thiyl and hydrogen radicals which initiate polymerization.
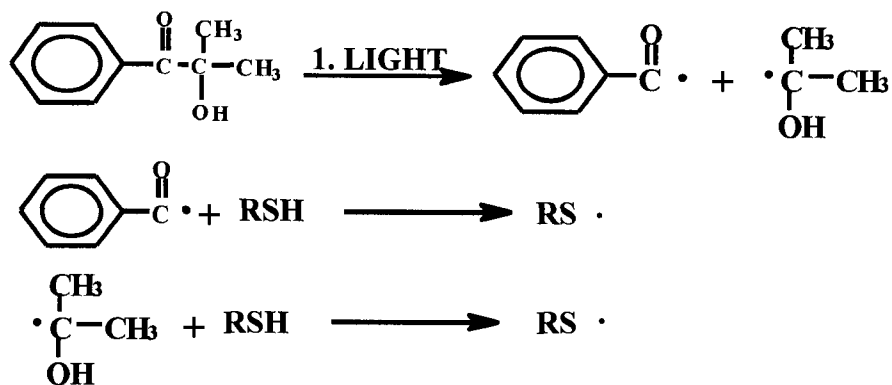
Figure 2. Norrish-type I photoinitiator–dimethoxyphenyl acetophenone (DMPA)
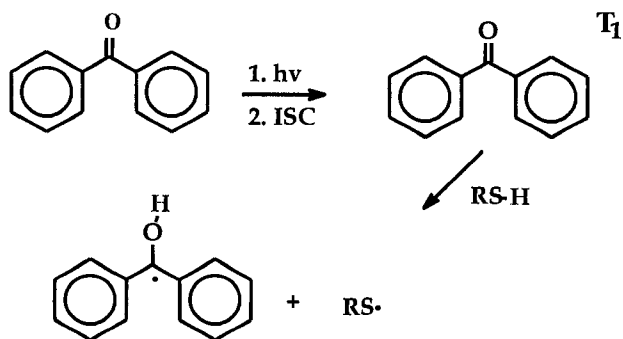
Figure 3. Norrish-type II photoinitiator–benzophenone

Photocuring of thiol-ene systems offer many advantages over traditional acrylate systems, including delayed gel points with high monomer conversion and low shrinkage, controlled polymeric structures and mechanical properties, and photoinitiatorless formulations with very little oxygen inhibition.[8-12] With typical carbon-centered polymerizations (acrylates, styrene, etc.), the free-radical process is inhibited by the presence of ambient oxygen. Oxygen inhibition either occurs at the initiation step or

propagation step. Oxygen may either quench the polymerization by reacting with initiator radicals or propagating fragments to form non-propagating peroxy radicals. [4, 8-12] Thus, acrylate polymerizations must be performed in inert atmospheres in order to prevent oxygen inhibition. For thiol-ene polymerizations, ambient oxygen reacts with a carbon radical to form a less reactive peroxy radical. [4, 8-12] The peroxy radical undergoes chain transfer with a thiol regenerating the thiyl radical: this process continues until the oxygen is consumed (See Figure 1). Hence, the free-radical chain process is not interrupted.

Some disadvantages associated with thiol-ene systems are odor problems, yellowing, and poor shelf-life stability due to incidental thermal polymerization at room temperature. Yellowing of clear coats is prominent when benzophenone, an aromatic ketone photoinitiator, is used to initiate polymerization since by-products are produced concurrently with the initiation process. Further, yellowing occurs upon continued exposure of the films produced to sunlight.

For thiol-ene polymerizations, the rate of thiol addition across a double bond is dependent upon the relative reactivities of the thiol and ene. The reactivities of thiols and enes are influenced by the nature of the substituents attached to each functional group. The order of ene reactivity toward thiol addition is as follows: vinyl ether >> allyl ether > alkene > acrylate >> diester >> styrene ≈ maleimides. [4, 8-12] The trend for ene reactivity shows that electron-rich enes such as vinyl ethers and alkenes are much more reactive than electron-poor enes such as acrylates or maleimides. Styrene, which is characterized by resonance stabilized radicals, is a poor ene for participating in thiol-ene radical chain processes due to stability of the carbon-centered radical.

Thiol- ene photopolymerization proceeds by a step growth copolymerization process, whereas acrylates proceed by a chain growth homopolymerization, yielding a reaction mixture of low molecular weight species, i.e. dimers, trimers, tetramers, etc., at low conversion. High conversion is reached before gelation occurs to generate a homogeneous polymer network. For thiol-ene systems, the gel point equation (Equation 1) can be used to predict gel conversion, α, where r is the stoichiometric thiol/ene molar ratio, f_{thiol} is the thiol functionality, and f_{ene} is the ene functionality. [4, 11] The conversion of an ensuing network provides pertinent information on the structure development of the polymer matrix.

(1) $$\alpha = [1/r(f_{thiol}-1)(f_{ene}-1)]^{1/2}$$

Several studies show how thiol concentration directly affects the crosslink density and flexibility of thiol-ene cured films. [13-15] Correlating thiol concentrations with changes in polymer mechanical and thermal properties in order to demonstrate the relationship between thiol concentration and polymer crosslinking, it has been shown that as the concentration of thiol increases, the T_g of the polymer decreases indicating a more flexible polymer matrix, presumably due to the reduction in crosslink density and the concomitant presence of the thiol ether bonds. [13, 14] The uniformity of crosslinking increases with increasing thiol concentration as the breadth of the glass transition from the glassy to rubbery region is reduced. [13, 14] Also, photocrosslinking is enthalpically favored for polymers made with low concentrations of thiol. [15] Several multifunctional

thiols have been synthesized and used in this research to elucidate the inherent structure-property relationship of thiol functionality and polymer crosslinking.

Glass Transition Temperature

The glass transition is defined as a rapid decrease of molecular mobility upon cooling of an amorphous material.[16-18] For polymeric materials, the physical state changes gradually from a rubber state having long-range segmental chain movement to a solid (glassy) state with reduced long-chain mobility as temperature decreases.[16-22] The glass transition temperature (T_g) is an important polymeric characteristic. At T_g, abrupt changes in polymer behavior occur in a discontinuous manner based on a second-order thermodynamic transition process, i.e. the specific heat capacity is discontinuous although enthalpy is a continuous function of temperature.[16-22] Upon cooling, sudden changes in thermal and mechanical properties, including stiffness, heat capacity, impact and tensile strength, refractive index, thermal expansion coefficient, and elongation occur upon reaching the glass transition.[16-22] Glass transitions are observed for both amorphous and semicrystalline polymers.

Several structural factors affect T_g. Polymer features including flexible, methylene groups in the main chain, long, aliphatic side chain groups, increased tacticity and symmetry, and branching favor lower T_g values, along with the addition of plasticizers (small-molecule liquids).[16-23] Rigid polymer backbones, bulky and rigid side groups, increased polarity and molecular weight, and crosslinking are features that favor an increase of T_g.[16-22] The free volume theory states that a glass transition temperature occurs for a given polymer at a critical universal free volume suggesting that any factors

that affect free volume, in turn, affect T_g.[16-22] Based on the free volume theory, the rigidity or flexibility of a polymer affects the amount of unoccupied (free) volume available for chain mobility, i.e., large and bulky side groups or crosslinks restrict the mobility along the main chain and raise T_g and long-chain alkyl side groups affect packing of polymer chains by introducing free volume thus decreasing T_g. Other theories explain glass transition based upon thermodynamic and kinetic approaches.[16-22] The thermodynamic theory predicts that the glass transition occurs when the conformational entropy has a value of zero. The kinetic theory relates free volume and segmental mobility along the polymer backbone to explain the rate dependence of T_g.

There are several methods used to observe the glass transition temperature of a given polymer such as differential scanning calorimetry (DSC), dynamic mechanical analysis (DMA), and volumetric measurements.[16-18] The observed T_g is a kinetic glass transition temperature, which is highly dependent on the scan rate and test temperature. Upon cooling, the free volume of a polymer decreases as the material transforms from rubber to a glass, and, based on the kinetic theory, the response of free volume change is effected by the scan rate during the glass transition, i.e., the apparent T_g is raised at a fast scan rate compared to a slower scan rate. The change in chain mobility is faster than the change in free volume; therefore, the system does not reach equilibrium with respect to free volume creating excess volume at the observed kinetic transition for fast rates.[16-19] Throughout this dissertation study, DSC experiments were performed to obtain glass transition temperatures of multithiol-multiene and thiol-ene/POSS based networks. The sensitivity of DSC is limited for highly crosslinked networks due to the small heat

capacity (ΔC_p) values between glassy and rubbery regions. Therefore, DMA is used in conjunction with DSC to monitor T_g.

DMA measures the viscoelastic response of a polymer to a sinusoidal stress to provide information related to the viscous loss of energy. The storage modulus (stored energy), loss modulus (dissipated energy or heat), and the tan δ damping term (ratio of loss modulus to storage modulus) resulting from the phase difference of stress and strain are used for observing the glass transition and secondary transitions for a given polymer. The primary relaxation transition maximum (α-peak in the loss modulus curve) corresponds to the glass transition temperature of the crosslinked network while the secondary relaxation transition (β-peak of loss modulus curve) is attributed to local molecular motions. The damping term, tan δ, is associated with the partial loosening of the polymer structure. For a crosslinked network, the maximum of tan δ which, at a frequency of 1 Hz, is generally 15-20 °C above the glass transition temperature obtained by DSC, and the width of the tan δ curve changes with respect to crosslink density.[16-18, 21, 24-27] The increased crosslink density raises the glass transition temperature and rubber modulus as well as broadens the tan δ curve resulting from the heterogeneity in the distribution of crosslinked regions. In this dissertation, the shift in the glass transition temperature and the change in the shape of the tan δ curves are used to determine the mechanical structure of thiol-ene networks (Chapters 4, 5, and 6).

Enthalpic Relaxation

Enthalpic relaxation, or physical aging, is the structural recovery of a polymer in a glassy state from a nonequilibrim state to an equilibrium state over time for a given temperature, which may be studied by the thermodynamic parameter enthalpy.[28] As the

polymer is cooled from melt (equilibrium liquid) to glass (nonequilibrium solid), a rapid

decrease of long-range segmental motions occurs during the glass transition so that the

polymer chains are frozen into nonequilibrium states with an excess enthalpy. [16-22, 28]

Rapid structural rearrangements of the polymer chain needed to accommodate

temperature changes slow down significantly at the glass transition and the polymer

chains are "frozen in" preceding the formation of an equilibrium state for a given cooling

rate. If the cooling is arrested at a temperature below T_g, the glass will be

thermodynamically driven to reduce excess enthalpy by relaxation, or release, of the

"frozen in" molecular motions in order to reach an equilibrium state at a given

temperature. [28, 29] Physical aging has significance in engineering applications including

melt processing of thermoplastics and the associated time-dependent property changes. [28]

The most common technique for observing enthalpic relaxation is differential

scanning calorimetry (DSC), by which the specific heat is measured as a function of

temperature at a constant heating rate. [28-30] For a typical DSC scan, enthalpic relaxation is

observed as a peak superimposed on the curve of the glass transition region. The peak is a

consequence of the new, rapid structural recovery of the polymer with increasing

temperature as the polymer transforms from a nonequilibrium state in the glass to an

equilibrium state in the rubber. [29] The area of the curve is used to determine the changes

in enthalpy during aging at a temperature below T_g. [28, 29] In Chapter 6 of this dissertation,

DSC analysis of enthalpic changes is used to understand the effects of POSS inclusion

into a thiol-ene network.

Nanocomposites

The development of polymeric nanocomposites is a growing field of research over the past several years. Polymeric nanocomposites consist of a polymer matrix filled with particles that are smaller than 100 nm in at least one dimension, which can be obtained by dispersing small particles in a polymer. The typical nanofiller is a clay, but graphite, single-wall and multiple-wall carbon nanotubes, double layered hydroxides, silica[31, 32], titania,[33, 34] and polyhedral oligomeric silsesquioxane (POSS) have also been used. In this study, POSS-based thiol-ene nanocomposites will be examined.

Polyhedral Oligomeric silsesquioxane (POSS)

POSS, or polyoligomeric silsesquioxane, has recently garnered much interest in academic and industrial research.[35-37] POSS molecules are ideal structures for inclusion into polymer networks since these particles resemble silica with combined organic and inorganic properties and offer opportunities for obtaining truly dispersed nanocomposite materials. [31] POSS molecules have been successfully incorporated into polymers via copolymerization, grafting, and blending. The various methods of copolymerization used that have been used are ring-opening metathesis polymerization (ROMP), conventional and atom-transfer radical polymerization, and condensation polymerization.[31, 38-40] POSS inclusion into a polymer involves blending into the polymer matrix, incorporation into the polymer backbone through covalent bonds, or attached as functionalized pendant groups along the chain of linear polymers. POSS pendant groups have been used in building blocks for rigid acrylenic, acetylinic, and olefinic polymers, and have been functionalized with groups such as amines, ureas, carbamates, etc.[31, 41, 42] Typically,

POSS is added into the backbone via copolymerization of a single, polymerizable group into polyurethane, polypropylene, and epoxy backbones. The inclusion of POSS particles has been reported to both increase and decrease T_g, increase oxygen permeability, increase mechanical strength, increase hydrophobicity, increase surface hardening, and reduce flammability and heat evolution.[31, 32]

There are two basic types of POSS structures: 1) ladder-type, and 2) cubic or cage type. POSS cages are nanosized particles (1-3 nm) that offer a unique blend of organic and inorganic characteristics having an empirical structure (($RSiO_{1.5}$)$_n$) that varies both in cage size and types of organic pendant groups. POSS cage sizes may vary (n = 8, 10, 12, 14) and can have reactive and/or nonreactive organic substituents attached at each corner of the cage.[31, 32] Reactive substituents enable POSS particles to be chemically incorporated into the polymer matrix. Nonreactive substituents enhance the compatibility of POSS cages with the monomer mixture thus improving the solubility of the inorganic cage in the organic medium. The cubic type POSS is ideal for preparation of single-phase nanocomposites due to the geometry of the cube and the hybrid nature of the particle. Topologically, the spherical structure of POSS allows better interaction between the particle and polymer through the accessibility of its organic moieties, whereas, the hybrid nature of the particle improves the compatibility of the inorganic core with an organic medium.[31] Synthetic routes of POSS nanoparticles include condensed POSS formation via a one-step hydrolytic condensation of trifunctional monomers, $XSiY_3$, where X is a chemically inert substituent or H, and Y is a chemically reactive substituent, such as Cl or alkoxy, and incomplete condensation by various condensation reactions.[31, 43]

Possible applications of POSS include POSS dendrimers for drug delivery and micelle mimics, surface modification, coatings, catalysts and catalyst supports, selective gas permeable membranes, high performance polymers, and nanoscale reactors.[31, 32] For research discussed in this dissertation, the inclusion of POSS cages into a thiol-ene crosslinked network was studied in order to understand the structure/property relationship of POSS in thiol-ene networks (Chapters 5 and 6).

Summary

Thiol-ene photopolymerization offers many advantages over traditional acrylate photosystems including fast polymerization rates in air and inert conditions, high monomer conversion, low shrinkage, and photonitiatorless systems. Although this technology was developed in the late 1970's, [10, 44-48] renewed interest in thiol-ene photopolymerization has grown due to its enhanced physical properties, adhesion, high uniformity of crosslink density, and ability to polymerize in air. There is considerably opportunity for exploring the relationship between monomer structure and polymer property since considerable fundamental knowledge of thiol-ene polymerizations is still not fully understood.

The development of polymeric nanocomposites is a growing field in the coatings and electronics applications including hybrid nanocomposite systems. Typical inorganic addititives are clays, zeolites, metal oxides, and silicate-based particles such as POSS. Although thiol-ene polymers have salient features, i.e. good adhesion, flexibility, and mechanical properties, enhancement in flammability is needed to expand thiol-ene coatings into high-temperature applications. A fundamental study of silicate-based thiol-

ene network will provide vital information on the changes in flammability as well as morphology and physical/mechanical properties of the thiol-ene network structure upon the inclusion of an organically-hybridized inorganic particle.

Limitations of polymerization kinetics exist with thiol-ene photopolymerizations including slow polymerization rates with electron-deficient enes. Copolymerization of thiol with unsaturated polyester, an electron-poor ene, is achieved at a considerably slower rate than copolymerization of thiol with vinyl ether, an electron-rich ene. Therefore, an alternative method is needed to obtain improved reactions of thiols with any electron-deficient ene. The amine-catalyzed thiol-Michael addition reaction can be a reasonable alternative process for adding thiol to an electron-poor ene at fast rates. [49] Hence, thiol-ene technology will significantly benefit from the utility of an amine-catalyzed thiol Michael reaction as a polymerization process. To date no kinetic studies have appeared for thiol-Michael addition reactions. One short chapter (chapter 7) will deal with some basic kinetics of thiol-ene amine catalyzed reactions and establishment of the methodology for measuring the reaction rates.

REFERENCES

[1] Roffey, C. G. *Photogeneration of Reactive Species for UV Curing*, John Wiley and Sons: New York, **1997**.

[2] Foussier, J. P. *Photoinitiation, Photopolymerization and Photocuring*, New York: Hanser **1993**.

[3] Dusek, K. In *Developments in Polymerization, Vol. 3*; Harvard, R. N., Eds.; Applied Science: London, **1982**; Ch. 4.

[4] Hoyle, C. E.; Lee, T. Y.; Roper, T. *J. Poly. Sci.* **2004**, *42*, 5301-5338.

[5] Papas, P. *Radiation Curing, Science and Technology*. Plenum Press, NY, **1992**.

[6] Lowe, C.; Oldring, P. K. T. *Chemistry and Technology of UV and EB Formulations for Coatings, Inks and Paints.* SITA Technology Ltd, London, **1991**.

[7] Turro, N. J. *Modern Molecular Photochemistry*, University Science Books: California, **1991**.

[8] Kloosterboer, J. G.; Van de Hei, G. M.; Boots, H. M. *J. Poly. Commun.* **1984**, *25*, 354-357.

[9] Bowman, C. N.; Anseth, K. S. *Macromol. Symp.*, **1995**, *93*, 269-276.

[10] Morgan, C. R.; Magnotta, F.' Ketley, A. D. *J. Poly. Sci.A.* **1977**, *15*, 627-645.

[11] Jacobine, A. F. *Radiation Curing in Polymer Science and Technology III: Polymerization Mechanisms*, J. D. Fouassier and J. F. Rabek, Eds., Elsevier, London, **1993**; Ch. 7, 219-286.

[12] Cramer, N. B.; Bowman, C. N. *J. Polym. Sci. A*, **2001**, *39*, 3311-331.

[13] Cramer, Neil B. and Bowman, C., *J. Polym. Sci. A*, **2001**, *39*, 3311.

[14] Cramer, Neil B. and Bowman, C., *Polym, Prep.*, **2003**, *44*.

[15] Lecamp, L.; Houllier, F.; Youssef, B.; and Bunel, C., *Polymer*, **2001**, *42*, 2727.

[16] White, T. J.; Guymon, C. A. *Poly Mat.: Sci. and Eng.* **2003**, *89*, 452-453.

[17] Nielsen, L. E.; Landel, R. F. *Mechanical Properties of Polymers and Composites*, Marcel Dekker, New York, Ch. 1, 4. **1994**.

[18] Landel, R. F.; Fedors, R. F. *Mechanical Behavior of Materials*, Vol. III, Society of Material Science, Kyoto, Japan, **1972**, p. 496.

[19] Gedde, U. W. *Polymer Physics*, Kluwer Academic Publishers, Netherlands, Ch. 5, **1999**.

[20] Gibbs, J. H.; DiMarzio, E. A. *J. Chem. Phys.*, **1958**, *28*, 373-383.

[21] Adams, G.; Gibbs, J. H. *J. Chem. Phys.*, **1965**, *43*, 139-146.

[22] Nielsen, L. E.; *J. Macro. Sci. Rev. Macromol. Chem.*, **1969**, *3*, 69-103.

[23] Nielsen, L. E.; Buchdahl, R.; Levreault, R. *J. Appl. Phys.*, **1950**, *21*, 607.

[24] Struik, L. C. E. *Annals of the New York Academy of Sciences*, **1976**, *279*, 78-85.

[25] Struik, L. C. E. *Poly. Eng. and Sci.*, **1977**, *17*, 165-173.

[26] Murayama, T.; Bell, J. P. *J. Poly. Sci A.*, **1970**, *8*, 437-445.

[27] Langley, N. R.; Ferry, J. D. *Macromolecules*, **1968**, *1*, 348-352.

[28] Hutchinson, J. M., *Prog. Polym. Sci.*, **1995**, *20*, 703-760.

[29] Lin, Y. G.; Sautereau, H.; and Pascault, J. P.; *J. Appl. Polym. Sci.*, **1986**, *32*, 4595-4605.

[30] Dantras, E.; Dandurand, J.; Lacabanne, C.; Caminade, A. M., and Majoral, J. P.; *Macromolecules*, **2002**, *35*, 2090-2904.

[31] Zhang, q.; Argher, L. A., *Langmuir*, **2002**, *18*, 10435-10442.

[32] Percy, M. J., Michailidou, V.; Armes, S. P.; Perrchot, C.; Watts, J. F.; Greaves, S. J., *Langmuir*, **2003**, *19*, 2072-2079.

[33] De Tacconi, N. R.; Carmona, J.; Balsam, W. L.; Rajeshwar, K., *Chem. Mater.*, **1998**, *10*, 26-26.

[34] Wang, S. X.; Zhang, L. D.; Su, H.; Zhang, Z. P.; Li, G. H.; Meng, G. W. Zhang, J.; Wang, Y. W.; Fan, J. C.; Gao, T., *Physics Lett.*, **2001**, *281*, 59-63.

[35] Pielichowski, K.; Nuguna, J.; Janwoski, B.; and Pielichowski, J.; *Adv. Polym. Sci.*, **2006**, *201*, 225-296.

[36] Baney, R. H.; Itoh, M.; Sakakibara, A.; and Suzuki, T.; *Chem. Rev.*, **1995**, *95*, 1409-1430.

[37] Li, G.; Wang, L.; Ni, H.; and Pittman, Jr., C. U.; *J. Inorg./Organometallic Polym.*, **2002**, *11*, 123-154.

[38] Kim K. M., Ouchi Y., Chujo Y.; *J. Mater. Chem.*, **2003**, *49*, 341.

[39] Choi J., Tamaki R., Kim S. G., Laine R. M., *Chem. Mater.*, **2003**, *15*, 3365.

[40] Mather P. T.; Jeon H. G.; Romo-Uribe A.; Haddad T. S.; Lichtenhan J. D.; *Macromolecules*, **1999**, *32*, 1194.

[41] Shea K. J., Loy D. A., Webster O. W.; *J. Am. Chem. Soc.*, **1992**, *114*, 6700.

[42] Corriu R. J. P., Moreau J. J. E., Thepot P., Man M. W. C, *Chem. Mater.*, **1992,** 4, 1217.

[43] Feher F. J., Soulivong D., Lewis G. T., *J. Am. Chem Soc.*, **1997**, *119*, 11323.

[44] Morgan, C. R.; Ketley, A. D.; *J. Rad. Cur.*, **1980**, *7*, 10.

[45] Morgan, C. R.; Ketley, A. D., *J. Polym. Sci. Polym. Lett. Ed.*, **1978**, *16*, 75.

[46] Gush, D. P.; Ketley, A. D., *Mod. Paint Coat.*, **1978**, *68*, 58.

[47] Bush, R. W.; Ketley, A. D., Morgan, C. R.; Whitt, D. G., *J. Rad. Cur.*, **1980**, 20.

[48] Morgan, C. R., **1974**, US Patent 3,784,524.

[49] Lee, Tai Y.; Kaung, W.; Joensson, E. Sonny; Lowery, K.; Guymon, C. A.; Hoyle, C. E. *J. Polym. Sci. A: Polym. Chem.*, **2004**, *42*, 4424.

CHAPTER II

RESEARCH OBJECTIVES

This research is divided into three focus areas that relate to issues fundamental to monomer synthesis and thiol-ene photopolymerization. The three primary topics are designed to define the structure/property relationship between monomer functionality and properties of a thiol-ene network, provide basic information of amine-catalyzed thio-Michael addition reactions, and establish structure/property relationships of silicate-based thiol-ene nanocomposites. The fundamental concepts derived from this work will promote future technological developments in the area of thiol-ene polymerization. Specifically, this work is designed to:

1. Examine the effect of thiol functionality on the polymerization kinetics and thermal and mechanical behavior of thiol-allyl ether systems.

2. Probe the relationship between structure and thermal/mechanical/physical behavior development in crosslinked silicate-based thiol-ene nanocomposites.

3. Analyze the interaction of POSS with the thiol-ene matrix by examining the free volume changes upon inclusion of POSS into crosslinked thiol-ene networks.

4. Evaluate the rates of an amine-catalyzed thiol Michael addition reaction to electron-deficient enes.

The first objective (Chapter 4) focuses on an approach to designing hyperbranched-type thiol structures and the development of thiol-ene materials with a potentially expanded range of properties since the influence of thiol functionality on the kinetics of thiol-ene photopolymerization is not currently fully understood. This study will provide

understanding of the role of thiols during polymerization and expand the fundamental knowledge of thiol-ene kinetics. The kinetics of the crosslinked network will be related to the thermal and mechanical behavior of the networks such as glass transition temperature and tensile strength. This research will provide a foundation for the synthesis of novel, branched-type thiols that are unavailable by commercial means.

The second, third and fourth objectives (Chapters 5 and 6) will address the development of novel silicate-based thiol-ene nanocomposites by chemically incorporating the nanoparticles into the thiol-ene polymer backbone. The addition of silicate particles to a thiol-ene network presents some problems including aggregation, compatibilization and alteration of the polymerization kinetics. A considerable opportunity exists for the development of thiol-ene materials that have reduced flame spread while conserving the traditional properties of thiol-ene polymers such as flexibility, low glass transition temperatures, homogeneous network formation, and fast kinetics. This research will focus on the inclusion of organically-hybridized inorganic particles into thiol-ene networks and its impact upon thermal, mechanical, and physical properties, along with the polymerization kinetics. This study will also establish the relationship between POSS particles and free volume changes by positron annihilation lifetime spectroscopy (PALS) and oxygen flux measurements. Finally, the effect of POSS inclusion in the thiol-ene matrix on the physical aging of thiol-ene polymers will be addressed to provide insight on how incorporated POSS particles enthalpic relaxation with respect to POSS concentration during physical aging of the thiol-ene network.

CHAPTER III

EXPERIMENTAL

A variety of experimental methods were used in this research to elucidate chemical

structures and characterize photopolymerization kinetics, thermal, mechanical, and

physical properties, thermal decomposition, gas permeability, surface hydrophobicity,

and nanoparticle size distribution. A detailed description of these instruments and

experimental procedures are described in this chapter.

Polymer Film Formation–Multithiol-allyl ether Polymer

Thin film samples containing 50:50, 60:40, 40:60, 70:30, and 30:70 thiol:ene

molar mixtures were photocured using a Fusion Epiq 600 UV cure line at a line speed of

12.19 m/min and a light intensity of 2.29 W/cm^2. Reaction mixtures containing different

molar ratios of thiol and ene and 2 mol% photoinitiator (Darocur 1173) were cast onto a

glass substrate using an 8 mil drawdown bar. Sample thickness was ~150-200 microns.

These samples were used exclusively for DSC analysis. Thick film samples prepared

from stoichiometric (50:50 thiol:ene) and unstoichiometric (60:40 and 70:30 thiol:ene)

reaction mixtures containing 2 mol% photoinitiator (Darocur 1173) were cast down onto

a glass substrate using a 40-mil drawdown bar. Sample thickness was ~ 0.3-0.7 mm. The

final cured films were cut into dog-bone shapes (5 mm x 20 mm) as described in ASTM

638-94b. These samples were used for tensile property measurements.

Polymer Film Formation–POSS/thiol-ene Nanocomposites

Film samples containing 0, 1, 5, 10, 20, and 50 ene mol% POSS/thiol-ene

copolymers and 0, 2.2, 10.2, 18.8, 32.4, and 57.8 wt% POSS/thiol-ene blends were

photocured using a Fusion Epiq 6000 UV cure line at a line speed of 12.19 m/min and a light intensity of 2.23 W/cm^2. For the POSS/thiol-ene copolymers, reaction mixtures contained equal molar ratios of thiol and ene, and the ene concentration (POSS and allyl ether) was varied. The blended systems contained 50:50 thiol:ene molar mixtures with only the weight percentages of POSS varied. The photoinitiator used was Darocur 1173 (2 wt%). Each reaction mixture was stirred manually and sonicated for 5 min to ensure efficient mixing of the POSS molecules in the thiol and ene comonomers. Thin film samples, which were applied to a glass substrate using a 20 mil drawdown bar, had a thickness of ~200-250 microns. These samples were used for thermal (differential scanning calorimetry and thermogravimetric analysis) and mechanical (dynamic mechanical analysis and nanoindentation) analysis, and physical measurements (Persoz hardness, pencil hardness, water contact angle measurements, and burn tests). Additional thin film samples were prepared by casting reaction mixtures containing 20 mol% (32.4 wt%) POSS onto a glass substrate using a 9 mil drawdown bar. These samples, having an average thickness of ~225 microns, were used to obtain oxygen flux measurements. Thick samples (~ 1 mm) were photocured in glass scintillation vials using a Rayonet photochemical reactor (300 nm) for a total cure time of 3 hours. The samples were cut into square shapes having dimensions 1 mm x 10mm x10 mm for free volume measurements (positron annihilation lifetime spectroscopy), and 1 mm x 3.5 mm x 1 mm for physical measurement (shore A hardness).

Nuclear Magnetic Resonance Spectroscopy

^{1}H and ^{13}C nuclear magnetic resonance (NMR) spectroscopy was performed using a Bruker 300 MHz NMR. NMR was used to identify reaction products and access reactant purity. The solvent for NMR characterization was deuterated $CDCl_3$ for the elucidation of monomeric thiol structure and functionality (Chapter 4) and deuterated DMSO, which contained trimethylsilane (TMS) as an internal standard, for elucidation of POSS monomer structure and functionality (Chapters 5 and 6).

Real-time Infrared Spectroscopy

Real-time Fourier-transform infrared (FTIR) is a useful tool for measuring individual monomer group conversion as a function of exposure time to a light source. This technique measures the loss of functional groups and, thus, the rate of conversion of each system component. The real-time IR (RTIR) instrumental setup (Figure 1) has a UV lamp source, IR light source, and an MCT detector. A sample is placed between NaCl plates and irradiation is controlled via a shuttered UV light source. Photopolymerization, initiated with or without a photoinitiator, is followed by an IR source directed through the sample plate and recorded by the detector.

A modified Bruker IFS 88 was used to collect real-time infrared spectra photoreactions and photopolymerizations. The changes in assigned peak area/heights were used to calculate monomer conversions as shown in Equation 1, where A_0 is the initial peak of the area/height and A_t is the peak height area/height at any given time, t, after initiation of the reaction by UV radiation. Conversion values have an approximate error of $\pm 2\%$.

(1)   Conversion = $[A_0 - A_t]/A_0$

Samples, with a thickness of approximately 20 microns, were placed in a horizontal

sample holder preceding irradiation with UV-light. Ultraviolet light from an Oriel lamp

system with a 200 Watt high pressure mercury-xenon lamp was channeled through an

electric shutter and fiber optic into the sample chamber. Upon exposure to UV radiation,

infrared absorption spectra were measured by a liquid nitrogen cooled MCT detector at a

scan rate of 1 scan/sec and a resolution of 4 cm^{-1} (Chapters 4, 5, and 6) or 0.5 scan/sec

(Chapter 7) and a resolution of 4 cm^{-1}.
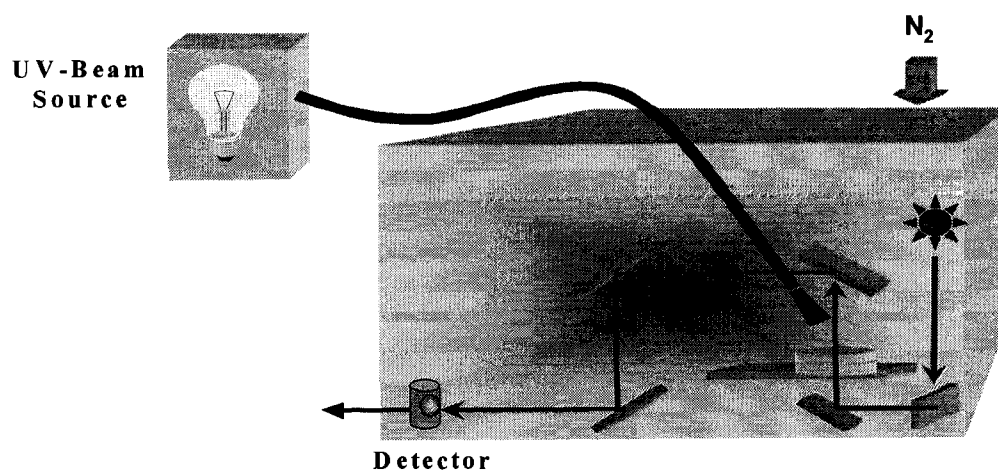
Figure 1. Real-time infrared (RTIR) instrumental setup.

Photo-Differential Scanning Calorimetry

Photo-DSC is a differential calorimeter that measures the rates of photopolymerization by recording the heat flow from the reaction as a function of time of the resultant exotherm curves (See Figure 2). The peak maximum of the exotherm curve (H_{max}) represents the maximum rate of polymerization. The instrument (Figure 3) operates by measuring differences in the voltage required to maintain the sample cell and reference cell at the same temperature. An electronic shutter controls the light emitted from the lamp and filters can be used to reduce the light intensity or select a particular wavelength. Light is transmitted through quartz windows to the sample and reference cells and the resultant exotherm is converted by an A/D converter and stored on a computer for processing. The lamp source was a 450 Watt medium pressure mercury lamp from Ace Glass placed above the DSC sample head. Samples of 2.00 ± 0.1 mg were weighed into crimped aluminum pans and photopolymerized in an inert environment by nitrogen purge for three minutes prior to irradiation. Sample thicknesses were approximately 200 μm.

In this research, peaks of exothermic plots of heat release were used to qualitatively measure the maximum rates of polymerization for free-radical photopolymerizations. Qualitatively, the peak of the exotherm is proportional to the maximum rate of polymerization and is used to directly compare different systems. Comparisons of peak maxima coupled with the times at peak maxima can be used to determine differences in speed of polymerizations. Additional quantitative information is extracted from the photopolymerization exothermic plot. Polymerization rates of photochemical reactions can be calculated from the amount of heat released which is

directly proportional to the number of monomer units converted to polymer. The polymerization rate (R_p) is dependent on the functionality (f), sample mass (m), enthalpy of polymerization (ΔH), molecular weight (MW), and the quantity of heat released (Q) as shown in Equation 2.

(2) $$R_p = [Q * (MW)]/[(f) * (m) * (\Delta H)]$$

Additionally, percent monomer is obtained from a comparison of total heat release and the theoretical enthalpy of polymerization for a given sample and size. The total amount of heat released during the polymerization is given by the integrated area under the exothermic curve.
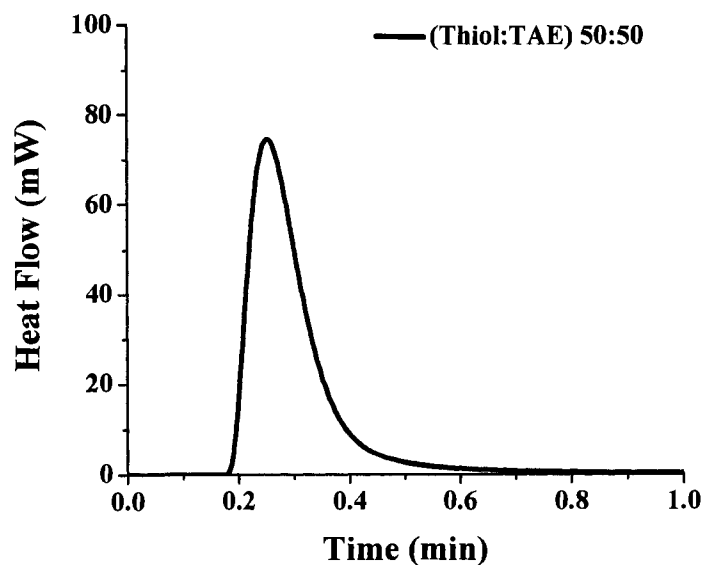
Figure 2. Photo-DSC. A typical exothermic plot of a thiol-ene polymerization (50:50 thiol:ene molar ratio).
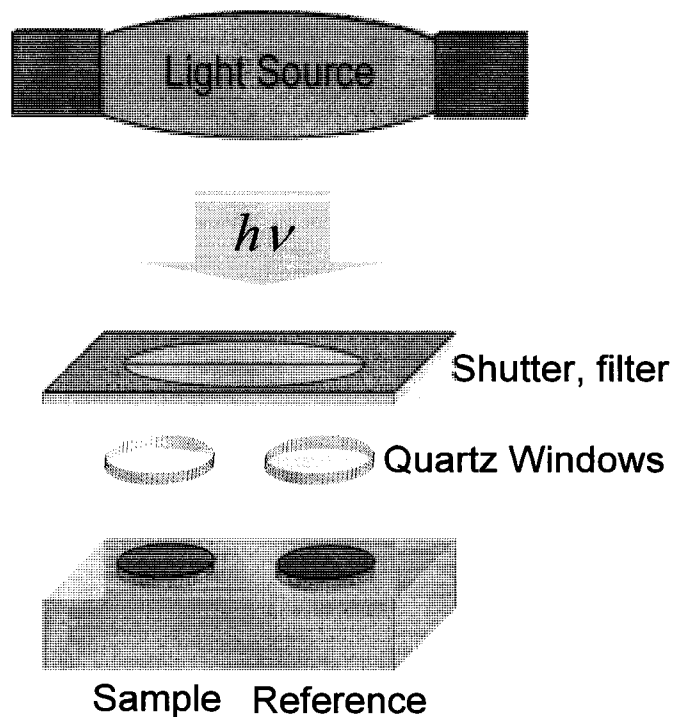
Figure 3. Photo-DSC instrumental setup.

Differential Scanning Calorimetry

Differential scanning calorimetry (DSC) is a practical tool for analyzing thermal transitions and performing annealing experiments. A TA Q1000 DSC was used to monitor glass transition temperature by heating samples from -90 °C to 40 °C(multithiol-allyl ether polymers, and thiol-ene/POSS copolymers and blends) and -90 °C to 90 °C (pure POSS monomers) at a rate of 10 °C/min under a constant nitrogen flow. Polymer samples of 3-10 mg were weighed and sealed in specially crimped aluminum pans, and POSS monomer samples of 1-4 mg were weighed in open aluminum pans. Annealing experiments were performed on a TA DSC 2920. Samples weighing 3- 10 mg were

placed in specially crimped aluminum pans. Experiments were systematically carried out over a temperature range from $T_{rubber} = T_g + 20$ to $T_{glass} = T_g - 50$ °C at a cooling rate of 0.2 °C/min followed by a heating rate of 5 °C/min. Sample thickness was ~150-200 microns for multithiol-allyl ether polymers and ~200-250 microns for thiol-ene/POSS copolymers and blends.

Dynamic Mechanical Analysis

Storage modulus (E') and loss tangent (tan δ = E''/E') curves as a function of temperature were evaluated using a TA DMA 2920. The thickness of each sample was typically 200-250 microns and width of 5 mm and a length of 25 mm. Experiments were performed in the tensile mode over a temperature range of of -60 °C to 40 °C. (An exception was the solid-phase separated blend, which was done at a temperature range of -50 °C to 80 °C.) The heating rate and force amplitude applied to the samples were kept at 2 °C/min and 15 μN, respectively. All storage modulus data is plotted in logarithmic scale as a function of temperature.

Thermogravimetric Analysis

Thermogravimetric analysis, performed on a TA 2050 Thermogravimetric Analyzer, was used to determine the mass loss as a function of temperature by heating 10 mg samples to 500 °C at a rate of 10 °C/min in air. Sample thickness was ~200-250 microns.

Positron Annihilation Lifetime Spectroscopy

Positron annihilation lifetime spectroscopy (PALS) is a powerful tool used to measure "hole" free volume and the distribution of free volume of amorphous and semicrystalline polymers. The positron (e+), the antiparticle of an electron, is injected into a polymer medium which may undergo a process of annihilation as a free positron with an electron or capture an electron to form a bound state known as the positronium (Ps). The bound state may be a para-positronium (pPs) with antiparallel spin having a lifetime (τ_1) of less than 0.5 ns or an ortho-positronium (oPs) with parallel spin having a lifetime of 1-4 ns in condensed matter. The more important of the two bound states is the ortho-positronium, which resides in the holes of free volume within the polymer. Free volume and its distribution are theoretically related to lifetime, τ_3, of the oPs in the polymer medium and the decay intensity, I, of the signal collected, respectively, and it can be shown that hole size and hole size distribution are proportional to these parameters. The lifetime, τ, is the time difference between detection of the birth and death signals. The positron is emitted from a radioactive source and concurrently channeled through a detector to obtain a birth signal and the polymer medium where it is converted into oPS. Upon annihilation of oPS, the death signal is detected by a second detector. The emitted positron and annihilated oPS have a signal reading of γ_{birth} = 128 MeV and γ_{death} = 0.511 MeV, respectively.

PALS measurements were conducted using a custom built instrument employing ^{22}Na as the positron source. The spectrometer, equipped with a special vacuum chamber and temperature control system, is comprised of BaF_2 scintillation crystals and photomultiplier tubes, a fast-fast coincidence system based on EC&G Ortec NIM

modules (model 583 constant-fraction discriminators), and a model 566 time-to-amplitude converter. Positron lifetime spectra were collected using a PCA multichannel analyzer. Special software, PATFIT-88, was used to process the data in order to extract mean oPs lifetimes and decay intensities. Samples, which were photocured in glass scintillation vials using a Rayonet photochemical reactor (300 nm lamp source) for a total cure time of 3 hours, were cut at a specified area (10 mm x 10 mm). Sample thickness was ~1mm.

Gas Permeation Measurements

Oxygen flux, J(t), at 1 atm pressure, and 23 °C was measured using a Mocon OXTRAN 2/21 unit (ASTM-D 3985-81). This apparatus employs a continuous-flow method to measure J(t) through polymeric films or thin sheets. Permeability, P, and diffusion coefficient, D, are obtained by performing a two-parameter least squares fit of the experimental flux data to the equation (3). The solubility, S, is obtained from the relationship [P = D * S]. Before every testing, film specimens were masked, glued using an epoxy based composition on aluminum foil with a circular exposure area of 5×10^4 m^2, then carefully conditioned in pure nitrogen inside the unit to remove traces of atmospheric oxygen, in order to obtain the non-steady state oxygen flux required for diffusion coefficient measurements. Average film thickness (~225 microns) was determined using a micrometer with the accuracy of individual thickness measurements approximately ±0.001 mm.

Contact angle measurements

Surface hydrophicity of silicate-based thiol-ene nanocomposites were observed by performing water contact angle measurements with a Ramé-Hart Model 200 contact angle goniometer. A series of three contact angle measurements were collected using a 10-µl droplet of deionized, distilled for each film sample. Sample thickness was ~250 microns.

Dynamic Light Scattering

Dynamic light scattering (DLS) experiments were performed at ambient temperatures using a Nanotrac NPA252 Combination analyzer equipped with a 3 mW external laser diode probe operating at 780 nm. The mean volume and number distribution of particle sizes were extracted by modified Mie calculations of the power spectrum obtained from light scattering of non-spherical silicate particles.

Viscosity Measurements

Viscosity measurements were obtained using a Brookfield Digital Viscometer Model. Measurements were obtained at various rotational velocities (1333 and 2666 RPM) after allowing the spindle to rotate for 1 min to determine the viscosities of silicate-based monomers at 30 °C.

Tensile Property Measurements

The tensile strength of the thiol-ene polymers was studied using mechanical testing system (MTS) model RT/10. Samples were cut into dogbone shape having geometric specifications described in ASTM 638-94b. Stress-strain measurements were conducted at temperature 50 °C above the T_g values of each samples at a strain rate of 8 %/min. Sample thickness was 0.3-0.7 mm.

Physical Properties Measurements

Persoz pendulum hardness was measured with a BYK Gardner Pendulum Hardness Tester according to ASTM D 4366. This method evaluates hardness by measuring the damping time of an oscillating pendulum, which is dependent upon the viscoelastic behavior of the coating. The pendulum sets upon the coating surface with two stainless steel balls which oscillates on the surface with an applied pressure when set into motion. A period of oscillation is 1 sec. Damping will be stronger or weaker base on the elasticity of the coating. Hard, glasslike substrates dissipate energy much less than soft, rubbery material; therefore, weak damping is correlates to materials that have high elasticity and exhibit glasslike behavior at the surface, i.e., damping on a glass surface is reflected with 430 ± 10 sec pendulum oscillation. For soft materials with no elasticity, pendulum damping is stronger.

Scratch resistance of each coating surface was determined by using a pencil hardness test with a series of pencils of varying hardness according to ASTM method D 3363 00. When testing for hardness, a coated panel is placed on a horizontal surface. The

pencil is firmly held against the film and then pushed away at a 45° angle in a 0.25-inch stroke. The starting pencil hardness is randomly selected and then continued up or down the scale depending if the coating was scratched. The hardest pencil that will not scratch the surface is determined. The scale of pencil hardness ranges from 9B-1B for soft lead and 1H-9H for hard lead with 9B and 9H being the softest and hardest leads, respectively. Persoz pendulum hardness was measured with a BYK Gardner Pendulum Hardness Tester according to ASTM D 4366. Persoz pendulum hardness measures energy damping caused by the viscoelastic characteristics of a material. A pendulum with 2 steel balls (500 g and 8 mm diameter) is placed on the coating surface. When set into motion, the pendulum oscillates between a deflection start angle (12°) and a deflection end angle (6°) within one second, i.e. 1 oscillation = 1 sec, and pressure is applied to the surface by the two steel balls. Damping is related to the viscoelastic response of a coating, i.e. a high number of oscillations is characteristic of a glasslike coating. Burn tests were performed on free-standing thin films (~250 microns) using ASTM method D 568 56 T. The films, which are cut in geometrical dimension of 6 mm (length) x 1mm (width), are ignited by a flame source, and time is recorded from the start of flame ignition to the extinction of the flame and/or total consumption of film by a flame. Shore A hardness was measured with a Type A durometer (Model 306L, PTC, Inc.) according to ASTM D 2240 00. Each sample is indented with a foot indenter at the surface of the thick film sample, and a durometer value is recorded and used to calculate the amount of force (N) required for fracture failure by indentation.

Chapter IV

THE EFFECT OF THIOL FUNCTIONALITY ON THE NETWORK FORMATION

USING KINETIC AND THERMOMECHANICAL ANALYSES

ABSTRACT

An investigation of the effect of thiol functionality (f_{thiol} = 2, 3, 4, 5.6, 8.1, and 11) on network formation was conducted by analyzing the kinetics and thermal/mechanical properties of thiol-ene networks. Novel multifunctional thiol monomers, having functionalities of 2 (**T2**), 5.6 (**T5.6**), 8.1 (**T8.1**), and 11 (**T11**), were synthesized by an amine-catalyzed thio-Michael addition reaction. This synthetic process is a facile method for synthesizing thiol monomers with branched structures that are not commercially available. The multifunctional thiols were copolymerized with multifunctional allyl ethers (functionality = 2 (diallyl ether (**DAE**) and functionality = 3 ((triallyl ether (**TAE**)) by a photoinduced polymerization. Photo-DSC analysis shows that the maximum rate of polymerization, R_{pmax}, is roughly equivalent for all monomeric thiol functionalities (an exception occurs for samples with T2) suggesting that thiol functionality has no significant effect on polymerization rate. Real-time FTIR analysis shows that total conversion is >90% for all monomeric thiol functionalities, although the gel equation predicts that gelation should occur at low conversions for samples prepared with thiol functionality greater than 4, which if the gel equation applied would suggest that the final overall conversions should be much less than actually observed. High conversions are attributed to looping events occurring concomitantly with network formation thus

reducing the effective network density. The glass transition temperature and tensile strength are shown to increase with thiol functionality of 4 or less due to formation of highly dense networks, while leveling off for samples made from thiols with functionality greater than 4. This is certainly not what would be predicted from the traditional gel equation.

INTRODUCTION

Thiol-ene photopolymerization offers many advantages over traditional acrylate photopolymerization processes. Desirable features of thiol-ene photopolymerization include fast polymerization rates in air, [1-7] photoinitiatorless reactions, [2-4] low shrinkage at high monomer conversion[3,4] and, most importantly, versatility in ene monomer selection. [5-11] Almost any type of ene can participate in a thiol-ene polymerization with fast rates of cure. This is advantageous since many ene comonomers with various chemical structures and functionalities are commercially available. The range of polymer properties is usually dictated by the ene structure due to the narrow selection of multifunctional thiol monomers that are available commercially.

The basic thiol-ene photopolymerization is a two-step radical chain process involving a propagating/chain transfer sequence resulting in thiol addition across the ene double bond (Equation 1). [6]

$$RS\bullet + R'CH{=}CH_2 \xrightarrow{\quad k_p \quad} R'C\bullet H{-\!-}CH_2SR \qquad (1a)$$

$$R'C\bullet H{-\!-}CH_2SR + RSH \xrightarrow{\quad k_{CT} \quad} R'CH_2{-\!-}CH_2SR + RS\bullet \qquad (1b)$$
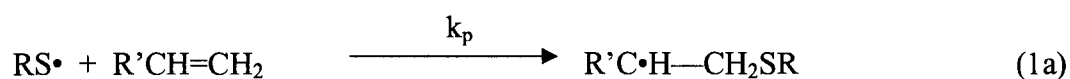
In thiol-ene photopolymerizations, the polymerization rates (R_p) are subject to the type of ene comonomer used, and, more specifically, the electron density of the double bond. The order of ene reactivity is vinyl ether > allyl ether > acrylate >>> unsaturated ester, i.e. the fastest polymerization rates occur for copolymerizations involving electron-rich enes. [4]

Hoyle and Jonsson et al. have investigated the photopolymerization kinetics of a tetrathiol-tetravinyl ester copolymerization process, and found that the system gives fast rates of polymerization and high conversions of functional groups. [7] Although these systems exhibit desirable kinetic behavior, little is known about the influence of thiol functionality on the kinetics of the thiol-ene photopolymerization and the ensuing polymer network. This work reports on the influence of thiol functionality on the polymerization of various multifunctional thiol-triallyl ether systems and multifunctional thiol-diallyl ether systems. The effect of thiol functionality on the polymerization rates, functional group conversions (of both thiol and ene groups), and the resulting thermal and mechanical properties of the networks generated is thus established.

EXPERIMENTAL

Synthetic method for Novel Multifunctional Thiol Monomer Mixtures

The series of multifunctional thiol monomers (functionality = 2, 6, 9, and 12) were synthesized using an amine-catalyzed thio-Michael addition reaction between multifunctional thiol and acrylate components. The base thiol components, trimethylolpropane tris (3-mercaptopropionate) and pentaerythritol tetrakis (3-mercaptopropionate), were used as received (Aldrich). The acrylate components, ethyl acrylate (Aldrich), 1, 6-hexanediol diacrylate (Sartomer), trimethylolpropane triacrylate (Aldrich), and pentaerythritol tetraacrylate (Sartomer), were used as received. The catalyst for each reaction was diethyl amine (Aldrich) which was used as received. For each reaction, an acrylate/amine mixture containing 2 mol% amine (thiol) was added

slowly to thiol resulting in a mixture of acrylate/thiol with excess thiol (25 mol% excess),

while stirring at a rate of 1.0 to 1.6 mL/h using a KDS 100 syringe pump system (kd

Scientific) for a total time of 3-5 hours. The reaction was then allowed to sit at room

temperature for at least 6 hours before the reaction products were analyzed.

Titrimetric Assay of Thiol Functionality

The assay of thiols using this titrimetric method involves the reaction of thiol and

silver ions in a pyridine solution to form free protons and silver mercaptide precipitant,

which is titrated with sodium hydroxide using a phenolphthalein indicator to determine

the number of equivalent thiol groups.[8] A 0.4 M silver nitrate solution (5 mL) is added to

a 0.0018 moles of thiol in 15 mL of pyridine causing the precipitation of silver

mercaptide. After the addition of 100 mL of distilled water and 3-4 drops of

phenolphthalein indicator, the solution is titrated with 0.1 N sodium hydroxide to a light

pink end point along with a color change of the precipitant from yellow to a white. The

concentration of thiol groups was then calculated by Equation 1.

(1)

$$\frac{\text{Molecular Weight (g/mol)} * \text{Volume of Titrant (L)} * \text{Normality of Base (N)}}{\text{Mass (thiol) (g)}}$$

Calculations:

T2

$$\frac{498.68\ (\text{g/mol}) * 0.014\ (\text{L}) * 0.089\ (\text{N})}{0.29\ (\text{g})} = 2$$

T5.6

$$\frac{1024.75 \ (g/mol) * 0.0168 \ (L) * 0.089 \ (N)}{0.27 \ (g)} = 5.6$$

T8.1

$$\frac{1443.89 \ (g/mol) * 0.0178 \ (L) * 0.089 \ (N)}{0.28 \ (g)} = 8.1$$

T11

$$\frac{1842.02 \ (g/mol) * 0.0166 \ (L) * 0.089 \ (N)}{0.25 \ (g)} = 11$$

Instrumentation

The ^{1}H NMR spectra of the monomeric thiol mixtures were obtained on a Bruker AC-300 spectrometer using 5 mm o.d. tubes. Sample concentrations were about 15% (w/v) in CDCl$_3$.

Real-time FTIR analysis was performed on an IFS-88 Bruker spectrometer. By measuring the decrease in the peak area with time, it was possible to obtain conversions of thiol and ene groups versus time. Samples placed between NaCl plates (~ 20 microns thick) were irradiated by the filtered UV light with a 1.0 neutral density filter (light intensity 18.7 mW/cm^2). The peak assignments for the thiol and allyl ether were 2570 cm^{-1} and 1670 cm^{-1}, respectively.

Photo-differential Scanning Calorimetry exotherms (photo-DSC) were obtained using a Perkin-Elmer DSC-7 modified by adding quartz windows to the sample head

cover. Samples (2 mg) were placed in aluminum DSC pans and irradiated with filtered UV light. The light intensity of the full arc was 38.9 mW/cm^2, and the actual light intensity used to expose samples was 3.89 mW/cm^2 after passing through a 1.0 neutral density filter.

Differential scanning calorimetry (DSC) was performed on a TA Q1000 DSC. Samples (3-8 mg) were placed in aluminum pans and heated from -90 °C to 40 °C at a heat ramp of 10 °C/min.

The tensile strength of the thiol-ene polymers was studied using a Mechanical Testing System (MTS) model RT/10. Samples were cut into dogbone shape having geometric specifications (5 mm x 20 mm) described in ASTM 638-94b and film thickness of 0.3-0.7 mm using a 40 mil drawdown bar. Stress-strain measurements were conducted at a temperature 50 °C above the T_g of each sample at a strain rate of 8 mm/min using a 100 N load cell as the applied force.

Polymer film formation

Allyl Pentaerythritol (triallyl ether) was obtained from Perstorp Specialty Chemical Company. Phototinitiator Darocur 1173 was obtained from Ciba Specialty Chemicals, Inc. Trimethylopropane tris (3-mercaptopropionate) (TriThiol), butyl mercaptopropionate, and diethyl amine were purchased from Aldrich Chemical Company. All samples were used as received.

Thiol-ene films containing 50:50, 30:70, 40:60, 70:30, and 60:40 thiol:allyl ether molar mixtures were photocured on a Fusion 6000 UV cure line. Reaction mixtures contained different molar ratios of thiol to ene in addition to 2 mol% photoinitiator

(Darocur 1173). A 400-W Fusion D-bulb lamp was used as the light source, and each film was cured at a line speed of 12.19 m/min and a light intensity of 2.29 W/cm^2. Each film, obtained by application on glass substrate with an 8-mil drawdown bar, had a thickness of ~150–200 microns. These samples were used in DSC analysis.

RESULTS AND DISCUSSION

Herein, the impact of thiol functionality on the photopolymerization and ensuing network formation for various systems involving the copolymerizations of novel and commercially-available multi-thiol and multi-ene components shown in Figure 1, along with their formula names and acronyms, is described. The reaction mixtures used to compare the structural effects were comprised of 30:70, 40:60, 50:50, 60:40, and 70:30 molar mixtures of thiol to ene functional groups. Each mixture contained 2 wt% photoinitiator (Darocur 1173). These reaction compositions were used for each multi-thiol/multi-ene monomer combination.

Syntheses of Novel Multifunctional Thiol Monomers

In general, novel multifunctional thiol monomers T2, T5.6-T11 (whose structures and acronyms are given in Figure 1) were synthesized by a catalyzed Michael addition of a multifunctional aliphatic thiol to the electron-deficient vinyl group of a multifunctional acrylate.[9] No solvents were required for the reaction, although an excess of thiol was used to ensure that only one thiol group per thiol monomer reacted with each vinyl group. For this study, diethyl amine was first added to the acrylate where no doubt much of the diethyl amine was consumed by a Michael addition with the acrylate. Typically, for

T5.6-T12, the corresponding acrylate/diethyl amine (2 mol%) mixture was added dropwise to an excess of thiol with constant stirring of the reaction mixture. For T2, the thiol to acrylate group concentration ratio was 3:1. For T5.6-T11, no purification methods were used to remove excess thiol; therefore, the final product was a thiol monomer mixture.

The final product was characterized using proton NMR to confirm the formation of the thioether bonds and the disappearance of the acrylate vinyl groups. (Figure 2) As shown in Figure 2, after the reaction of the thiol and acrylate vinyl groups, the acrylate protons at 6.4, 6.2 and 5.8 ppm are absent. New proton peaks at 2.8 and 2.6 ppm are due to the methylene protons adjacent to sulfur in the thio-propionate group. The chemical shifts for the other protons are identical to the proton shifts in the original acrylate and thiol species (See Figure 1 and Table 1). The functionality of each thiol monomer was determined by a titrimetric assay [8] of the thiol monomer mixture (Table 2).

This synthetic method is a useful tool for synthesizing the mixtures containing highly branched thiols as well as lower functional thiol mixtures with the composite functionality listed in Table 2. These branched thiols monomers (T2, T5.6-T11) offer unique architectures that are unavailable commercially and expand the range of thiol functional species. Theoretically, thiol monomers can be synthesized by reaction of any suitable unsaturated group and thiol as is clearly demonstrated by the syntheses of samples T2, T5.6, T8.1, and T11.

Kinetics Study of Multifunctional Thiol-Allyl Ether Photopolymerizations

Kinetic analyses were conducted via photo-DSC and real-time infrared (RTIR) to

determine how functionality and concentration affected the polymerization of the

multifunctional thiol systems and multifunctional allyl ethers (ene functionality is 2 or 3).

Specifically, we investigated how thiol average functionality and concentration affected

the polymerization rates (photo-DSC) and the functional group conversions of thiol and

allyl ether (RTIR) for the photopolymerizations of the multifunctional thiol-allyl ether

systems. The exothermic plots (heat flow versus reaction time) and peak areas (area

(under the exotherm) vs. thiol mol%), which is the total heat released by the conversion

of double bonds, for the series of multifunctional thiol-allyl ether photopolymerizations

are shown in Figure 3 (a-b) and Figures 4 -8 (a-d) (Note that the mole percent

concentration of thiol functional groups is denoted directly on the figures as SH50, SH60,

SH70, SH40, and SH30 corresponding to samples with 50, 60, 70, 40 and 30 mole

precent thiol based on 100 mole percent being a combination of the thiol plus the ene

molar functional groups). For all of the multithiol-DAE systems and mutithiol-TAE

mixtures, fast rates of polymerization are achieved. In each case, the exotherm maximum

is lowest for the system having the 30:70 thiol-ene molar functional group ratio

representing an off stoichiometric mix. For samples with thiol concentration greater than

the ene concentration (the 60:40 and 70:30 thiol:ene samples) the rate generally

decreased. And, for each basic system the sample with the 50:50 thiol:ene molar

functional group concentration had the highest peak area, i. e., the highest total extent of

thiol-ene reaction per sample weight. This is certainly consistent with the equal

stoichiometric ratio of thiol to ene functional groups for the 50:50 molar mixtures in each

case. The photo-DSC plots in Figure 9 which accumulates the results in Figures 3-8 for each of the 50:50 molar ratio of thiol:ene in the thiol-DAE and thiol-TAE mixtures shows that reasonably fast rates (Figure 9 (a and c)) and conversions (area under the exotherm) (Figure 9 (b and d)) are attained in each case. Taking into account variations in actual total molar concentrations in each sample of the thiol and ene functional groups in each system, the fact that there is no significant drop in rates and total conversions for the systems with higher thiol functionalities (T5.6, T8.1, and T11) is remarkable and certainly is contrary to what would be expected if the traditional gel equation were obeyed. The results in Figure 9 should be interpreted in the context of the average molecular weight (MW) per thiol group (thiol equivalent weight) for a given thiol monomer in the reaction mixture since this will affect the actual total amount of thiol and ene functional groups which are in a given 2 mg sample used to generate the photo-DSC exotherm curves. Thus, the small differences of the total amounts of heat released (areas under the exotherm) for the reaction of each thiol monomer with the respective DAE or TAE ene as shown in Figure 9 b and d when the thiol equivalent weights in Table 3 are taken into account clearly indicate that thiol:ene samples with even the highly functional thiols (T5.6, T8.1 and T11) result in essentially equivalent conversions to those obtained for the systems with the T2, T3, and T4 thiols. This conclusion is affirmed by the real-time infrared results described next

The real-time infrared (RTIR) plots (% Conversion versus UV irradiation time) for the multithiol-DAE and multithiol-TAE systems at molar concentrations of 50:50, 40:60, 60:40, 30:70, and 70:30 thiol to allyl ether ene functional group concentrations (Figures 10-19) show near complete (> 90%) conversion of the thiol or ene component

that is at the lowest concentration for each multifunctional thiol-allyl ether system. In the

case of the 50:50 molar mixtures in Figures 10 and 11, the conversion is essentially 100

% for both thiol and ene groups; even for the case where the thiol functionality is 8.1 or

11! This is presumably due to looping (multiple reactions) between the two enes and the

thiol. Table 4 lists the conversions at gelation predicted by calculations from the

standard gel equation 2 for each of the systems at 50:50 molar ratio. The experimental

values for the ultimate conversion of thiol and ene functional groups far exceed the

calculated gel points (α) predicted by the gelation equation (2) for each sample. This is

especially significant for samples that contain T5.6, T8.1, and T11 where the gel equation

(Table 4) would predict that gelation occurs at conversions substantially below 0.5

fractional conversions and hence it would not be expected that the final conversions

under the experimental conditions (low light intensity) would be essentially equal to

those obtained for samples made from T2, T3 and T4 thiols.

$$\alpha = \frac{1}{[r(f_{thiol}-1)(f_{ene}-1)]^{0.5}} \quad , \quad r = \text{ratio of thiol to ene molar} \quad (2)$$
$$\text{functional groups}$$

This kinetic conversion behavior, exhibited by high conversions and delayed gelation, is

strong evidence that localized events of looping (Figure 20 illustrating multiple reactions

between thiol and ene groups of the same interacting occur during the polymerization

which result in higher functional group conversions being required to attain gelation and,

hence, an overall higher final conversion than would be expected if the system gelled at

the fractional conversion calculated by the gel equation. This is one of the better and

clearer reported illustrations of the break down of the gel equation for systems with one

of the functional groups greater than 4. Consequently, for samples prepared from thiols with functionality of greater than 4, the kinetic results in this section both from photo-DSC and RTIR measuremnts suggest that the thermal and mechanical properties should also certainly be affected by the reduced crosslink density compared to what would be expected if Equation 2 was obeyed. The thermal and mechanical properties of the thiol-ene films will be discussed in the next section in the context of the apparent breakdown in the gel equation suggested by the kinetic data in this section.

Thermal and Mechanical Analyses of Multifunctional Thiol-Allyl Ether Photopolymers

The thermal and physical properties of films made from the multithiol-TAE and multithiol-DAE systems were characterized by DSC and tensile strength stress-strain measurements. In Figures 21-26, plots of the DSC scans and the corresponding glass transition temperatures (T_g) versus thiol functionality for the multithiol-TAE systems at varying thiol concentrations are shown. First consider the results in Figure 21 for the 50:50 molar functional group mixtures of TAE and each thiol. Initially, for these systems, note that the T_g increases with thiol functionality as the thiol functionality increases from 2 to 4 from -35 °C for the T2-TAE network to -17 °C and -12 °C for the T3-TAE and T4-TAE networks followed by only marginal change for samples made with T5.6 to T11 (Figure 21). For nonstoichiometric molar ratios between the TAE and thiols in Figure 22, the T_g also increased similarly for the network systems formed from mixtures comprised of thiols with a functionality of 4 or less, leveling off for samples prepared from thiols with functionality from 6 to 12. The results for the 70:30 thiol:ene based systems all exhibited very low T_gs with a moderate increase in T_g with increase in thiol functionality from 3 to 12: the small increase in T_g noted for the samples prepared

from T5.6-T11 in Figure 23 may result from the concentration of unreacted thiol functional groups which would tend to reduce the inherent multiple crosslinks (looping) formed between given ene and thiol molecules, and hence an increase in T_g. The DSC results in Figures 24-27, which include networks prepared from stochiometric (50:50 thiol:ene molar functional group ratio) and non-stochiometric mixtures (60:40 and 70:30 thiol:ene molar functional group ratio), the T_g values did not increase with the thiol functionality. Additionally, enthalpic relaxation, which is observed as minimum peaks in the glass transition region, occurred for most networks formed from mixtures with low functional thiols (where the functionality is less than or equal to 4), although in some cases a small enthalpy relaxation was observed for samples formed from T5.6.

For all systems, the elastic modulus, which is obtained form the slope of the tensile stress-strain plot, shows an initial increase with thiol functionality (for functionalities of 4 or less) in Figures 27-32. For the 50:50 thiol:ene based films (Figure 27), the resultant tensile modulus increases as the thiol functionality increases from T2 to T4, and then essentially levels off commensurate with the results obtained for the T_g values in Figure 21, i.e., modulus values of 3.4 MPa, 3.9 MPa, 6.9 MPa, 6.0 MPa, 7.6 MPa, and 8.0 MPa, respectively, for films prepared from samples with T2, T3, T4, T5.6, T8.1, and T11. For unstoichiometric networks, the changes in T_g and elastic modulus at 60:40 and 70:30 thiol to allyl ether molar ratios follow a similar trend with increasing thiol functionality (Figures 28 and 29), although the increase in modulus for the 70:30 mixtures (Figure 29) was not as pronounced and followed the general trend observed for the T_g values in Figure 23. Note that stress-strain plots for samples prepared from T2-TAE, T3-DAE and T4-DAE could not be made since the materials were too soft for

measurements using a 100 N load cell. As stated in the previous section, the formation of

looped structures in the polymer network greatly reduces its effective network density,

which, subsequently, affects the thermal and physical properties. Certainly in the 50:50

and 60:40 thiol:ene mixtures, substantial changes occur in the network when the

functionality of thiol is increased to 4, leading to the formation of a more uniform and

dense network. The networks formed with thiols having functionalities greater than 4

show insignificant differences in tensile modulus values. For the set of multithiol-DAE

networks (see results in Figures 30-32) at any molar concentrations of thiol and allyl

ether, it was not possible to evaluate networks for any samples where the thiol had a

functionality of 3 or less. For the 70:30 thiol:ene molar mixtures, films made from thiols

with functionality of 4 or less were soft and stress-strain measurements could not be

made. Although it is much more difficult to assess the samples prepared with DAE

which is difunctional, in general it can be concluded that for samples where measuremnts

could be made, the modulus exhibited little change indicating again the importance of

looping in network formation.

CONCLUSION

The kinetic, thermal and mechanical results presented for the photopolymerization

of thiol-ene systems provide one of the best illustrations in the literature for the

breakdown of the traditional gel equation in predicting the conversions associated with

gelation for the step-growth polymerization of multifunctional components where the

functionality of one of the components exceeds 4. Specifically, the kinetic analyses of

the photopolymerization of a series of multithiol-DAE and multithiol-TAE systems

where the thiol component has average functionality ranging from 2 to 11 indicate that the functionality of the thiol does not significantly affect the functional group conversion. Copolymerization of highly functional thiol monomer results in the formation of looped structures within the network. The presence of the looped structures reduces the effective crosslink density of the network compared to that expected for samples that behaved according to the gel equation, causing a distinct effect on the network thermal and mechanical properties. A network is formed with increasing T_g and tensile strength with thiol functionality when the thiol functionality is relatively low (functionalities of 4 or less), while samples prepared from higher functional thiols (functionalities greater than 4) show little change in T_g and tensile strength due to the looping process.

REFERENCES

[1] Reddy, S. K.; Cramer, N. B.; Kalvaitas, M.; Lee, T.; Bowman, C. N., *Austr. J. Chem.*, **2006**, *59*, 586-593.

[2] Cramer, N. B.; Reddy, S.; Bowman, C. N., *Polym. Prep.*, **2004**, *45*, 55-56.

[3] Bowman, C. N.; Carioscia, J.; Lu, H,; Stansbury, J. W., PCT Int. Appl., **2005**, 34 pp.

[4] Carioscia, J. A.; Lu, H.; Stanbury, J. W.; Bowman, C. N., *Dental Mat.*, **2005**, *21*, 1137-1143.

[5] Reddy, S. K.; Cramer, N. B.; Bowman, C. N., *Macromolecules*, **2006**, *39*, 3681-3687.

[6] Jacobine, A. F. In *Radiation Curing in Polymer Science and Technology III, Polymerisation Mechanisms*, Fouassier, J. D., Rabek, J. F., Eds.; Elsevier Applied Science: London, 1993; Vol. 3, p. 219.

[7] Lee, T.; Kaung, W.; Joensson, E. S,; Lowery, K.; Guymon, C. A.; Hoyle, C. E., *J. Polym. Sci., A*, **2004**, *42*, 4424-4436.

[8] Saville, B. *Analyst*, **1961**, *86*, 29-32.

[9] Van Dijk, J. and Theodorus, M. *PCT*, 0064959, **2000**.
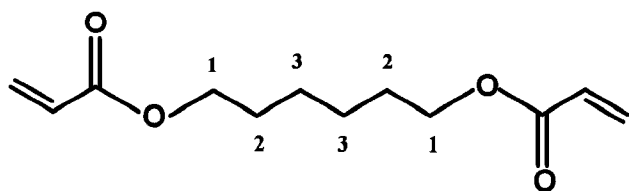
1,6-hexanediol Diacrylate (**HDDA**)
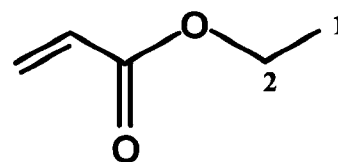
Ethyl Acrylate
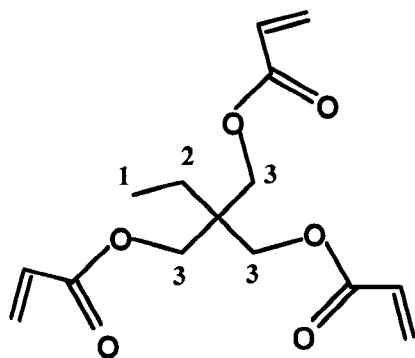
Trimethylolpropane Triacrylate (**TMPTA**)
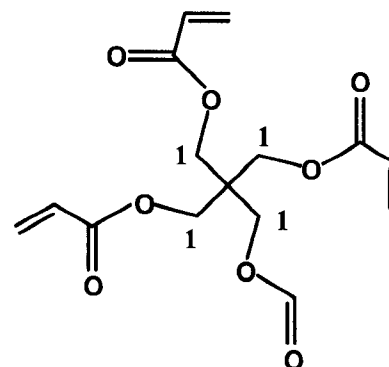
Pentaerythritol tetraacrylate (**PETA**)
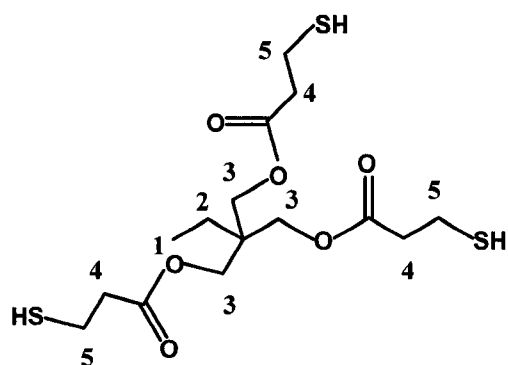
Trimethylolpropane tris (3-mercaptopropionate)

(**TriThiol**)
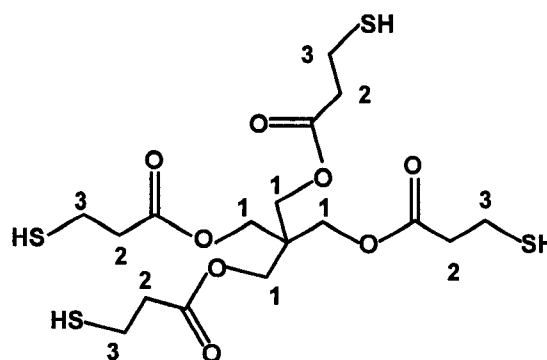
Pentaerythritol tetrakis (3-mercaptopropionate

(**TetraThiol**)
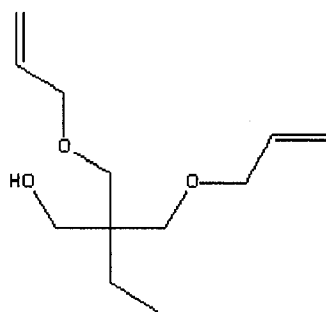
Trimethylolpropane Diallyl Ether

DAE
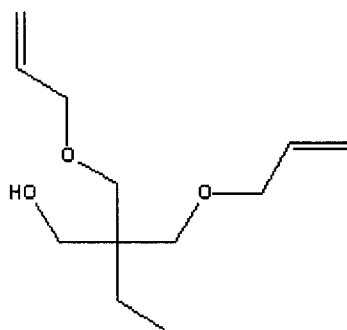
Triallyl Ether Allyl Pentaerythritol

TAE
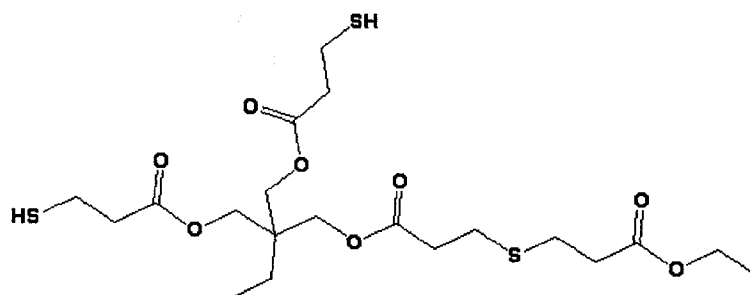
T2
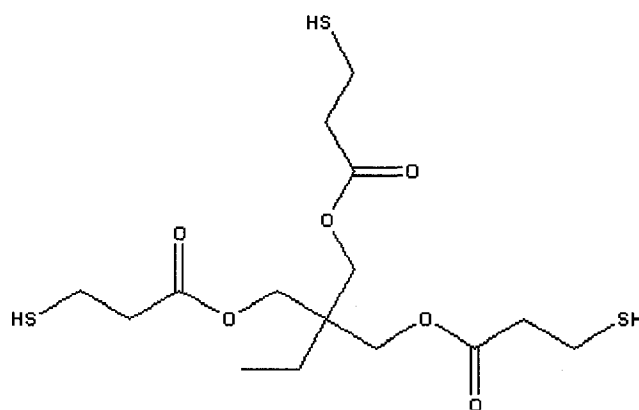
Trimethylolpropane tris(3-mercaptopropionate)

T3
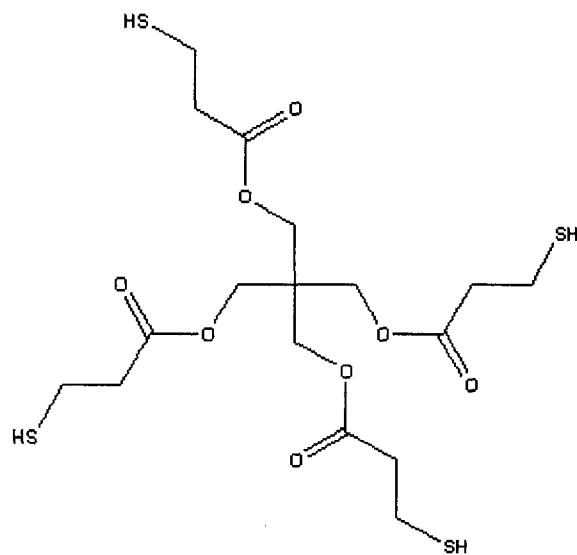
Pentaerythritol tetrakis(3-mercaptopropionate)

T4
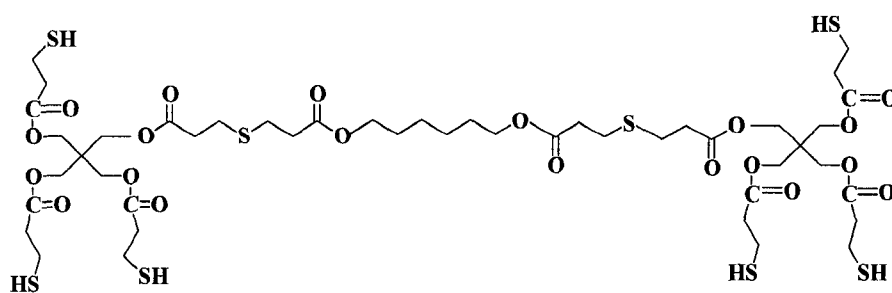
T5.6
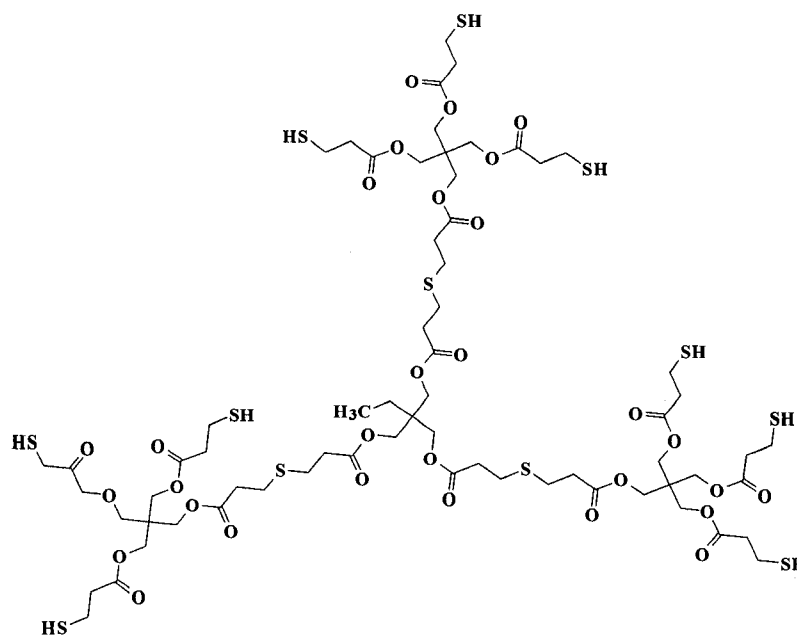
T8.1
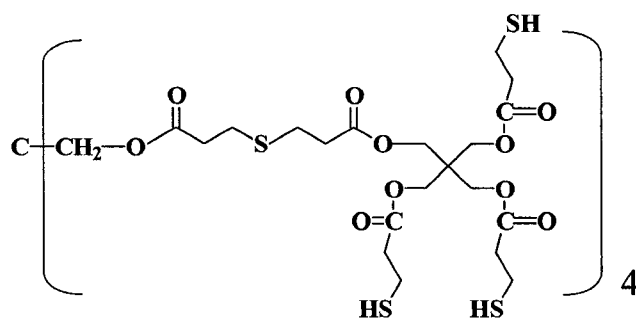
T11

Figure 1. The chemical structures of the multithiol and multiene components, along with their formula names and acronyms.
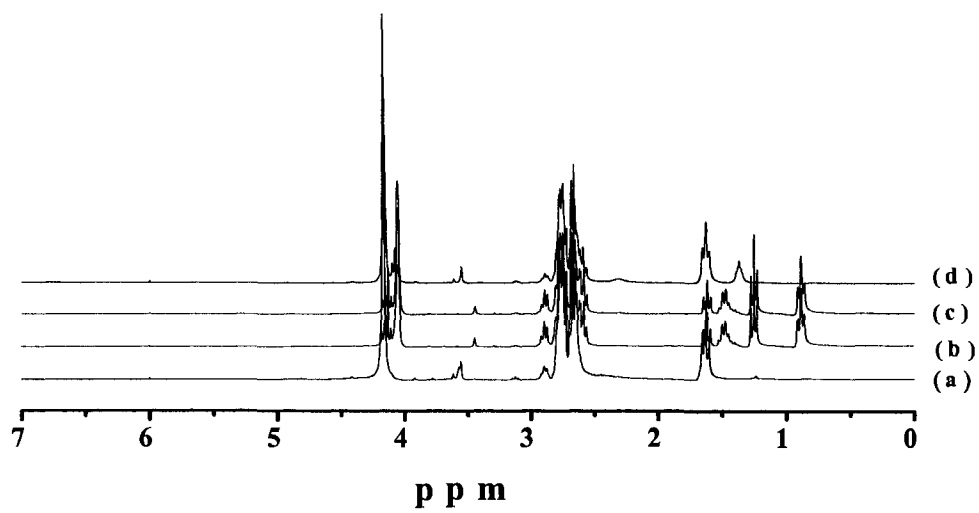
Figure 2. Proton NMR. Spectra of the synthesized multifunctional thiols: a) T2, b) T5.6, c) T8.1, and d) T11.
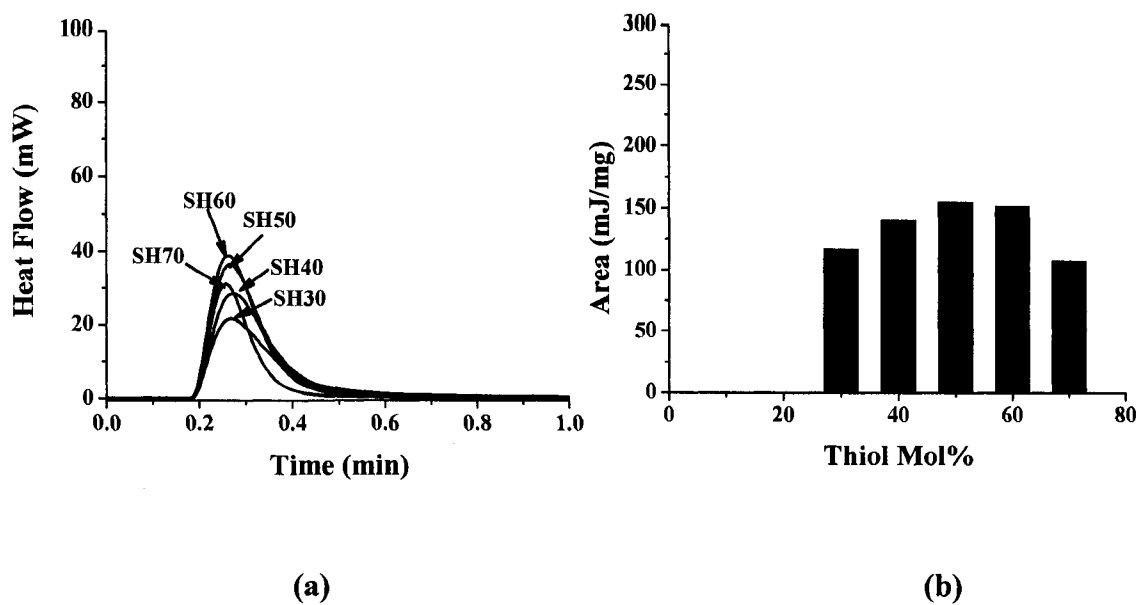
Figure 3. Photo-DSC. a) Exothermic plots (Heat Flow vs. Time) and b) plots of peak areas (Area (under the exotherm) vs. Thiol Mol%) of T2:TAE photopolymerizations at various concentrations. Light intensity of 3.89 mW/cm^2 using a 1.0 neutral density filter.
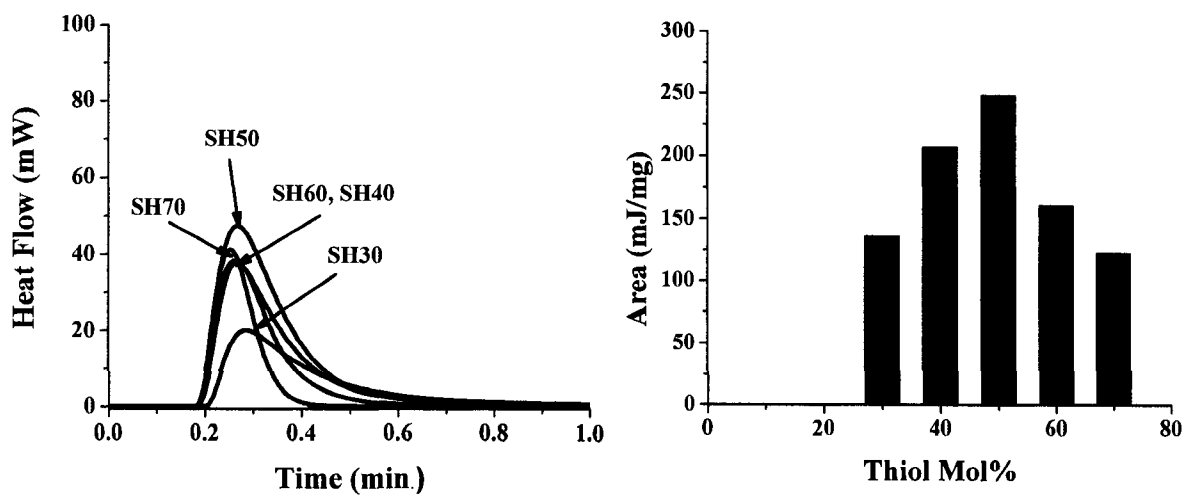
(a)

(b)
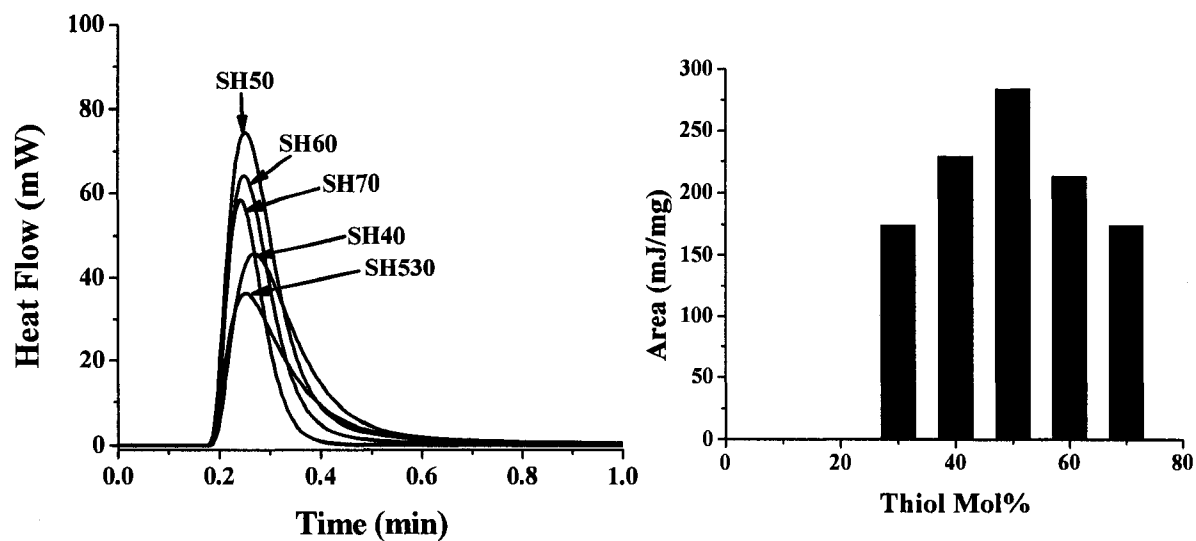
(c)

(d)

Figure 4. Photo-DSC. a) Exothermic plots (Heat Flow vs. Time) and b) plots of peak areas (Area (under the exotherm) vs. Thiol Mol%) for T3:DAE and c) exothermic plots (Heat Flow vs. Time) and d) plots of peak areas (Area (under the exotherm) vs. Thiol Mol%) for T3:TAE at various concentrations. Light intensity of 3.89 mW/cm^2 using a 1.0 neutral density filter.
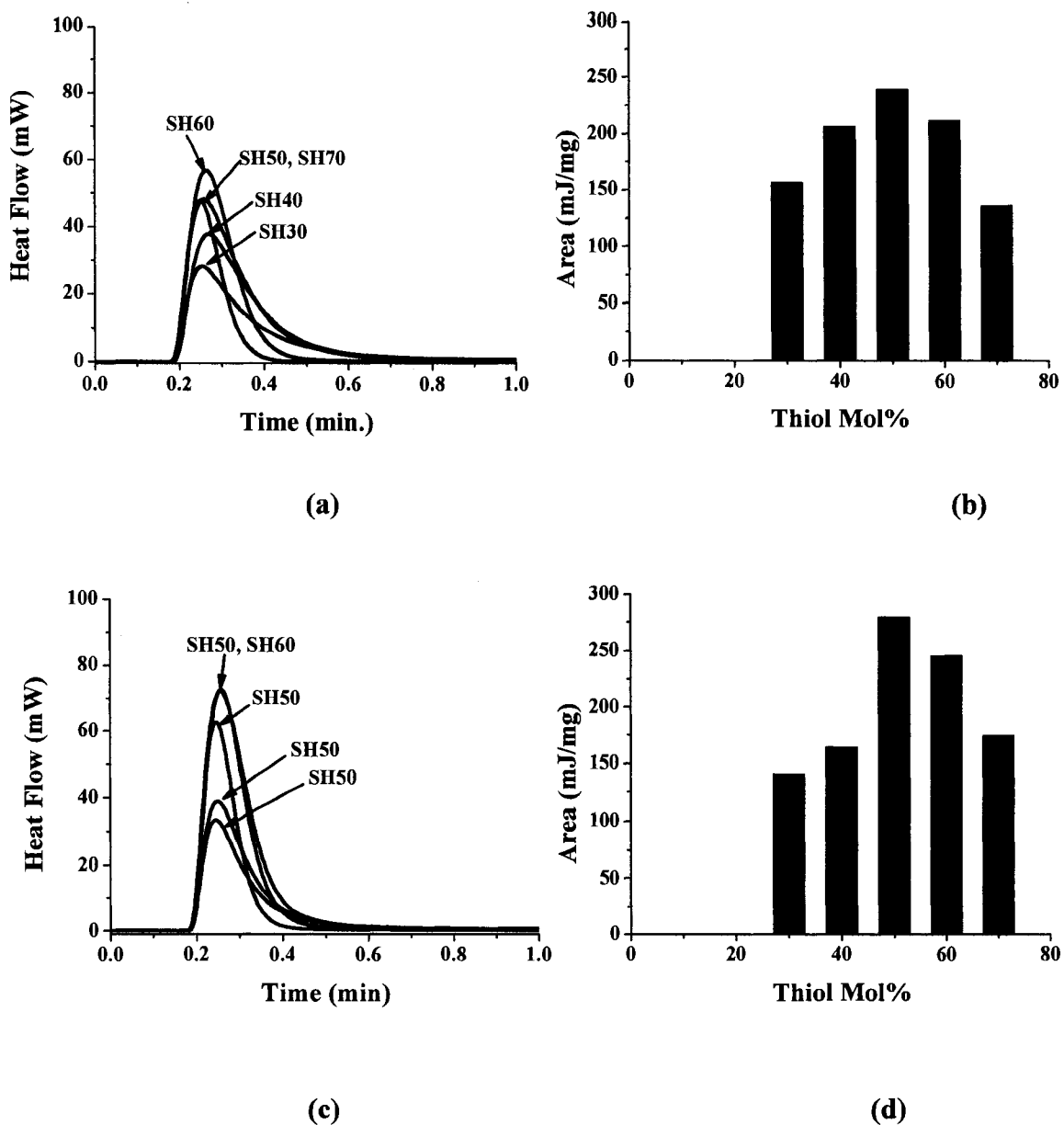
Figure 5. Photo-DSC. a) Exothermic plots (Heat Flow vs. Time) and b) plots of peak areas (Area (under the exotherm) vs. Thiol Mol%) of T4:DAE and c) exothermic plots (Heat Flow vs. Time) and d) plots of peak areas (Area (under the exotherm) vs.Thiol Mol%) for T4:TAE photopolymerizations at various concentrations. Light intensity of 3.89 mW/cm^2 using a 1.0 neutral density filter.

(a)

(b)

(c)

(d)
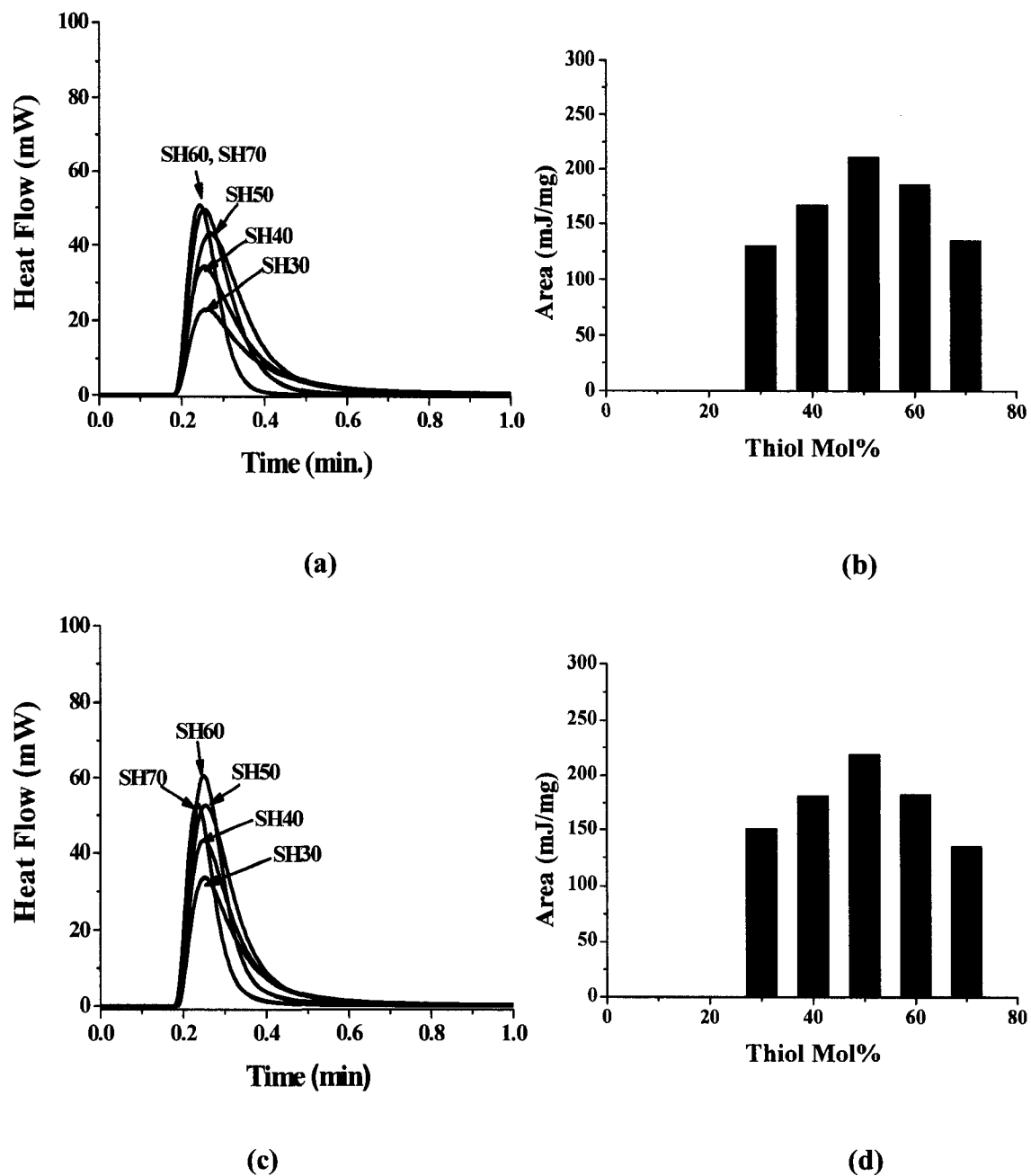
Figure 6. Photo-DSC. a) Exothermic plots (Heat Flow vs. Time) and b) plots of peak areas (Area (under the exotherm) vs. Thiol Mol%) of T5.6:DAE and c) exothermic plots (Heat Flow vs. Time) and d) plots of peak areas (Area (under the exotherm) vs. Thiol Mol%) for T5.6:TAE photopolymerizations at various concentrations. Light intensity of 3.89 mW/cm² using a 1.0 neutral density filter.

(a)

(b)

(c)

(d)
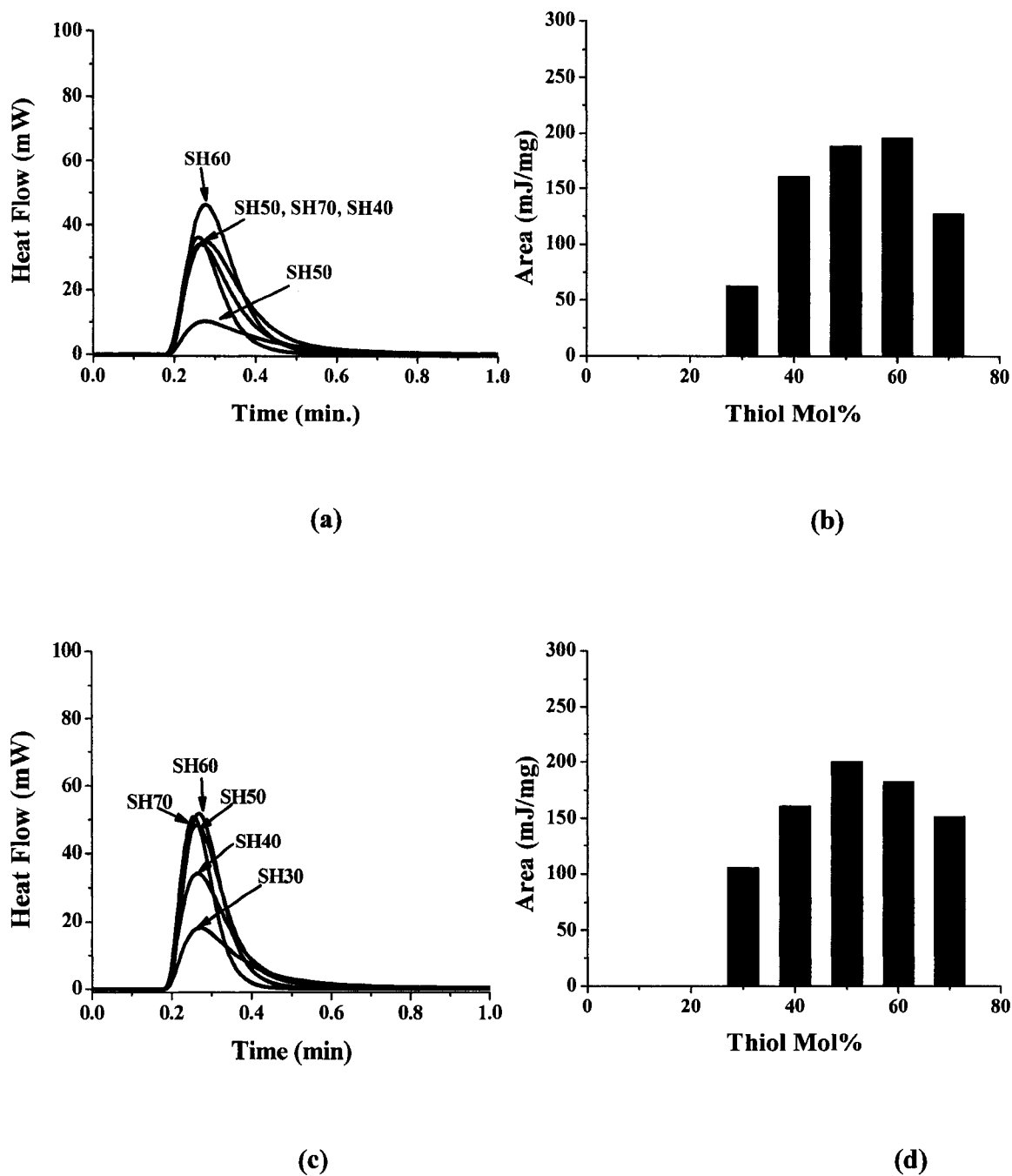
Figure 7. Photo-DSC. a) Exothermic plots (Heat Flow vs. Time) and b) plots of peak areas (Area (under the exotherm) vs. Thiol Mol%) of T8.1:DAE and c) exothermic plots (Heat Flow vs. Time) and d) plots of peak areas (Area (under the exotherm) vs. Thiol Mol%) for T8.1:TAE photopolymerizations at various concentrations. Light intensity of 3.89 mW/cm² using a 1.0 neutral density filter.

(a)

(b)

(c)

(d)
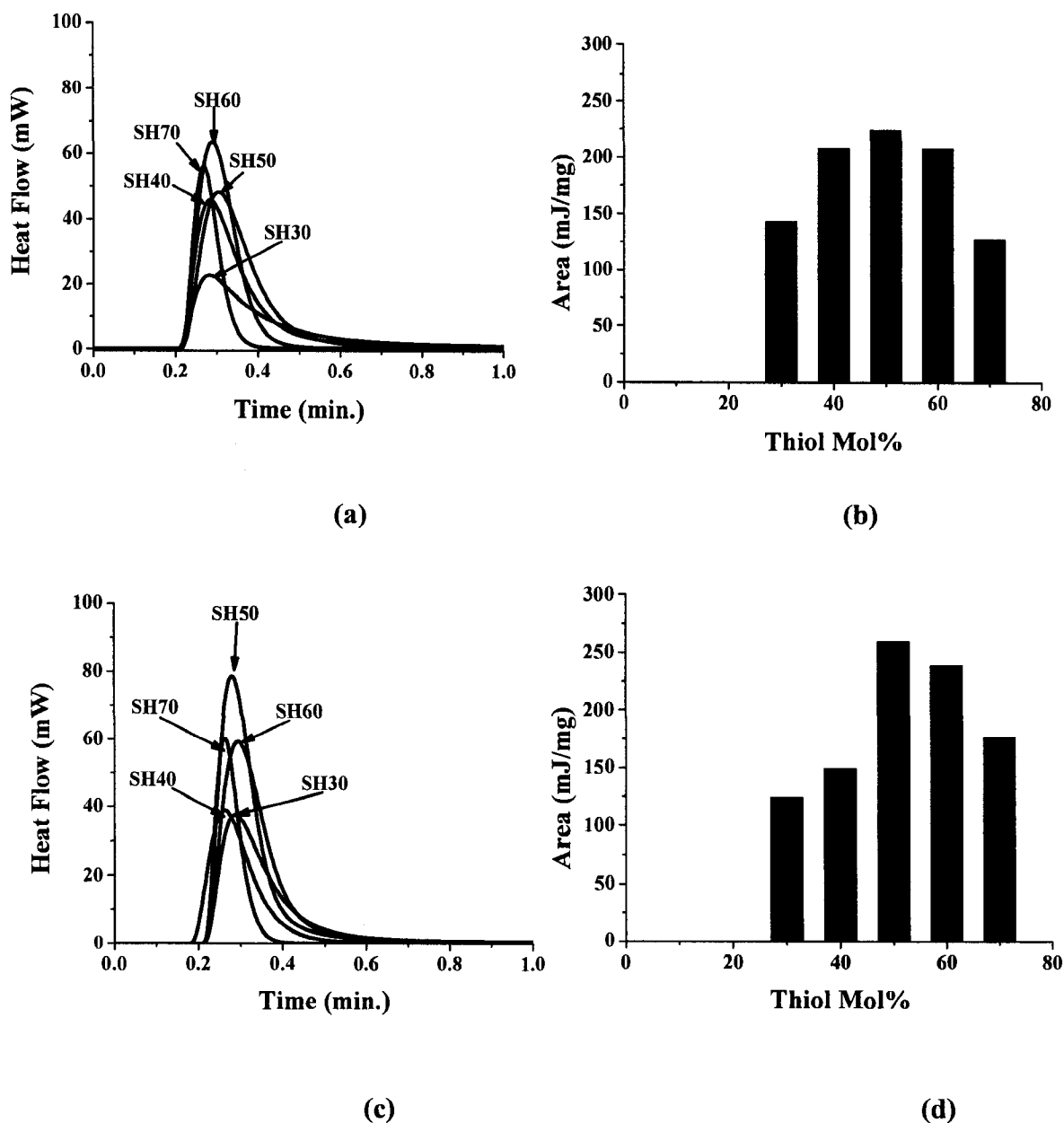
Figure 8. Photo-DSC. a) Exothermic plots (Heat Flow vs. Time) and b) plots of peak areas (Area (under the exotherm) vs. Thiol Mol%) of T11:DAE photopolymerizations and c) exothermic plots (Heat Flow vs. Time) and d) plots of peak areas (Area (under the exotherm) vs. Thiol Mol%) for T11:TAE photopolymerizations at various concentrations. Light intensity of 3.89 mW/cm^2 using a 1.0 neutral density filter.
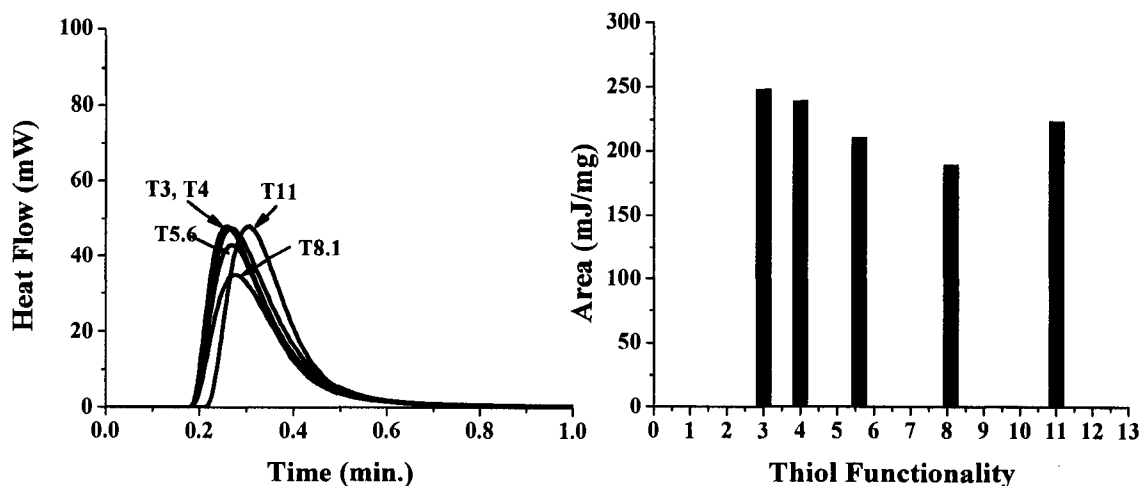
(a)

(b)
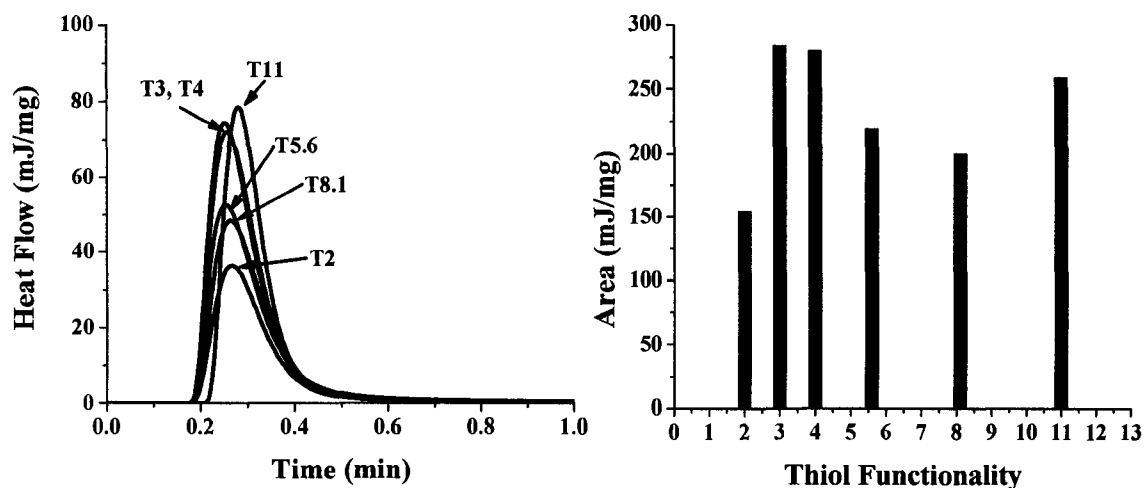
(c)

(d)

Figure 9. Photo-DSC. a) Exothermic plots (Heat Flow vs. Time) and b) plots of peak areas (Area (under the exotherm) vs. Thiol Functionality) of T3-11:DAE at equal molar concentrations of thiol and allyl ether and c) exothermic plots (Heat Flow vs. Time) and d) plots of peak areas (Area (under the exotherm) vs. Thiol Functionality) of T3-11:TAE photopolymerizations at equal molar concentrations of thiol and allyl ether. Light intensity of 3.89 mW/cm^2 using a 1.0 neutral density filter.

(a)

(b)
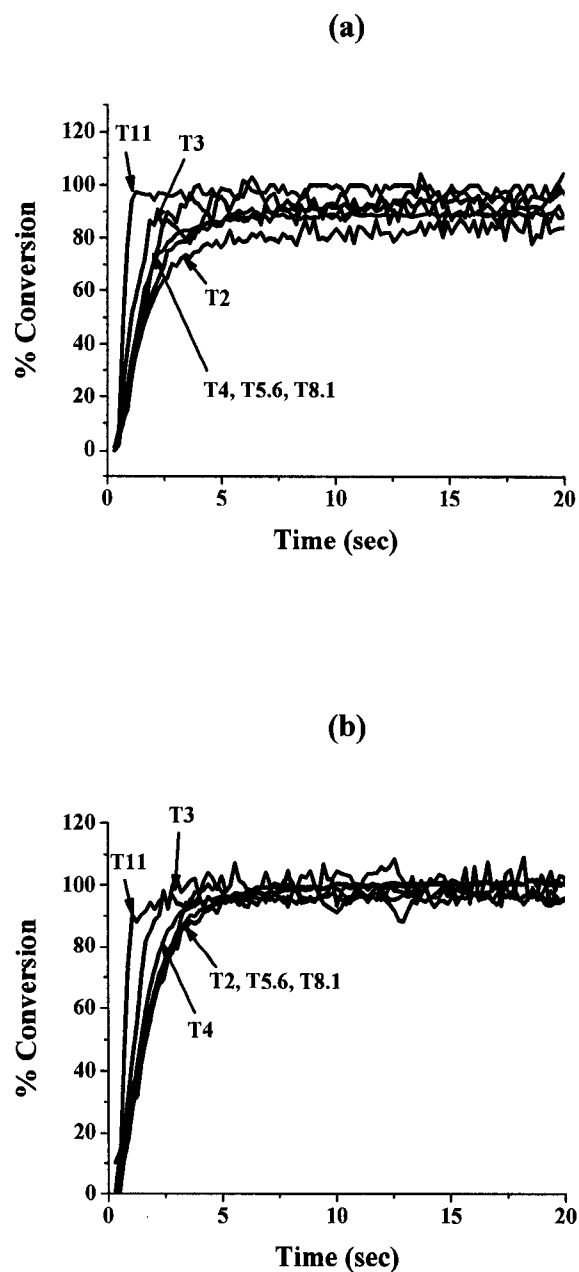
Figure 10. RTIR-based plot (% Conversion vs. Time) of TAE and the series of multifunctional thiols using 50:50 (thiol:ene) molar ratio. Peak depletion was measured at a) 3100 cm^{-1} for ene conversion and b) 2570 cm^{-1} for thiol conversion. Light intensity is 18 mW/cm^2 using a 1.0 neutral density filter.

(a)

(b)
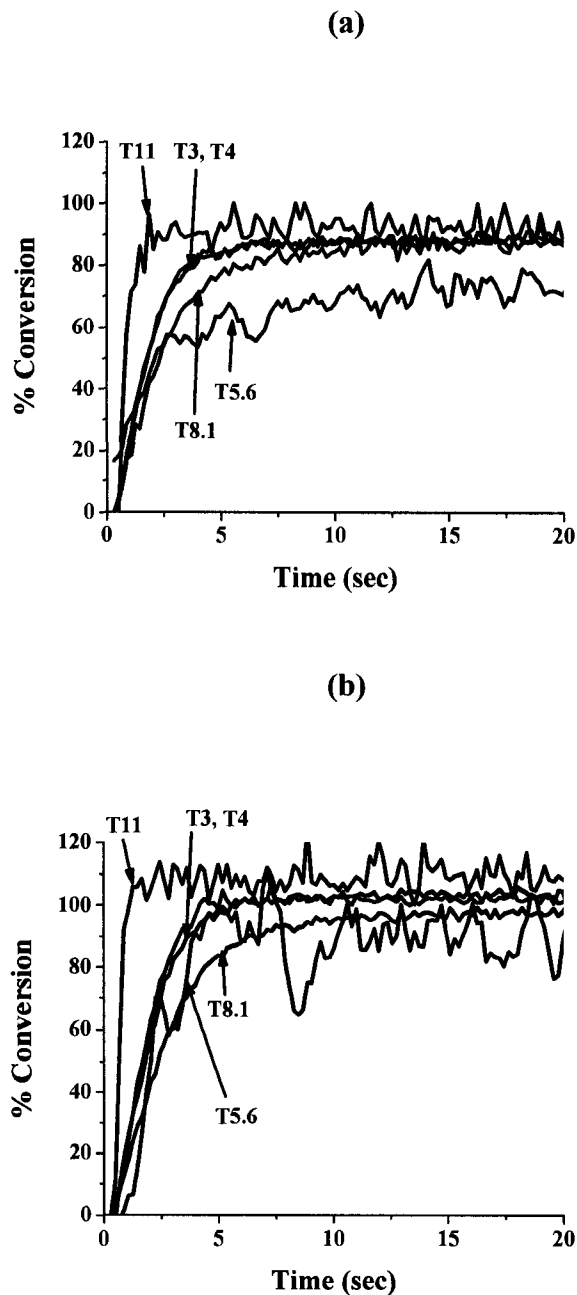
Figure 11. RTIR-based plot (% Conversion vs. Time) of DAE and the series of multifunctional thiols using 50:50 (thiol:ene) molar ratio. Peak depletion was measured at a) 3100 cm^{-1} for ene conversion and b) 2570 cm^{-1} for thiol conversion. Light intensity is 18 mW/cm^2 using a 1.0 neutral density filter.

(a)

(b)
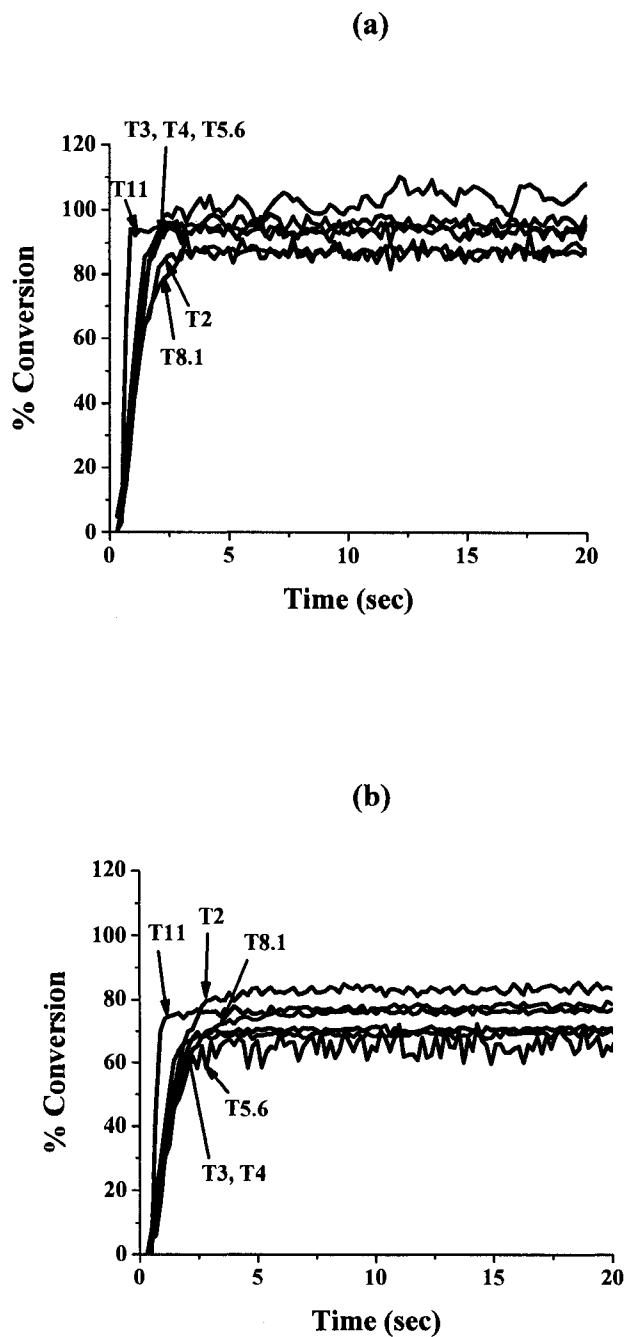
Figure 12. RTIR-based plot (% Conversion vs. Time) of TAE and the series of multifunctional thiols using 60:40 (thiol:ene) molar ratio. Peak depletion was measured at a) 3100 cm^{-1} for ene conversion and b) 2570 cm^{-1} for thiol conversion. Light intensity is 18 mW/cm^2 using a 1.0 neutral density filter.

(a)

(b)
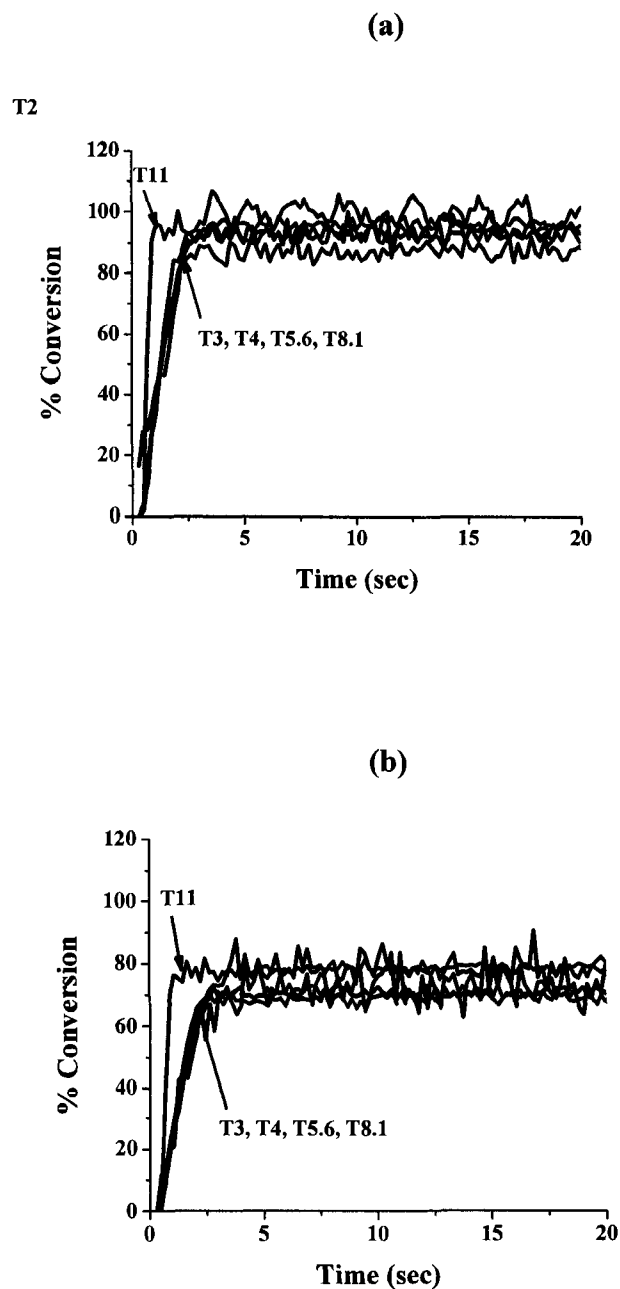
Figure 13. RTIR-based plot (% Conversion vs. Time) of DAE and the series of multifunctional thiols using 60:40 (thiol:ene) molar ratio. Peak depletion was measured at a) 3100 cm^{-1} for ene conversion and b) 2570 cm^{-1} for thiol conversion. Light intensity is 18 mW/cm^{2} using a 1.0 neutral density filter.

(a)

(b)
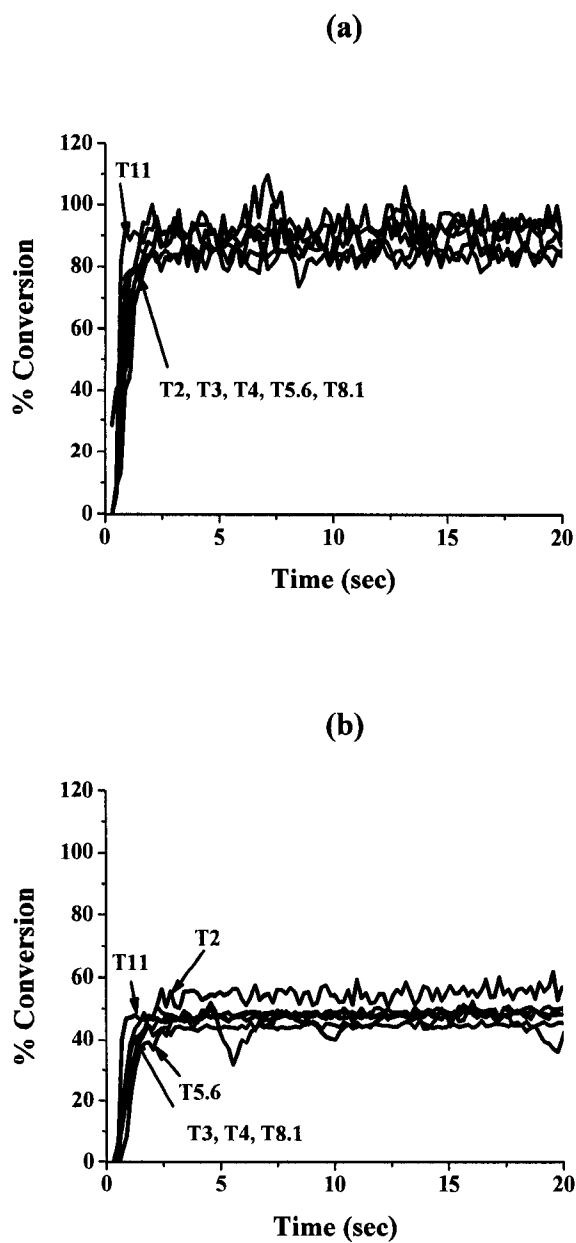
Figure 14. RTIR-based plot (% Conversion vs. Time) of TAE and the series of multifunctional thiols using 70:30 (thiol:ene) molar ratio. Peak depletion was measured at a) 3100 cm^{-1} for ene conversion and b) 2570 cm^{-1} for thiol conversion. Light intensity is 18 mW/cm^2 using a 1.0 neutral density filter.

(a)

(b)
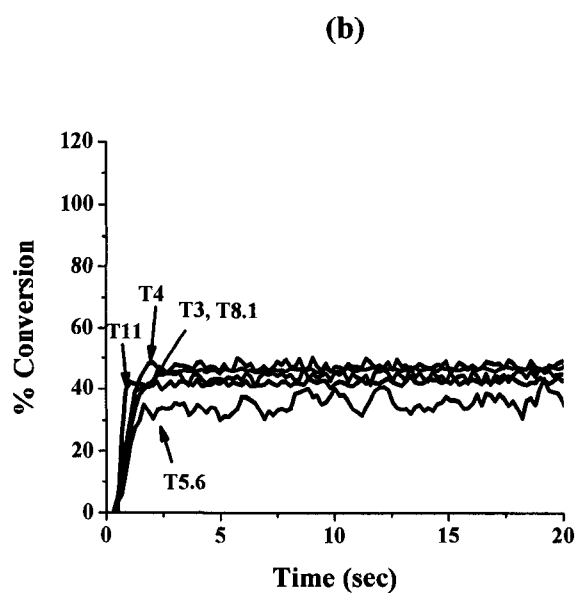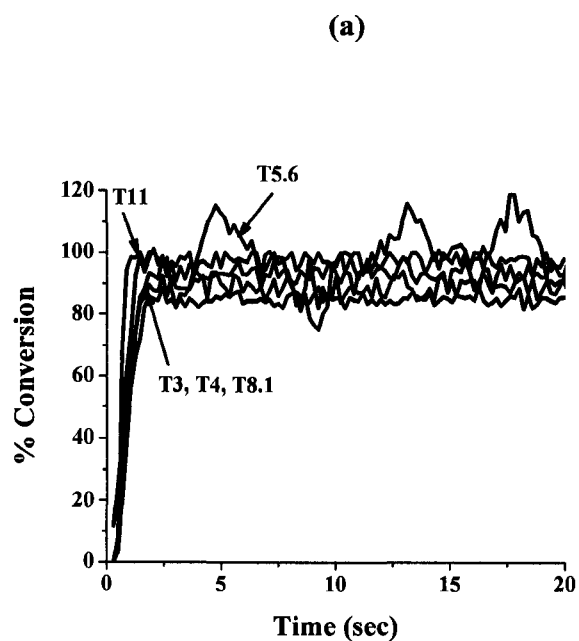
Figure 15. RTIR-based plot (% Conversion vs. Time) of DAE and the series of multifunctional thiols using 70:30 (thiol:ene) molar ratio. Peak depletion was measured at a) 3100 cm^{-1} for ene conversion and b) 2570 cm^{-1} for thiol conversion. Light intensity is 18 mW/cm^2 using a 1.0 neutral density filter.
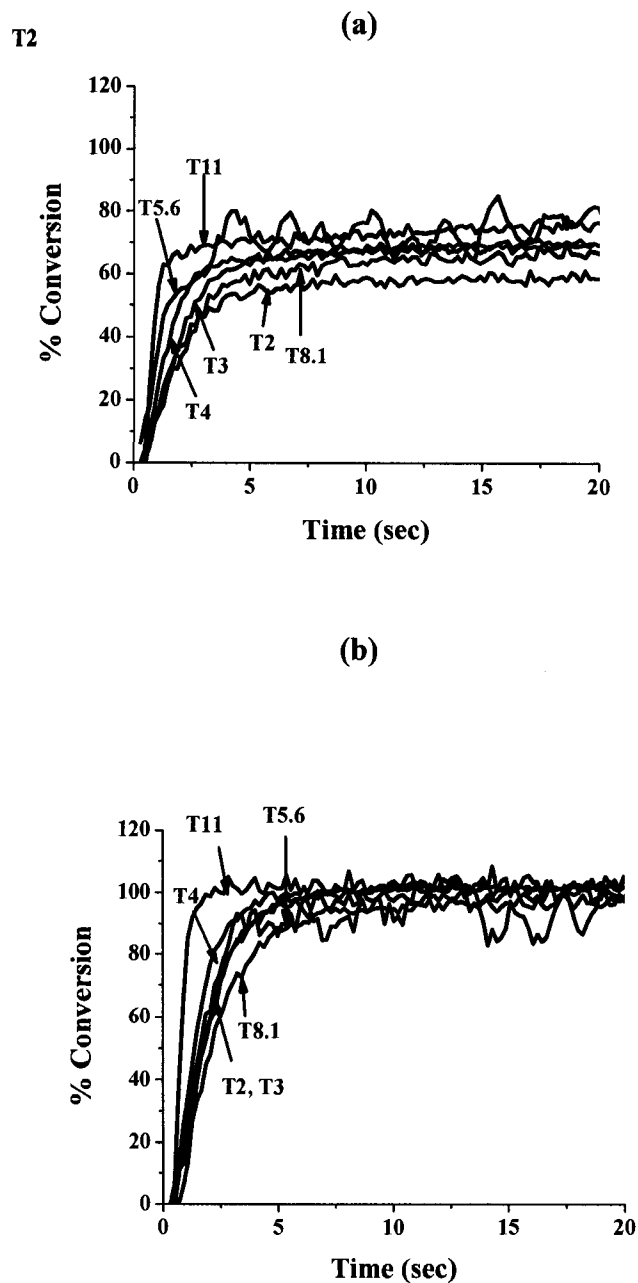
Figure 16. RTIR-based plot (% Conversion vs. Time) of TAE and the series of multifunctional thiols using 40:60 (thiol:ene) molar ratio. Peak depletion was measured at a) 3100 cm^{-1} for ene conversion and b) 2570 cm^{-1} for thiol conversion. Light intensity is 18 mW/cm^2 using a 1.0 neutral density filter.

(a)

(b)
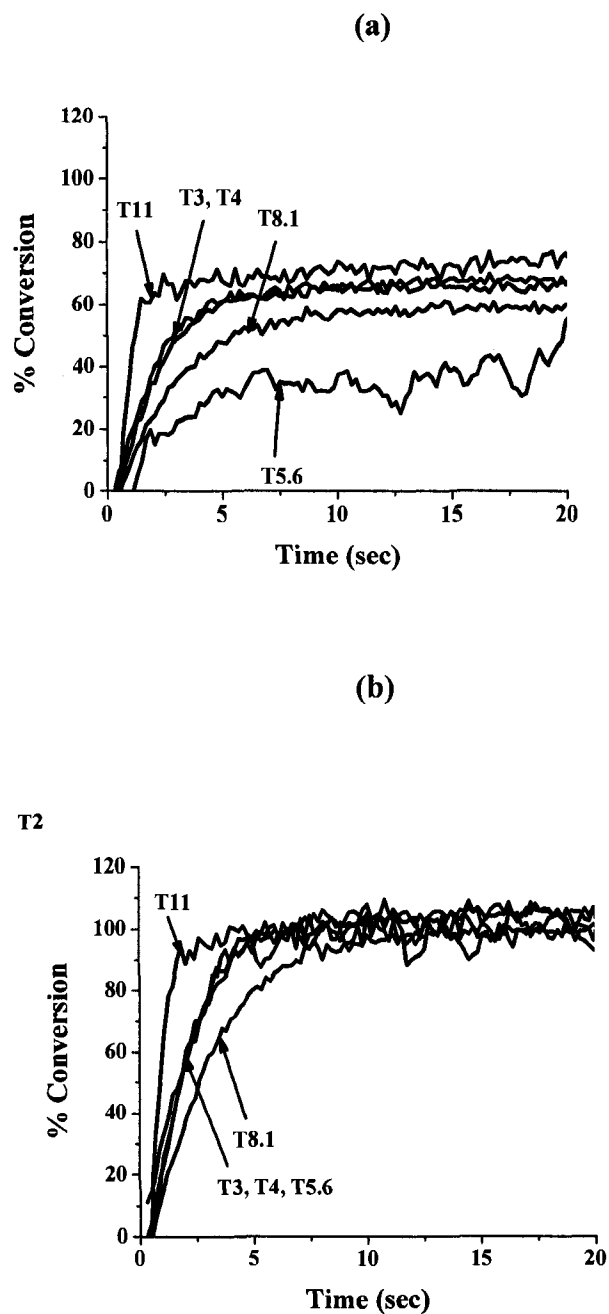
Figure 17. RTIR-based plot (% Conversion vs. Time) of DAE and the series of multifunctional thiols using 40:60 (thiol:ene) molar ratio. Peak depletion was measured at a) 3100 cm^{-1} for ene conversion and b) 2570 cm^{-1} for thiol conversion. Light intensity is 18 mW/cm^2 using a 1.0 neutral density filter.

(a)

(b)
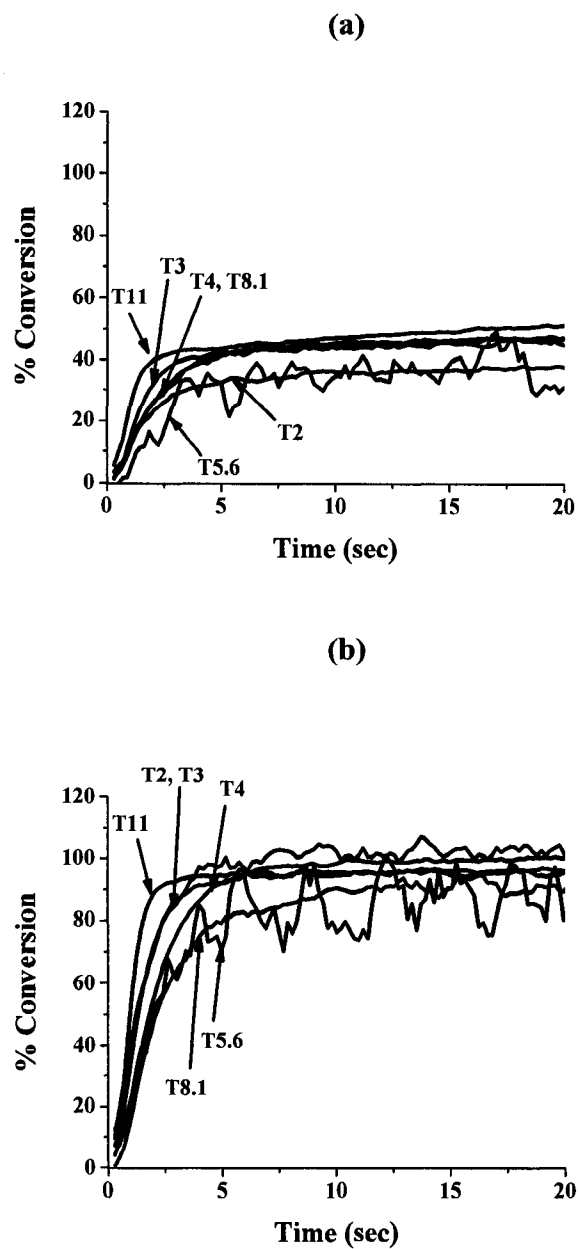
Figure 18. RTIR-based plot (% Conversion vs. Time) of TAE and the series of multifunctional thiols using 30:70 (thiol:ene) molar ratio. Peak depletion was measured at a) 3100 cm^{-1} for ene conversion and b) 2570 cm^{-1} for thiol conversion. Light intensity is 18 mW/cm^2 using a 1.0 neutral density filter.

(a)

(b)
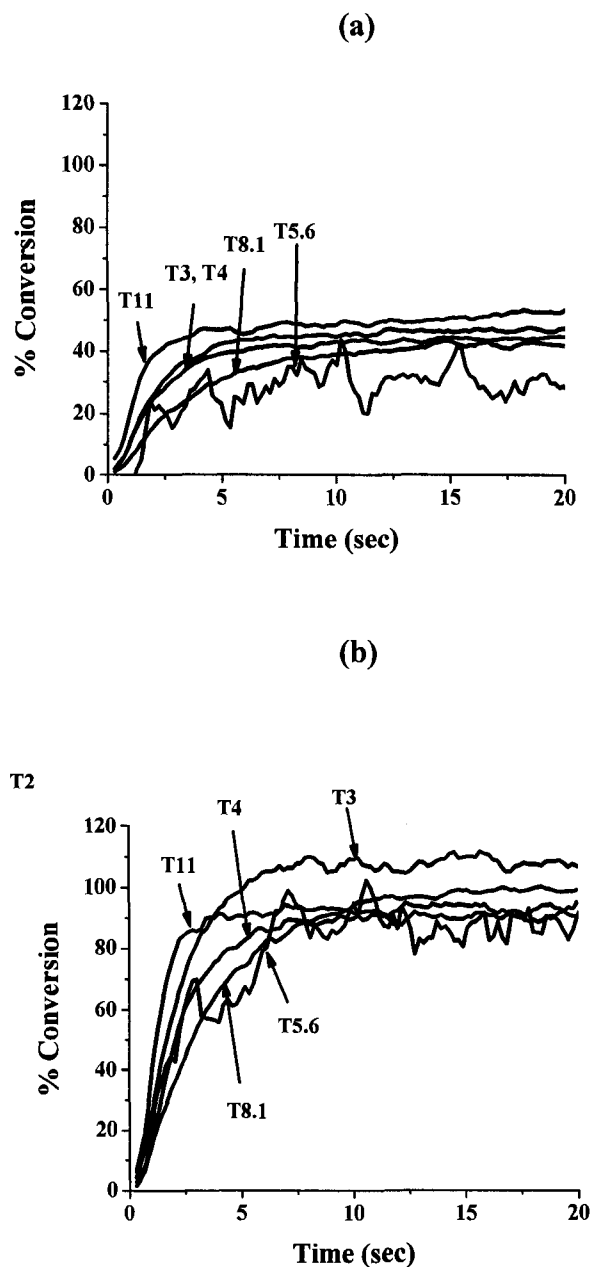
Figure 19. RTIR-based plot (% Conversion vs. Time) of DAE and the series of multifunctional thiols using 30:70 (thiol:ene) molar ratio. Peak depletion was measured at a) 3100 cm^{-1} for ene conversion and b) 2570 cm^{-1} for thiol conversion. Light intensity is 18 mW/cm^2 using a 1.0 neutral density filter.
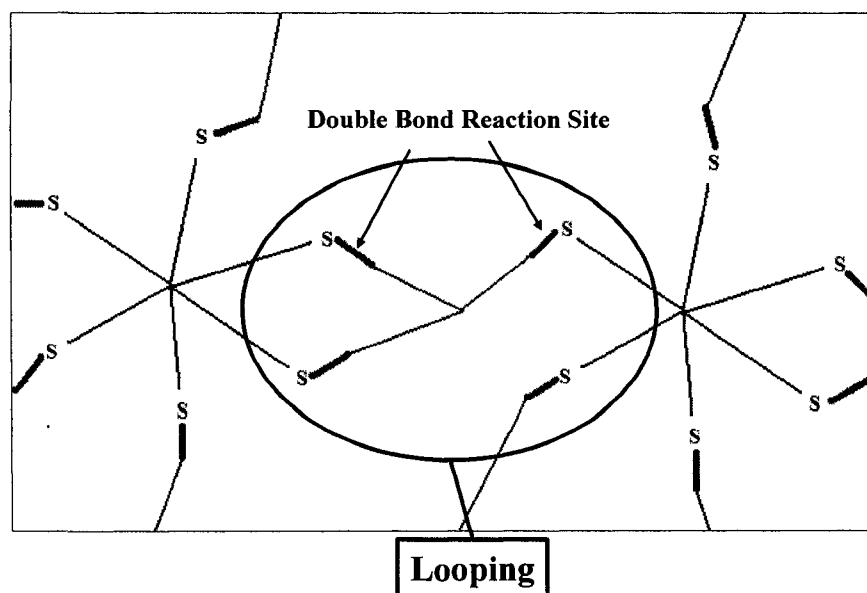
Figure 20. Structure of looped structures within the crosslinked thiol-ene network.
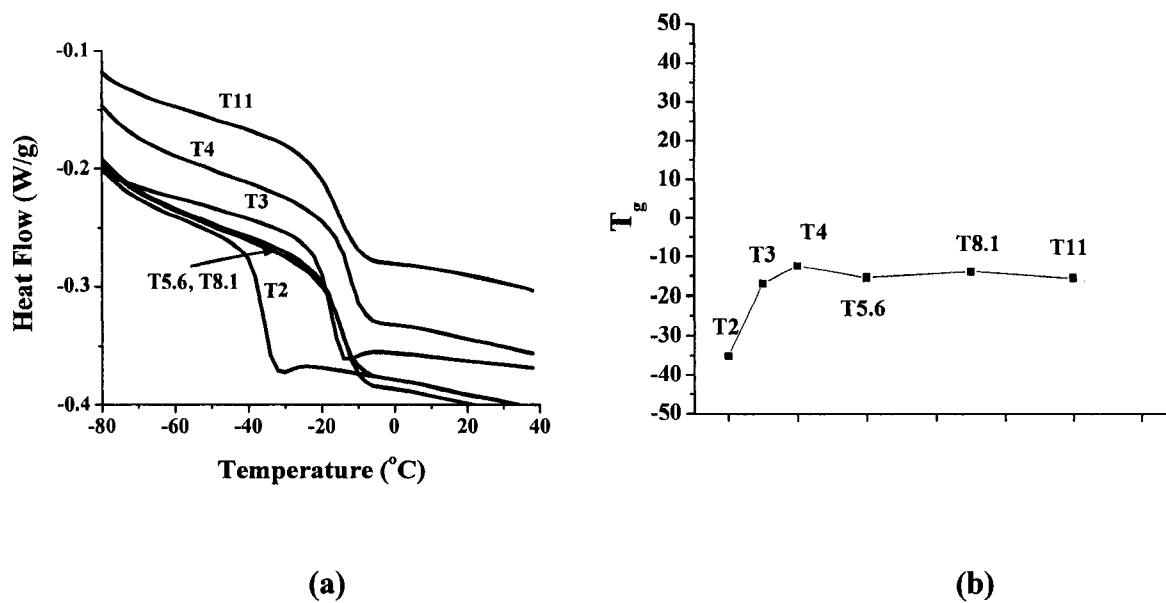
Figure 21. a) DSC exotherms (Heat flow vs. Temperature) and b) plot of Glass transition temperature vs. Thiol functionality for 50:50 thiol to ene molar concentrations for copolymers of multifunctional thiols and TAE.
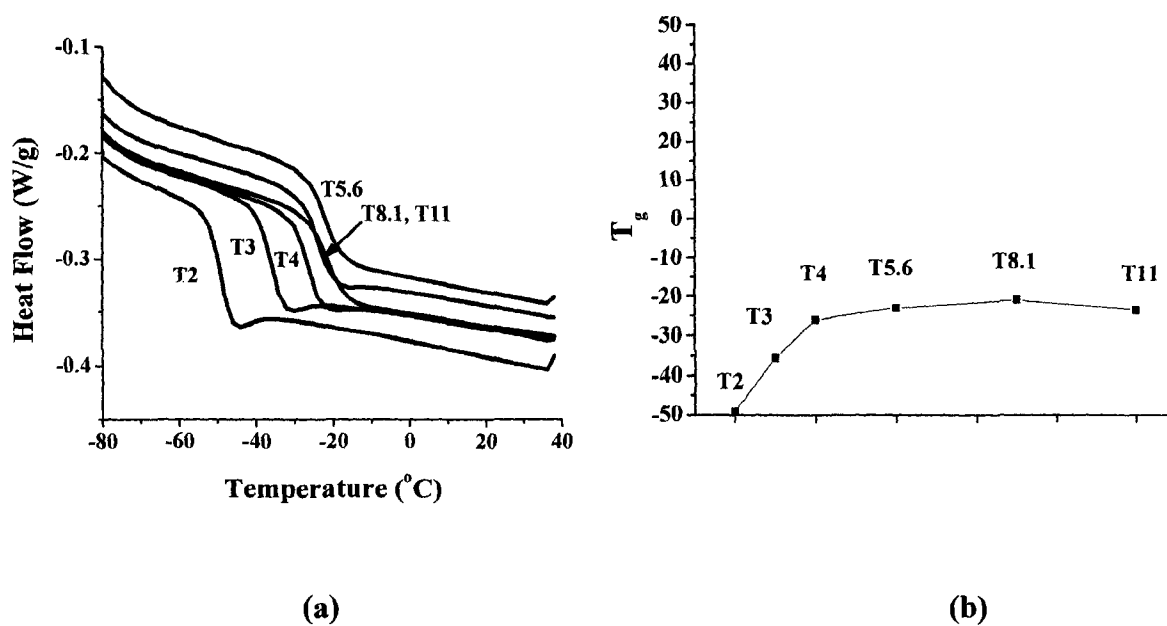
Figure 22. a) DSC exotherms (Heat flow vs. Temperature) and b) plot of Glass transition temperature vs. Thiol functionality for 60:40 thiol to ene molar concentrations for copolymers of multifunctional thiols and TAE.
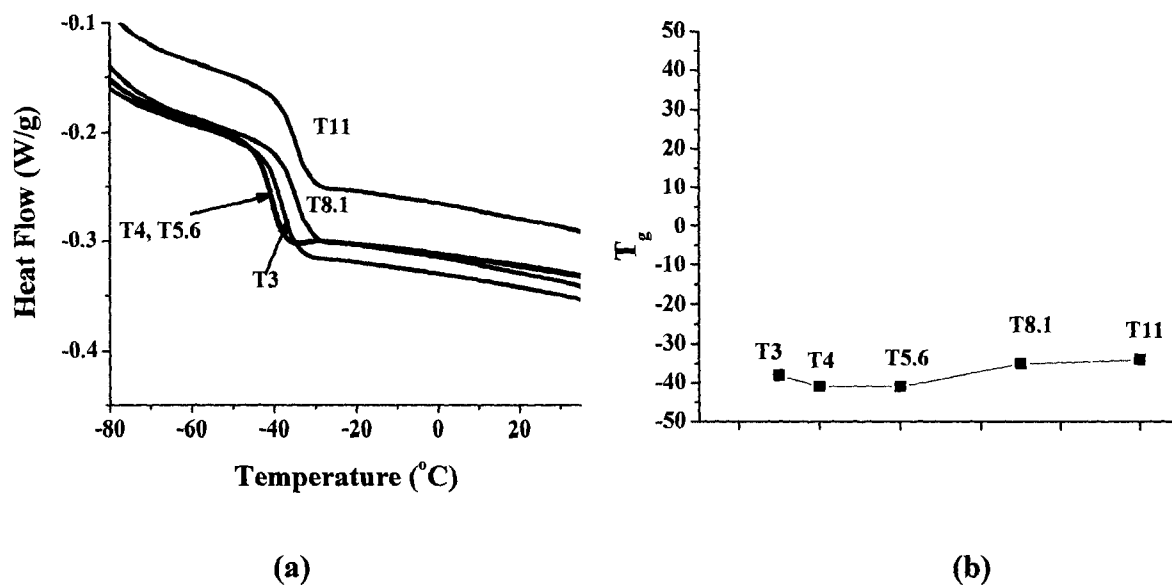
Figure 23. a) DSC exotherms (Heat flow vs. Temperature) and b) plot of Glass transition temperature vs. Thiol functionality for 70:30 thiol to ene molar concentrations for copolymers of multifunctional thiols and TAE.
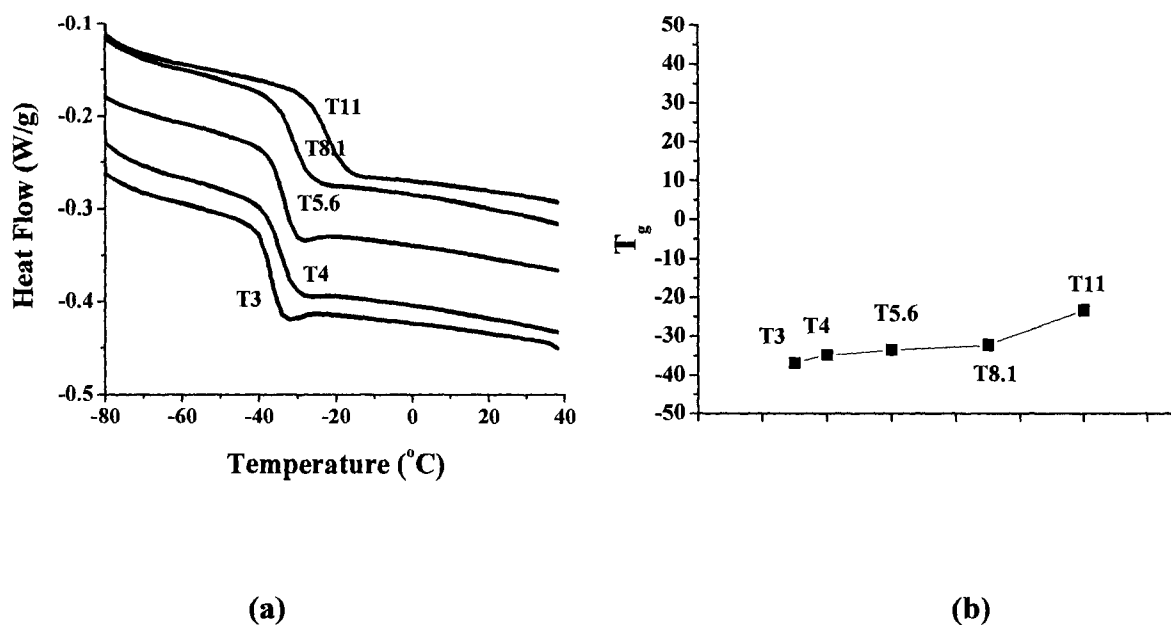
Figure 24. a) DSC exotherms (heat flow vs. temperature) and b) plot of glass transition temperature vs. thiol functionality for 50:50 thiol to ene molar concentrations for copolymers of multifunctional thiols and DAE.

(a)   **(b)**
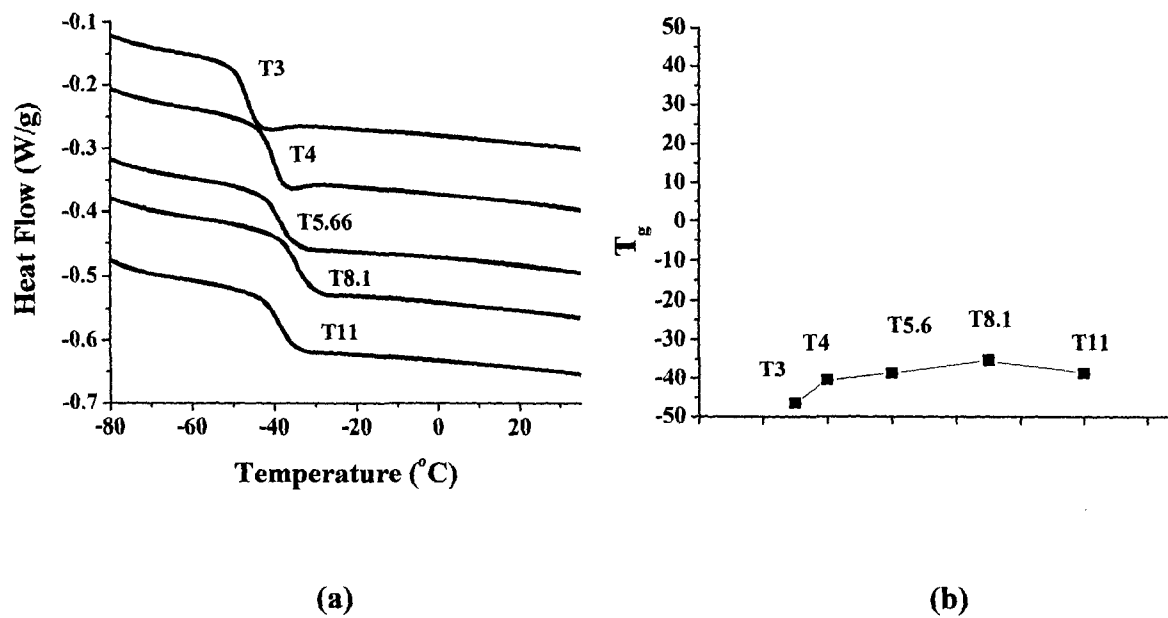
Figure 25. a) DSC exotherms (Heat flow vs. Temperature) and b) plot of Glass transition temperature vs. Thiol functionality for 60:40 thiol to ene molar concentrations for copolymers of multifunctional thiols and DAE.
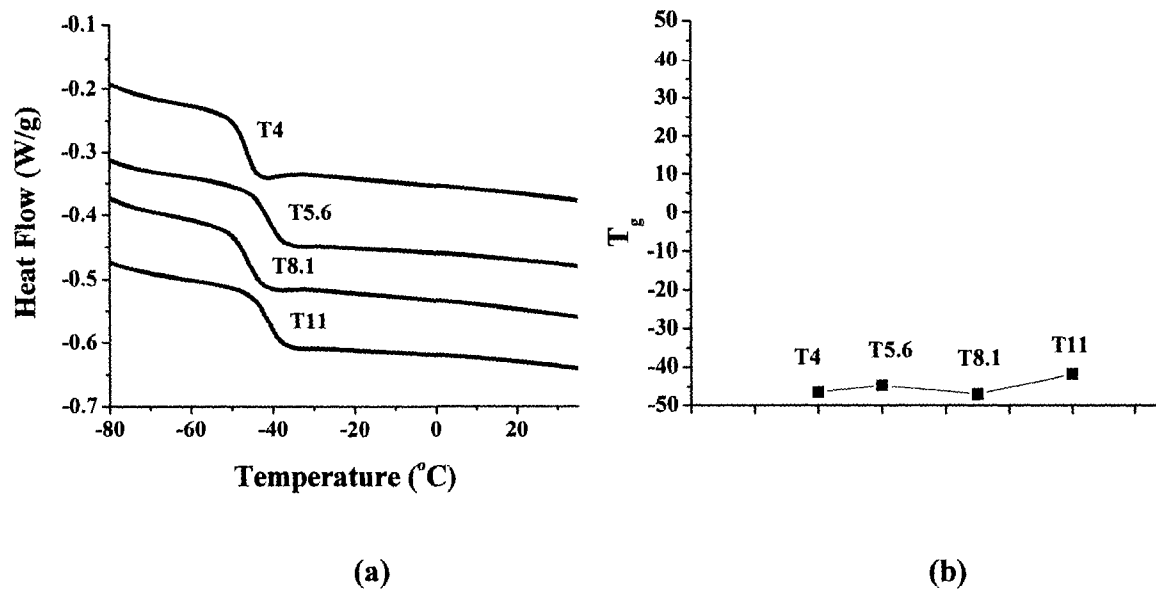
Figure 26. a) DSC exotherms (Heat flow vs. Temperature) and b) plot of Glass transition temperature vs. Thiol functionality for 70:30 thiol to ene molar concentrations for copolymers of multifunctional thiols and DAE.

(a)

(b)
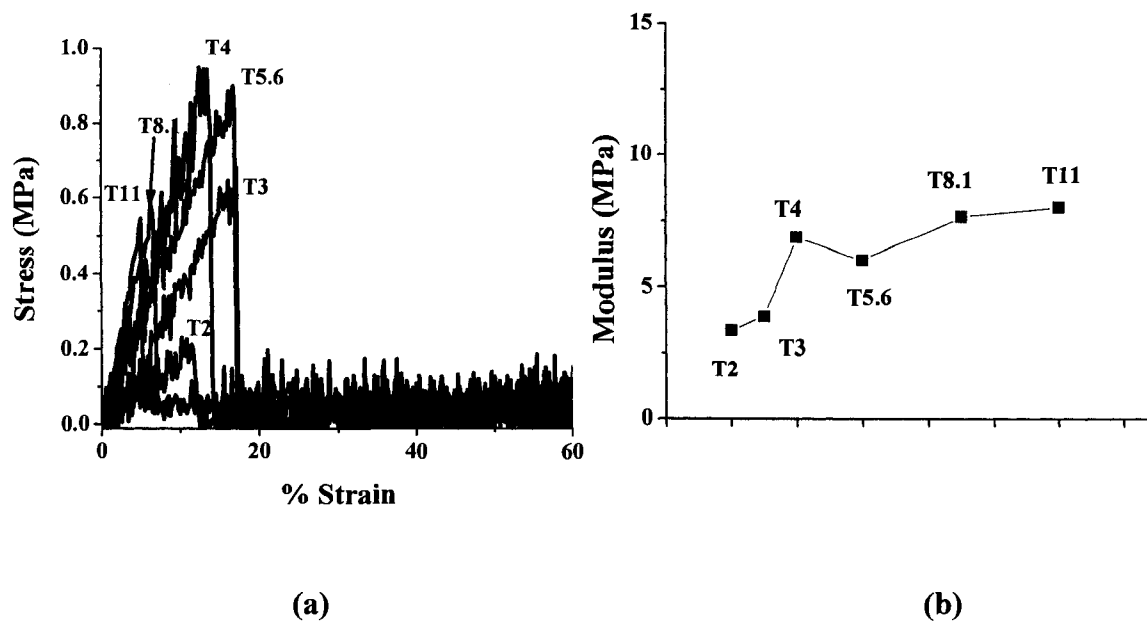
Figure 27. a) Plot of % Strain vs. Stress and b) plot of Modulus vs Thiol functionality for 50:50 thiol to ene molar concentrations for copolymers of multifunctional thiols and TAE.

(a)   **(b)**
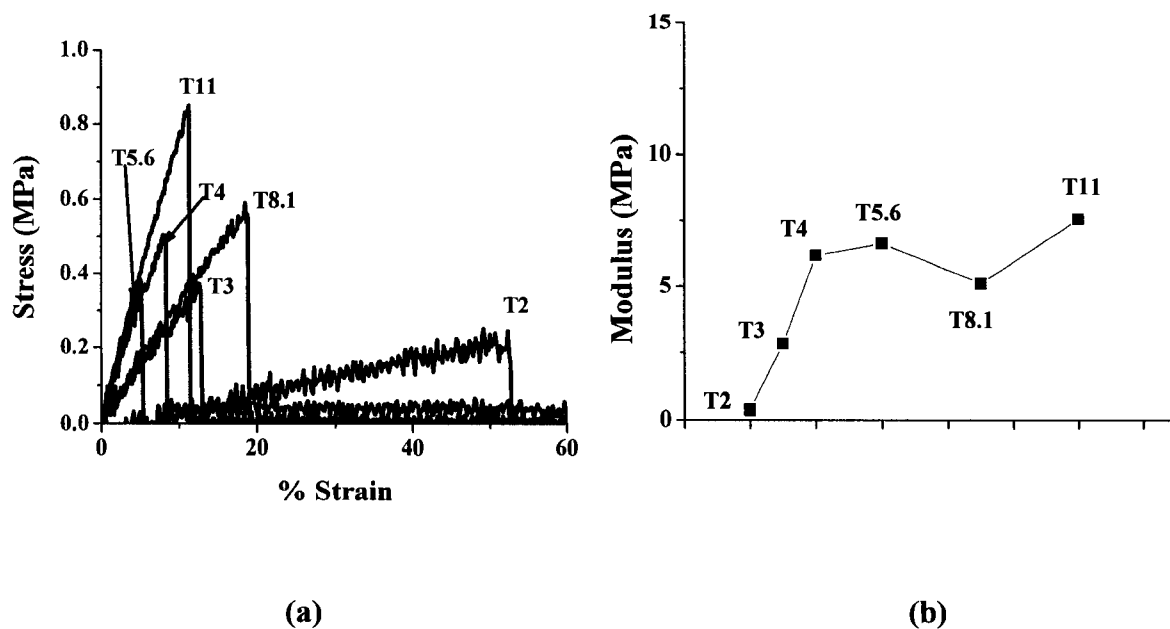
Figure 28. Plot of % Strain vs. Stress and b) plot of Modulus vs. Thiol functionality for 60:40 thiol to ene molar concentrations for copolymers of multifunctional thiols and TAE.

(a)

(b)
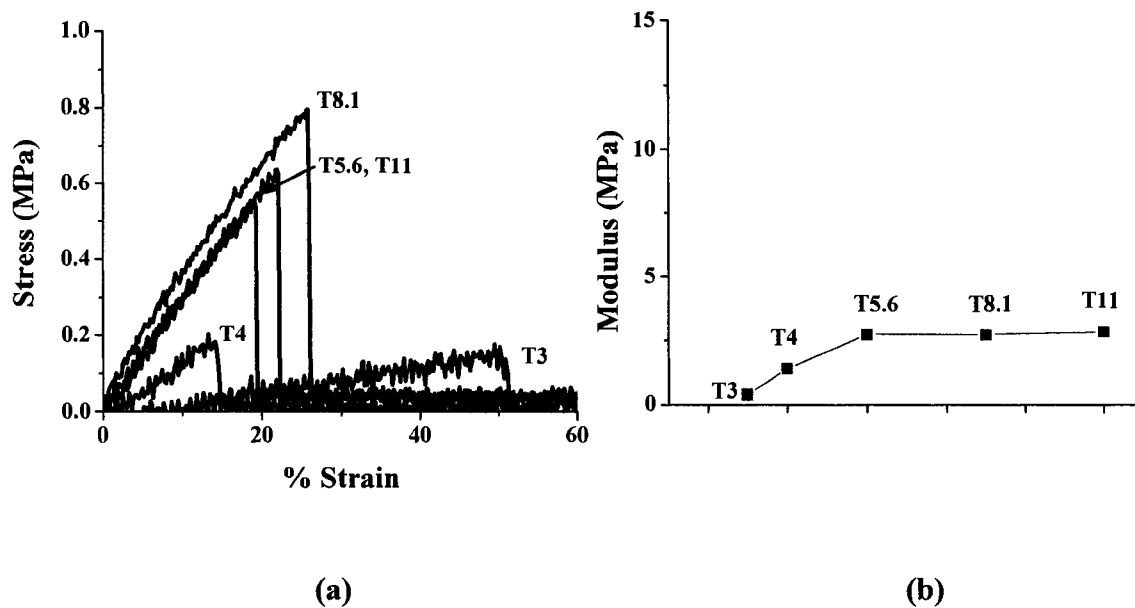
Figure 29. Plot of % strain vs. Stress and b) plot of Modulus vs. Thiol functionality for 70:30 thiol to ene molar concentrations for copolymers of multifunctional thiols and TAE.
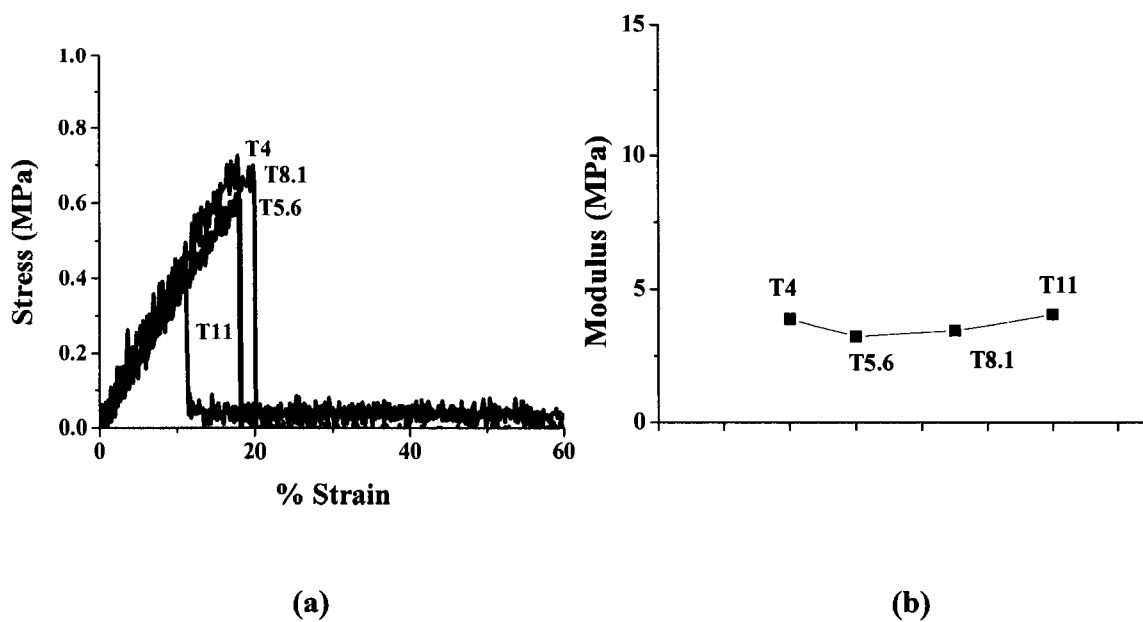
Figure 30. Plot of % Strain vs. Stress and b) plot of Modulus vs. Thiol functionality for 50:50 thiol to ene molar concentrations for copolymers of multifunctional thiols and DAE.

82
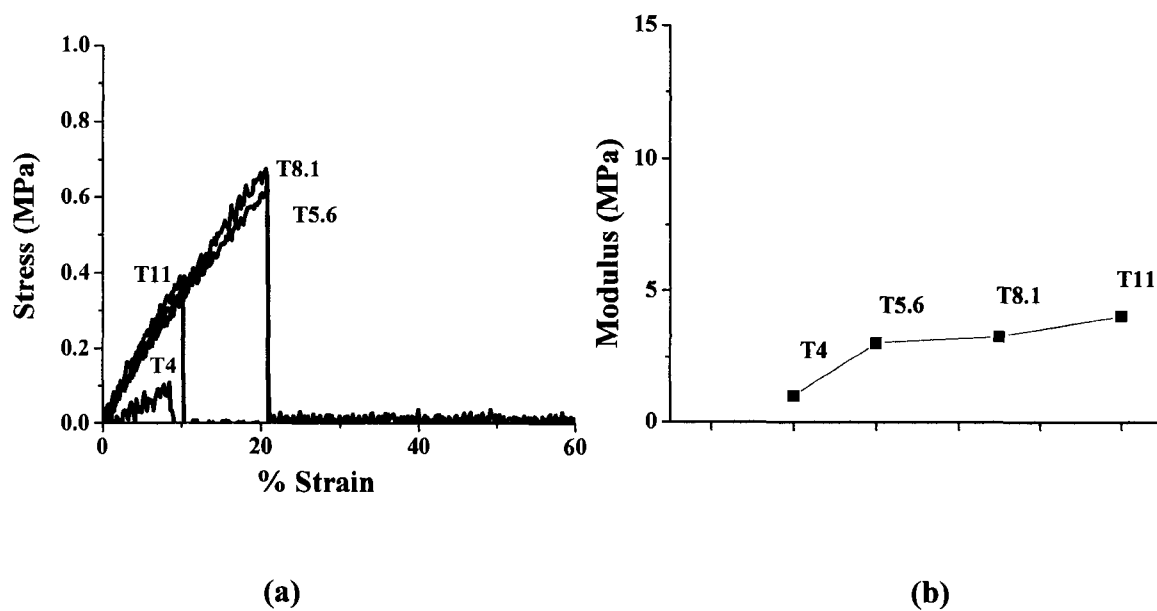
Figure 31. a) Plot of % Strain vs. Stress and b) plot of Modulus vs. Thiol functionality for 60:40 thiol to ene molar concentrations for copolymers of multifunctional thiols and DAE.
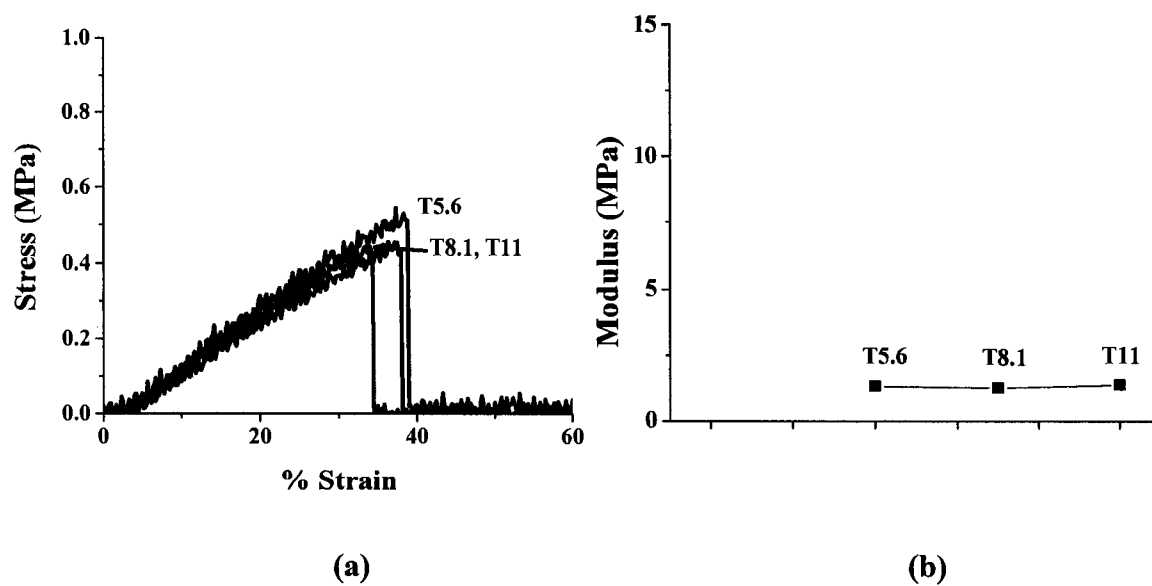
Figure 32. Plot of % Strain vs. Stress and b) plot of Modulus vs. Thiol functionality for 70:30 thiol to ene molar concentrations for copolymers of multifunctional thiols and DAE.

Proton Assignments (δ)						
	HDDA	Ethyl Acrylate	TMPTA	PETA	TriThiol	Tetra Thiol
1	4.1	1.3	0.9	4.1	0.9	4.0
2	1.7	4.1	1.6	-------	1.5	2.8
3	1.4	-------	4.1	-------	4.0	2.7
4	-------	-------	-------	-------	2.8	-------
5	-------	-------	-------	-------	2.7	-------

Table 1. Proton assignments for acrylate components of synthesized multifunctional thiols.

Thiol	Functionality
T2	2
T6	5.6
T9	8.1
T12	11

Table 2. The average functionalities of synthesized multifunctional thiol monomers as determined by a titrimetric assay.

	MW/Thiol
T2	249.3
T3	132.9
T4	122.2
T6	183.0
T9	178.3
T12	167.5

Table 3. Molecular weight distribution per thiol functional group.

	Fractional Conversion		α	
	DAE	TAE	DAE	TAE
T2	-----	.89	----	.71
T3	.80	.91	.71	.50
T4	.91	.90	.58	.41
T6	.92	.92	.47	.33
T9	.93	.94	.35	.25
T12	.92	.93	.29	.20

Table 4. List of experimental fractional functional group conversions and the calculated gel points (α) obtained during copolymerization for 50:50 molar ratios of multithiol/multiene reactions.

CHAPTER V

THE INFLUENCE OF VINYL POLYHEDRAL OLIGOMERIC SILSESQUIOXANE

(POSS) ON THE NETWORK STRUCTURE AND KINETICS OF POSS-BASED

TRITHIOL-TRIALLYL ETHER BLENDS AND COPOLYMERS

ABSTRACT

The changes in thermal, mechanical, and physical properties of trithiol-TAE (triallyl

ether) films were measured with respect to increasing polyhedral silsesquioxane (POSS)

concentrations in order to understand how POSS compatibility affects film morphologies

of a nanocomposite series. Compatibilization of POSS particles improves the solubility of

the silicate particles in the organic medium. A comparative analysis of thiol-ene systems

where POSS is physically blended and chemically incorporated into the network shows

the importance of covalent bonding on physical and thermal properties. POSS molecules

with a combination of both vinyl and carboxylate pendant groups and with only

carboxylate pendant groups were synthesized. The chemically modified POSS particles

containing vinyl groups were incorporated into a trithiol-triallyl ether (TriThiol-TAE)

polymer networks by a thiol-ene free radical photopolymerization at ene molar

concentrations of 0, 1, 5, 10, 20 and 50 ene mol%. POSS molecules with pendant

carboxylate groups and those with isobutyl groups were blended into TriThiol-TAE

networks with equivalent weight percentages of POSS at concentrations of 2.2 wt%, 10.2

wt%, 18.8 wt%, 32.4 wt%, and 57.8 wt%. Surface hardness and scratch resistance were

measured by Persoz pendulum, shore A, and pencil hardness tests. DSC and DMA were

used to obtain thermal and mechanical properties of the copolymer and blends. The

results show that clear separate phases (solid or liquid) of POSS-rich domains are formed when POSS is simply blended into the matrix. The mechanical/physical properties decrease upon the increasing concentration of vPOSS-Bu$_2$ due to increased POSS-rich regions.

The kinetics of vPOSS-Bu$_2$ copolymerization with thiol (TriThiol) and triallyl ether (TAE), as measured by real-time FTIR and photo-DSC, show that polymerization rates and functional group conversions decrease with the increase of vPOSS-Bu$_2$, particularly at 20 and 50 mol% vPOSS-Bu$_2$. Polymerization rates and conversions are unaffected by the presence of POSS (POSS-iBu and vPOSS-Bu$_1$) when the POSS component is physically mixed into the TriThiol-TAE matrix. Positron annihilation lifetime spectroscopy (PALS) measurements indicate that free volume is increased when liquid POSS (vPOSS-Bu$_1$ and vPOSS-Bu$_2$) is incorporated into the TriThiol-TAE network by physical or chemical methods. Positron annihilation lifetimes increased with an increase in vPOSS-Bu$_1$ or vPOSS-Bu$_2$ concentrations, although oxygen permeation does not significantly increase with free volume changes. The thermal stability and burn rates of thin films were analyzed by TGA and an ASTM burn test for thin films.

INTRODUCTION

POSS nanoparticles (1-3 nm) are organically hybridized silicate cage structures having an empirical formula $((RSiO_{1.5})_n)$ and varying cage sizes (n = 8, 10, 12, 14).[1] The structure of the POSS nanoparticle consists of an inorganic core and an organic periphery with reactive and/or nonreactive organic substituents at each corner of the silicate cage.[1] The characteristics of POSS nanoparticles are attributed to the chemical nature of their inorganic core, which is inherently thermally stable.[1,2]

Molecular dispersion of POSS nanoparticles is influenced by the compatibilization of POSS with the base comonomers and the method of incorporation into host polymer networks.[1-3] The compatibilization of the silicate particles is impacted by the type and number of organic substituents attached to the silicate core which can potentially inhibit phase separation of the organic and inorganic phases and improve the solubility of the inorganic particles in the organic medium.[2] Additionally, the concentration of POSS particles influences the formation of separate phases of inorganic and organic components.[3] POSS particles may be incorporated into a host polymeric system by blending or copolymerization.[4-5]

Pittman et al. detailed in a review on organic/POSS copolymers that nano-reinforced styrene, epoxy and norbornene copolymers exhibit significantly enhanced thermal stability with increased POSS concentration.[1] There are scattered reports that under the right conditions polymeric systems with increased energy absorption upon impact,[6] reduced surface friction,[7] and enhanced hydrophobicity[8] may occur with the addition of POSS nanoparticles.

Thiol-ene polymers are a unique class of photopolymers with many desirable characteristics such as good adhesion, flexibility, and mechanical strength that are attributed to the presence of the thioether bond and the high uniformity and crosslink density of the network.[9] Thiol-ene photopolymers are attractive systems to study since network formation involves fast polymerization kinetics of virtually any multifunctional thiol and multifunctional ene group, which include ene structures such as vinyl ethers, allyl ethers, acrylates, and vinyl siloxanes.[10] Other salient features of thiol-ene photopolymerization include fast polymerization rates in inert and oxygen-rich environments, and photoinitiatorless polymerizations.

The basic thiol-ene photopolymerization involves a two-step free radical sequence of propagation/chain transfer of thiol addition across the ene double bond (Scheme 1).[7]

$$RS\bullet + R'CH=CH_2 \xrightarrow{\quad k_p \quad} R'C\bullet H—CH_2SR \qquad (1a)$$

$$R'C\bullet H—CH_2SR + RSH \xrightarrow{\quad k_{CT} \quad} R'CH_2—CH_2SR + RS\bullet \qquad (1b)$$
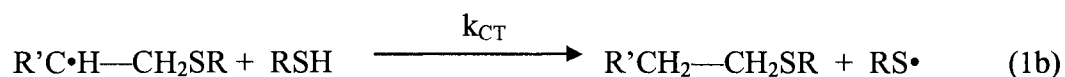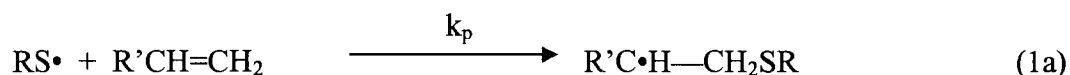
Although, thiol-ene materials have many desirable characteristics, the base networks are organic and are thus subject to rapid flame spread and they may be soft due to the flexible thio-ether bond.

Herein, it is demonstrated that the addition of POSS by physical mixing or chemical incorporation can have some influence on the thermal and mechanical behavior of a thiol-ene network. The physical and mechanical properties of the POSS modified thiol-ene networks are correlated and discussed in the framework of the corresponding film morphology.

EXPERIMENTAL

Materials

Allyl pentaerythritol (TAE) was obtained from Perstorp Specialty Chemical

Company. The phototinitiator, 2,2-dimethyl-2-hydroxy acetophenone (Darocur 1173),

was obtained from Ciba Specialty Chemicals, Inc. Trimethylopropane tris(3-

mercaptopropionate) (TriThiol), butyl 3-mercaptopropionate, and diethyl amine were

purchased from Aldrich Chemical Company and used as received. Vinyl POSS and

POSS-*i*Bu were donated by Hybrid Plastics (see Figure 1 for chemical structures).

Synthetic method for vinyl POSS modification

The POSS monomers (vPOSS-Bu$_1$ and vPOSS-Bu$_2$ as shown in Figure 1) with both

vinyl and ester groups were synthesized as follows (method given for synthesis of

vPOSS-Bu$_2$). A 20-g vinyl POSS mixture (Hybrid Plastics) was charged into a 250-mL

flask with 60 mg of diethyl amine and 25 mL THF. The solution was slowly added to 25

g of butyl 3-mercaptopropionate in 3-4 mL aliquots every 10 minutes while stirring. The

mixture was stirred for at least 6 hours before the solvent THF was removed by

rotovaporization (2 hours) at a temperature of 40 °C. After complete evaporation of THF,

oil remained that contained the product (vPOSS-Bu$_2$). The final product (vPOSS-Bu$_1$ or

vPOSS-Bu$_2$) was analyzed by proton and carbon NMR (Figure 2) to confirm the

consumption of the vinyl bond and the formation of the thioether bond. Peak assignments

and peak multiplicities are described in Table 1 for the organic substitutent (**Bu**) on

vPOSS-Bu$_1$ and vPOSS-Bu$_2$, and starting materials. The completed reaction of vPOSS-

Bu₁ was confirmed by the disappearance of the vinyl proton and carbon peaks at ~6.0

ppm (Figure 2a) and 140 ppm (Figure 2c) and the appearance of peaks **c** and **d** (see

Figures 2a & 2c and Table 1) for the methylene groups adjacent to the POSS vinyl cage

in proton and carbon NMR spectra. Likewise, the conversion of vinyl groups to

methylene groups were confirmed by the appearance of peaks **c** and **d** (see Figures 2b &

2d and Table 1) for vPOSS-Bu₂ modification. The functionality of vPOSS-Bu₂ (6 vinyl:4

Bu) was determined by the ratio of the integrated peaks of the **vinyl** group and methylene

group (**4**) adjacent to the oxygen group in the ester shown in Figure 2b. Upon integration

of the peaks, **4** was assigned an integration value of 200 (100 per proton) and used as a

reference peak for assigning integration peaks for all other protonated groups. The ratio

(r) of vinyl to ester (butyl 3-mercaptopropionate) protons (0.44) was used to calculate the

average number of vinyl groups remaining after the reaction of thiol and vinyl POSS

using Equation 1. The average functionality of vinyl POSS cage was 10.

$$r = \frac{2 * \text{Peak integration value (\textbf{vinyl})}}{3 * \text{Peak integration value (\textbf{4})}}, \quad \text{and} \quad \text{No. of vinyl groups} = \frac{10\,r}{(1 + r)} \quad (1)$$

Photocuring of TriThiol-TAE systems

vPOSS-Bu₂/Thiol-Ene copolymer mixtures containing 0 mol%, 1 mol%, 5 mol%, 10

mol%, 20 mol%, and 50 mol% and vPOSS-Bu₁/Thiol-Ene and POSS-*i*Bu/Thiol-Ene

blends containing weights equivalent to the molar concentrations of the mixtures of 0

wt%, 2.2 wt% , 10.2 wt%, 18.8 wt%, 32.4 wt%, and 57.8 wt% were photocured on a

Fusion Epiq 6000 UV cure line. Reaction mixtures contained equal moles of thiol and

ene functional groups in addition to 2 wt% photoinitiator (Darocure 1171). Each reaction mixture (prepolymerization) was stirred manually and then sonicated for 5 minutes to ensure efficient mixing of the POSS molecules in the thiol and ene comonomers. For the series of vPOSS-Bu$_2$/Thiol-Ene films, reaction mixtures were maintained for 50:50 thiol:ene molar ratios, and the concentration of each ene was varied. The blended systems contained 50:50 thiol:ene molar ratios with only the weight percentages of POSS (vPOSS-Bu$_1$ and POSS-iBu) varied. A 400-W D-bulb lamp was used as the light source. Each film, obtained by casting onto glass with a 20 mil draw down bar, had a film thickness of 200-250 microns and was cured with a light intensity of 2.23 W/cm^2 and a line speed of 12.19 m/min. These samples were used specifically for thermal (DSC (differential scanning calorimetry), and TGA (thermogravimetric analyis)), mechanical (DMA (dynamic mechanical analysis) and nanoindentation), and physical (Persoz hardness, pencil scratch, and burn tests) analysis of the thiol-ene polymers and blends. Thick film samples (~1 mm) were used exclusively for shore A hardness measurements and PALS (positron annihilation lifetime spectroscopy) analysis. The reaction mixtures (50:50 thiol:ene molar ratios) were placed into glass scintillation vials and photocured in a Rayonet photochemical reactor for a total cure time of 3 hours.

Kinetic analysis

Real-time Fourier Transform IR (real-time FTIR) was performed on an IFS-88 Bruker spectrometer. From analysis of the appropriate peaks, it was possible to obtain actual conversions of thiol and ene groups versus time. Sample preparation included stirring and sonication (5 min) of equal molar reaction mixtures of thiol and ene (triallyl

ether and vPOSS-Bu2). Samples were placed between NaCl plates and irradiated by the UV light filtered with a 1.0 neutral density filter when monitoring vPOSS-Bu$_2$/Thiol-Ene copolymerization and a 0.8 neutral density filter when monitoring vPOSS-Bu$_1$/Thiol-Ene and POSS-iBu/Thiol-Ene polymerizations. The light intensity of the full arc was 187 mW/cm^2 (vPOSS-Bu$_2$/Thiol-Ene copolymers) and 125.5 mW/cm^2 (vPOSS-Bu$_1$/Thiol-Ene and POSS-iBu/Thiol-Ene blends), whereas, the light intensity used for sample exposure was 18.7 mW/cm^2 (copolymers) and 19.88 mW/cm^2 (blends). The peak assignments for the thiol, allyl ether, and vinyl groups on the POSS cage (vPOSS-Bu$_2$) were 2570 cm^{-1}, 1640 cm^{-1}, and 1600 cm^{-1}, respectively. Sample thickness was ~20 microns.

Photo-differential scanning calorimetry (photo-DSC) of vPOSS-Bu$_2$/Thiol-Ene copolymerization was performed using a Perkin-Elmer DSC-7 modified by adding quartz windows to the sample head cover. A medium-pressure mercury lamp was used as the light source. The light intensity of the full arc was ~49.3 mW/cm^2 approximately with a lower light intensity of ~4.93 mW/cm^2 used for the exposure obtained by incorporating a 1.0 neutral density filter. The resultant exotherms are directly related to the photopolymerization rates. Samples were prepared by stirring (manually followed by sonication (5 min)) of 50:50 (thiol:ene) molar reaction mixtures. The prepared samples (2 ± 0.1 mg) were place in specially crimped aluminum pans having an area of 1.257 x 10-3 cm^2. Total conversion (area under the exotherm) of functional groups (thiol and ene (allyl ether and/or vPOSS-Bu$_2$) were calculated using Equation 2, where A = area under the curve.

$$[(\int (A\ (mW/cm^2)) * Sample\ Area\ (cm^2) * (Sample\ Mass\ (mg))^{-1}]\qquad(2)$$

Thermal, mechanical, and physical analysis

Analysis of thermal properties were measured by a DSC Q1000 analyzer (TA Instruments) from -90 ° to 40 °C (copolymers) or -90 °C to 80 °C (blends) at a heating rate of 10 °C/min to measure heat flow (mW) of the polymer as a function of temperature. Glass transition temperatures (T_g) were obtained at the inflection point of the DSC curve found in the glass transition region and melting temperatures (T_m) were obtained as the peak minimum of the DSC curve found in the melting region. Samples were approximately 3-10 mg. Thermal analysis of the pure POSS monomers (POSS-*i*Bu, vPOSS-Bu$_1$, vPOSS-Bu$_2$) were measured from -90 °C to 90 °C at a heating rate of 10 C/min to obtain T_g (vPOSS-Bu$_1$ and vPOSS-Bu$_2$) and T_m (POSS-*i*Bu).

Analysis of mechanical properties was measured by a TA DMA 2920 to obtain storage modulus (E') and loss tangent (tan δ = E''/E') curves as a function of temperature. Thin film samples, prepared with a 20 mil drawdown bar and having a thickness of ~250 microns, a width of 5 mm, and a length of 25 mm, were heated at a scan rate of 2 °C/min over a temperature range of -60 °C to 40 °C (vPOSS-Bu$_1$/Thiol-ene and vPOSS-Bu$_2$/Thiol-Ene) and -50 °C to 100 °C (POSS-*i*Bu/Thiol-Ene). Measurements were performed in the tensile mode. All storage modulus data is plotted in a logarithm scale as a function of temperature.

Dynamic light scattering was performed to determine particle size distribution of the POSS nanoparticles in trithiol/triallyl ether using a Nanotrac NPA252 combination analyzer equipped with a 3 mW external laser diode probe operating at 780 nm. Modified

Mie calculations of the power spectrum obtained from light scattering determined the mean volume and number distribution of particle sizes for the non-spherical silicate POSS particles.

A Hysitron TriboIndenter was used in a closed loop/feedback displacement method to measure surface hardness by nanoindentation. The tip used was a Berkovich diamond tip with an included angle of $142.3°$ with an average radius curvature of 100-200 nm. Indents were made on a 4x4 grid with a separation between indents of 15 μm. The indents were made using a lift height of 100 nm followed by a displacement of 2500 nm into the surface of the samples at a rate of 500 nm/sec. Drift measurements were done over 20 seconds with the analysis of drift being measured over the final 10 seconds of the test with a preload force of 0.5 μN. The thickness of film samples, obtained by 20 mil drawdown bar, was determined by a micrometer to be ~ 200 microns.

Oxygen flux, J(t), at 1 atm pressure, and 23 °C was measured using a Mocon OXTRAN 2/21 unit (ASTM-D 3985-81). This apparatus employs a continuous-flow method to measure J(t) through polymeric films or thin sheets. Permeability, P, and diffusion coefficient, D, are obtained by performing a two-parameter least squares fit of the experimental flux data to the Equation (3) based upon Fick's second law (Equation 4), where P = permeability, p = permeant gas pressure, l = film thickness, D = diffusivity, c = permeant gas concentration, and t = time. Diffusivity, D, is derived from the non-steady state region (slope), and permeability, P, is derived from the steady state region of the experimental flux curve. The solubility, S, is obtained from the relationship [P = D * S]. Before every testing, film specimens were masked, glued using an epoxy based composition on aluminum foil with a circular exposure area of 5×10^{-4} cm^2, then

carefully conditioned in pure nitrogen inside the unit to remove traces of atmospheric oxygen, in order to obtain the non-steady state oxygen flux required for diffusion coefficient measurements. Films were prepared by using a 9 mil drawdown bar onto a glass substrate and photocured on Fusion Epiq 3000 cure line. Reaction mixtures (50:50 thiol:ene molar ratios) were stirred manually followed by sonication (5 min). Average film thickness (~225 microns) was determined using a micrometer with the accuracy of individual thickness measurements approximately ±0.001 mm.

$$J(t) = \frac{Pp}{l}[1 + 2\sum_{n=1}^{\infty}(-1)^n \exp(-D\pi^2 n^2 t / l^2)] \tag{3}$$

(Fick's second law) $$\frac{\partial c}{\partial t} = D\frac{\partial^2 c}{\partial x^2} \tag{4}$$

Scratch resistance of each Trithiol-TAE film was determined by using a pencil hardness test (ASTM D 3363 00) with a series of pencils of varying hardness. Thin films were prepared using a 20 mil drawdown bar onto a glass substrate, with films having thickness of ~250 microns. The range of pencil lead hardness is graded from softest (9B-B) to mid-grade (F and HB) to hardest (H-9H). Persoz pendulum hardness was measured with a BYK Gardner Pendulum Hardness Tester according to ASTM D 4366. Burn tests were performed on free-standing thin films (~250 microns) using ASTM method D 568 56 T. Shore A hardness was measured with a Type A durometer (Model 306L, PTC, Inc.) according to ASTM D 2240 00. Thick samples, having a thickness of ~1 mm and an

area of 3.5 mm^2, were photocured using a Rayonet photochemical reactor (300 nm) for a total cure time of 3 hours.

Spectroscopic analysis

^{1}H and ^{13}C nuclear magnetic resonance (NMR) spectroscopy was performed using a Bruker 300 MHz NMR. The solvent for NMR characterization was deuterated DMSO. A complete description of the peak assignments for vPOSS-Bu$_1$ and vPOSS-Bu$_2$ have been described in the synthetic method of the experimental section.

Positron annihilation liftetime spectroscopy (PALS) measurements were conducted using a custom built instrument employing ^{22}Na as the positron source. The spectrometer, equipped with a special vacuum chamber and temperature control system, is comprised of BaF$_2$ scintillation crystals and photomultiplier tubes, a fast-fast coincidence system based on EC&G Ortec NIM modules (model 583 constant-fraction discriminators), and a model 566 time-to-amplitude converter. Positron lifetime spectra were collected using a PCA multichannel analyzer. Special software, PATFIT-88, was used to process the data in order to extract mean oPs lifetimes and decay intensities. Thick samples (1 mm x 1mm x 1mm) were prepared from photocured samples that were 1 mm x 10 mm x 10 mm and were obtained by exposing to a Rayonet photochemical reactor equipped with 300 nm lamps for a total cure time of 3 hours.

RESULTS AND DISCUSSION

The chemical structures of vinyl POSS particles modified with butyl 3-mercaptopropionate (vPOSS-Bu$_1$ and vPOSS-Bu$_2$) and POSS particles containing isobutyl groups (POSS-iBu), TriThiol (trimethylolpropane tris (3-mercaptopropionate), and TAE (triallyl ether) are shown in Figure 1. vPOSS-Bu$_2$ has four reactive vinyl groups capable of participating in thiol-ene copolymerization directly. Herein, the focus is on a series of POSS thiol-ene copolymers (vPOSS-Bu$_2$/TriThiol-TAE) containing 0 mol%, 1 mol%, 5 mol%, 10 mol%, 20 mol%, and 50 mol% and blends (POSS-iBu/TriThiol-TAE and vPOSSBu$_1$/TriThiol-TAE) containing 0 wt%, 2.2 wt%, 10.2 wt%, 18.8 wt%, 32.4 wt%, and 57.8 wt% (except POSS-iBu/TriThiol-TAE: excess POSS results in poor polymer films and was not evaluated further) which are weights that are equivalent to the molar concentrations of vPOSS-Bu$_2$ used to make the thiol-ene copolymers, respectively. The effect of blending POSS into the thiol-ene network versus reacting POSS and incorporating it into the matrix structure on the film properties of the photocured TriThiol-TAE network is probed.

POSS/Trithiol-TAE Blends

The POSS components with no reactive ene functional groups, POSS-iBu and vPOSS-Bu$_1$, were blended into a TriThiol-TAE sample at 2.2 wt%, 10.2 wt%, 18.8 wt%, 32.4 wt%, and 57.8 wt% and the subsequent mixture photopolymerized. The thermal and mechanical behavior of the cured networks were analyzed by differential scanning calorimetry (DSC) and dynamic mechanical analysis (DMA), and their physical behavior

was measured by pencil scratch, Persoz pendulum, and shore A durometer hardness tests. Persoz pendulum hardness measures energy damping caused by the viscoelastic characteristics of a material. Hard, glasslike materials dissipate energy much less than soft, rubbery materials; therefore, a high number of oscillations is characteristic of materials that are glasslike at the surface. The pencil hardness test was performed to analyze the scratch resistant behavior of the materials and shore A hardness was used to determine the resistance of the material to indentation.

DSC analysis of the POSS-iBu/TriThiol-TAE blends show observable T_g s near -16 °C (Figure 3) that exhibit little change, except for a very small increase in the onset of the glass transition for the sample with 32.4 wt% POSS-iBu. In samples with POSS-iBu, a melt temperature (T_m) at 60 °C is observed at all concentrations of POSS-iBu with the peak area increasing with increasing POSS-iBu content consistent with the melting point (T_m = 60 °C) observed for a pure POSS-iBu (Figure 4). Prior to polymerization, large particles (> 400 nm) of POSS-iBu were visibly observed as a precipitant in the 1:1 molar mixture of TriThiol-TAE with POSS-iBu and smaller particles (40-43 nm) were detected by dynamic light scattering (DLS) analysis at all concentrations, indicating phase separation of POSS-iBu prior to polymerization (Figure 5 shows histograms of particle size distributions). Physical observations of the final cured films (Pictures 1a-d) show opaque films with large, crystalline aggregates within the TriThiol-TAE matrix, even at low loadings (2.2 wt%) of POSS-iBu. The observation of a separate T_g for TriThiol-TAE and a T_m for POSS-iBu at low POSS loadings clearly demonstrates the incompatibility of POSS-iBu with the TriThiol-TAE network. As a result of the distinct phase separation, only a very small increase in the rubbery modulus (30 °C) with increasing POSS loadings

(Figure 6) was observed. Likewise, no significant changes in width of tan delta plots at full width half maximum (FWHM) and only a small increase in T_g (found at peak maximum of the tan delta plots) are observed with increasing concentrations of POSS-iBu (Figure 7). In an attempt to determine the effect of phase separation of the POSS-iBu crystalline regions on the polymerization kinetics, the conversions of the ene and thiol were monitored in real time using infrared spectroscopy. The resultant conversion versus time plots in Figure 8 for thiol and allyl ether for 0, 10.2, and 57.8 wt% of POSS loadings shows that the presence of aggregated POSS-iBu has no affect on the kinetics of the thiol-ene copolymerization and the network formation of TriThiol and TAE. (Note that the thiol conversion is absent in Figure 8a as a result of fluctuations of the base line during kinetic analysis. The total thiol conversion is the same as the total ene (allyl ether) conversion.)

In solution prior to polymerization, vPOSS-Bu$_1$ was incompatible with the 1:1 molar TriThiol-TAE mixture: the DLS results in Figure 9 show that particle sizes with 40-nm diameter and greater were observed by DLS analysis of all of the solutions comprised of the TriThiol and TAE monomer indicating reduced miscibility of the vPOSS-Bu$_1$ in each case (the histograms of size distribution are found in Figures 9). DSC analysis of vPOSS-Bu$_1$/TriThiol-TAE films (Figure 10) shows two distinct observable glass transitions occurring for all cured systems containing vPOSS-Bu$_1$, with no significant shift of the glass transition temperatures (T_{g1}) of either the low temperature vPOSS-Bu$_1$ transition or that of the continuous thiol-ene network: the lower glass transition is observed at a significantly lower temperature ($T_{g2} = -75.7$ °C) that the thiol ene network in a region essentially identical to that of the pure vPOSS-Bu$_1$ (Figure 11).

In Pictures 2a-d, the increasing translucency of the cured netwoks with increasing vPOSS-Bu$_1$ concentration is attributable to the presence of the phase separated liquid vPOSS-Bu$_1$. The effects of phase separation of liquid vPOSS-Bu$_1$ on the mechanical behavior are shown in Figures 12 and 13. As the vPOSS-Bu$_1$ is added, the rubbery modulus and the onset of the glass transition are slightly lowered along with a small broadening in the transition region. In Figure 14, RTIR kinetic results for the thiol and ene functional groups in the TriThiol-TAE system clearly indicate that even for the system with the highest loading (57.8 wt%) of vPOSS-Bu$_1$., the conversion reaches almost 100 % conversion. (Note that the thiol conversion is absent in Figure 14a as a result of fluctuations of the base line during kinetic analysis. The total thiol conversion is the same as the total ene (allyl ether) conversion.) Hence, even with the relatively low light intensity used, the reaction is quantitative and unhindered by the presence of vPOSS-Bu$_1$. This is not unreasonable since it is phase separated and apparently does not interfere in any respect with the polymerization process.

Table 2 shows the results of physical measurements of the photocured vPOSS-Bu$_1$/Trithiol-TAE and POSS-iBu/Trithiol-TAE systems. For both cured systems, the scratch resistance and Persoz hardness decreased with increased weight percentages of POSS particles, although the changes in pencil hardness (decrease) and damping (increase) are more pronounced for the photocured POSS-iBu/Trithiol-TAE systems. Phase separation and poor compatibilization of the POSS components (POSS-iBu and vPOSS-Bu$_1$) and limited interaction between the POSS components and the network contributes to the decrease in hardness and scratch resistance of the films. The durometer hardness (shore A) of both systems shows different trends with increasing POSS

loadings. Observation of the durometer hardness of the vPOSS-Bu$_1$/TriThiol-TAE

networks shows that fracture failure increases, i.e. applied force decreases, as the POSS

loading increases. For POSS-*i*Bu/TriThiol-TAE blends, the durometer hardness increases

upon the addition of POSS at low loading (2.2 wt%) and levels off at higher loadings. In

the case of durometer hardness for POSS-iBu/TriThiol-TAE blends, blooming of POSS

particles to the surface may contribute to the increase in the contact of the shore A probe

with POSS particles. Nonetheless, there is no question that the energy needed to indent

the TriThiol-TAE films increases with POSS content even though it is not incorporated

into the network.

vPOSS-Bu$_2$/Trithiol-TAE Networks

As shown in the analysis of the blends in the previous section, physically mixing

of two different POSS molecules did not result in incorporation into the thiol-ene

network. Good dispersion of POSS-iBu as well as vPOSS-Bu$_1$, even though it had

substituent groups somewhat similar to those of the TriThiol, in the TriThiol-TAE

prepolymerization mixture, was unattainable and hence the POSS components were

essentially excluded from the networks produced by photopolymerization. It is expected

that direct chemical incorporation of POSS molecules should be possible by

functionalization of POSS particles with reactive vinyl groups. In order to generate

POSS with reactive vinyl groups, i.e. vPOSS-Bu$_2$ (see Figure 1), four vinyl groups on

the 10-functional vinyl POSS particles were reacted with butyl 3-mercaptopropionate in

an attempt to improve the compatibilization of vinyl POSS with the thiol (TriThiol) and

allyl ether (TAE) comonomers. The inclusion of vPOSS-Bu$_2$ into a thiol-ene network

involved the copolymerization of thiol with allyl ether and vinyl groups while maintaining a 1:1 molar ratio of total thiol functional groups (TriThiol) to total ene functional groups (TAE + vPOSS-Bu$_2$). The vPOSS-Bu$_2$ particles were incorporated at ene molar concentrations of 0 mol%, 1 mol% (2.2 wt% vPOSS-Bu$_2$), 5 mol% (10.2 wt% vPOSS-Bu$_2$), 10 mol% (18.8 wt% vPOSS-Bu$_2$), 20 mol% (32.4 wt% vPOSS-Bu$_2$), and 50 mol % (57.8 wt% vPOSS-Bu$_2$), which corresponds to the weight percentages of vPOSS-Bu$_1$ added to TriThiol-TAE discussed previously. Notably, it is assumed that there is 100 total moles (corresponding to a 100 mol percent total) of functional groups (thiol + allyl ether + vinyl) present in the sample, and hence there are 50 relative moles of thiol groups and 50 relative moles of ene groups in each system. In order to ascertain the ability of all components to react, the incorporation of vPOSS-Bu$_2$ into the crosslinked network was first analyzed by real-time IR (RTIR) using a relatively low light intensity. Figure 15 shows the resultant conversion plots of the thiol, allyl ether, and vinyl groups for all molar concentrations of vPOSS-Bu$_2$ of the TriThiol-TAE/ vPOSS-Bu$_2$ systems. For the neat TriThiol-TAE system, RTIR based conversion (Figure 15) shows that thiol and allyl ether groups completely polymerize after approximately 20-30 seconds exposure. By comparison, for the sample with 1, 5, and 10 mol%, the total molar conversion of each functional group and conversion rate of vPOSS-Bu$_2$ was only slightly reduced (Figure 15). For 20 and 50 mol% of total ene, under the conditions of the polymerization process an observable decrease in the total molar conversions of the thiol and ene groups accompanied a reduced conversion rate for each species indicating that the presence of vPOSS-Bu$_2$ (Figure 15); note that in all cases the total ene conversion (allyl ether on TAE + vinyl on vPOSS-Bu$_2$) is essentially equal to the total thiol conversion for a given

exposure time. Closer examination of the allyl ether and vinyl ene conversions, it is obvious that while all of the allyl ether groups are converted, there still remains vinyl groups unconverted. It is expected that even using the high light intensities and doses used to make the networks that were evaluated for thermal and mechanical properties, there might be unconverted vinyl groups left. This will be considered further. A comparison of the polymerization exotherms (Figure 16) of the 0, 1, 5, 10, 20 and 50 mol% vPOSS-Bu$_2$ show that the maximum rates of polymerization decrease as the concentration of vPOSS-Bu$_2$ increases. The peak height of each curve, which corresponds to the maximum polymerization rate of each mixture, decreased in the order of 84 mW, 79 mW, 62 mW, 52 mW, 29 mW, and 23 mW for 0, 1, 5, 10, 20, and 50 mol% vPOSS-Bu$_2$, respectively. The especially large drops in the exotherm peak maximum for the samples containing 20 and 50 mol% of vPOSS-Bu$_2$ is consistent with the RTIR results in Figure 15. The large reduction in rate for the samples with 20 and 50 mol% vPOSS-Bu$_2$ results from incomplete conversion of the vinyl ene groups as well as a total reduction in polymerizable ene and thiol group molar concentrations in the mixture due to the high molecular weight per double bond of the ene and a possible contribution from a slower rate constant for addition of thiyl radical to the vinyl functional group. Another contribution for the changes observed in the polymerization rates and conversions of the TriThiol-TAE/ vPOSS-Bu$_2$ systems may result from the significant amount (concentration) of aggregates present in the monomer solution, particularly at high vPOSS-Bu$_2$ concentrations (i.e. 20 and 50 mol%). At all concentrations of vPOSS-Bu$_2$, the mean number of particle sizes in the pre-polymerization mixtures increased from 16 nm, to 40 nm to 53 nm for 1 mol%, 10 mol%,

and 50 mol%, respectively, indicating that aggregation of the vPOSS-Bu$_2$ particles occurs

prior to polymerization. This is particularly important for the samples with large vPOSS-

Bu$_2$ concentrations since they constitute a larger portion of the reactive ene groups and

can thus limit the final conversion. These phase separated species (see DLS results in

Figure 17) can reduce the polymerization rate. Previous studies of various POSS

nanocomposites have observed the formation of aggregates for materials containing low

and high concentrations of POSS. [11-12] Pittman, et. al observed the presence of aggregates

in a vinyl ester system at 10 wt% POSS.[9] In Picture 3 (a-e), thin film samples are slightly

hazy for high concentrations ($\geq$ 20 mol%) vPOSS-Bu$_2$ suggesting that the inclusion of

vPOSS-Bu$_2$ aggregates limits the formation of separate inorganic and organic phases as

observed with the blended systems (POSS-iBu/TriThiol-TAE and vPOSS-Bu$_1$/TriThiol-

TAE. But, instead, the inclusion of vPOSS-Bu$_2$ aggregates creates a network consisting

of aggregated POSS-rich regions and POSS-poor regions. By comparison, the changes in

polymerization rates and conversions upon the inclusion of POSS in the network were

not observed for simple mixing of the POSS-iBu and vPOSS-Bu$_1$ with the TriThiol-TAE

system, i.e., as already indicated in Figure 14, the conversions and polymerization rates

of vPOSS-Bu$_1$ containing systems were unaffected by the presence of vPOSS-Bu$_1$.

DSC analysis of photocured vPOSS-Bu$_2$/TriThiol-TAE networks (Figure 18a)

shows broadening in the glass transition region along with a significant shift of the T$_g$ to

lower temperatures as the higher ene concentrations (20 and 50 mol%) of vPOSS-Bu$_2$.

This is consistent with the lower than quantitative conversion of the vinyl functional

groups on vPOSS-Bu$_2$ and the low T$_g$ of DSC analysis of pure vPOSS-Bu$_2$ (T$_g$ = -76 °C

as shown in Figure 18b) which when incorporated into the network should, per a simple

combining concept of T_gs, results in an intermediate glass transition region   DMA results

in Figures 19 and 20 (and Table 3) reflect onset in the glass transition region at

significantly lower temperatures and broadening of the glass transition region in accord

with the presumption of lower conversion and the incorporation of the flexible vPOSS-

Bu_2 into the network, i. e., the observation of broadening of the tan δ plots (full width at

half height (FWHM) increased) and decrease of T_g suggests that changes in the network

morphology are significant at the higher (20 and 50 mol%) vPOSS-Bu_2 concentrations.

The FWHM value increased from 10.9 °C for neat TriThiol/TAE to 18.2 °C for 50 mol%

vPOSS-Bu_2/TriThiol-TAE and the T_g decreased from -7.9 °C for TriThiol/TAE to -20.2

°C for 50 mol% vPOSS-Bu_2/TriThiol-TAE, respectively. Further examination of storage

modulus (E') plots (Figure 20) shows a small increase of the rubbery modulus up to 10

mol% vPOSS-Bu_2, i.e. E' = 13.2 MPa, 12.41 MPa, and 19.37 MPa for 0 mol%, 1 mol%,

and 10 mol% vPOSS-Bu_2/TriThiol-TAE, respectively, with substantial decreases to E' =

4.31 MPa and 0.833 MPa for 20 mol% and 50 mol% vPOSS-Bu_2/TriThiol-TAE,

respectively. This is clear indication of an incomplete polymerization due to aggregation

of vPOSS-Bu_2 molecules at the higher concentration in the TriThiol-TAE pre-

polymerization mixture: this incomplete conversion would be expected to not only lead

to a lower network linking density, but also vPOSS-Bu_2 aggregates attached to the

network, both of which would lead to a low storage modulus (E') in the rubbery region.

Figure 21a, the master curve plots of force vs. distance for nanoindentation,

shows that the amount of force needed to penetrate the film surface at a depth of 2.5 μm

increased significantly increased with vPOSS-Bu_2 molar concentrations from 200 μN for

0% to 989 μN for 50%. A plot of nanoindenter modulus vs. vPOSS-Bu_2 mol% (Figure

21b) shows nanomodulus measurement results that complement the bulk modulus

obtained by DMA for ene molar concentrations up to 10 mol%, i.e. the bulk tensile

moduli were 13 MPa, 12 MPa, and 19 MPa and the indentation nanomoduli were 28

MPa, 25 MPa, and 30 MPa for 0 mol%, 1 mol%, and 10 mol%, respectively.

Conversely, the indentation nanomodulus increased to 35 MPa and 50 MPa, whereas,

bulk tensile modulus decreased to 4.31 MPa and 0.833 MPa for 20 and 50 mol%,

respectively. It is concluded that the high indentation nanomodulus obtained at higher

concentrations suggests that the nanoindentation measurements due to the probe end size

are sensitive to POSS-Bu$_2$ aggregates at the surface.

In order to evaluate the effect of increasing vPOSS-Bu$_2$ concentration on other

physical and mechanical properties, additional static hardness measurements were made

for comparison (Table 2) with the DMA results in Figure 19. The pencil hardness (i.e.

scratch resistance), Persoz hardness, and durometer hardness moderately increase from

neat TriThiol-TAE (2H, 184 seconds, and 4.25 N) to 10 mol% vPOSS-Bu$_2$/TriThiol-TAE

(6H, 255 seconds, and 4.63 N), but decrease for 20 mol% vPOSS-Bu$_2$/TriThiol-TAE (4H,

255 seconds, and 4.35N) and to 50 mol% vPOSS-Bu$_2$/TriThiol-TAE (2H, 79 seconds,

and 3.39N); this is certainly in agreement with the DMA modulus results and

demonstrates that the combination of incomplete conversion at the higher vPOSS-Bu$_2$

samples (20 and 50 mol%) and the chemical attachment of POSS-rich aggregates

contributes to the decrease of hardness causing fracture failure (pencil hardness and

durometer hardness) and damping (Persoz) to increase.

Thermal stability and burn rates of vPOSS-Bu$_2$/TriThiol-TAE networks.

TGA shows that the thermal char of the vPOSS-Bu$_2$ containing network increases with the vPOSS-Bu$_2$ concentration (Figure 22). The photocured film obtained from the neat TriThiol-TAE system retained less than 5 wt% of char, whereas the sample from the 50 mol% vPOSS-Bu$_2$/Trithiol-TAE mixture retained more than 60 wt% char due to the thermal stability of the silicate structure. Interestingly, the cured network systems containing high concentrations of vPOSS-Bu$_2$ ($\geq$ 20 mol%) show a 5-wt% loss at lower temperatures, i.e. T$_{deg}$ (5 wt% loss) = 344 °C, 343 °C, 333 °C, 328 °C, 304 °C, and 278 °C for 0, 1, 5, 10, 20 and 50 mol% vPOSS-Bu$_2$/TriThiol-TAE, respectively. Incomplete conversion of the 20 and 50 mol% vPOSS-Bu$_2$ and/or S-C-C-Si bond scission may contribute to the onset of degradation at a lower temperature.

Burn rates of POSS containing TriThiol-TAE network

The burn rates (plotted in Figure 23) of all three types of POSS containing thiol-ene networks decreased with increasing POSS concentration, whether the POSS component is physically mixed (vPOSS-Bu$_1$ or POSS-iBu) or chemically bound (vPOSS-Bu$_2$) to the TriThiol-TAE network. The burn rates of the crystalline, solid phase blends significantly decreased from 11.2 in^2/second, to 9.3 in^2/second, to 7.95 in^2/second, to 3.32 in^2/second, to 2.21 in^2/second for 0, 2.2, 10.2, 18.8, and 32.4 wt% POSS-iBu/TriThiol-TAE photocured samples. However, the changes in burn rates were greater for the systems with vPOSS-Bu$_1$, i.e. the burn rates for 0, 2.2, 10.2, 18.8, 32.4, and 57.8 wt% vPOSS-Bu$_1$/TriThiol-TAE photocured samples are 11.2 in^2/second, 4.59 in^2/second, 3.1 in^2/second, 2.04 in^2/second, 3.16 in^2/second, and 2.76 in^2/second, respectively. The burn rates of vPOSS-Bu$_2$/TriThiol-TAE photocured samples decreased from 11.2 in^2/second,

to 6.24 in^2/second, to 4.63 in^2/second, to 4.68 in^2/second, to 4.63 in^2/second and finally to 4.06 in^2/second for 0, 1, 5, 10, 20, and 50 mol% vPOSS-Bu$_2$/TriThiol-TAE, respectively. A substantial decrease in the burn rates is observed even upon incorporation of liquid vPOSS-Bu$_2$ nanoparticles into the thiol-TAE network. And, in general, the initial decrease in burn rate is less effective for the crystalline POSS (POSS-iBu).

Free volume of POSS Containing Thiol-TAE networks

PALS (positron annihilation lifetime spectroscopy) was used to observe the effects of POSS inclusion on free volume of the TriThiol-TAE matrix in order to understand the consequences of the addition by physical or chemical methods. For PALS, the intensity and lifetime (τ_3) measurements of the ortho-positronium (oPs) provide information concerning the hole size distribution and hole size of free volume within the polymer matrix. The intensity of oPs decay is directly related to the number of voids (holes) present within the polymer, whereas the lifetime of oPs, τ_3, is related to size of the voids found within the network. Figure 24 shows the plots of Intensity vs. POSS wt% and Lifetime vs. POSS wt% for the POSS/TriThiol-TAE blends with separate solid phase (POSS-iBu/TriThiol-TAE) and liquid phase (vPOSS-Bu$_1$/TriThiol-TAE) components and copolymers formed from photopolymerization of the vPOSS-Bu$_2$/TriThiol-TAE where reaction occurs between thiol and the two ene components. A comparison of the PALS parameters for each system demonstrates the influence of POSS physical state (crystalline or amorphous) and type of POSS inclusion (physical or chemical) upon the free volume of the final photocured films. In the case of physical addition (by mixing) of POSS-iBu (crystalline) into the TriThiol-TAE matrix, a

significant change in intensity (increase, Figure 24a) and lifetime (decrease, Figure 24b)

is observed as the POSS loading increased from 0 to 2.2 wt% steadily changing as POSS

loadings increase to 32.4 wt%. PALS measurement obtained for pure POSS-iBu (100%

in Figure 24) is used as a control variable to define the effect of crystalline POSS on free

volume. The initial change in intensity and lifetime at low POSS loading (2.2 wt%) is

substantial, indicating that mixing POSS-iBu at low loadings has a significant effect on

the distribution and size of free volume. As the concentration of POSS-iBu increases, the

free volume increases to a value comparable to pure crystalline POSS-iBu showing that

the material with respect to free volume behaves less as an amorphous polymer and more

as large, crystalline particles. The physical addition of vPOSS-Bu_1 (amorphous) to the

TriThiol-TAE matrix affects free volume changes by significantly changing the size of

the holes (cavities) embedded within the TriThiol-TAE matrix, i.e. lifetime

measurements increase with increasing vPOSS-Bu_1 loading (Figure 24b). The changes in

intensity are minimal with the increase of vPOSS-Bu_1 loading. Note that PALS

measurements of the pure vPOSS-Bu_1 are unattainable since the molecules are in liquid

state; therefore, a comparison of the changes in the vPOSS-Bu_1/TriThiol-TAE blended

systems with respect to pure vPOSS-Bu_1 is not possible. Upon the chemical incorporation

of vPOSS-Bu_2, a liquid POSS, via copolymerization of the vinyl and thiol groups,

significant changes in intensity (decrease, Figure 24a) and lifetime (increase, Figure 24b)

are observed with increasing vPOSS-Bu_2 concentration. The plot of intensity versus

POSS concentration (Figure 24a) shows that the number of voids decreases with

increasing vPOSS-Bu_2 ene molar concentration suggesting that holes created within the

vPOSS-Bu_2 cages are immeasurable by PALS analysis. As a consequence of POSS

inclusion into the thiol-ene network, the observed changes in intensity are a consequence of free volume changes occurring within the TriThiol-TAE matrix (as indicted previously due to possible incomplete conversion and/or chemical attachment of POSS aggregates to the network) for which the amount of measurable free volume increases along with an increase of vPOSS-Bu$_2$ concentration. These results clearly show that the chemical incorporation of vPOSS-Bu$_2$ into the TriThiol-TAE network affects free volume by increasing the size of holes found within the network structure. Note that the change in lifetime measurements (Figure 24b) are analogous when liquid POSS (vPOSS-Bu$_1$ and vPOSS-Bu$_2$) is added by physical (mixing) or chemical (copolymerization) methods and may be correlated to the interaction of the organic substituents (**Bu**, Figure 1) with the TriThiol-TAE matrix.

Oxygen Flux Measurements for POSS Containing Thiol-TAE networks

Oxygen flux measurements were used to understand the effect of POSS in thiol-ene networks on gas transport in correlation with the free volume changes observed by PALS analysis: samples containing 32.4 wt% (20 mol%) POSS were chosen for examination. The oxygen flux curves (oxygen flux vs. time) for neat TriThiol-TAE, vPOSS-Bu$_1$/TriThiol-TAE (32.4 wt%), and vPOSS-Bu$_2$/Trithiol-TAE (20 mol%) networks are shown in Figure 25 along with permeation constants, P, for each system in Table 4. Gas permeation constants are derived from the oxygen flux curve, i.e. gas permeation occurs at the point of steady state O$_2$ flux as shown in Figure 25.

Oxygen flux measurements were unattainable for POSS-iBu/TriThiol-TAE blend (32.4 wt%) since oxygen flux was extremely high and exceeded the experimental limit

for oxygen flow (> 700 cc cm m^{-2} day^{-1}): this is consistent with the results for free

volume reported by PALS. When the O_2 permeation constants (P) of vPOSS-

Bu$_1$/TriThiol-TAE and vPOSS-Bu$_2$/TriThiol-TAE are compared to the flux parameters of

neat TriThiol-TAE polymer in Table 4, the changes in oxygen permeation were marginal

for vPOSS-Bu$_1$/TriThiol-TAE (decrease) and vPOSS-Bu$_2$/TriThiol-TAE (increase).

Observation of the O_2 permeation shows that the inclusion of POSS by physical mixing

or chemical incorporation had little significant effect on oxygen transport properties of

the TriThiol-TAE network.

CONCLUSION

The compatibility and type of incorporation of POSS nanoparticles have a strong

influence on the morphology, although the mechanical and surface behavior of the thiol-

ene network structure shows no enhancement. When POSS particles (POSS-iBu and

vPOSS-Bu$_1$) are blended into the TriThiol-TAE matrix, separate POSS phases (solid or

liquid) are formed. The appearance of a second heat transition (T$_g$ (vPOSS-Bu$_1$) or T$_m$

(POSS-iBu)) occurs and the uniformity of the network is maintained as shown by DSC

analysis. DLS analysis of the blended systems of vPOSS-Bu$_1$/TriThiol-TAE prior to

polymerization demonstrates the affinity of POSS toward aggregation at low

concentration (10.2 wt%), although the chemical nature of the organic substituents (Bu)

are similar to the chemical nature of the TriThiol-TAE polymer backbone. Phase

separation of the POSS components (POSS-iBu and vPOSS-Bu$_1$) reduces mechanical and

physical film properties suggesting that POSS interaction with polymer network is

ineffective when POSS molecules are blended into the TriThiol-TAE matrix. As shown with POSS-iBu/TriThiol-TAE blends, scratch resistance and surface hardness dramatically decrease upon inclusion of POSS-iBu nanoparticles into the TriThiol-TAE network. Likewise, chemical incorporation of vPOSS-Bu$_2$ into the TriThiol-TAE network, as confirmed by real-time FTIR, reduces mechanical and physical properties of the final cured films at high concentrations (20 and 50 mol%). The interaction of vPOSS-Bu$_2$ and TriThiol-TAE is not significantly enhanced by compatibilization since DLS analysis shows vPOSS-Bu$_2$ aggregation at all concentrations. DSC analysis of vPOSS-Bu$_2$/TriThiol-TAE copolymers shows broadening in the glass transition and lower T$_g$ resulting from the incomplete conversion of POSS vinyl groups and/or chemical attachment of aggregates within the network. The reduced availability of vinyl groups, which are locked within the vPOSS-Bu$_2$ aggregates, reduces the network linking density, and, consequently, reduces mechanical (lower rubber modulus) and physical properties (less scratch resistance). However, TGA results showed that more material (char) is retained with an increase of vPOSS-Bu$_2$ concentration, with 5 wt% char retained for neat TriThiol-TAE and 60 wt% char retained for 50 mol% vPOSS-Bu$_2$/TriThiol-TAE. Additionally, flame spread of the material was reduced from 11.2 in^2/second for neat TriThiol-TAE to 6.23 in^2/second, 4.59 in^2/second, and 9.30 in^2/second containing only 1 mol% (2.2 wt%) vPOSS-Bu$_2$, (2.2 wt%) vPOSS-Bu$_1$, and (2.2 wt%) POSS-iBu, respectively. PALS analysis suggests that hole free volume of the matrix is increased upon the inclusion of liquid POSS (vPOSS-Bu$_1$ and vPOSS-Bu$_2$) into the network, although oxygen transport properties are unaffected by the presence of POSS in the network.

REFERENCES

[1] Pielichowski, K.; Nuguna, J.; Janowski, B.; and Pielichowsk, J.; *Adv. Polym. Sci.*, **2006**, *201*, 225-296.

[2] Li, G.; Wang, H., and, Pittman, Jr., C. U.; *J. Inorg./Organometallic Polym.*, **2002**, *11*, 123-154.

[3] Madbouly, S. A.; Otaigbe, J. U.; Nanda, A. K.; Wicks, D. A., *Macromolecules*, **2007**, *40*, 4982-4991.

[4] Huang, C.; Kuo, S.; Lin, F.; Huang, W.; Wang, C.; Chen, W.; Chang, F., *Macromolecules*, **2006**, *39*, 300-308.

[5] Chen, J.; Yao, B.; Su, W.; Yang, Y., *Polym.*, **2007**, *48*, 1756-1769.

[6] Li, G.; Wang, L.; Ni, H.; Pittman, Jr., C. U., *J. Inorg./Organometallic Polym.*, **2002**, *11*, 123-153.

[7] Zhang, X.; Huang, Y.; Wang, Tianyu; Liu, L.. *Nanoscience*, **2006**, *11*, 107-113.

[8] Misra, R.; Morgan, S. E. *Polym. Prep.*, **2006**, *47*, 410-411

[9] Liu, Y.; Ni, Y.; Zheng, S., *Macromol. Chem./Phys.*, **2006**, *207*, 1842-1851.

[10] Jacobine, A. F. In *Radiation Curing in Polymer Science and Technology III: Polymerization Mechanisms*; Fouassier, J. D.; Rabek, J. F., Eds.; London:Elsevier, 1993; Chapter 7.

[11] Li, G; Wang, L.; Toghiani, H..; Daulton, T. L.; Pittman, Jr., C. U., *Polym.*, **2002**, *43*, 4167-4176.

[12] Zhang, P.; Lee, S.; Yoonessi, M.; Liang, K.; Pittman, Jr., C. U., *Polym.*, **2006**, *47*, 2984-2996.

Vinyl POSS
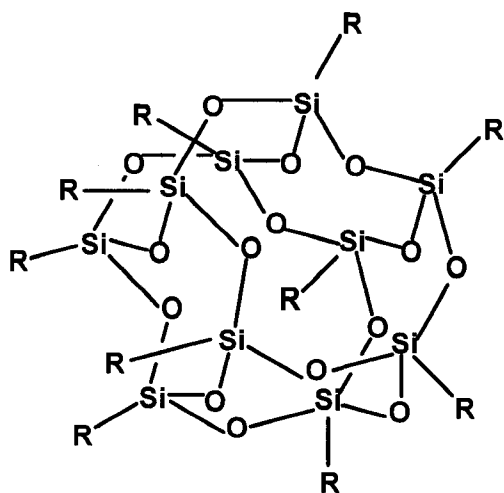
vPOSS-Bu₁
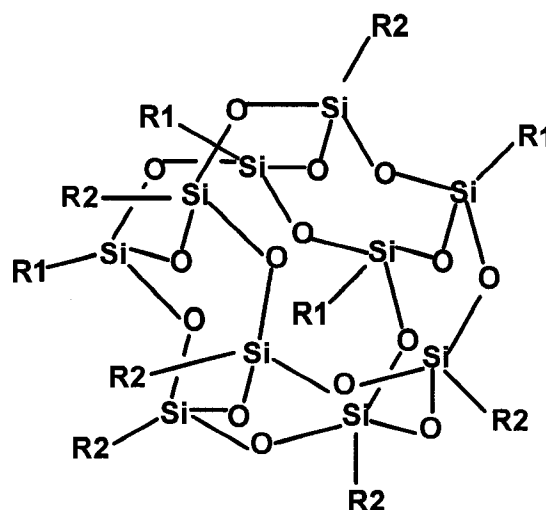
R = Butyl 3-mercaptopropionate (**Bu**)

vPOSS-Bu₂

R1 = Butyl 3-mercaptopropionate (**Bu**),
R2 = CH₂=CH–
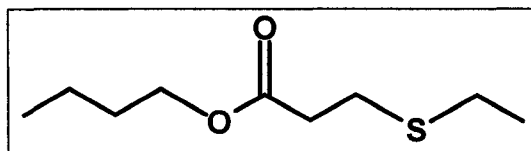
Bu
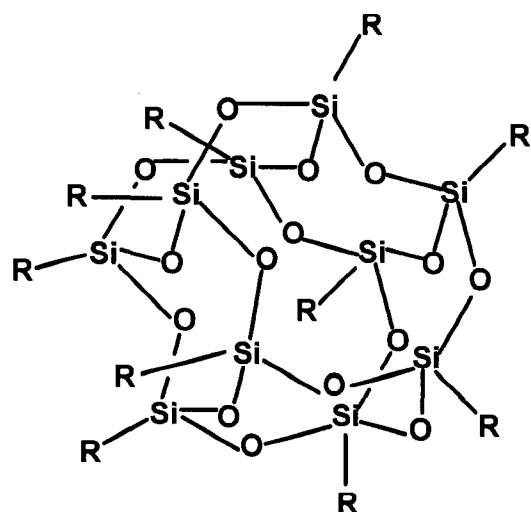
POSS-*i*Bu

R = Isobutyl (*i*Bu)
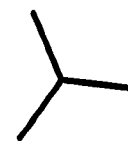
R = *i*Bu
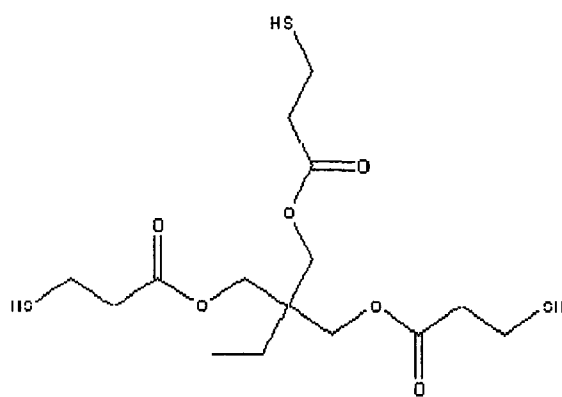
TriThiol
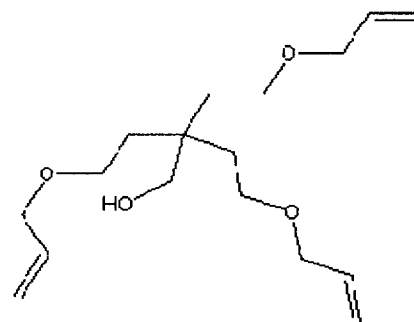
TAE

Figure 1. The chemical structures of the vinyl POSS, vPOSS-Bu₁, vPOSS-Bu₂, POSS-*i*Bu, trimethylolpropane tris (3-mercaptopropionate (TriThiol), and allyl ether pentaerythritol (TAE) comonomers.

(a)

(b)
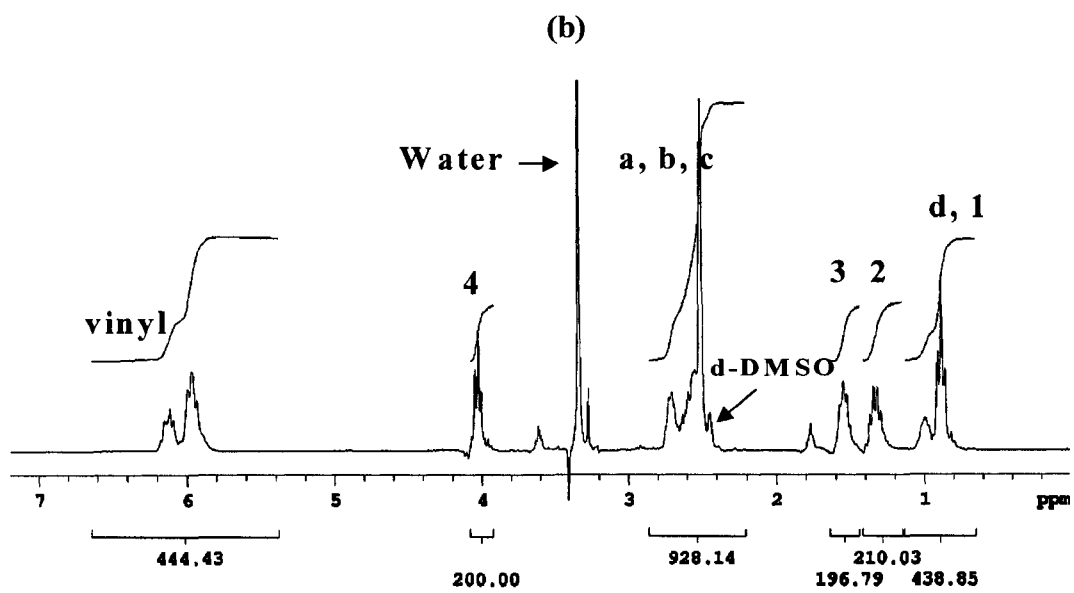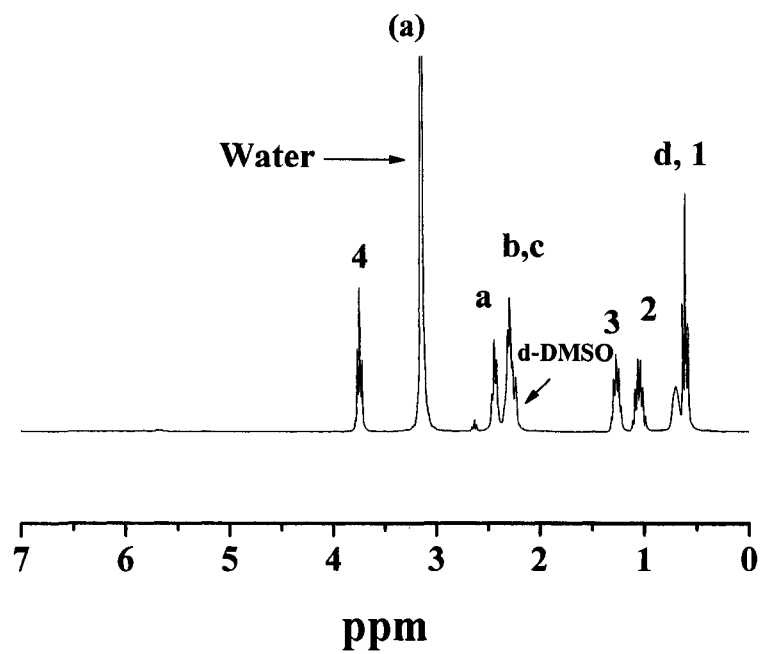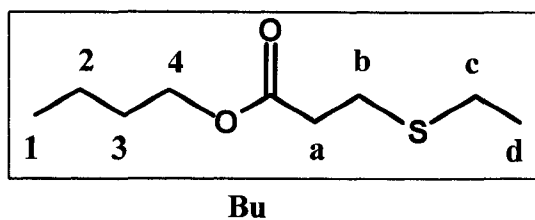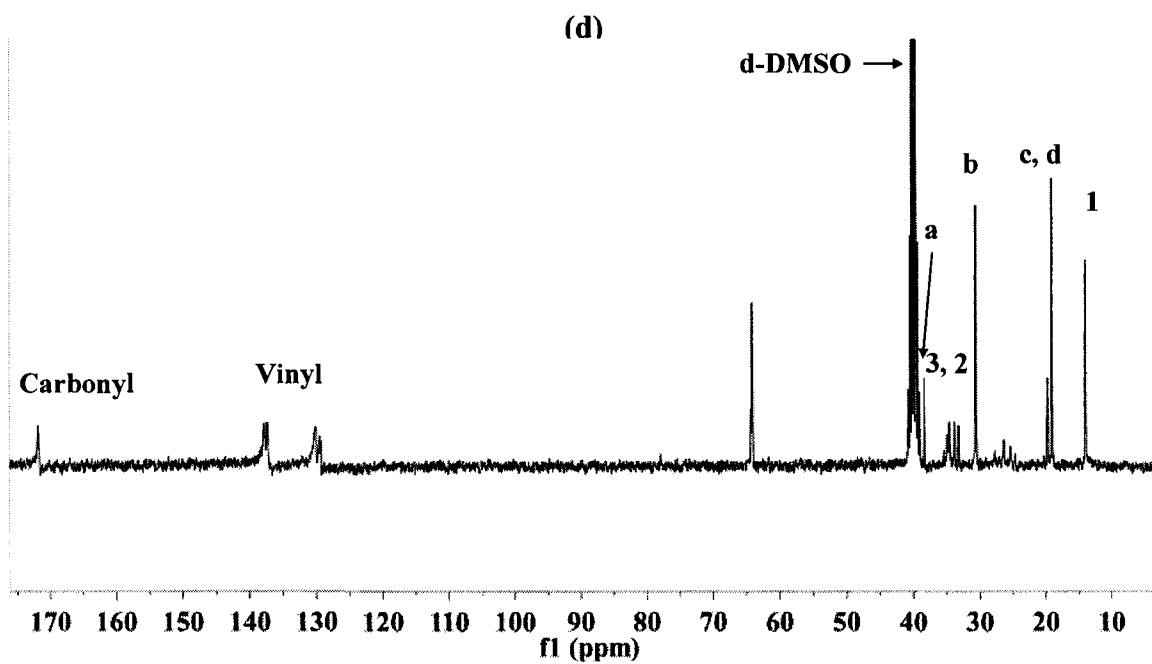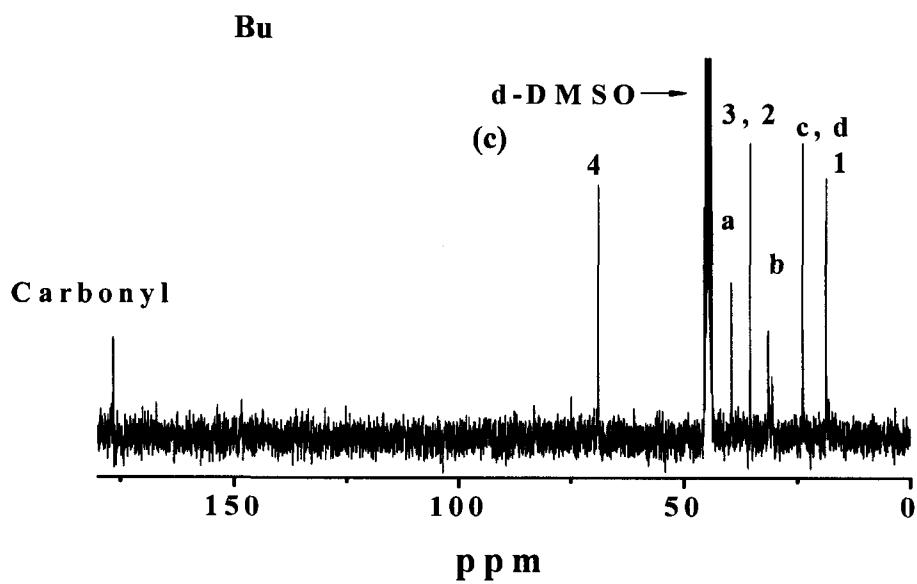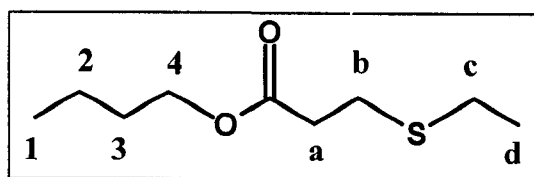
Figure 2. ^{1}H and ^{13}C NMR. a) Proton NMR of vPOSS-Bu$_1$, b) Proton NMR of vPOSS-Bu$_2$, c) Carbon NMR of vPOSS-Bu$_1$, and d) Carbon NMR of vPOSS-Bu$_2$.
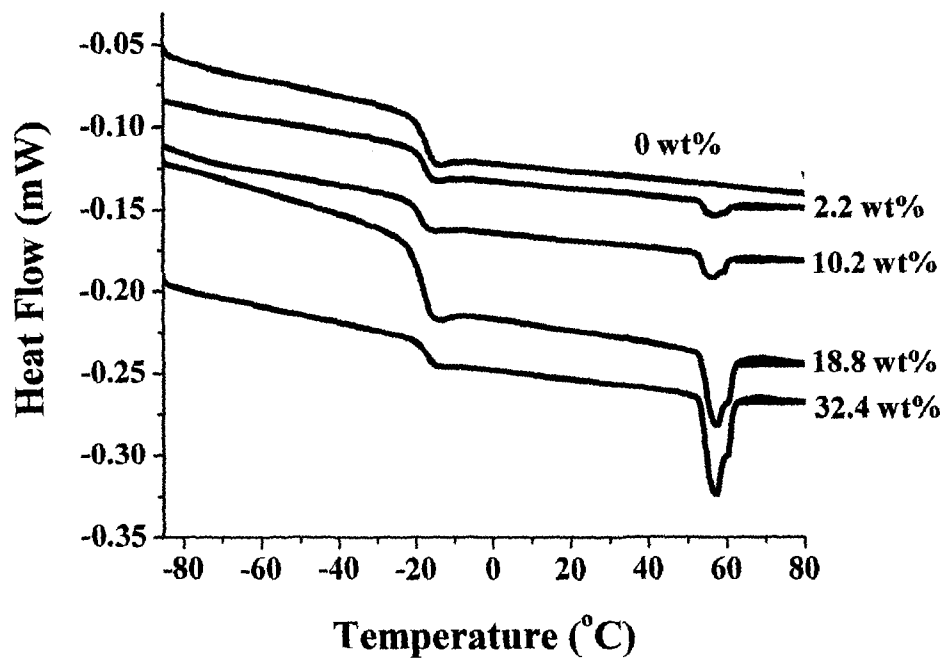
Figure 3. DSC analysis of the immiscible POSS-*i*Bu/TriThiol-TAE blends at 0, 2.2, 10.2, 18.8, and 32.4 wt% POSS-*i*Bu having a sample thickness of 250 microns.
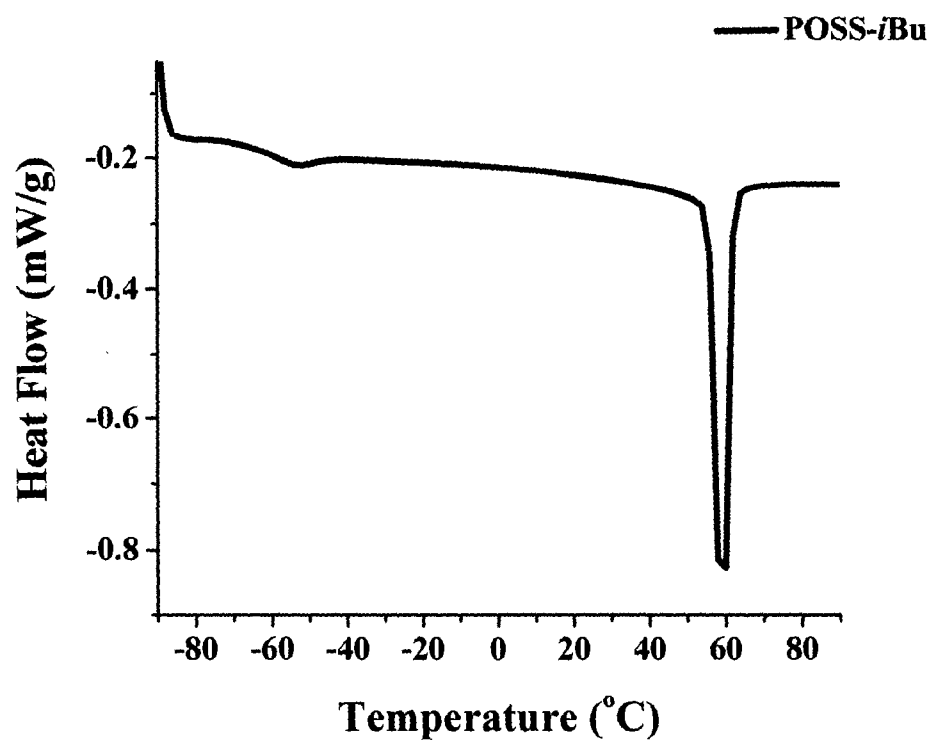
Figure 4. DSC analysis of the pure POSS-*i*Bu.
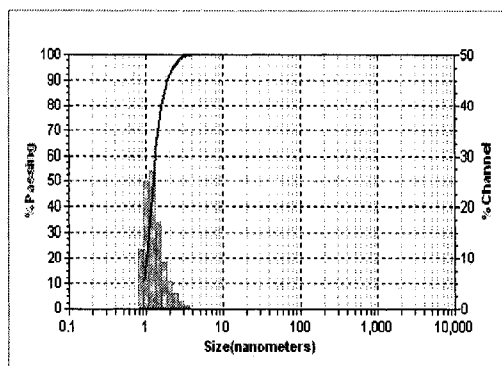
(a)
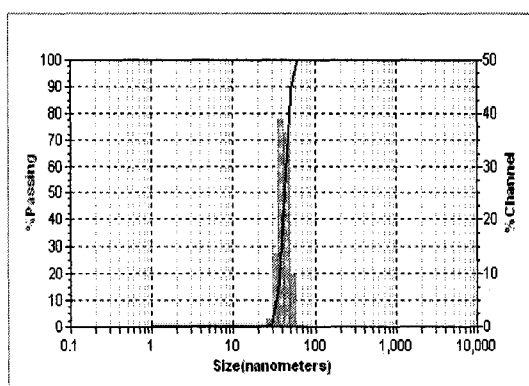
(b)

(c)
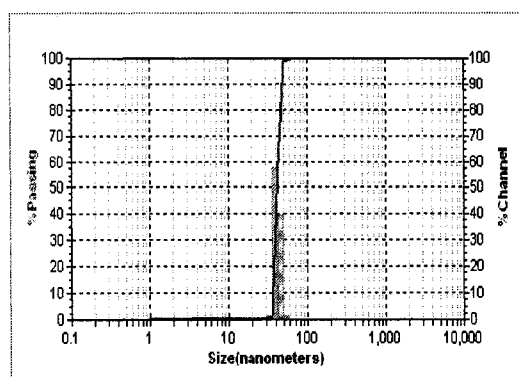
(d)
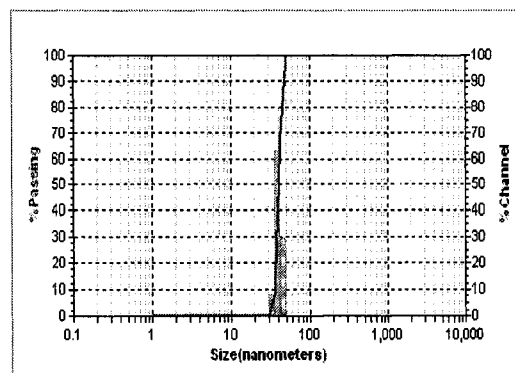
(e)

Figure 5. DLS particle analysis. Number distribution of POSS-*i*Bu in monomer solution for a) neat TriThiol-TAE, b) 2.2 wt%, bc) 10.2 wt%, d) 18.8 wt%, and e) 32.4 wt%.
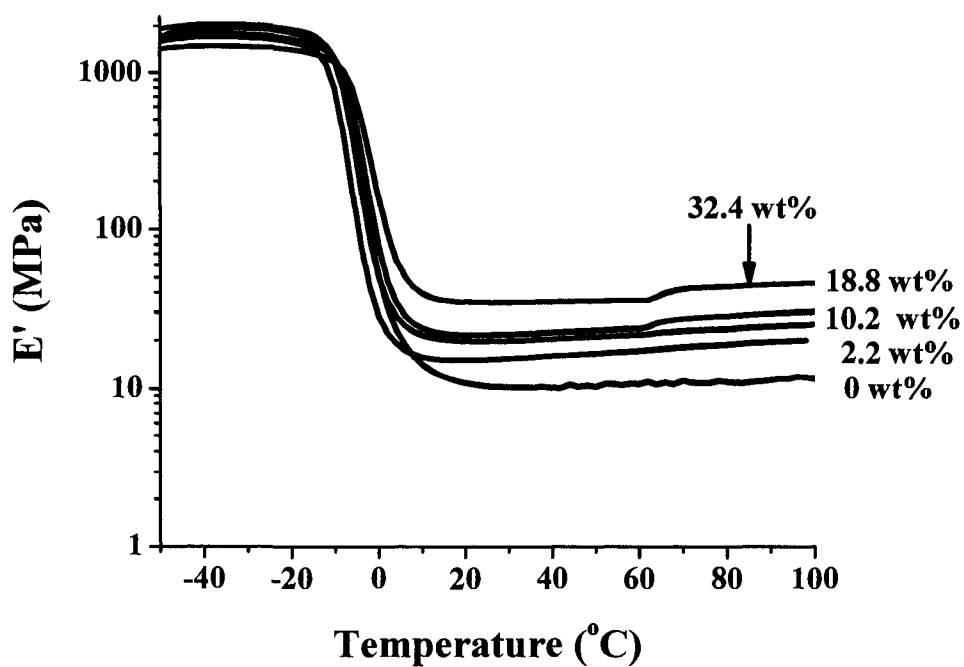
Figure 6. Storage modulus (E' vs. Temperature) for POSS-*i*Bu/TriThiol-TAE systems at 0, 2.2, 10.2, 18.8, and 32.4 wt% having a sample thickness of 250 microns.
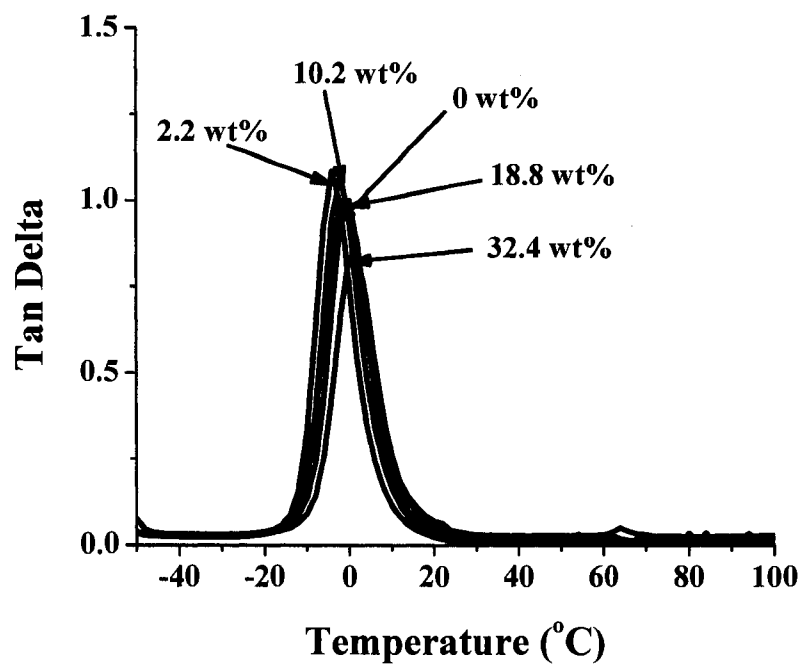
Figure 7. Tan delta plots for POSS-*i*Bu/TriThiol-TAE systems at 0, 2.2, 10.2, 18.8, and 32.4 wt% having a sample thickness at 250 microns.
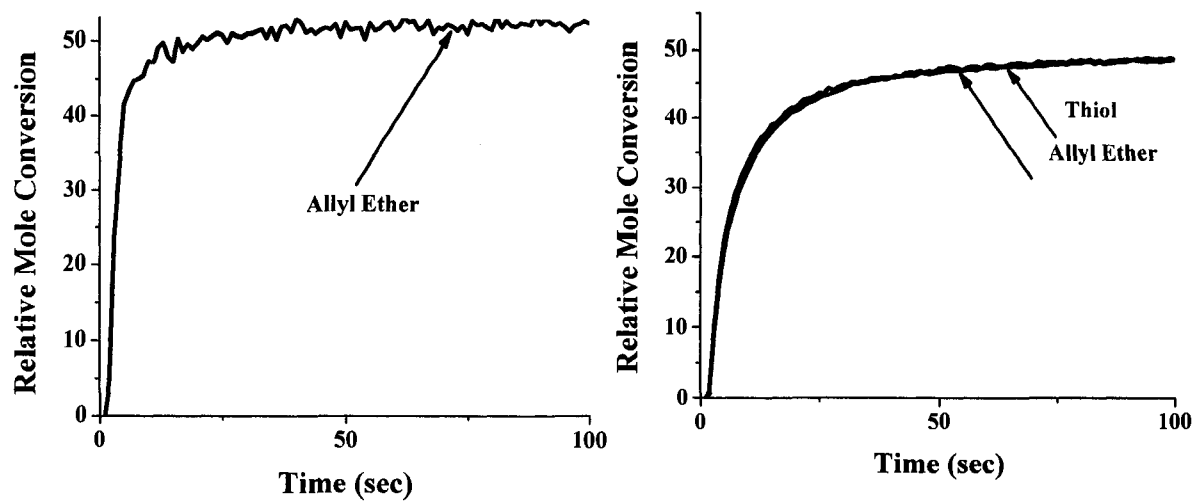
(a)

(b)
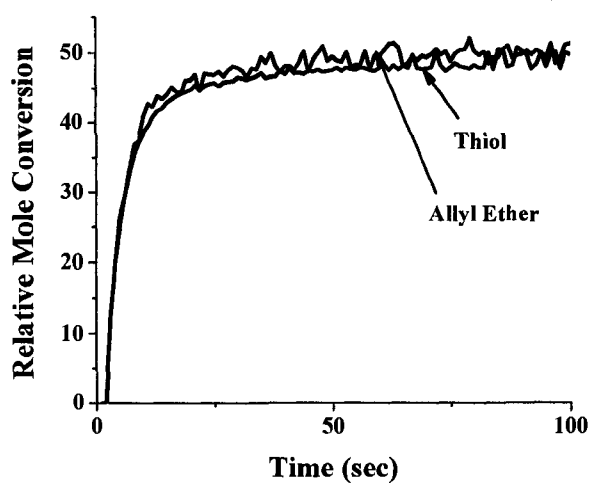
(c)

Figure 8. RT-FTIR based conversion of thiol and allyl ether groups for a) 0 wt% (See Appendix C for thiol conversion), b) 2.2 wt%, and c) 32.4 wt% POSS-iBu. Sample thickness is ~20 microns. Light intensity = 19.9 mW/cm^{-2}. Sample thickness was ~20 microns.
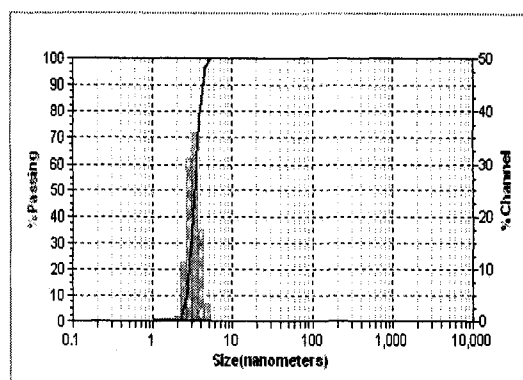
(a)
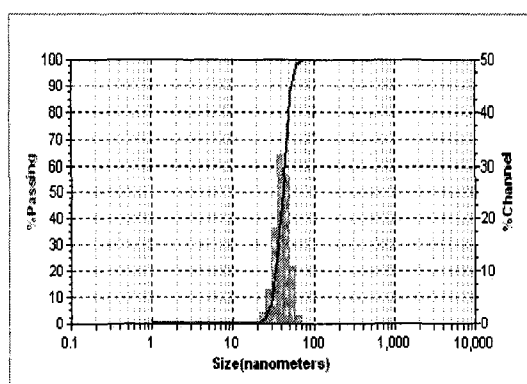
(b)
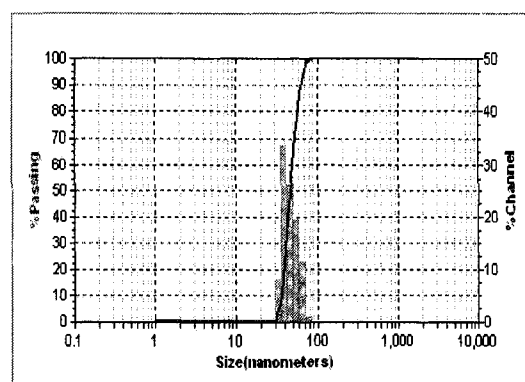
(c)
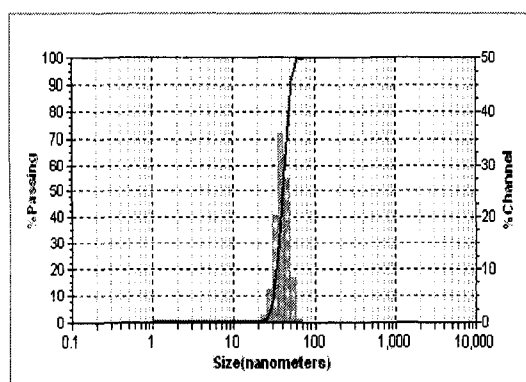
(d)
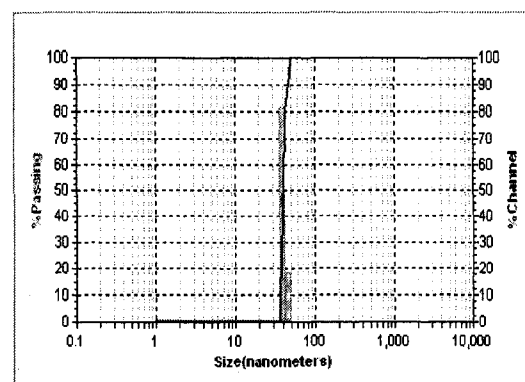
(e)

Figure 9. DLS particle analysis. Number distribution of POSS-iBu in monomer solution for a) 2.2 wt%, b) 10.2 wt%, c) 18.8 wt%, d) 32.4 wt%, and e) 57.8 wt%.
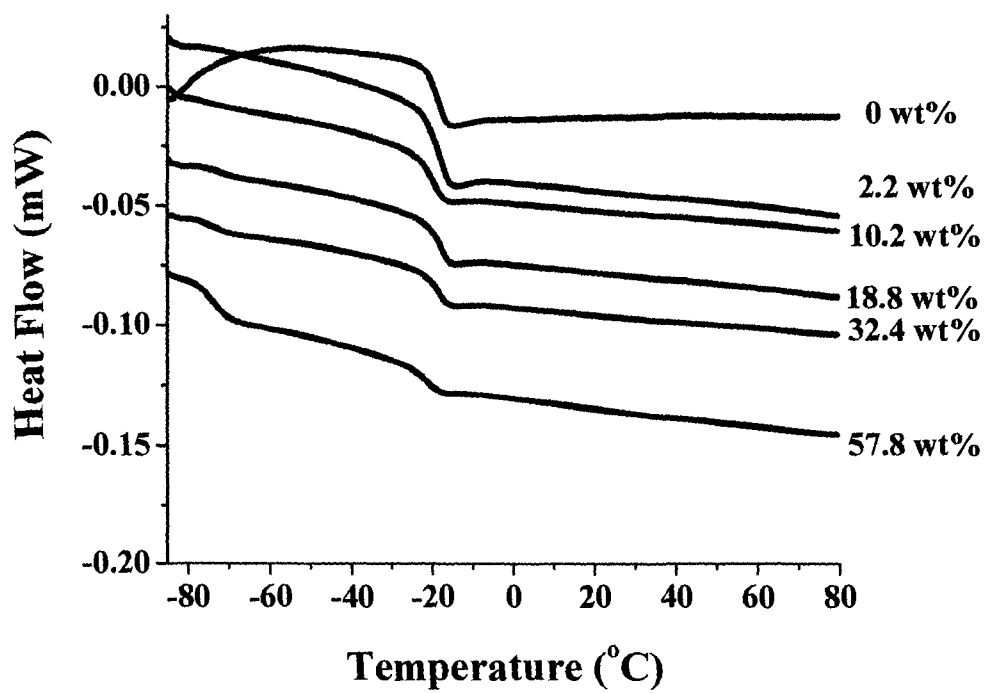
Figure 10. DSC analysis of the immiscible vPOSS-Bu₁/TriThiol-TAE blends at 0, 2.2, 10.2, 18.8, 32.4, and 57.8 wt% vPOSS-Bu₁ having a sample thickness of 250 microns.
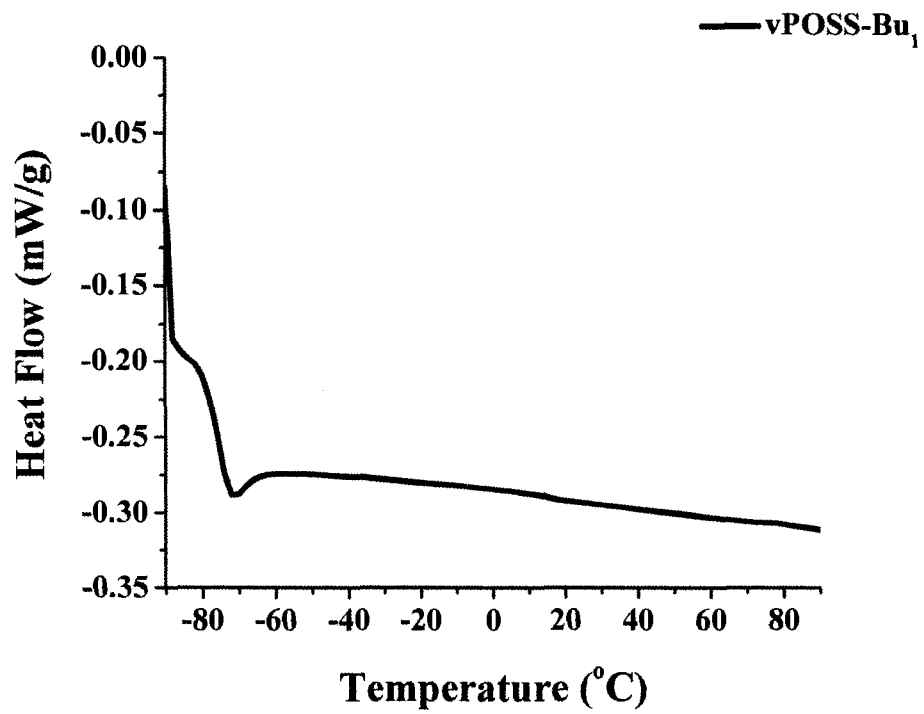
Figure 11. DSC analysis of pure vPOSS-Bu$_1$.
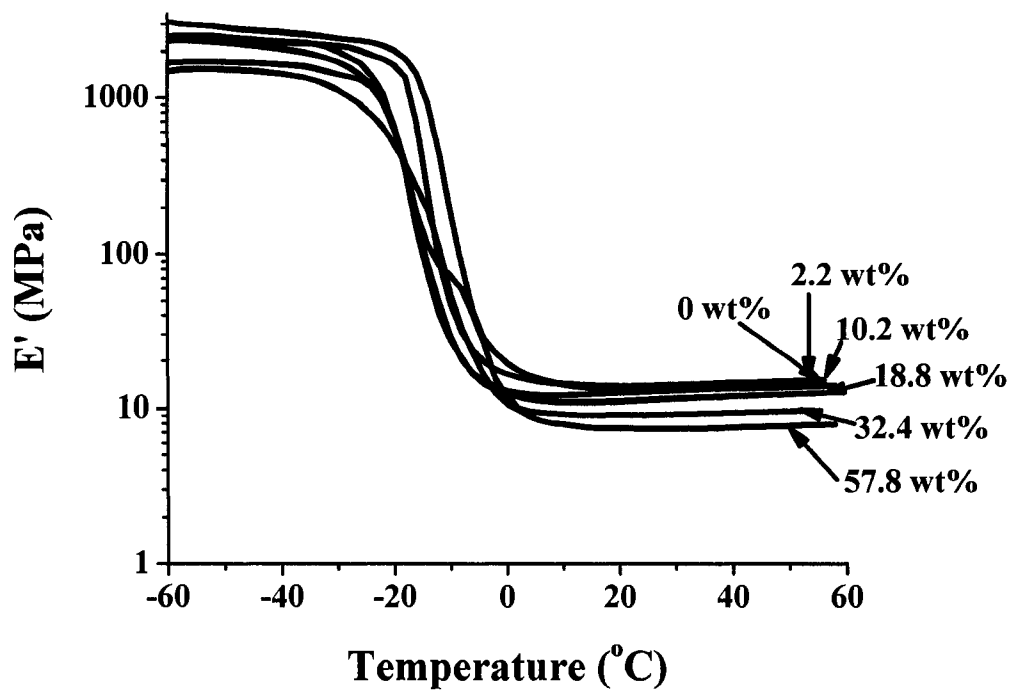
Figure 12. Storage modulus (E' vs. Temperature) for vPOSS-Bu₁/TriThiol-TAE systems at 0, 2.2, 10.2, 18.8, 32.4, and 57.8 wt% having a sample thickness of 250 microns.
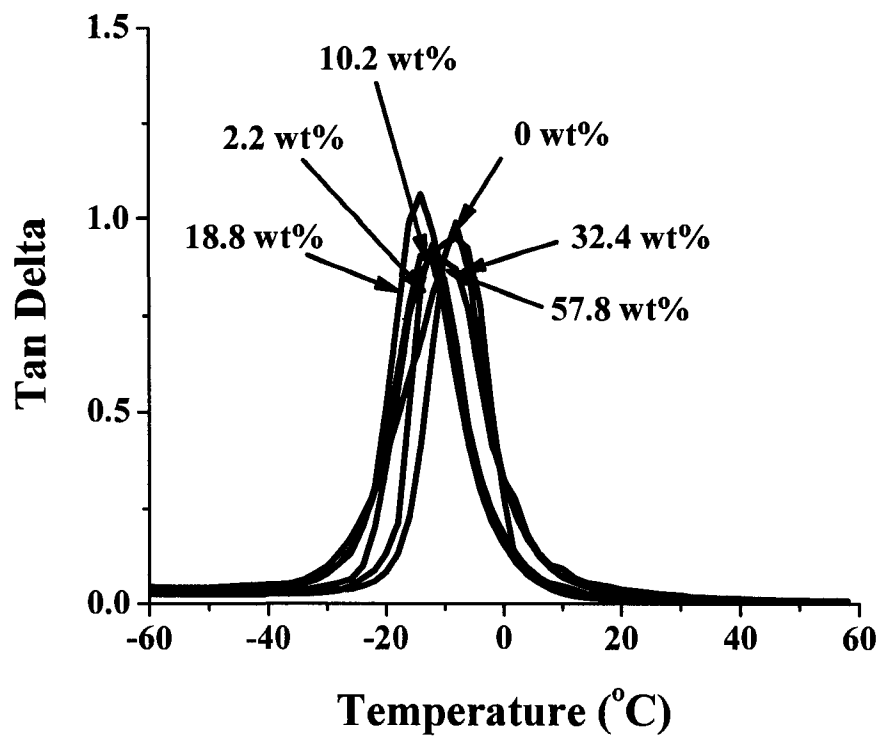
Figure 13. Tan delta plots for vPOSS-Bu$_1$/TriThiol-TAE systems having 0, 2.2, 10.2. 18.8. 32.4, and 57.8 wt% having a sample thickness of 250 microns.

(a)

(b)

(c)
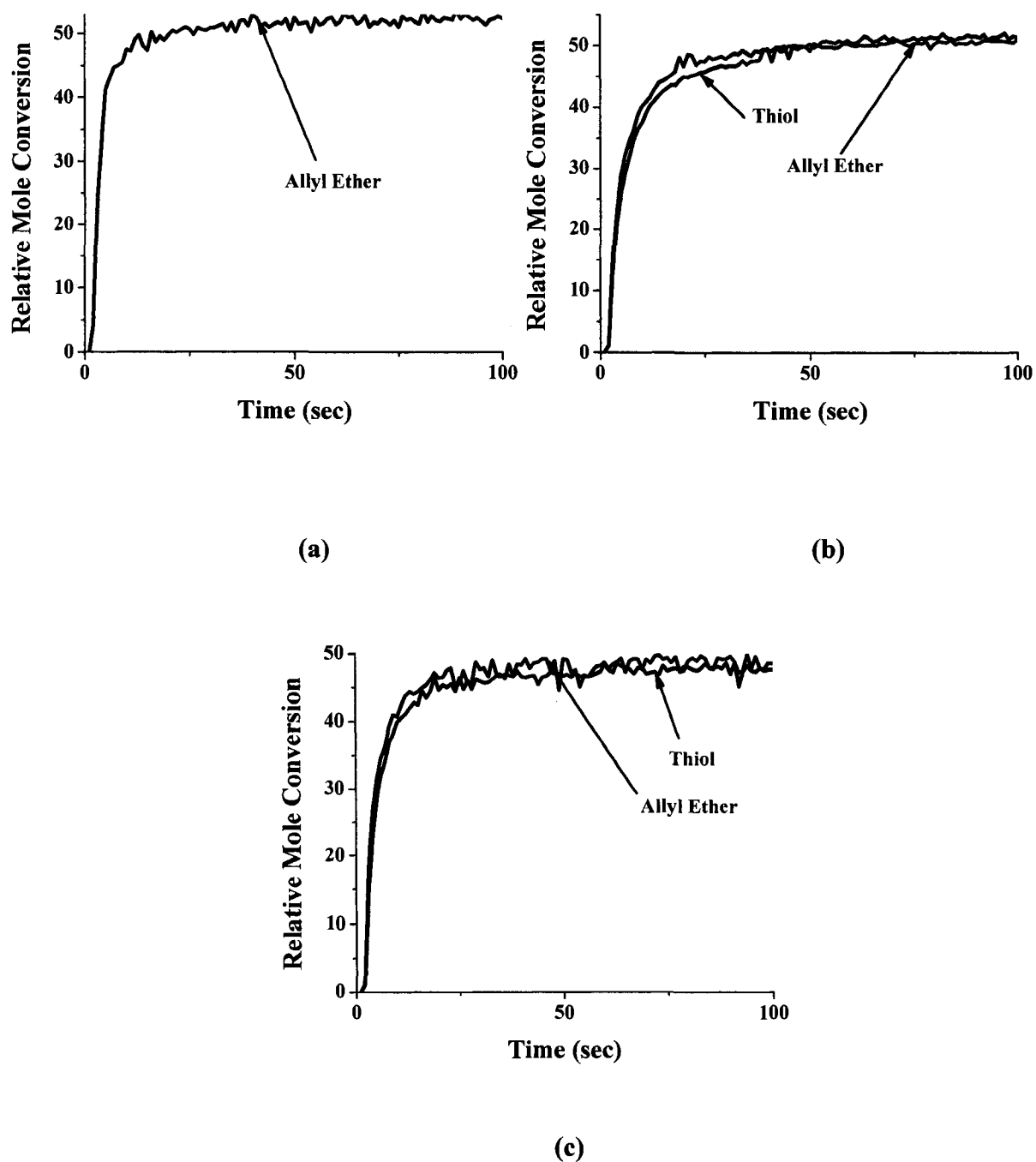
Figure 14. RT-FTIR based conversion of thiol and allyl ether groups for a) 0 wt% (See Appendix C for thiol conversion), b) 2.2 wt%, and c) 56.4 wt% vPOSS-Bu₁. Sample thickness was ~20 microns. Light intensity = 19.9 mW/cm⁻². Sample thickness was ~20 microns.
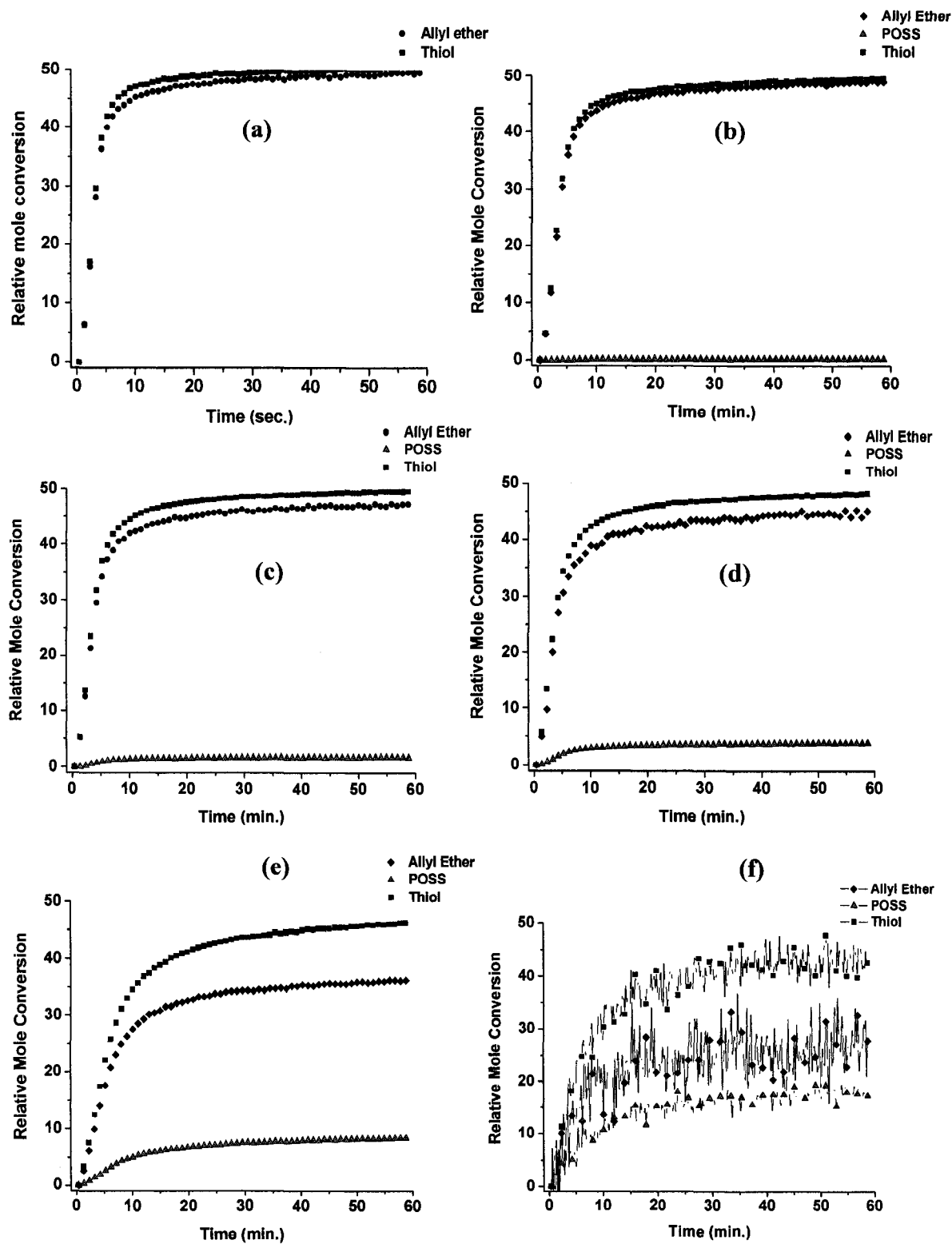
Figure 15. FT-RTIR-based mole conversion of thiol, allyl ether, and vinyl group conversions for a) 0 mol%, b) 1 mol% , c) 5 mol%, d) 10 mol%, e) 20 mol% ,and f) 50

mol% vPOSS-Bu$_2$/TriThiol/TriThiol-TAE copolymers. Light intensity is 18.7 mW/cm^2. Sample thickness was ~20 microns.
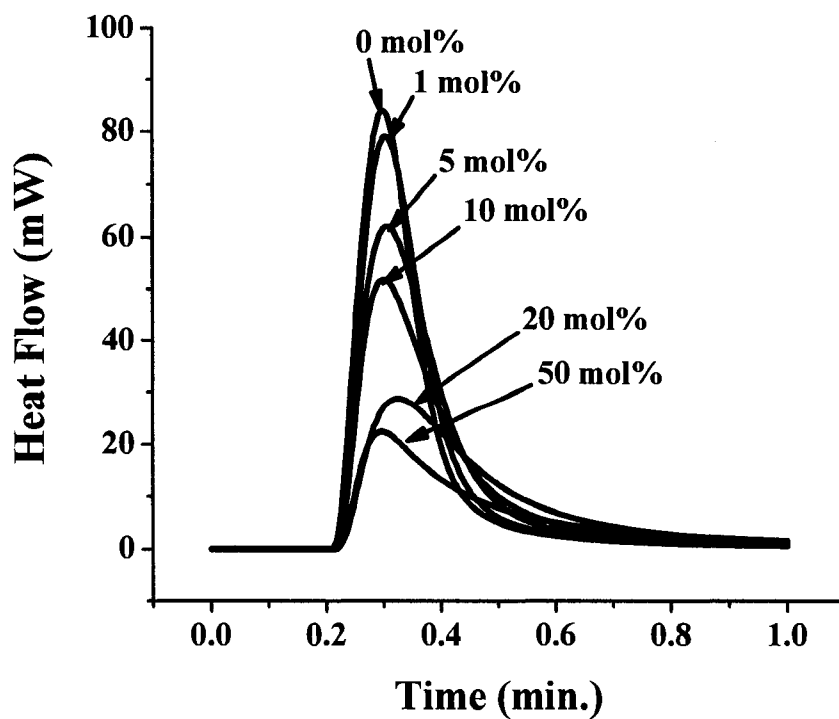
Figure 16. Photo-DSC. Exothermic plots of photopolymerizations of vPOSS-Bu$_2$/TriThiol-TAE systems for 0 mol%, 1 mol% , 5 mol%, 10 mol%, 20 mol% , and 50 mol% vPOSS-Bu$_2$. Light intensity was 4.93 mW/cm^2 using a 1.0 neutral density filter, and sample thicknesses were 200 microns.
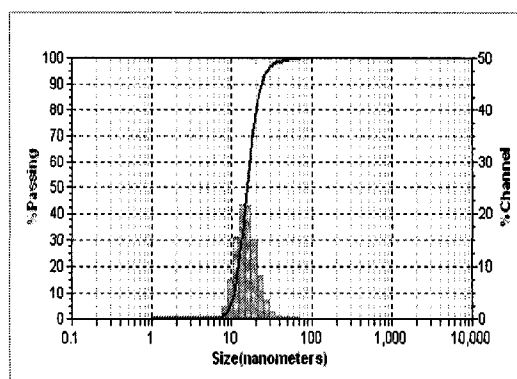
(a)
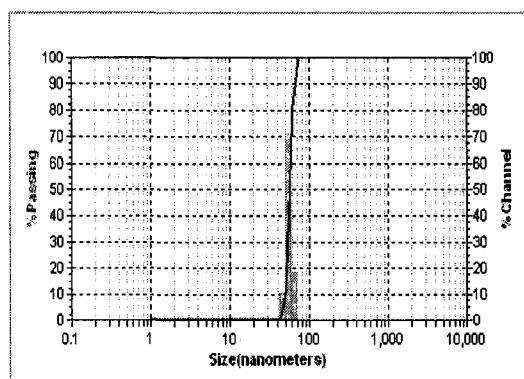
(b)
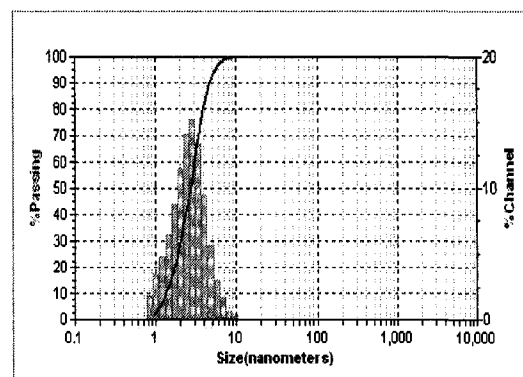
(c)
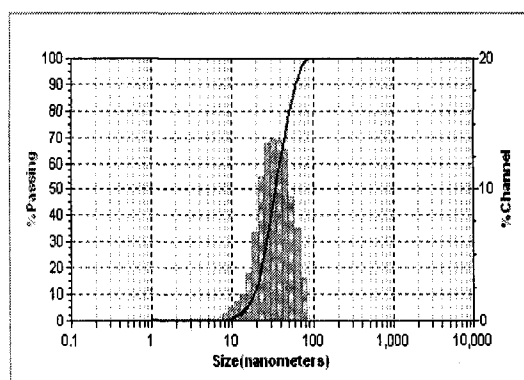
(d)
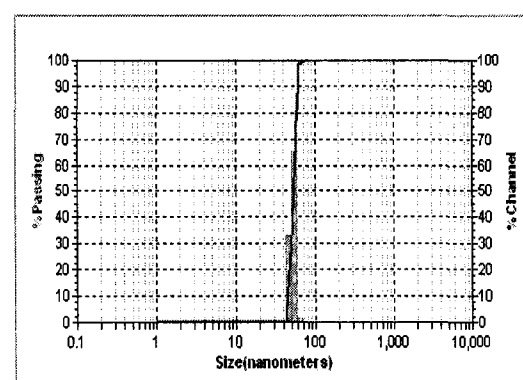
(e)

Figure 17. DLS particle analysis. Number distribution of vPOSS-Bu$_2$ in monomer solution for a) 1 mol%, b) 5 mol%, c) 10 mol%, d) 20 mol%, and e) 50 mol%.

(a)

(b)
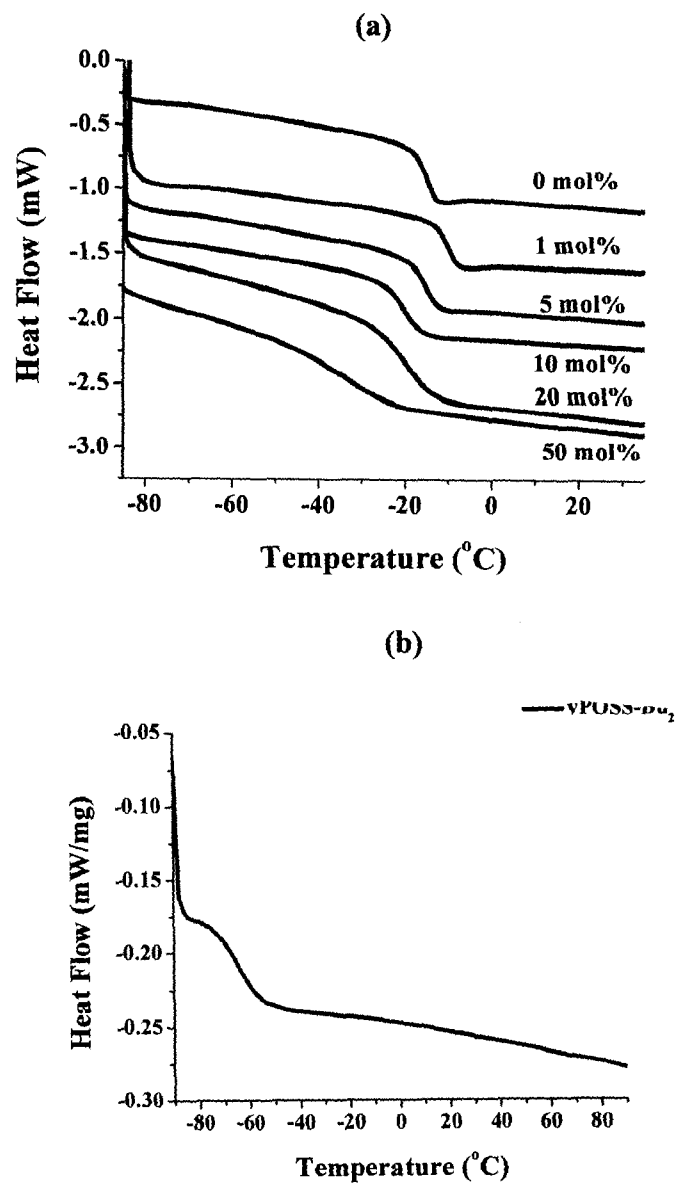
Figure 18. DSC analysis of the a) vPOSS-Bu₂/TriThiol-TAE copolymer at 0, 1, 5, 10, 20, and 50 mol% vPOSS-Bu₂ having a sample thickness of 250 microns and b) pure vPOSS-Bu₂ monomer.
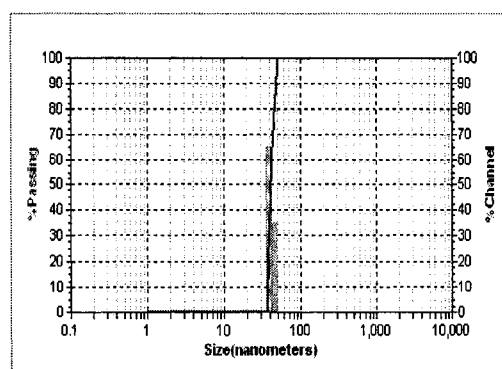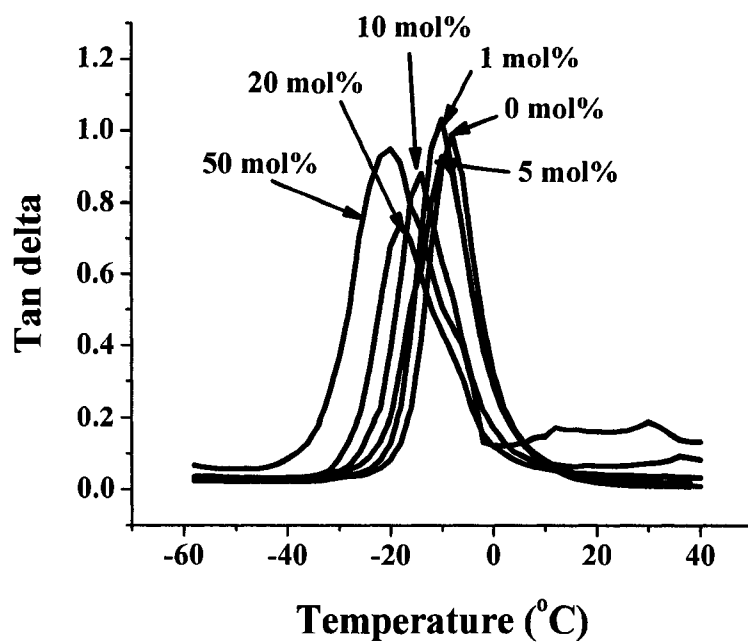
Figure 19. Tan delta plots for vPOSS-Bu₂/TriThiol-TAE systems at 0, 1, 5, 10, 20, and 50 ene mol% having a sample thickness of 250 microns.
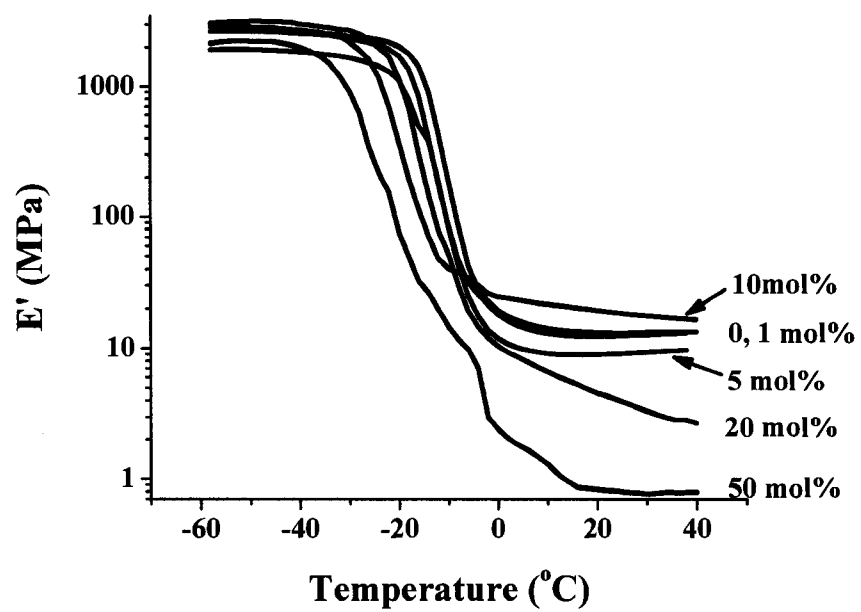
Figure 20. Storage modulus (E' vs. Temperature) for vPOSS-Bu₂/TriThiol-TAE systems at 0, 1, 5, 10, 20, and 50 mol% having a sample thickness of 250 microns.

(a)

(b)
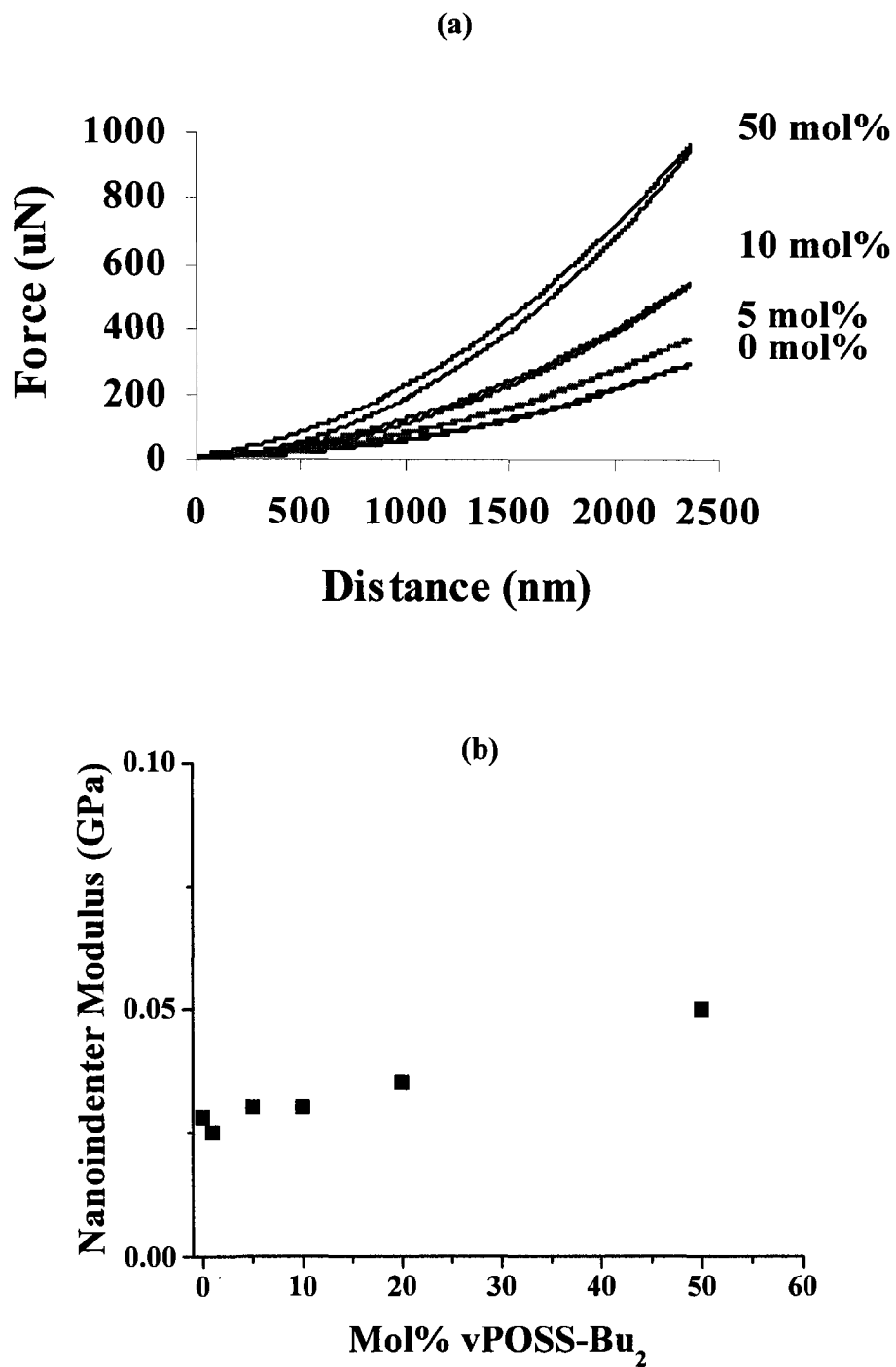
Figure 21. Nanoindentation. a) Master curve plots of Force vs. Distance and b) Linear plot of Nanoindenter modulus vs. Mol% vPOSS-Bu$_2$.
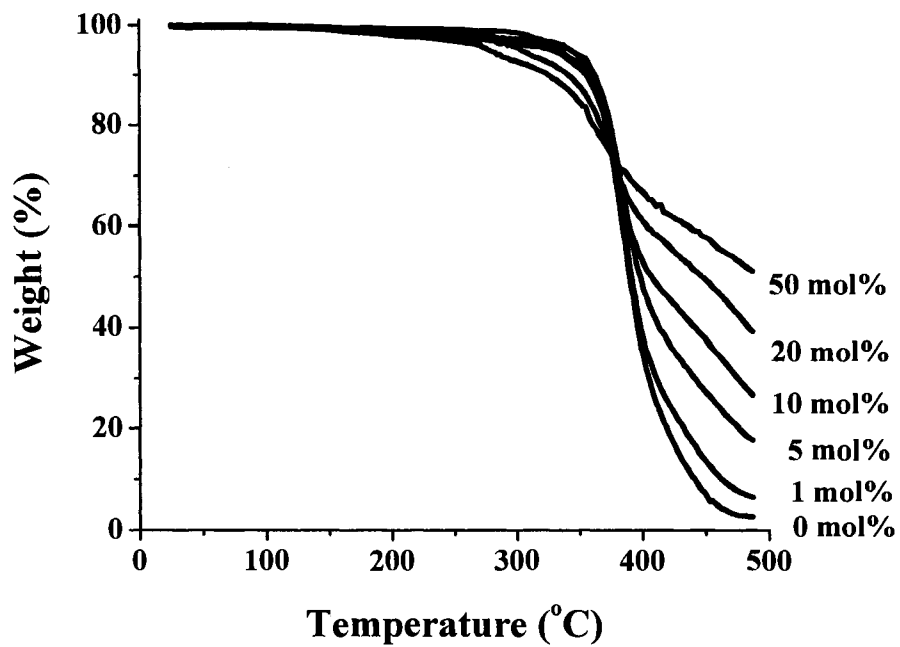
Figure 22. TGA analysis of the vPOSS-Bu$_2$/TriThiol-TAE copolymers at 0, 1, 5, 10, 20, and 50 mol%.
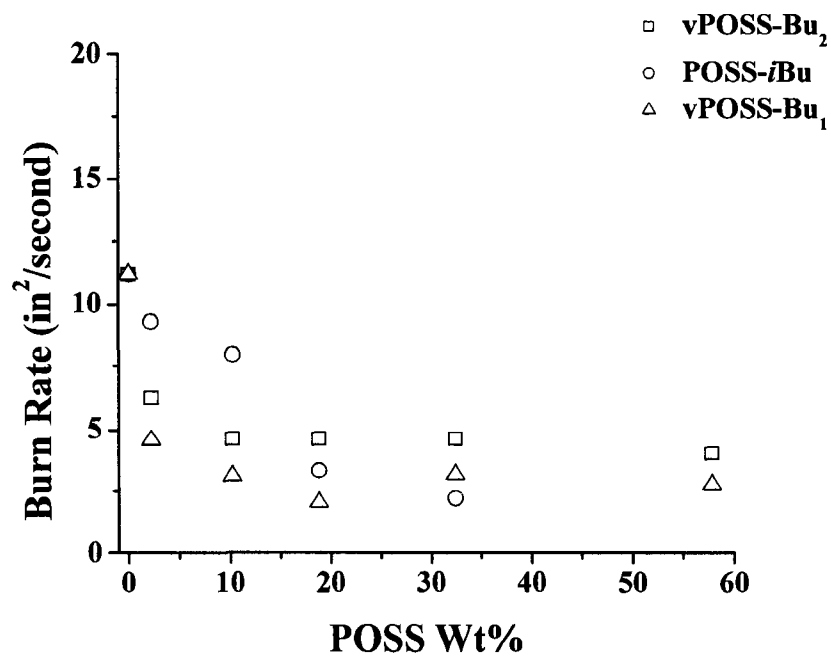
Figure 23. Plot of Burn rates vs. POSS wt% for vPOSS-Bu$_2$, POSS-iBu, and vPOSS-Bu$_1$ at 0, 2.2, 10.2, 18.8, 32.4, and 57.8 wt% having a sample thickness of 250 microns.
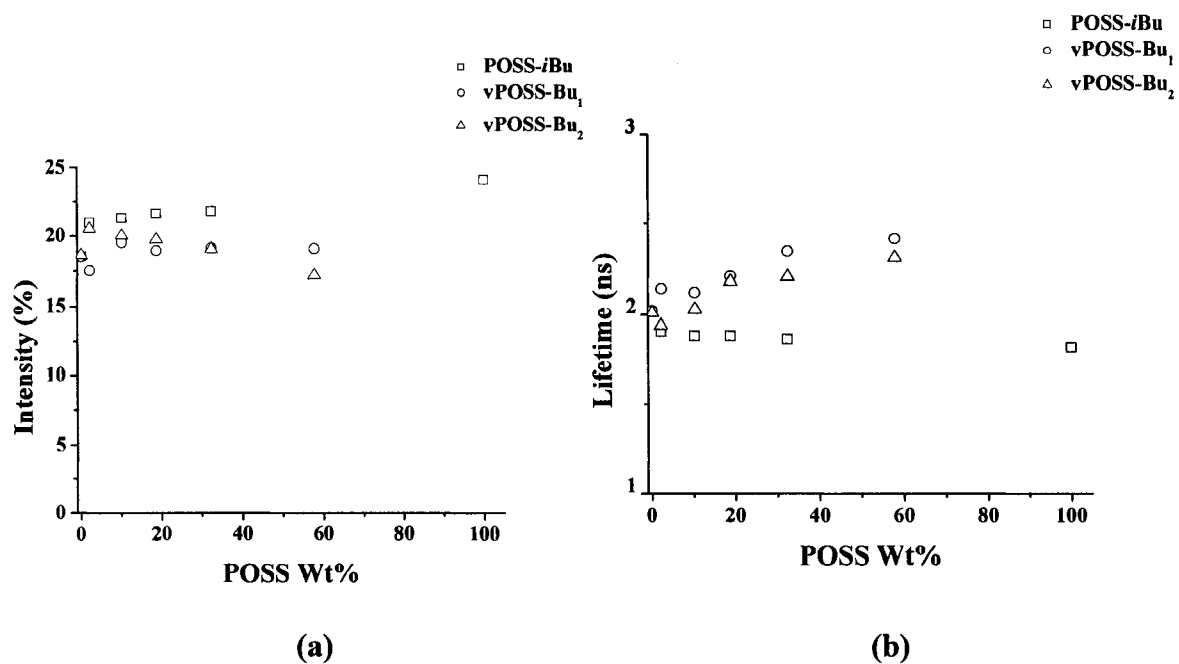
Figure 24. Plot of a) Decay intensity vs. % POSS wt% and b) Lifetime vs. % POSS wt% for vPOSS-Bu$_2$, POSS-iBu, and vPOSS-Bu$_1$ at 0, 2.2, 10.2, 18.8, 32.4, and 57.8 wt% having a sample thickness of 1 millimeter and sample area of 100 mm^2.
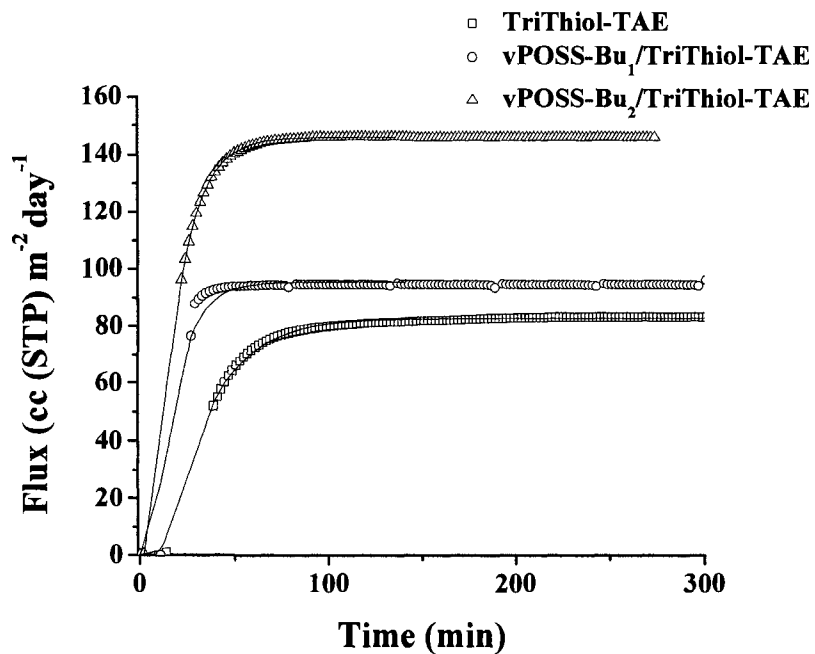
Figure 25. Oxygen flux measurements of neat TriThiol-TAE, vPOSS-Bu$_1$/TriThiol-TAE (32.4 wt%), and vPOSS-Bu$_2$/TriThiol-TAE (20 mol%) systems at 32.4 wt% having a sample thickness of 225 microns.

Vinyl POSS-Bu$_1$

	SH	1	2	3	4	a	b	c	d	C=O	CH$_2$=CH-
^{1}H (δ/multi)	———	0.9/t	1.3/m	1.5/m	4/t	2.7/t	2.6/t	2.6/q	1.0/t	———	———
^{13}C (δ/multi)	———	14/s	34/d	35/d	64/s	40/s	31/s	20/s	19/s	170/s	———

Vinyl POSS Bu$_2$

	SH	1	2	3	4	a	b	c	d	C=O	CH$_2$=CH-
^{1}H (δ/multi)	———	0.9/t	1.3/m	1.5/m	4/t	2.7/t	2.6/t	2.6/q	1.0/t	———	6.0/(d,t)
^{13}C (δ/multi)	———	14/s	34/d	35/d	64/s	40/s	31/s	20/s	19/s	170/s	135/d

Vinyl POSS

	SH	1	2	3	4	a	b	c	d	C=O	CH$_2$=CH-
^{1}H (δ/multi)	———	———	———	———	———	———	———	———	———	———	6.0/(d,t)
^{13}C (δ/multi)	———	———	———	———	———	———	———	———	———	———	135/d

Butyl 3-mercaptopropionate

	SH	1	2	3	4	a	b	c	d	C=O	CH$_2$=CH-
^{1}H (δ/multi)	1.6/t	0.9/t	1.3/m	1.5/m	4/t	2.7/t	2.6/t	2.6/q	1.0/t	———	———
^{13}C (δ/multi)	———	14/s	34/d	35/d	64/s	40/s	31/s	20/s	19/s	170/s	———

Table 1. List of proton and carbon peak assignments and peak splittings of vPOSS-Bu$_1$, vPOSS-Bu$_2$, vinyl POSS, and butyl 3-mercaptopropionate (s = singlet, d = doublet, t = triplet, q= quartet, m = multiplet).

POSS Particle	[POSS]	Shore A (N)	Persoz (seconds)	Pencil (lead grade)
vPOSS-Bu₁	0 wt%	4.75	184	2H
	2.2 wt%	4.98	176	H
	10.2 wt%	5.28	182	F
	18.8 wt%	4.83	200	F
	32.4 wt%	2.05	70	4B
	57.8 wt%	0	26	9B
POSS-iBu	0 wt%	4.30	184	H
	2.2 wt%	5.50	129	B
	10.2 wt%	5.88	103	4B
	18.8 wt%	5.73	101	6B
	32.4 wt%	5.73	88	9B
vPOSS-Bu₂	0 mol%	4.25	184	2H
	1 mol%	3.95	223	2H
	5 mol%	5.08	243	4H
	10 mol%	5.30	255	6H
	20 mol%	4.78	239	4H
	50 mol%	3.95	79	2H

Table 2. Shore A durometer, Persoz pendulum, and pencil hardnesses of the miscible vPOSS-Bu₁/TriThiol-TAE blend, immiscible POSS-iBu/TriThiol-TAE blend, and vPOSS-Bu₂/TriThiol-TAE copolymer.

Ene Mol%	Tg (°C)	FWHM
0	-7.88	10.94
1	-10.71	11.82
5	-9.71	13.56
10	-17.9	15.86
20	-16.3	12.66
50	-20.2	18.22

Table 3. List of glass transition temperatures and FWHM of loss tangent for vPOSS-Bu$_2$/TriThiol-TAE copolymers.

	Permeability (P) (cc (STP) cm m^{-2} day^{-1} atm^{-1})
TriThiol-TAE	1.759
vPOSS-Bu$_1$/TriThiol-TAE	1.464
vPOSS-Bu$_2$/TriThiol-TAE	2.788

Table 4. Permeation constants of oxygen gas for TriThiol-TAE, vPOSS-Bu$_1$/TriThiol-TAE, and vPOSS-Bu$_2$/TriThiol-TAE.
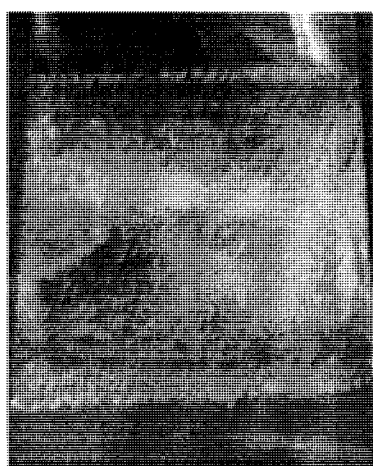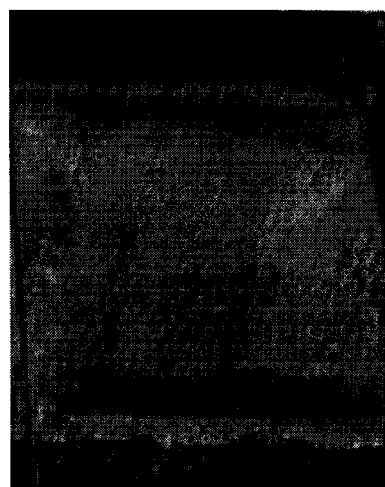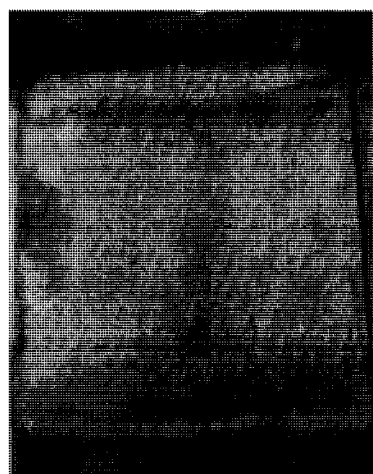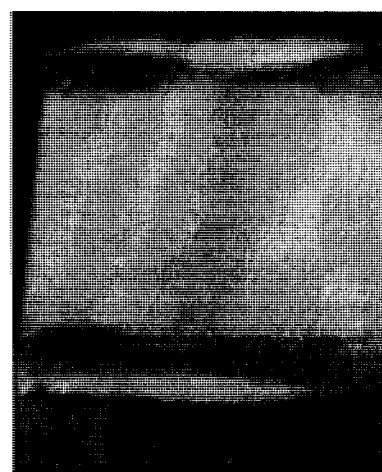
Picture 1. Pictorial illustrations of POSS-iBu/TriThiol-TAE blends of a) 2.2 wt%, b) 10.2 wt%, c) 18.8 wt%, and d) 32.4 wt% POSS-iBu.
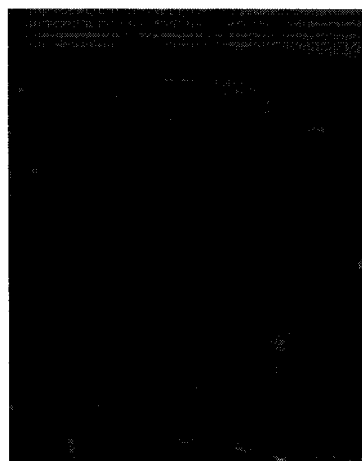
(a)

(b)
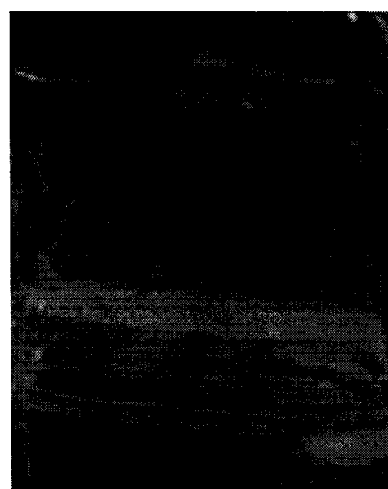
(c)
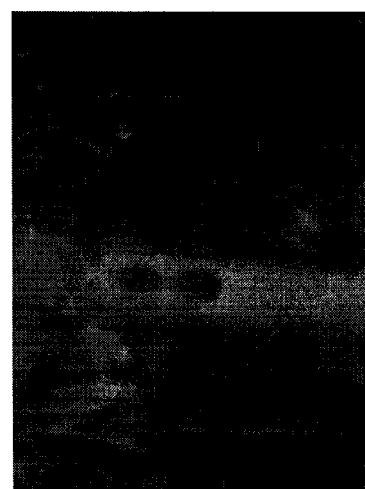
(d)

Picture 2. Pictorial illustrations of vPOSS-Bu₁/TriThiol-TAE blends of a) 2.2 wt%, b) 10.2 wt%, c) 18.8 wt%, and d) 32.4 wt% vPOSS-Bu₁.

(a) (b) (c)

(d) (e)
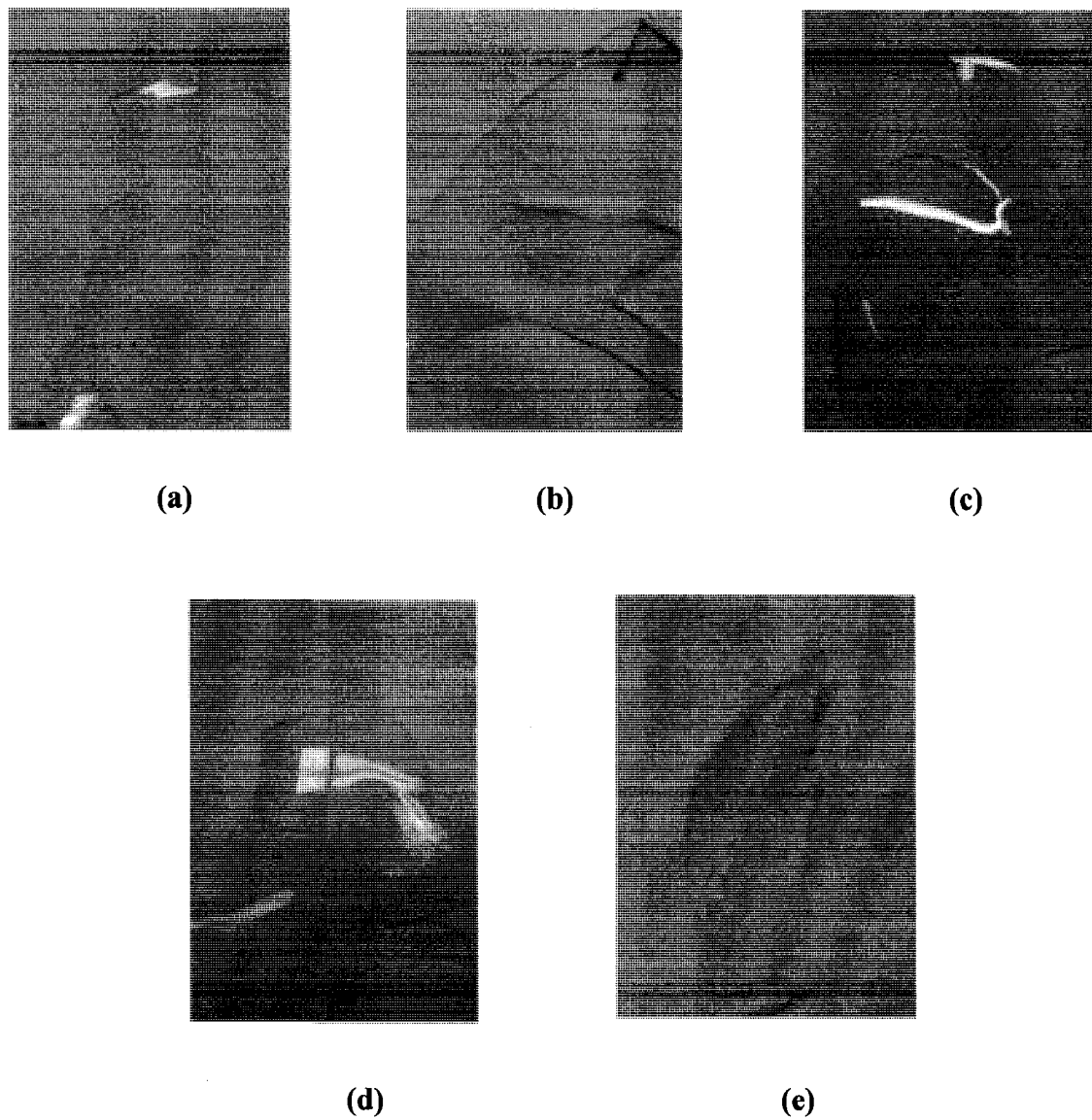
Picture 3. Pictorial illustrations of vPOSS-Bu$_2$/TriThiol-TAE blends of a) 1 mol%, b) 5 mol%, c) 10 mol%, d) 20 mol%, and e) 50 mol% vPOSS-Bu$_2$.

CHAPTER VI

THE INFLUENCE OF HYDROCARBON AN POLAR CONTENT ON THE

NETWORK STRUCTURE OF POSS-BASED THIOL-ENE NANOCOMPOSITES

ABSTRACT

The efficiency of vPOSS compatibilization within a trithiol-triallyl ether network was

investigated by varying the hydrocarbon content and polarity of its nonreactive

substituents. Vinyl POSS was modified with four ester groups, methyl thioglycolate

(vPOSS-MT), isooctyl 3-mercaptopropionate (vPOSS-IOMP), 3-mercaptopropionic acid

(vPOSS-MPA), and mercaptoacetic acid (vPOSS-MAA) and chemically incorporated

into a TriThiol-TAE polymer backbone at 1, 5, 10, 20, and 50 mol% via

copolymerization of vinyl and thiol induced by UV irradiation. The thermal, mechanical,

physical behaviors and morphology were investigated to understand the effects of POSS

compatibility upon inclusion of vPOSS into the TriThiol-TAE network. The efficiency of

vPOSS compatibility is shown to be strongly influenced by the hydrocarbon content of

the ester groups. DLS analysis of vPOSS-MT and vPOSS-IOMP show that vPOSS-MT,

having low hydrocarbon content, is miscible in the trithiol-triallyl ether mixture, whereas,

vPOSS-IOMP, having high hydrocarbon content, is immiscible in the trithiol-triallyl

ether mixture for all concentrations of vPOSS. Rubber modulus (E') and scratch

resistance do not change significantly with respect to vPOSS-MT ene molar

concentration up to 50 mol%; however, rubber modulus (E') and scratch resistance

decrease with vPOSS-IOMP ene molar concentration. An investigation of hydrogen

bonding on the dispersion of highly compatible vPOSS nanoparticles during polymerization is conducted by observing the changes in the thermal and mechanical properties with respect to vPOSS-MPA and vPOSS-MAA concentrations within the TriThiol-TAE network. The inclusion of vPOSS-MAA is shown to be well dispersed at all concentrations of vPOSS-MAA by DSC and DMA analyses, i.e. no broadening of the glass transition (DSC) and tan δ (DMA) is observed. Higher Tg's were observed and increased rubber modulus as a result of hydrogen bonding of the acid groups. PALS analysis and oxygen flux measurements show that POSS, whether molecularly dispersed (vPOSS-MT and vPOSS-MAA) or present in POSS-rich domains (vPOSS-IOMP), has little effect on free volume of the TriThiol-TAE network.

INTRODUCTION

Growing interest in applications of polymeric nanocomposite materials have expanded into a large field of study in the material sciences that primarily focuses on electronic and coatings applications. [1-19] Although the behavior of the polymeric composite matrix can be tailored by the addition of different types of nanoparticles, challenges in nanocomposite formulations exist since the impact of nanocomposite design on the morphology, dynamics, and properties of the surrounding polymer are hardly predictable. [1, 12] Polymeric behavior is limited upon the interaction of the bulk polymer and the nanoparticle in which the favorability of interfacial polymer/nanoparticle interaction and the degree of interfacial volume needed play a vital role. [1, 13, 14] Also, the distribution of the nanoparticle and its geometry affect polymeric properties via the heterogeneity of particle distribution and geometry. [1, 15] Effective compatibilization of POSS, in conjunction with POSS concentration, is necessary to limit decreases in mechanical and physical behavior when POSS is incorporated chemically into the TriTthiol-TAE (see Figure 1 for structures) network. [16-19]

Compatibilization of the vPOSS particle is important since the added organic structure can increase, or even decrease, the solubility of the inorganic core in the trithiol and triallyl ether comonomers prior to polymerization. If compatibilization of the basic POSS core in the initial mixture is accomplished, then it enhances the potential for incorporating the silicate particles throughout the subsequent polymerized TriThiol-TAE matrix with the possibility of significant enhancement of polymer behavior. Otherwise, if

compatibilization of the POSS core is poor, POSS-rich microdomains form, leading to a reduction in physical and mechanical properties of the photocured TriThiol-TAE networks. From the previous chapter (Chapter 5), it was shown how ineffective POSS compatibilization results in a decrease in some of the mechanical and physical properties of the thiol-ene network. At low and high concentrations of a chemically reactive POSS (vPOSS-Bu$_2$ with structure shown in Chapter 5) largePOSS-rich domains formed due to the loss of effective compatibilization into the cured network, which contribute to a decrease of surface hardness, scratch resistance, and the rubbery modulus of the TriThiol-TAE matrix. Observably, the solubility of vPOSS-Bu$_2$ decreased as the solvent concentration of TriThiol increased. From this study, it is apparent that the challenges faced in decreasing polymer network physical and mechanical properties when POSS derivatives are added can be addressed by increasing the compatibility of the POSS particles in the thiol-ene matrix, and, thus, reducing the formation of POSS-rich domains found. It can also be concluded from results in Chapter 5 that simple blending of an incompatible POSS particles into the thiol-ene matrix led to cured networks that were brittle and readily fractured as demonstrated with the addition of vPOSS-Bu$_1$ and POSS-iBu (see Chapter 5 for structures) which have no reactive ene groups for incorporation into the TriThiol-TAE network. Thus, the combination of a reactive group that locks the POSS core chemically into the network and the resulting POSS compatibility are both critical to achieve increases in network physical and mechanical properties.

In an effort to understand the influence of POSS compatibility on film morphology and properties, several modified POSS particles with varying hydrocarbon and polar content were chemically incorporated into the TriThiol-TAE network to

observe the changes in the morphological, thermal, mechanical, and physical behavior of the trithiol-triallyl ether network. The vinyl groups on vinyl POSS (see Chapter 5 for structure) were modified with four ester groups. The monofunctional thiols added to the silicate particle were methyl thioglycolate (MT), isooctyl 3-mercaptopropionate (IOMP), 3-mercaptopropionic acid (MPA), and mercaptoacetic acid (MAA) to give the corresponding vinyl POSS modified structures as shown in Figure 1a. Herein, this chapter will focus on the effects of hydrocarbon and polar content of the organic substituents on the compatibility of the POSS particle in the TriThiol-TAE network.

EXPERIMENTAL

Materials

Reagents used in the thiol-allyl ether photopolymerizations included allyl pentaerythritol (triallyl ether (TAE)), trimethylopropane tris(3-mercaptopropionate) (TriThiol), vinylPOSS, and 2-hydroxy-2-methyl-1-phenyl-1-propanone (Darocur 1173). Methyl thioglycolate, isooctyl 3-mercaptopropionate, 3-mercaptopropionic acid, mercaptoacetic acid, vinyl POSS, and diethyl amine were components used in the addition of thiol end groups across the vinyl groups on the vinylPOSS nanoparticle. Vinyl POSS was donated by Hybrid Plastics. All chemicals were used as received. The chemical structures of all components are shown in Figure 1.

Synthetic method for vinyl POSS modification

The POSS monomers (**vPOSS-MT, vPOSS-IOMP, vPOSS-3MPA, and vPOSS-MA**), with both vinyl and ester groups, were synthesized by addition of aliphatic thiols to the vinyl group of the vinyl POSS structure.[6] A 20-g vinyPOSS cage mixture (Hybrid Plastics) was charged into a 250-mL flask with 60-mg diethyl amine and 25 mL THF. The solution was slowly added to 16 g, 33 g, 16 g, and 14 g of methyl thioglycolate, isooctyl 3-mercaptopropionate, 3-mercaptopropionate, or mercaptoacetic acid, respectively, in 3-4 mL aliquots every 10 minutes while stirring. The solution was stirred for at least 6 hours before the solvent THF was removed by rotovaporization. After complete evaporation of THF, oil remained that contained the product. The final products (See Figure 1a for chemical structures) were analyzed by proton and carbon NMR (Figure 2) to confirm the consumption of the vinyl bond and the formation of the thioether bond. The conversion of vinyl groups to methylene groups were confirmed by the appearance of proton and carbon peaks **b** and **c** (Figures 2a and 2d) for vPOSS-MT and vPOSS-MAA, and peaks **c** and **d** (Figures 2b and 2c) for vPOSS-IOMP and vPOSS-MPA. Table 1 lists all peak assignments and peak splittings for vPOSS-MT, vPOSS-IOMP, vPOSS-MPA, vPOSS-MAA, and starting materials. The functionality of each modified vPOSS (4 vinyl:6 POSS) was determined by the ratio of the integrated peaks of the **vinyl** group (6.0) and a methyl or methylene group found on the ester (MT, IOMP, MPA, or MAA) shown in Figure 1a. Upon integration of the peaks for vPOSS-IOMP, the methylene peak (1) was assigned an integration value of 200 (100 per proton) and used as a reference peak for assigning integration peaks for all other protonated groups. The ratio (r) of vinyl to ester (butyl 3-mercaptopropionate), being determined as 0.51, was used to calculate the number of vinyl groups remaining after the reaction of thiol and vinyl POSS

using Equation 1. The average functionality of the vPOSS cage was 10. Likewise, the assigned reference peaks for integration were **c**, **d**, and **c** for vPOSS-MT, vPOSS-MPA, and vPOSS-MAA, respectively, with ratio values of 0.92, 0.42, and 0.72 for vinyl peak (6.0) to methyl peak (~1.0) in order to calculate the functionality of each modified POSS.

$$r = \frac{2* \text{ Peak integration value } (\mathbf{vinyl})}{3 * \text{Peak integration value } (\mathbf{4})}, \quad \text{and} \quad \text{No. of vinyl groups} = \frac{10\,r}{(1+r)} \quad (1)$$

Polymerization of functionalized POSS/TriThiol-TAE systems

POSS/Thiol-ene copolymers containing 0 mol%, 1 mol%, 5 mol%, 10 mol%, 20 mol%, and 50 mol% of each of the POSS derivatives in Figure 1 were photocured on a Fusion Epiq 6000 UV cure line. Reaction mixtures contained equal moles of thiol and ene functional groups in addition to 2 wt% photoinitiator, Darocur 1173. For the series of films, reaction mixtures were maintained at 50:50 thiol:ene molar ratios as the concentration of each ene was varied. Reaction mixtures were stirred manually and then sonicated for a total time of 5 min prior to photocuring. A 400-W D-bulb lamp was used as the light source. Each film was cured at a light intensity of 2.96 W/cm^2 and a line speed of 12.19 m/min. Each film had a film thickness of ~250 microns obtained by using a 20 mil drawdown bar and cast onto a glass substrate. The prepared samples were used for thermal analysis (DSC (differential scanning calorimetry)), mechanical analysis (DMA (dynamic mechanical analysis)), and physical analysis (water contact angle measurements, and pencil scratch and Persoz pendulum hardness tests). Thick film samples (~1 mm) were formulated for shore A hardness measurements and PALS

(positron annihilation lifetime spectroscopy) analysis. The stirred reaction mixtures (50:50 thiol:ene molar ratios) were placed into glass scintillation vials and photocured in a Rayonet photochemical reactor for a total cure time of 3 hours. Samples were cut into 10 mm x 10 mm sections after removing from scintillation vials.

Kinetic analysis

Real-time Fourier Transform IR (real-time FTIR) was performed on an IFS-88 Bruker spectrometer. From analysis of the appropriate peaks, it was possible to obtain actual conversions of thiol and ene groups versus time. Sample preparation included stirring and sonication (5 min) of equal molar reaction mixtures of thiol and ene (triallyl ether and vPOSS-Bu2). Samples were placed between NaCl plates and irradiated by the UV light filtered with a 1.0 neutral density filter when monitoring vPOSS-Bu$_2$/Thiol-Ene copolymerization and a 0.8 neutral density filter when monitoring vPOSS-Bu$_1$/Thiol-Ene and POSS-*i*Bu/Thiol-Ene polymerizations. The light intensity of the full arc was 125.5 mW/cm^2, whereas, the light intensity used for sample exposure was 19.88 mW/cm^2. The peak assignments for the thiol, allyl ether, and vinyl groups on the POSS cage (vPOSS-Bu$_2$) were 2570 cm^{-1}, 1640 cm^{-1}, and 1600 cm^{-1}, respectively. Sample thickness was ~20 microns.

Thermal, mechanical, and physical analysis

Dynamic light scattering (DLS) experiments were performed on trithiol/triallyl ether/functional POSS solutions at ambient temperatures using a Nanotrac NPA252 Combination analyzer equipped with a 3 mW external laser diode probe operating at 780

nm. The mean volume and number distribution of particle sizes were determined by modified Mie calculations of the power spectrum obtained from light scattering of non-spherical POSS particles.

Analysis of thermal properties were measured by a DSC Q1000 analyzer (TA Instruments) from -90 ° to 40 °C at heating rate of 10 °C/min to obtain heat flow (mW) of the polymer as a function of temperature. Also, the thermal properties of the pure POSS monomers were measured from -90 °C to 90 °C at a heating rate of 10 °C/min to obtain heat flow of the monomer as a function of temperature. Glass transition temperatures (T_g) were obtained at the inflection point of the DSC curve found in the glass transition region. Annealed samples used for physical aging measurements were measured from (T_g − 50 °C) to (T_g + 20 °C) at 5 °C/min after cooling from room temperature 0.2 °C/min. Thin film samples had a thickness of ~250 microns.

Mechanical properties were measured by a DMA 2920 thermal analyzer (TA instruments) to obtain storage modulus (E') and loss tangent (tan δ = storage modulus/loss modulus (E")) curves as a function of temperature. Mechanical analysis was performed in the tensile mode over a temperature range of -60 °C to 40 °C at a frequency of 1 Hz. The heating rate and force amplitude applied to the samples were maintained at 2 °C/min and 15 μN, respectively. All storage modulus data are plotted in logarithmic scale as a function of temperature. Each sample had a film thickness of 250 nm and a width of 5 mm and a length of 25 mm.

The changes in surface hydrophobicity as a function of POSS derivative content were observed by performing water contact angle measurements with a Ramé-Hart Model 200 contact angle goniometer. Three series of contact angle measurements were

collected using a 10-1 droplet of deionized, distilled water for each film sample. Viscosity measurements were obtained using a Brookfield Digital Viscometer Model. Measurements were obtained at various rotational velocities (1333 and 2666 RPM) after allowing the spindle to rotate for 1 min to determine the viscosities of silicate-based monomers at 30 °C. The thickness of each film sample was ~250 microns prepared by a 20 mil drawdown bar onto a glass substrate.

Oxygen flux, J(t), at 1 atm pressure, and 23 °C was measured using a Mocon OXTRAN 2/21 unit (ASTM-D 3985-81). This apparatus employs a continuous-flow method to measure J(t) through polymeric films or thin sheets. Permeability, P, and diffusion coefficient, D, are obtained by performing a two-parameter least squares fit of the experimental flux data to the Equation (3) based upon Fick's second law (Equation 4), where P = permeability, p = permeant gas pressure, l = film thickness, D = diffusivity, c = permeant gas concentration, and t = time. Diffusivity, D, is derived from the non-steady state region (slope), and permeability, P, is derived from the steady state region of the experimental flux curve. The solubility, S, is obtained from the relationship [P = D * S]. Before every testing, film specimens were masked, glued using an epoxy based composition on aluminum foil with a circular exposure area of 5 x 10^{-4} cm^2, then carefully conditioned in pure nitrogen inside the unit to remove traces of atmospheric oxygen, in order to obtain the non-steady state oxygen flux required for diffusion coefficient measurements. Films were prepared by using a 9 mil drawdown bar onto a glass substrate and photocured on Fusion Epiq 3000 cure line. Reaction mixtures (50:50 thiol:ene molar ratios) were stirred manually followed by sonication (5 min). Average

film thickness (~225 microns) was determined using a micrometer with the accuracy of individual thickness measurements approximately ±0.001 mm.

$$J(t) = \frac{Pp}{l}[1 + 2\sum_{n=1}^{\infty}(-1)^n \exp(-D\pi^2 n^2 t / l^2)] \qquad (3)$$

(Fick's second law) $\qquad \frac{\partial c}{\partial t} = D\frac{\partial^2 c}{\partial x^2} \qquad (4)$

Persoz pendulum hardness was measured with a BYK Gardner Pendulum Hardness Tester according to ASTM D 4366. Scratch resistance of each Trithiol-TAE film was determined by using a pencil hardness test with a series of pencils of varying hardness. The range of pencil lead hardness is graded from softest (9B-B) to mid-grade (F and HB) to hardest (H-9H). [7] Each film sample had a film thickness of ~250 microns by using a 20 mil drawdown bar onto a glass substrate. Shore A hardness was measured with a Type A durometer (Model 306L, PTC, Inc.) according to ASTM D 2240 00. Thick samples, having a film thickness of ~1 mm and an area of 3.5 mm², were cured by a Rayonet photochemical reactor (300 nm) for a total cure time of 3 hours.

Spectroscopic analysis

[1]H and ^{13}C nuclear magnetic resonance (NMR) spectroscopy was performed using a Bruker 300 MHz NMR. The solvent for NMR characterization was deuterated DMSO. A complete description of the peak assignments for vPOSS-MT, vPOSS-IOMP, vPOSS-

MPA and vPOSS-MAA have been described in the synthetic method of the experimental section.

Positron annihilation liftetime spectroscopy (PALS) measurements were conducted using a custom built instrument employing ^{22}Na as the positron source. The spectrometer, equipped with a special vacuum chamber and temperature control system, is comprised of BaF_2 scintillation crystals and photomultiplier tubes, a fast-fast coincidence system based on EC&G Ortec NIM modules (model 583 constant-fraction discriminators), and a model 566 time-to-amplitude converter. Positron lifetime spectra were collected using a PCA multichannel analyzer. Special software, PATFIT-88, was used to process the data in order to extract mean oPs lifetimes and decay intensities. Thick samples (1 mm x 10mm x 10mm) were photocured using a Rayonet photochemical reactor equipped with 300 nm lamps for a total cure time of 3 hours.

RESULTS AND DISCUSSION

In the results from Chapter 5, recall that the miscibility of vPOSS-Bu$_2$ in the trithiol/triallyl ether solution was shown to significantly decrease as the molar concentrations of the POSS silicate particles increased as confirmed by DLS measurements. The mean number distributions of vPOSS-Bu$_2$ particle size generally increased subsequent with an increase of the vPOSS-Bu$_2$ component of the ene molar ratio (vPOSS-Bu$_2$:TAE) from 0.5:49.5 (1 mol%) to 25:25 (50 mol%) in the solution. The final samples with high vPOSS-Bu$_2$ were a little hazy indicating agglomerated particles

were in the final films. Therefore, it was concluded that vPOSS-Bu$_2$ was at least partially immiscible in the trithiol comonomer at all molar concentrations of vPOSS-Bu$_2$, and the ester, butyl 3-mercaptopropionate (Bu), at least with only four functional groups attached to each POSS molecule was inefficient as a compatibilizing group for the thiol-ene network. It is suggested that the miscibility of vPOSS-Bu$_2$ is aided by the presence of the carboxylate group on its ester substituents, but the effect of this group on solubility may be counteracted by the significant hydrocarbon content of the adjacent butyl group. The presence of the butyl group possibly influences the affinity of POSS nanoparticles toward aggregation, and, therefore, may play a substantial role in the formation of POSS-rich domains, leading to decrease in physical/mechanical properties with increasing vPOSS-Bu$_2$ concentration. In order to understand the effect of hydrocarbon content on POSS compatibility with the thiol-ene matrix, and, subsequently, the film properties of the silicate-based thiol-ene nanocomposite, vinyl POSS (vPOSS) was modified with methyl thioglycolate (vPOSS-MT) and isooctyl 3-mercaptopropionate (vPOSS-IOMP) having short and long aliphatic chains, respectively, on the ester. For this study, six vinyl groups on the 10-functional vinyl POSS (vPOSS) were reacted with the requisite thiol. The vinyl functionality of the modified nanoparticles, vPOSS-MT and vPOSS-IOMP, was reduced compared to vPOSS-Bu$_2$ to ensure that the organic content of the hybridized particle was sufficient to clearly observe the effect of the hydrocarbon chain on compatibilization and film morphology properties.

The modified vPOSS particles were chemically incorporated into a thiol-ene network via copolymerization of the vinyl groups (vPOSS-MT and vPOSS-IOMP) with thiol (TriThiol) and triallyl ether (TAE) at varying ene molar concentrations of 0, 1, 5,

10, 20, and 50 mol% of the POSS monomer while keeping a 1:1 molar ratio of total thiol functionality to total ene functionality (TAE + POSS monomer). The chemical structures of each substituent attached to the POSS cage at a corner silicon atome are shown in Figure 2 along with their proton and carbon NMR spectra. Observable differences in solubility of vPOSS-MT and vPOSS-IOMP based upon DLS measurements of the copolymer solutions show the influence of hydrocarbon content on the compatibility of the vPOSS particle with the thiol and allyl ether mixture (Table 2) prior to polymerization. Since the average size of a POSS cage is ~1-3 nm, a solution with well-dispersed particle content should contain particles having a size distribution of the same magnitude as molecular POSS. Accordingly, for all concentrations of vPOSS-MT, the recorded values of average number distribution of particle size were 1-3 nm. These numbers are essentially identical to that of the TriThiol-TAE with no POSS added. Therefore, the measurements show that vPOSS-MT is well-dispersed (solubilized) prior to polymerization. For DLS measurements of mixtures containing vPOSS-IOMP, POSS aggregates of 5-50 nm sizes were detected for all concentrations indicating that vPOSS-IOMP is a poor compatibilizing group for the thiol-ene mixture.

Upon inclusion of vPOSS-Bu$_2$ (see Chapter 5) into the thiol-ene network, the availability of reactive ene and thiol groups were significantly affected by the high molecular weight of vPOSS-Bu$_2$ per double bond. Photo-DSC exotherms and RTIR based kinetics confirmed that the reduction of rate and conversion corresponded to the reduction in concentration of available polymerizable groups available in the thiol-ene solution due to aggregation. In situ observation (RTIR) of functional group conversions and polymerization rates (Figure 3e) of 50 mol% vPOSS-IOMP containing system

showed that each functional group conversion was affected by aggregation of POSS nanoparticles when compared to the rate and molar conversions for neat TriThiol-TAE in equal molar reactions (50:50 relative moles assuming 100 total moles present) of thiol and total ene (TAE + POSS) groups. (Note that the thiol conversion is absent in Figure 3a as a result of fluctuations of the base line during kinetic analysis. The total thiol conversion is the same as the total ene (allyl ether) conversion.) A small reduction of polymerization rate and conversion is observed for 5 mol% vPOSS-IOMP (Figure 3d), while significant decrease of polymerization rate and conversion was observed for 50 mol% vPOSS-IOMP/TriThiol-TAE networks (Figure 3e), i.e. complete conversion of functional groups occurring within 10 seconds for neat TriThiol/TAE (Figure 3a) was unobservable for 50 mol% vPOSS-IOMP (17 relative moles reacted), which may result from the formation of aggregates at each concentration of POSS particle described. Notably, the reduction of rates and conversions was substantial for vPOSS-IOMP containing systems indicating that phase separation of POSS particles strongly impacted conversions and rates; accordingly, DLS analysis confirmed the presence of vPOSS-IOMP aggregates for all concentrations prior to polymerization. No significant changes in rate and conversions were observed for samples with 5 mol% and 50 mol% vPOSS-MT (Figure 3 b and c), where aggregation was unobserved by DLS analysis.

The POSS-rich domains found in the final cured network of vPOSS-Bu$_2$ containing systems resulted in a drop in modulus and other physical parameters with increased concentration (See Chapter 5). Observable changes (increase) in T$_g$ and rubbery modulus caused by POSS dispersion for styrene, epoxy, and methacrylate copolymers were reported [20-24] Likewise, changes (increase) in T$_g$ and modulus were observed for

vinyl ester systems containing dispersed POSS particles.[25] The changes in thermal

(increase T_g) and mechanical behavior (increase modulus) of POSS-based copolymers

cited in recent literature examined changes in polymer behaviour with respect to the

addition of POSS pendant groups. [26-30]

DSC analysis of the vPOSS-MT/TriThiol-TAE photopolymerized networks

showed only marginal changes in T_g from -13.6 °C for neat TriThiol-TAE to -22.4 °C for

50 mol% vPOSS-MT/TriThiol-TAE, with no significant change in the glass transition

broadening at all concentrations of vPOSS-MT (Figure 4a). The temperatures measured

at the onset, midpoint, and end of the glass transition region for neat TriThiol-TAE

polymer were -15.4 °C, -13.6 °C, and -12.2 °C, respectively, which compares to the T_g

range of -20.1 °C, -18.8 °C, and -16.4 °C for 5 mol% vPOSS-MT/TriThiol-TAE; -19.1

°C, -17.2 °C, and -15.3 °C for 10 mol% vPOSS-MT/TriThiol-TAE, and -28.8 °C, -22.4

°C, and -17.4 °C for 50 mol% vPOSS-MT/TriThiol-TAE . By comparison to the vPOSS-

Bu$_2$/TriThiol-TAE copolymers (Chapter 5) in which lowering of T_g and broadening in the

glass transition were observed, it is suggested that vPOSS-MT is well-dispersed

throughout the TriThiol-TAE network at all concentrations. DSC analysis of pure

vPOSS-MT (Figure 5) shows an observable T_g = - 31°C, and any influence of vPOSS-

MT enriched domains should cause a similar decrease in T_g for the vPOSS-MT/TriThiol-

TAE networks with increasing vPOSS-MT concentration. Similarly, DMA results

(Figure 6) showed negligible differences of T_g over the range of samples formed from

resins with vPOSS-MT, shifting from -10.7 °C for neat TriThiol-TAE to -8.20 °C for 50

mol% vPOSS-MT/TriThiol-TAE in conjunction with the lack of broadening in the glass

transition region as indicated by the changes in loss tangent (tan δ) shown in Table 3 and

the broadening of the DSC transitions. For example, the magnitude of broadening at full width at half maximum (FWHM) obtained from tan δ plots increased from 11.7 °C for neat TriThiol-TAE, to 13.5 °C for 5 mol% vPOSS-MT/TriThiol-TAE, 15.9 °C for 10 mol% vPOSS-MT/TriThiol-TAE, and finally to 19.4 °C for 50 mol% vPOSS-MT/TriThiol-TAE indicating that vPOSS-MT was well-dispersed throughout the TriThiol-TAE composite matrix. Consequently, the rubbery modulus at 30 °C shows no significant change upon the inclusion of vPOSS-MT at all concentrations (Figure 7). A plot of the rubbery modulus (E') versus POSS ene mol% in Figure 8 illustrated how vPOSS-MT dispersion correlates with modulus changes with respect to vPOSS-MT concentration when good dipersion of molecular vPOSS-MT particles is achieved at concentrations of vPOSS-MT up to 50 mol%. The values of E' are 9.59 MPa, 13.7 MPa, 15.5 MPa, and 8.56 MPa for neat TriThiol-TAE, 5 mol% vPOSS-MT/Trithiol-TAE, 20 mol% vPOSS-MT/TriThiol-TAE, and 50 mol% vPOSS-MT/TriThiol-TAE, respectively. In Picture 1 (a-e), the final cured films are clear and transparent, even at high concentrations (20 and 50 mol%), as a result of good dispersion of vPOSS-MT within the network. Also, the surface hardness and scratch resistances show no significant enhancement at high concentrations of vPOSS-MT (Figures 9 and 10). Specifically, surface hardness, as measured by Persoz pendulum analysis increased from 195 seconds to 231 seconds to 188 seconds for neat TriThiol-TAE, 20 mol% vPOSS-MT/TriThiol-TAE, and 50 mol% vPOSS-MT/TriThiol-TAE, respectively. Likewise, scratch resistance, as measured by pencil hardness changed from H to 5H to 3H for neat TriThiol-TAE, 20 mol% vPOSS-MT/TriThiol-TAE, and 50 mol% vPOSS-MT/TriThiol-TAE, respectively. Finally, Shore A hardness values of 4.4N, 5.0 N, and 5.1 N were obtained for film

samples prepared neat TriThiol-TAE, 20 mol% vPOSS-MT/TriThiol-TAE, and 50 mol% vPOSS-MT/TriThiol-TAE, respectively (Figure 11).

As opposed to the results for the vPOSS-MT based films, a decrease in T_g and the broadening of the glass transition region and tan δ plots illustrates how the addition of vPOSS-IOMP, which is characterized by a long hydrocarbon chain attached to the POSS core, has a very different effect on the thermal and mechanical behavior of the base TriThiol-TAE network. From DSC plots, T_g values were observed to decrease continuously from -15.3 °C to -37.9 °C with increasing vPOSS-IOMP concentration, and similarly, the loss tangent curves showed a significant decrease of T_g from -10.9 °C to -22.1 °C for neat TriThiol-TAE and 50 mol% vPOSS-IOMP/TriThiol-TAE, respectively (Figures 12 and 13). The temperatures (Figure 12a) of the onset, midpoint and end of the DSC based glass transition region was -18.3 °C, -15.3 °C, and -14.2 °C; -21.0 °C, -18.39 °C and -16.5 °C; -25.4 °C, -21.1 °C, and -20.8 °C; and -40.0 °C, -37.9 °C, and -28.5 °C for neat TriThiol-TAE, 5 mol% vPOSS-IOMP/TriThiol-TAE, 10 mol% vPOSS-IOMP/TriThiol-TAE, and 50 mol% vPOSS-IOMP/TriThiol-TAE , respectively. The changes of FWHM of the loss tangent (Figure 13) were 13.4 °C, 13.5 °C, 14.1 °C, and 19.1 °C for the same systems. These results were predictable given that vPOSS-IOMP aggregation occurs in solution prior to copolymerization with thiol (Table 2). DSC analysis of pure vPOSS-IOMP shows an observable T_g = -69 °C (Figure 12b) and the observable shift of T_g (vPOSS-IOMP/TriThiol-TAE copolymers) to lower temperatures and broadening indicates that POSS-rich domains are formed within the final cured network. Physical observation of the final cured films (Picture 2 (a-e)) shows translucent films that appear slightly hazy as the concentration of vPOSS-IOMP increases confirm

that vPOSS-IOMP aggregates are locked within the TriThiol-TAE network. The changes

in rubbery storage modulus (Figures 14 and 15) and pencil hardness (Figure 16) of the

vPOSS-IOMP/TriThiol-TAE polymer at all concentrations of vPOSS- demonstrate a

continuous decrease with respect to vPOSS-IOMP concentrations. By contrast, hardness,

as measured by Persoz pendulum hardness (Figure 17) and shore A hardness (Figure 18)

tests, are slightly higher than neat TriThiol-TAE for all concentrations of vPOSS-IOMP

thus indicating a blooming of POSS molecules to the surface. In order to further examine

the vPOSS-IOMP at the surface, water contact angle measurements were measured to

analyze the changes in surface hydrophobicity since POSS particles are very

hydrophobic. The surface of neat TriThiol-TAE is moderately hydrophobic as indicated

by a water contact angle of 70.8°. Upon the inclusion of vPOSS-IOMP, the water contact

angle increased from 78.5° to 84.0° to 83.5° for 1 mol% vPOSS-IOMP/TriThiol-TAE,

10 mol% vPOSS-IOMP/TriThiol-TAE, and 50 mol% vPOSS-IOMP/TriThiol-TAE,

respectively, therefore, indicating that the presence of vPOSS-IOMP at the surfaces

increases with respect to vPOSS-IOMP concentration in the cured matrix. Thus, at high

concentrations, a sufficient amount of vPOSS-IOMP at the surface creates hard domains

that are easily measured by Persoz pendulum and shore A hardness (Figure 17 and 18)

and contact angle measurements. Likewise, vPOSS-IOMP at the surface probably

contributes to the brittleness that is displayed by fracture failure upon scratching. Finally,

it is noted that in contrast to the results for vPOSS-IMOP the water contact angle for the

vPOSS-MT/TriThiol-TAE network did not change significantly with respect to vPOSS-

MT concentration, thus demonstrating the high compatibility of vPOSS-MT with the

vPOSS-MT/TriThiol-TAE based network (Table 4).

Recapping, the hydrocarbon content of an organic substituent was shown to

influence the compatibility of POSS nanoparticles and impact aggregation of the silicate

particles. Minimal changes in the final network (constant T_g and lack of broadening in

the glass transition) were consequences of effective compatibilization of vPOSS-MT in

the network, and, although vPOSS-MT particles were well dispersed throughout the

network, the modulus, surface hardness, and fracture resistance were not shown to

improve with increased vPOSS-MT concentration.

Consideration of the aggregation of vPOSS modified with thiol acids, 3-

mercaptopropionate (MPA) and mercaptoacetic acid (MAA), it is first noted (Table 2)

that no large scale aggregation (via DLS measurements) of POSS molecules takes place

in the solution prior to polymerization. Accordingly, the thiol acids, analogs of methyl

thioglycolate, are miscible in the copolymer solution based upon the DLS measurements

(Table 2). The measured viscosities (30 °C) of 282 Poise and 411 Poise for vPOSS-MPA

and vPOSS-MAA, respectively (see Table 5), were recorded indicating a hydrogen

bonding of acid groups in the pre-polymerization mixture. A comparison of IR scans of

the vPOSS modified with thiol acids (MPA and MAA) and methyl thioglycolate (MT)

shows a broad peak at 3500 cm^{-1} for MAA and MPA, which is absent for MT in the same

region, indicating that hydrogen bonding of the acid groups occurs (Figure 19). vPOSS-

MAA and vPOSS-MPA were successfully incorporated into the TriThiol-TAE network at

5 and 50 mol% as shown in Figure 20, although polymerization rates and conversions are

significantly reduced at 50 mol% vPOSS-MPA and 50 mol% vPOSS-MAA. By

comparison to neat TriThiol-TAE, complete conversion of thiol in TriThiol-TAE occurs

in 10 seconds whereas the thiol conversions in 10 seconds for 50 mol% vPOSS-

MAA/TriThiol-TAE (13 relative moles) and 50 mol% vPOSS-MPA/TriThiol-TAE (4 relative moles) are significantly less. (Note that the thiol conversion is absent in Figure 19a as a result of fluctuations of the base line during kinetic analysis. The total thiol conversion is the same as the total ene (allyl ether) conversion.) By visible observation of the final cured films (Picture 3(a-e) and Picture 4(a-e)), the films appear slightly hazy, especially at high concentrations (20 and 50 mol%) at which a significant amount of POSS aggregates (vPOSS-MPA and vPOSS-MAA) are chemically attached to the network.

In each case of acid-modified POSS, the POSS particles (vPOSS-MAA and vPOSS-MPA) are well dispersed vPOSS-MAA and vPOSS-MPA throughout the TriThiol-TAE network up to 20 mol%, i.e. broadening in the glass transition is not large (Figures 21 and 25). Higher T_g's, and a fairly constant or increasing values for the rubbery modulus values (30 °C) are observed with increasing concentrations of vPOSS-MPA for vPOSS-MPA/TriThiol-TAE (Figures 22-24) and vPOSS-MAA for vPOSS-MAA/TriThiol-TAE (Figures 26-28) based systems. Presumably this results from hydrogen bonding due to the acid groups in vPOSS-MPA and vPOSS-MAA that are incorporated into the network, which could make up for any lack of conversion of vinyl double bonds on vPOSS-MPA or vPOSS-MAA. It appears as though any deleterious effect of vPOSS-MPA and vPOSS-MAA enriched domains (50 mol%) are compensated by the hydrogen bonding of the acid groups attached to POSS molecules incorporated into the network. Additionally, DSC analysis of vPOSS-MAA and vPOSS-MPA show observable T_g = -30 °C and T_g = -31 °C, respectively, which are significantly high due to

hydrogen bonding of the acid groups (Figures 21b and 25b) than for vPOSS-MT (Figure 4) and vPOSS-IOMP (Figure 12).

Only marginal differences (probably within experimental error) in Persoz hardness, scratch resistance and Shore A hardness were observed at all concentrations as shown in Figures 29 and 30 for vPOSS-MPA/TriThiol-TAE and Figures 31 and 32 for vPOSS-MAA/TriThiol-TAE. Water contact angle measurements (Table 4) showed neglible changes suggesting that essentially the surface was unaffected by high concentration of POSS particles, in agreement with the results in Figures 29-32. While the presence of the POSS particless based on vPOSS-MAA and vPOSS-MPA has a significant effect on the thermal and mechanical behavior of the network, the hardness and scratch properties are not greatly affected.

Burn rates of POSS containing TriThiol-TAE network

A comparison of burn rates (plotted in Figure 33) of TriThiol-TAE networks containing vPOSS-Bu$_2$ (found in Chapter 5), vPOSS-MT, and vPOSS-MAA clearly showed the influence of POSS dispersion on the reduction of flame spread. The burn rates for networks containing vPOSS-MT dramatically decreased from 11.2 in^2/sec to 2.33 in^2/second for neat TriThiol-TAE and 1 mol% vPOSS-MT/TriThiol-TAE, respectively, leveling off to lower rates of 3.10 in^2/sec, 2.69 in^2/sec, 2.31 in^2/sec, and 1.55 in^2/sec for 5, 10, 20, and 50 mol% vPOSS-MT/TriThiol-TAE, respectively. By comparison, the initial change in burn rates (decrease) for vPOSS-Bu$_2$ and vPOSS-MAA is significantly less, i.e. burn rates decrease from 11.2 in^2/sec for neat TriThiol-TAE to 6.23 in^2/sec and 5.17 in^2/sec for 1 mol% vPOSS-Bu$_2$/TriThiol-TAE and 1 mol% vPOSS-MAA/TriThiol-TAE, respectively. The burn rates for networks containing vPOSS-MAA

continue to decrease from 5.18 in^2/sec, 4.13 in^2/sec, 3.44 in^2/sec, and 2.82 in^2/sec for 5, 10, 20, and 50 mol% vPOSS-MAA/TriThiol-TAE, respectively. For all concentrations, the burn rates of networks containing vPOSS-MT are significantly lower possibly due to the influence of molecular dispersion on the burn rates of the film.

Free volume of vPOSS-MT/TriThiol-TAE and vPOSS-IOMP/TriThiol-TAE networks

PALS measurements of o-Ps intensity and lifetime (τ_3) show how molecularly dispersed vPOSS-MT and vPOSS-MAA, and POSS rich domains of vPOSS-IOMP, in relation to their hydrocarbon content, affect free volume within the TriThiol-TAE network. Recall in Chapter 5 that intensity measurements of vPOSS-Bu$_2$, which are related to the number of voids present, decreased with increased POSS concentration; voids created by the incorporated POSS cages were immeasurable. Also, the initial increase of lifetimes at low concentration, which is directly related to the size of voids, resulted from interaction between the polymer and the organic substituents (R = Bu) on the inorganic silicate particles or organic substituents within the POSS-rich domains as the concentration of POSS increased. Likewise, a plot of o-Ps intensity measurements vs. mol% POSS (Figure 34a) for the vPOSS-MT and vPOSS-MAA containing systems show that the number of voids decreased as the concentration of vPOSS-MT increased suggesting that the voids created by POSS cages are immeasurable. By contrast, the intensity measurements (Figure 34a) for vPOSS-IOMP containing systems increased marginally with increase of vPOSS-IOMP concentration. Presumably, o-Ps formation is affected by the presence of long, aliphatic chains located on the POSS corners showing that the distribution of hole free volume is unaffected by the presence of POSS at all

concentrations. The chain length of methyl thioglycolate (MT) and mercaptoacetic acid (MAA) are inadequate in assisting formation of o-Ps.

Also, in Figure 34b, a plot of lifetimes vs. Mol% POSS shows marginal changes in lifetime (τ_3) measurements of the vPOSS-MT and vPOSS-MAA containing systems suggesting that free volume changes in the network are insignificant with respect to vPOSS-MT and vPOSS-MAA concentration and the interaction between the polymer and vPOSS-MT and vPOSS-MAA particles is favorable, even at high concentrations. Conversely, free volume significantly increased upon the inclusion of vPOSS-IOMP at all concentrations as shown in Figure 34b. Contributions of free volume increase may result from unfavorable interaction between the particle and vPOSS-IOMP and the presence of long aliphatic chains on the periphery of the POSS cage.

Oxygen flux measurements demonstrate the effects of free volume on gas transport properties. A significant amount of free volume increases the permeability of oxygen gas through the polymer network, whereas the barrier properties are increased by a significant loss of free volume within the network. The incorporation of vPOSS-MT and vPOSS-MAA into the TriThiol-TAE network shows marginal changes in free volume by PALS analysis. These well-dispersed POSS particles (20 mol%) demonstrate no significant change in gas transport of oxygen within the TriThiol-TAE network, i.e. permeability, diffusivity, and solubility of oxygen are not changed significantly (Figure 35).

CONCLUSION

The effectiveness of compatibility of modified POSS nanoparticles in a TriThiol-TAE network has been shown in relation to the hydrocarbon content of the ester substituent group. When the ester group has a short aliphatic chain, the mechanical and physical properties increased moderately with increasing POSS concentration as demonstrated by inclusion of vPOSS-MT into the network. DSC analysis of vPOSS-MT/TriThiol-TAE shows that vPOSS-MT are well dispersed within the TriThiol-TAE network, i.e. broadening in the glass transition to lower T_g was unobservable at all concentrations. Upon the inclusion of vPOSS-IOMP particles into the TriThiol-TAE network, the rubber modulus and scratch resistance decreased with respect to vPOSS-IOMP concentration as a result of the increased hydrocarbon content of the ester. DLS measurements show the presence of vPOSS-IOMP aggregation prior to photopolymerization. Broadening of the glass transition range is observed in the loss tangent curve which corresponds with observed changes in the network caused by vPOSS-IOMP enriched domains within the TriThiol-TAE network. RTIR analysis of vPOSS-MT and vPOSS-IOMP containing systems showed that polymerization rates and conversions were affected by the formation of POSS-rich domains during network formation. PALS measurements of intensity and τ_3 suggest that free volume did not change significantly with POSS dispersion and compatibility. The organic substituents (R) of POSS particles significantly affect intensity, i.e. intensity decreased with increased vPOSS-MT while changing marginally with increased vPOSS-IOMP. Negligible changes in free volume for vPOSS-MT containing systems indicated favorable interactions

between the vPOSS-MT particles and the polymer at all concentrations, whereas

increased changes in free volume for vPOSS-IOMP containing systems resulted from

unfavorable interactions between the polymer and vPOSS-IOMP particle and the

presence of long, aliphatic chains on the POSS particles.

The inclusion of acid-modified vPOSS (vPOSS-MPA and vPOSS-MAA) was

shown to increase T_g. No significant broadening in the glass transition region occurred

due to hydrogen bonding effects, and the network mechanical properties were not

significantly reduced, again, probably due to hydrogen bonding of the acid groups

incorporated into the network. DMA analysis of vPOSS-MAA/TriThiol-TAE systems

showed a continual increase of the rubbery modulus (30 °C). PALS analysis and oxygen

flux measurements showed that dispersed vPOSS-MAA had little effect on free volume

changes within the TriThiol-TAE network.

REFERENCES

[1] Schadler, L. S.; Brinson, L. C. *JOM*, **2007**, *59*, 53-60.

[2] Kukhta, A. V.; Kolesnik, E.E.; Lesnikovich, A. I.; Nichik, M. N.; Kudlash, A. N.; Vorobyova, S. A.; *Syn. React in Inorg./ Metal-Org., and Nano-Metal Chem.*, **2007**, *37*, 333-339.

[3] Vaia, R. A; Maguire, J. F.; *Chem. of Mat.*, **2007**, *19*, 2736-2751.

[4] Naous, W.; Yu, X.; Zhang, Q.; Naito, K.; Kagawa, Y.; *J. Poly. Sci., B*, **2006**, *44*, 1-20.

[5] Ash, B. J.; Siegel, R, W.; Schadler, L. S.; *Macromolecules*, **2004**, *37*,1466-1473.

[6] Xia, Z.; Riester, L; Curtin, W.; Sheldon, B. W.; Liang, J.; Chang, B.; Xu, J. M.; *Acta Mater.*, **2004**, *52*, 931-944.

[7] Liu, T.; Phan, I.; Shen, L.; Chow, S.; Zhang, W.; *Macromolecules*, **2004**, *37*, 7214-7222.

[8] Karak, N., *J. Polym. Mat.*, **2006**, *23*, 1-20.

[9] Smith, G. D.; Bedrov, D.; Li, L.; Buytner, O.; *J. Chem. Phys.*, **2002**, *117*, 9478-9489.

[10] Arshady, R., *Microspheres, Microcap., and Liposomes*, **2002**, *5*, 1-29.

[11] Mylvaganam, K.; Zhang, L. C., *Recent Patents on Nanotechnology*, **2007**, *1*, 59-65.

[12] Vaia, R. A.; Maguire, J. F., *Chem.Mat.*, **2007**, *19*, 2736-2751.

[13] Rittigstein, P.; Priestley, R. D.; Broadbelt, L. J.; Torkelson, J. M. *Nature Mat.*, **2007**, *6*, 278-282.

[14] Rittigstein, P.; Torkelson, J. M., *J. Polym. Sci., B*, **2006**, *44*, 2935-2943.

[15] Abyaneh, Majid Kazemian; Paramanik, D.; Varma, S.; Gosavi, S. W.; Kulkarni, S. K. *J. Phys. D: Applied Phys.*, **2007**, *40*, 3771-3779.

[16] Huang, C.; Kuo, S.; Lin, F.; Huang, W.; Wang, C.; Chen, W.; Chang, F., *Macromolecules*, **2006**, *39*, 300-308.

[17] Kopesky, E. T.; Haddad, T. S.; McKinley, G. H.; Cohen, R. E., *Polym.*, **2005**, *46*, 4743-4752.

[18] Xu, H.; Yang, B.; Wang, J.; Guang, S.; Li, C., *Macromolecules*, **2005**, *38*, 10455-10460.

[19] Soong, S. Y.; Cohen, R. E.; Boyce, M. C., *Polym.*, **2007**, *48*, 1410-1418.

[20] Song, X..; Geng, H.; Li, Q., *Polym.*, **2006**, *47*, 3049-3056.

[21] Strachota, A.; Kroutilova, I.; Kovarova, J.; Matejka, L.., *Macromolecules*, **2004**, *37*, 9457-9464.

[22] Li, G. Z.; Cho, H.; Wang, L.; Toghiani, H.; Pittman, C. U., Jr., *J. Polym. Sci., A*, **2005**, *43*, 355-372.

[23] Weickmann, H.; Delto, R.; Thomann, R.; Brenn, R.; Doell, W.; Muelhaupt, R., *J. Mat. Sci.*, **2007**, *42*, 87-92.

[24] Zhang, Z.; Liang, G.; Wang, J.; Ren, P., *Polym. Composites*, **2007**, *28*, 175-179.

[25] Li, G. Z.; Wang, L.; Toghiani, H.; Daulton, T. L.; Pittman, C. U., *Polym.*, **2002**, *43*, 4167-4176.

[26] Kim G. M., Qin H., Fang X., Mather P. T., *J Polym. Sci., B*, **2003**, *41*, 3299-3313.

[27] Fu B. X., Yang L., Somani R. H., Zong S. X., Hsiao B. S., Phillips S., Blanski R., Ruth P., *J. Polym. Sci., B*, **2001**, *39*, 2727-2739.

[28] Zheng L., Farris R. J., Coughlin E. B.,*Macromolecules*, 34, **2001**, 8034-8039.

[29] Mather P. T., Jeon H. G., Romo-Uribe A., Haddad T. S., Lichtenhan J. D., *Macromolecules*, **1999**, *32*, 1194-1203.

[30] Ramirez C., Vilarino J. M. L., Abad M. J., Barral L., Bouza R., Cano J., Diez F. J., Garcia-Garabal S., Lopez J., *J. Appl. Polym. Sci.*, **2004**, *92*, 1576-1583.

Vinyl POSS-MT

	SH	1	2	3	4	5	6	7	a	b	c	d	C=O	CH₂=CH-
^{1}H (δ/multi)	-------	3.7/s	-------	-------	-------	-------	-------	-------	3.6/t	2.6/t	1.0/d	-------	-------	6.0/(d,t)
^{13}C (δ/multi)	-------	57/s	-------	-------	-------	-------	-------	-------	37/s	31/s	19/s	-------	170/s	135/d

Vinyl POSS IOMP

	SH	1	2	3	4	5	6	7, 8	a	b	c	d	C=O	CH₂=CH-
^{1}H (δ/multi)	-------	4.0/t	1.6/m	1.2/m	1.2/m	1.0/q	2.65/m	0.8/d	2.6/t	2.7/t	2.5/t	0.8/t	-------	6.0/(d,t)
^{13}C (δ/multi)	-------	-------	-------	-------	-------	-------	-------	-------	-------	-------	-------	-------	-------	-------

Vinyl POSS-MPA

	SH	1	2	3	4	5	6	7	a	b	c	d	C=O	CH₂=CH-
^{1}H (δ/multi)	-------	-------	-------	-------	-------	-------	-------	-------	2.6/t	2.5/t	2.45/t	0.9/t	-------	6.0/(d,t)
^{13}C (δ/multi)	-------	-------	-------	-------	-------	-------	-------	-------	39/s	31/s	30/s	19/s	172/s	135/d

Vinyl POSS-MAA

	SH	1	2	3	4	5	6	7	a	b	c	d	C=O	CH₂=CH-
^{1}H (δ/multi)	-------	-------	-------	-------	-------	-------	-------	-------	3.7/s	2.6/q	0.9/t	-------	-------	6.0/(d,t)
^{13}C (δ/multi)	-------	-------	-------	-------	-------	-------	-------	-------	40/s	31/s	20/s	19/s	170/s	135/d

Vinyl POSS

	SH	1	2	3	4	5	6	7	a	b	c	d	C=O	CH₂=CH-
^{1}H (δ/multi)	-------	-------	-------	-------	-------				-------	-------	-------	-------	-------	6.0/(d,t)
^{13}C (δ/multi)	-------	-------	-------	-------	-------				-------	-------	-------	-------	-------	135/d

Methyl Thioglycolate

	SH	1	2	3	4	5	6	7	a	b	c	d	C=O	CH₂=CH-
^{1}H (δ/multi)	1.5/t	3.7/s	-------	-------	-------				3.6/t	-------	-------	-------	-------	-------
^{13}C (δ/multi)	-------	57/s	-------	-------	-------				37/s	-------	-------	-------	170	-------

Isooctyl 3-mercaptopropionate

	SH	1	2	3	4	5	6	7	a	b	c	d	C=O	CH₂=CH-
^{1}H (δ/multi)	1.4/t	4.0/t	1.6/m	1.2/m	1.2/m	1.0/q	2.65/m	0.8/d	2.6/t	2.7/t	-------	-------	-------	-------
^{13}C (δ/multi)	-------	-------	-------	-------	-------	-------	-------	-------	-------	-------	-------	-------	-------	-------

3-Mercaptopropionic Acid

	SH	1	2	3	4	5	6	7	a	b	c	d	C=O	CH₂=CH-
^{1}H (δ/multi)	1.6/t	-------	-------	-------	-------	-------	-------	-------	2.6/t	2.5/t	-------	-------	-------	-------
^{13}C (δ/multi)	-------	-------	-------	-------	-------	-------	-------	-------	39/s	31/s	-------	-------	172/s	-------

Mercaptoacetic Acid

	SH	1	2	3	4	5	6	7	a	b	c	d	C=O	CH₂=CH-
^{1}H (δ/multi)	1.6/t	-------	-------	-------	-------	-------	-------	-------	3.7/s	-------	-------	-------	-------	-------
^{13}C (δ/multi)	-------	-------	-------	-------	-------	-------	-------	-------	40/s	-------	-------	-------	172/s	-------

Table 1. List of proton and carbon peak assignments and peak splittings of vPOSS-MT, vPOSS-IOMP, vPOSS-MPA, vPOSS-MAA, vinyl POSS, methyl thioglycolate, isooctyl 3-mercaptopropionate, 3-mercaptopropionic acid, and mercaptoacetic acid. (s = singlet, d = doublet, t = triplet, q= quartet, m = multiplet).

Ene Mol% POSS	Particle Size (nm)			
	MT	IOMP	3MPA	MAA
1	2.93	6.99	1.13	1.02
5	1.04	31.7	0.95	0.91
10	1.98	43.9	0.97	1.08
20	0.93	47.5	0.97	0.92
50	0.93	47.6	1.28	0.95

Table 2. Particle size analysis by dynamic light scattering for each vPOSS/TriThiol-TAE at various ene molar concentrations.

Ene Mol% POSS	FWHM			
	MT	IOMP	3MPA	MAA
0	11.66	13.43	7.99	13.74
1	13.80	13.54	11.60	13.64
5	13.49	13.47	13.98	13.62
10	15.92	14.08	14.05	13.92
20	15.81	14.61	16.55	16.97
50	15.58	23.09	25.54	25.74

Table 3. DMA results of broadening in loss tangent curves at full width at half height (FWHM) for each vPOSS/TriThiol-TAE at various ene molar concentrations.

	Contact Angle (°)			
Ene Mol% POSS	MT	IOMP	3MPA	MAA
0	70.8	70.8	70.8	70.8
1	68.3	78.5	65.2	64.1
5	71.6	80.8	69.0	63.6
10	71.8	84.0	67.3	66.2
20	71.0	82.0	69.6	67.0
50	60.6	83.5	66.5	65.2

Table 4. Water contact angle measurements for each vPOSS/TriThiol-TAE at various ene molar concentrations.

	η (Poise)
TriThiol	1.15
TAE	-----
MT	80.8
IOMP	7.29
3MPA	282
MAA	411

Table 5. Viscosity measurements for each modified vPOSS nanoparticle.

(a)
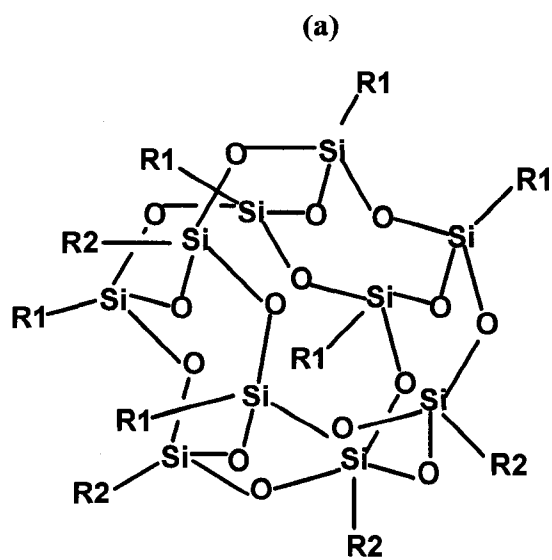
R1 = CH₂=CH–
R2 = 1) Methyl thioglycolate (**MT**), 2) Isooctyl 3-mercaptopropionate (**IOMP**), 3) 3-mercaptopropionate (**MPA**), 4) Mercaptoacetic acid (**MAA**).

(1)

MT

(2)

IOMP

(3)

MPA

(4)

MAA

(b)

(c)

TriThiol

(TAE)

(d)
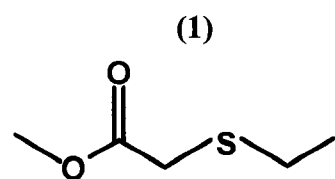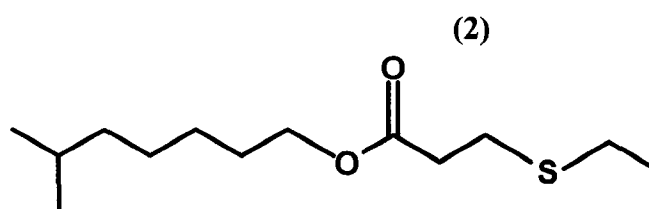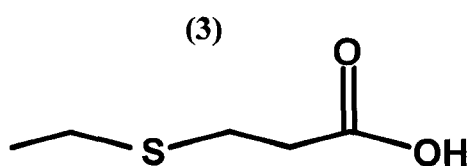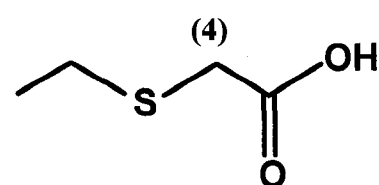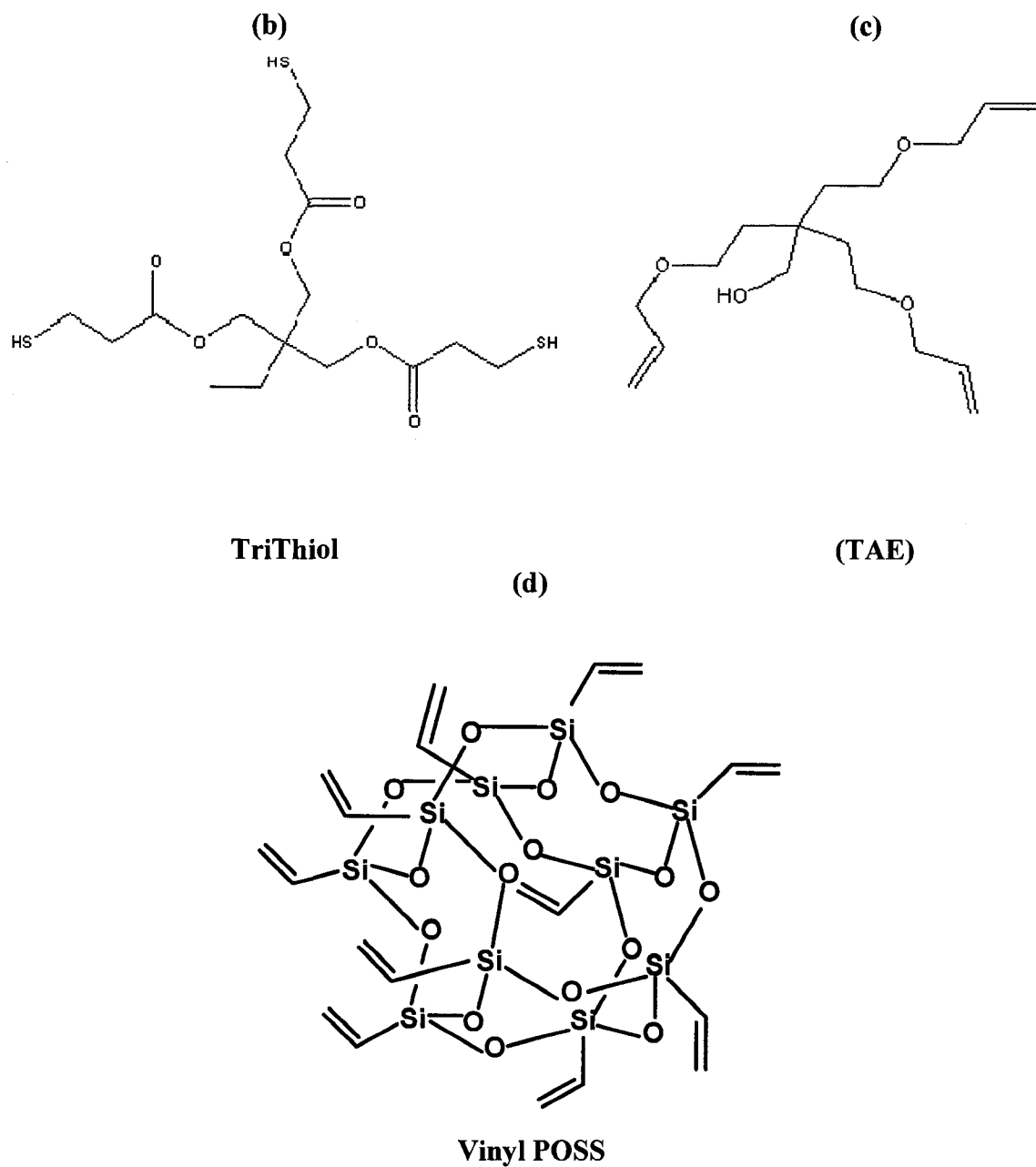
Vinyl POSS

Figure 1. The chemical structures of the a) vPOSS-MT, vPOSS-IOMP, vPOSS-MPA, and vPOSS-MAA, b) Trimethylolpropane tris (3-mercaptopropionate (TriThiol), c) Allyl ether pentaerythritol (TAE) comonomers and d) vinyl POSS.
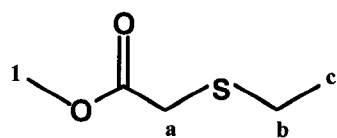
MT
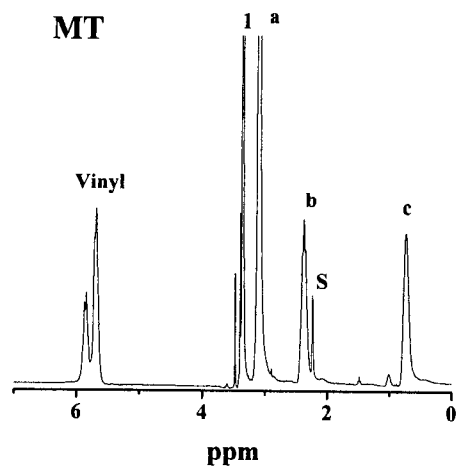
(a)
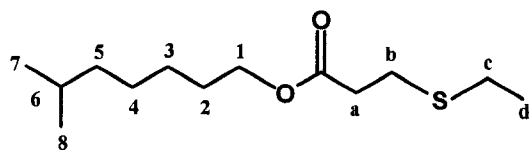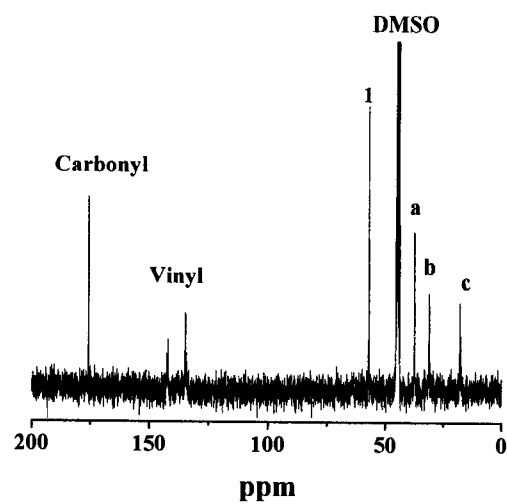
IOMP

(b)
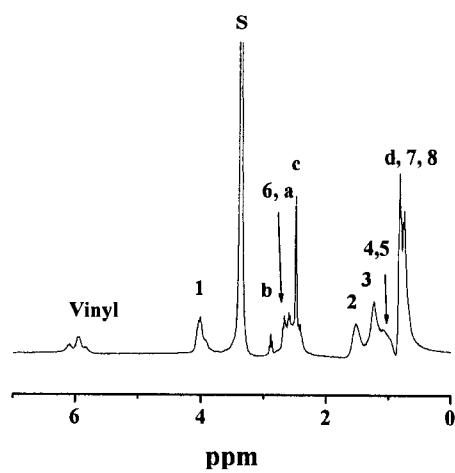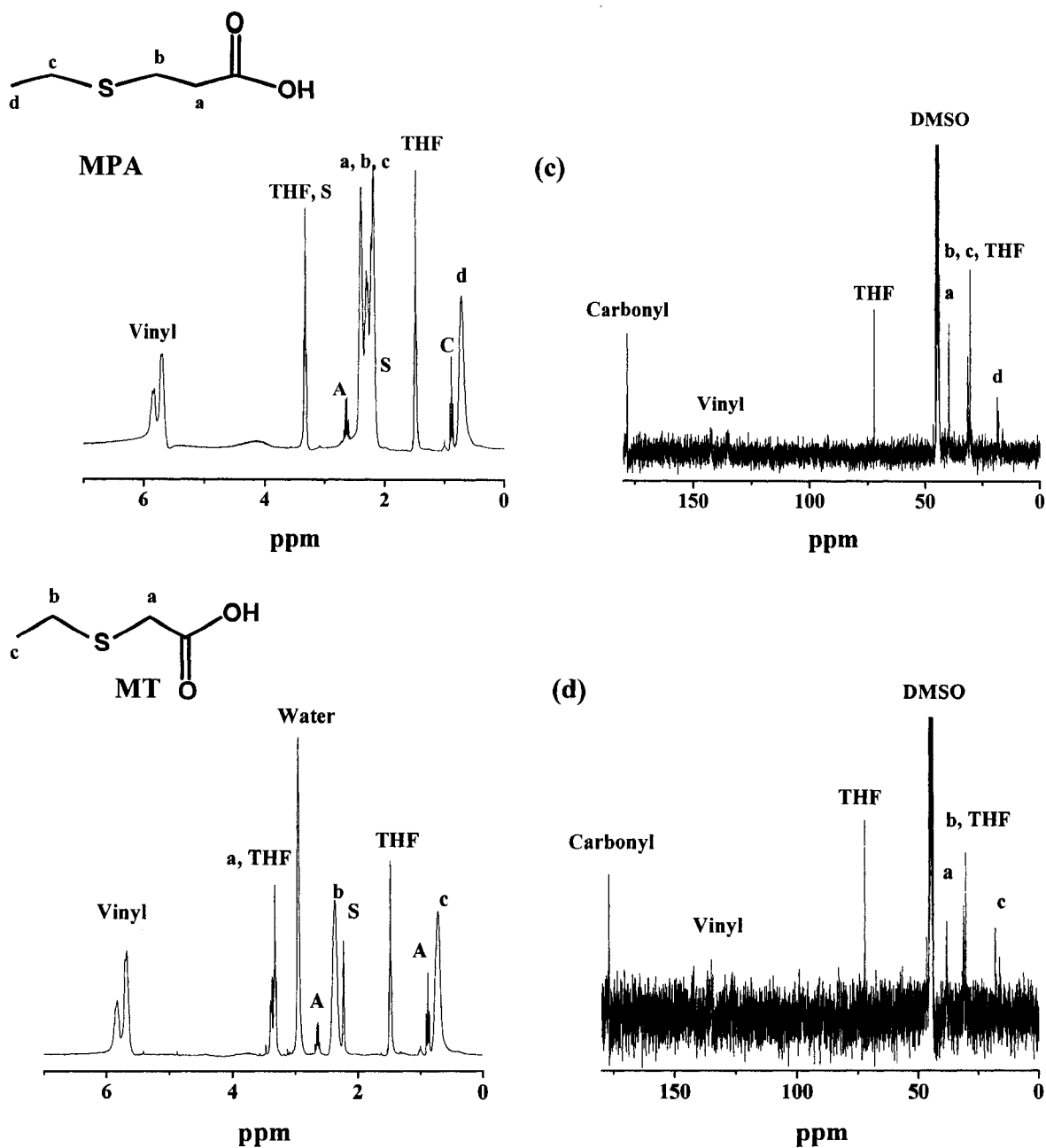
Figure 2. ^{1}H and ^{13}C NMR. a) Methyl thioglycolate, b) Isooctyl 3-mercaptopropionate (^{1}H NMR only), c) 3-mercaptopropionic acid, and d) Mercaptoacetic acid. (S = deuterated DMSO, A = amine impurity).
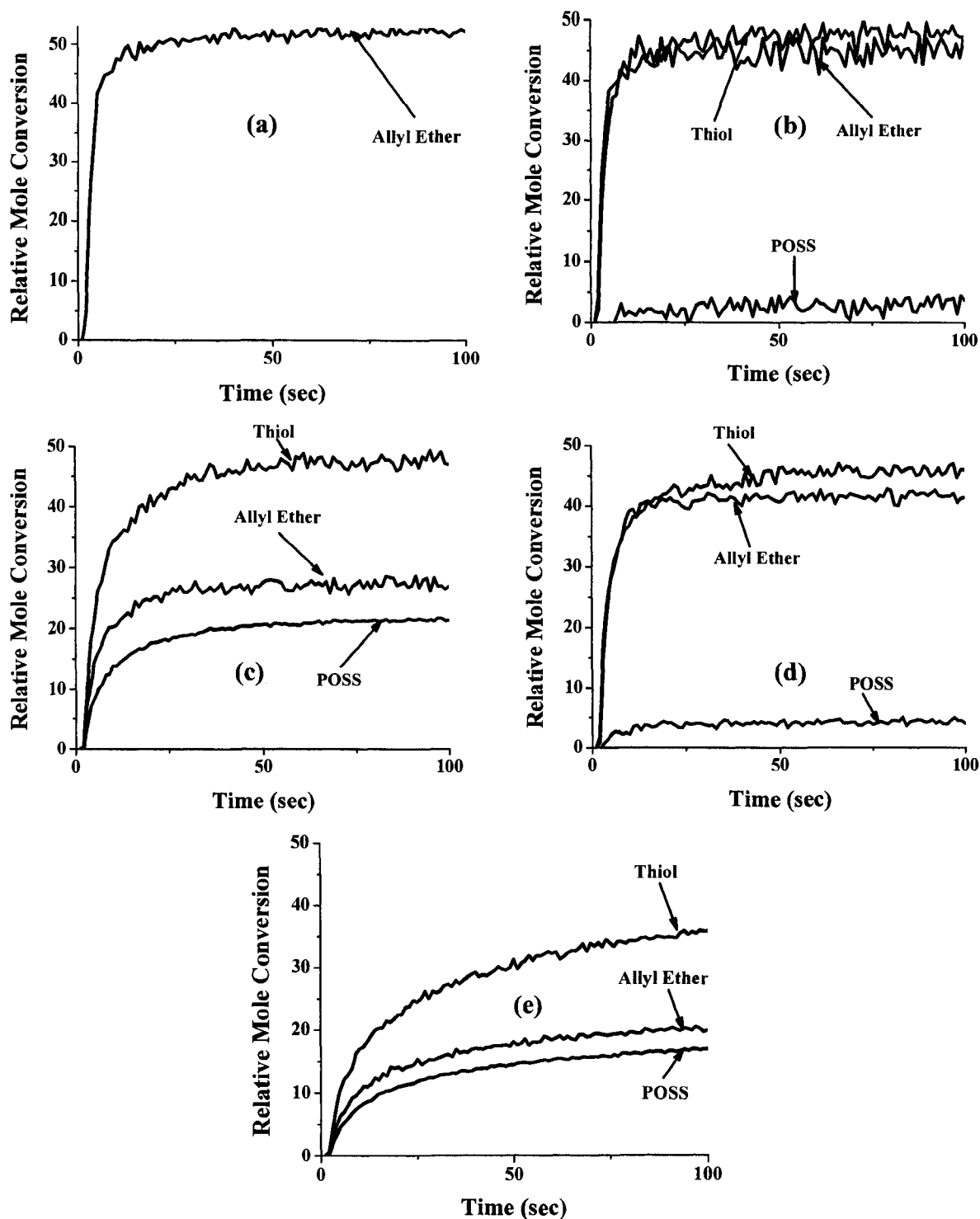
Figure 3. FT-RTIR-based conversion of thiol, vinyl POSS, and allyl ether groups for a) neat TriThiol-TAE (See Appendix C for thiol conversion) , b) 5 mol% vPOSS-MT c) 50 mol% vPOSS-MT d) 5 mol% vPOSS-IOMP, and e) 50 mol% vPOSS-IOMP. Sample thickness was ~20 microns. Light intensity = 19.9 mW/cm^{-2}. Sample thickness was ~20 microns.
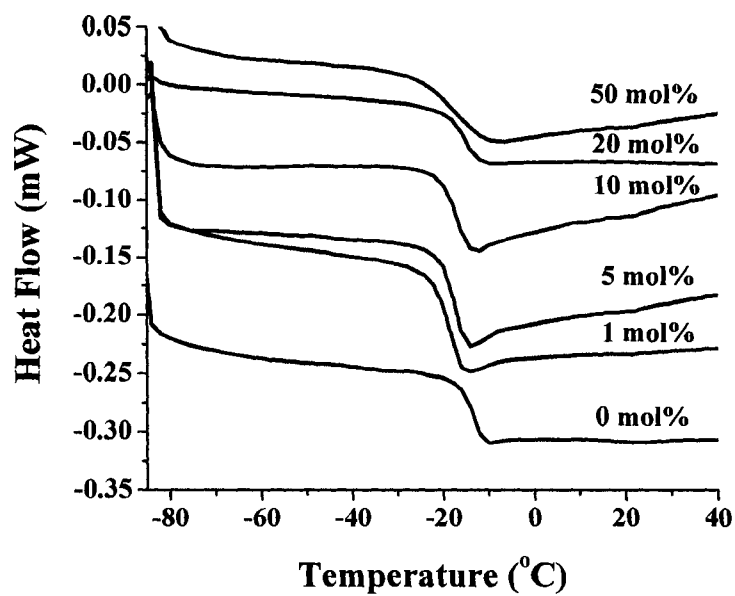
Figure 4. DSC curves of vPOSS-MT/TriThiol-TAE at various ene molar concentrations of vPOSS-MT.
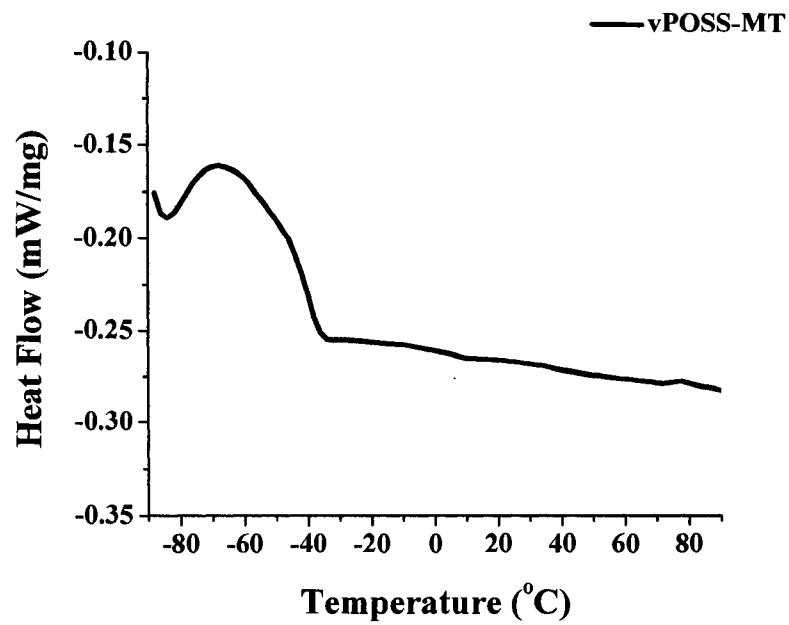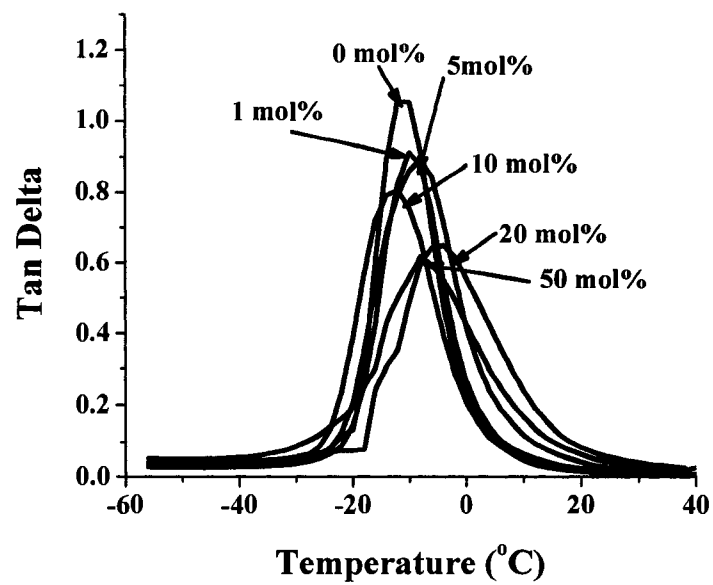
Figure 5. DSC curves of pure vPOSS-MT monomer.

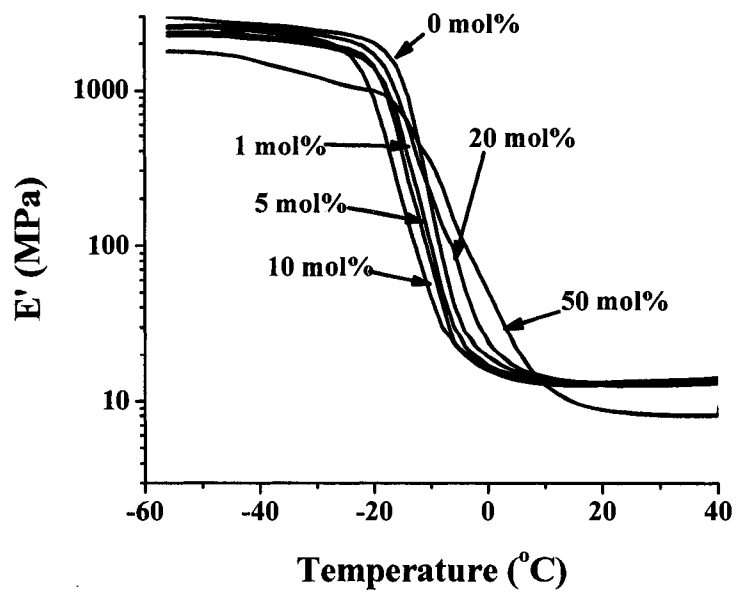**Figure 6.** DMA result of loss tangent curves of vPOSS-MT/TriThiol-TAE at various concentrations of vPOSS-MT.

Figure 7. DMA results of storage modulus curves of vPOSS-MT/TriThiol-TAE at various concentrations of vPOSS-MT.
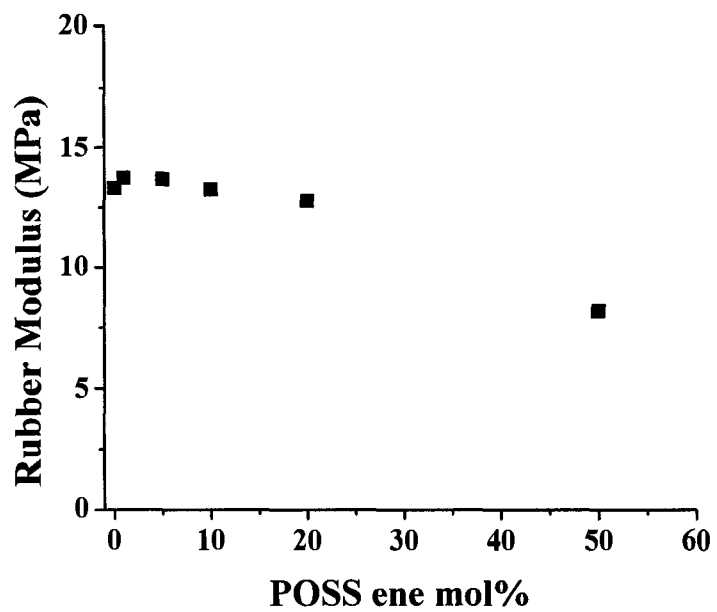
Figure 8. Rubber modulus vs. POSS ene mol% for vPOSS-MT/TriThiol-TAE at various concentrations of vPOSS-MT.
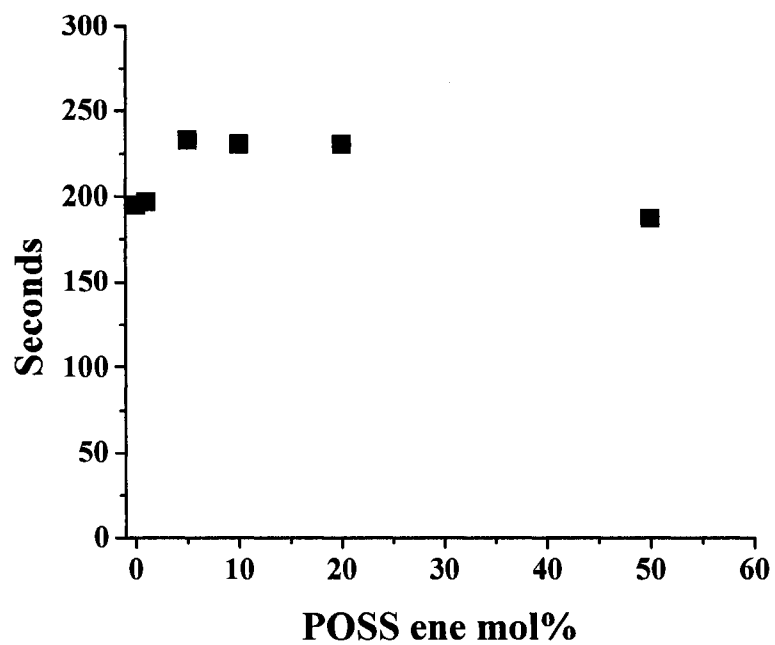
Figure 9. Plot of Persoz pendulum hardness (Oscillation (seconds) vs. POSS ene mol%) for vPOSS-MT/TriThiol-TAE at various concentrations of vPOSS-MT.
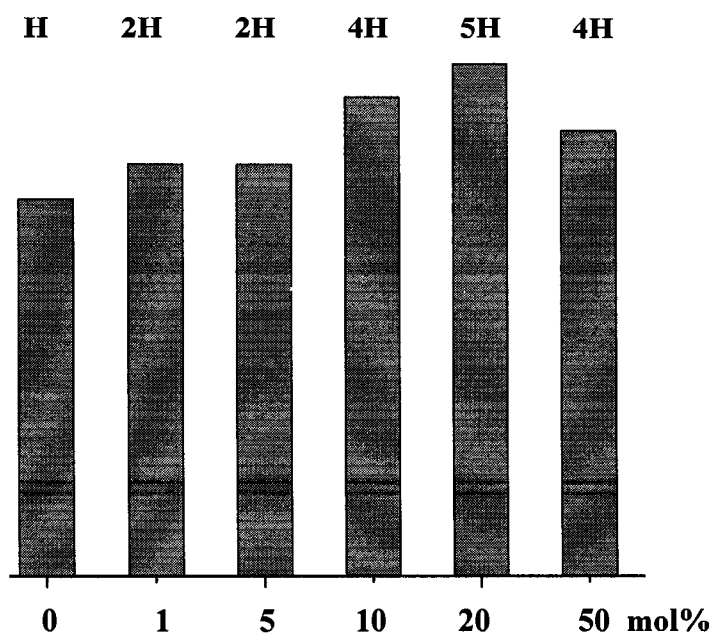
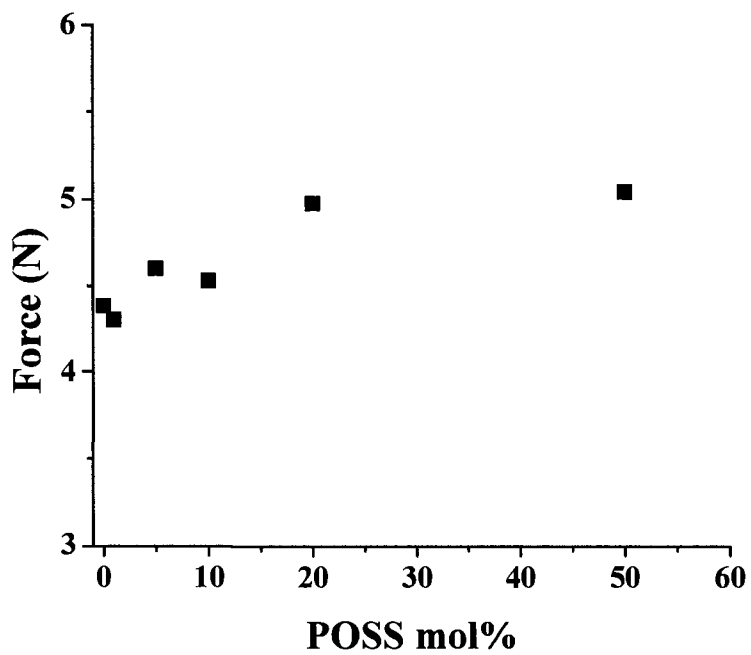**Figure 10.** Diagram of pencil hardness for vPOSS-MT/TriThiol-TAE at various concentrations of vPOSS-MT.

Figure 11. Plot of Shore A durometer hardness (Force vs. POSS mol%) for vPOSS-MT/TriThiol-TAE at various concentrations of vPOSS-MT.
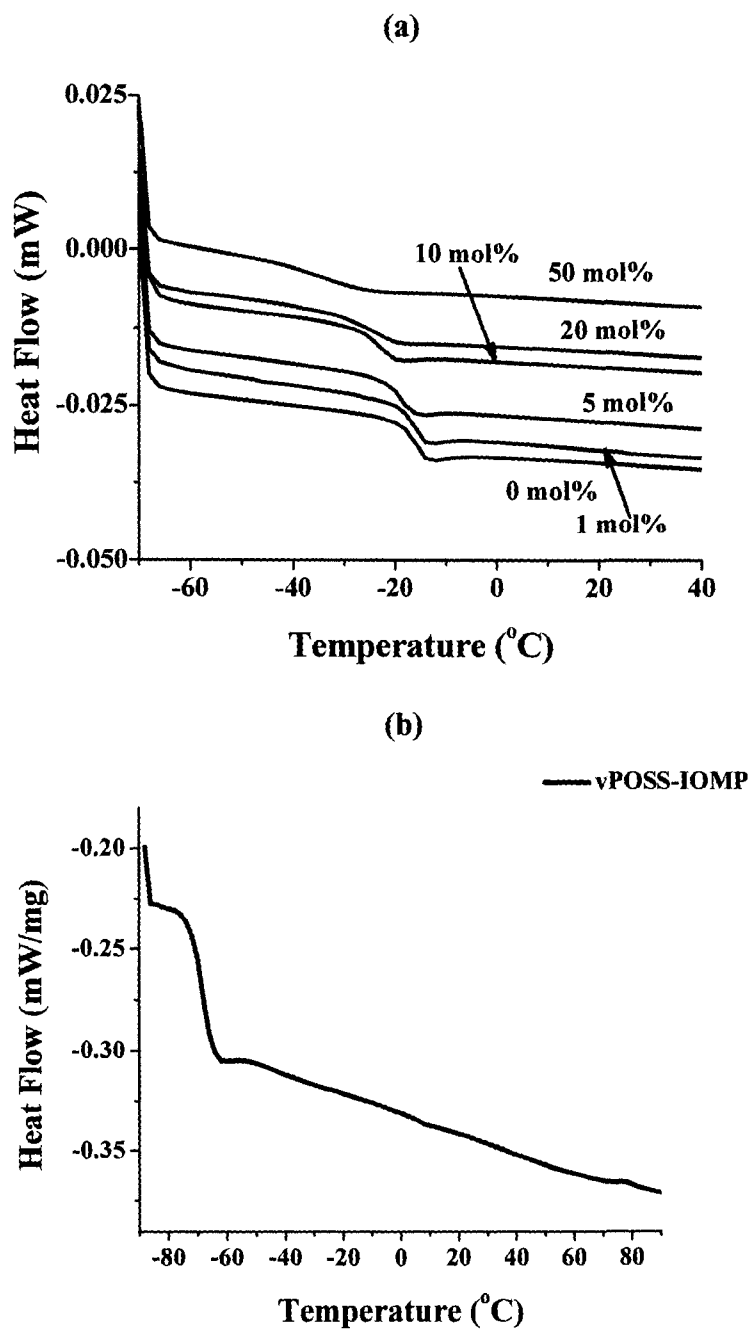
(a)

(b)

Figure 12. DSC curves of a) vPOSS-IOMP/TriThiol-TAE at various ene molar concentrations of vPOSS-IOMP and b) pure vPOSS-IOMP monomer.
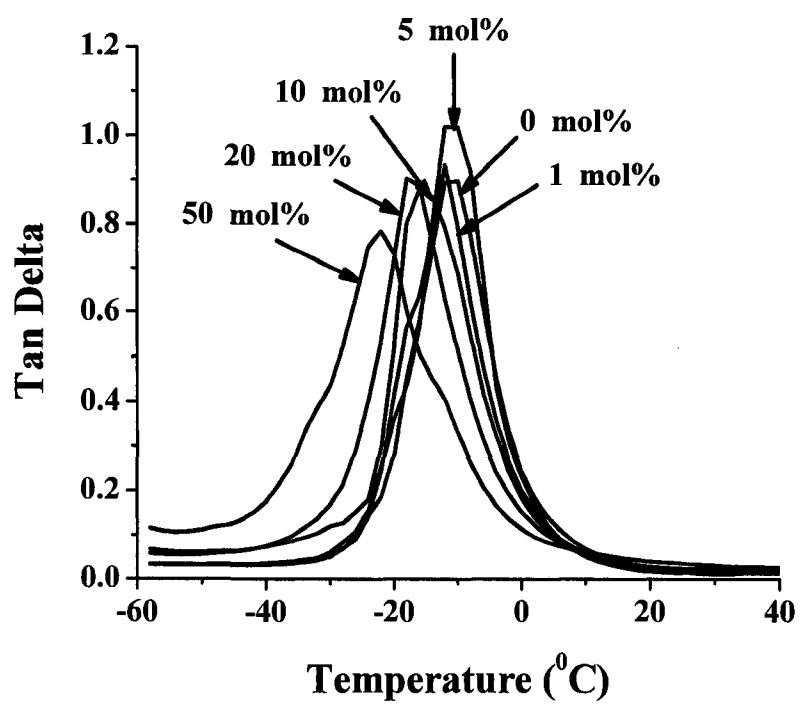
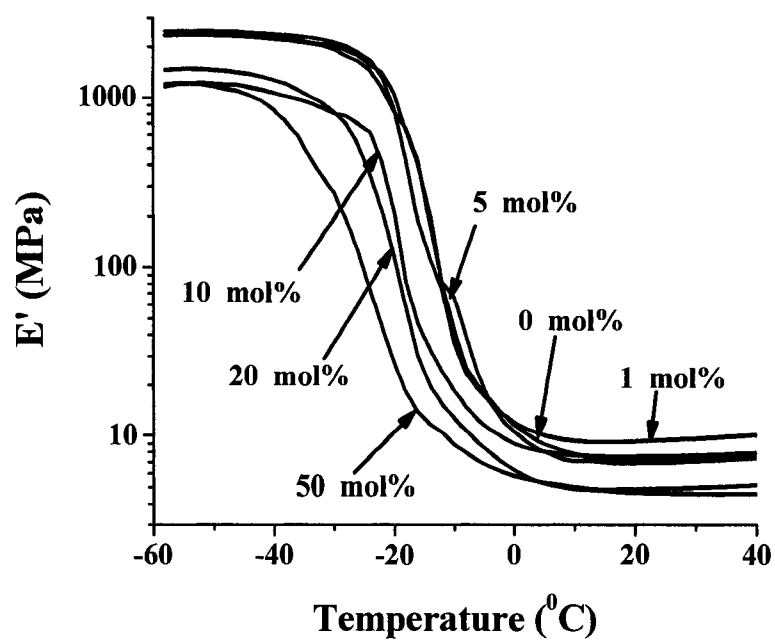**Figure 13.** DMA result of loss tangent curves of vPOSS-IOMP/TriThiol-TAE at various concentrations of vPOSS-IOMP.

Figure 14. Storage modulus (E') vs. POSS ene mol% for vPOSS-IOMP/TriThiol-TAE at various concentrations of vPOSS-IOMP.

Figure 15. Storage modulus (E') vs. POSS ene mol% for vPOSS-IOMP/TriThiol-TAE at various concentrations of vPOSS-IOMP.
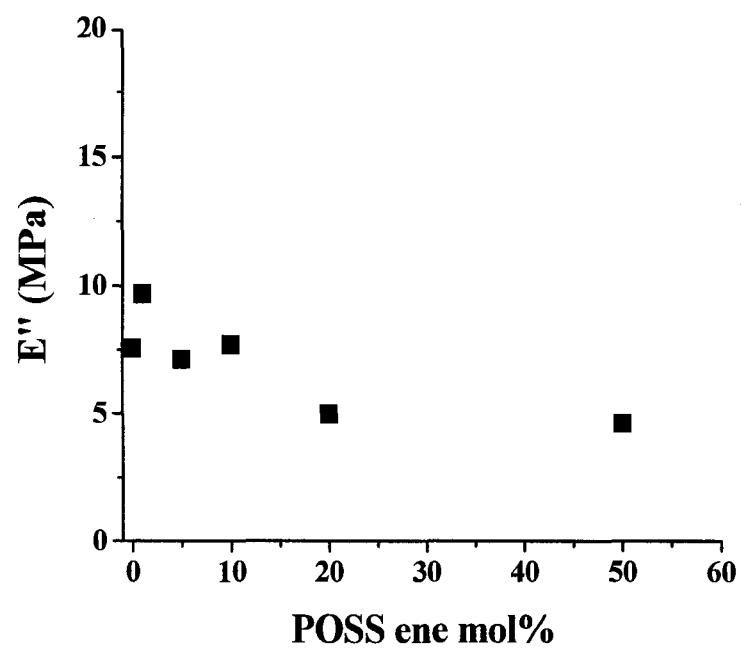
H   H   H   F   B   4B
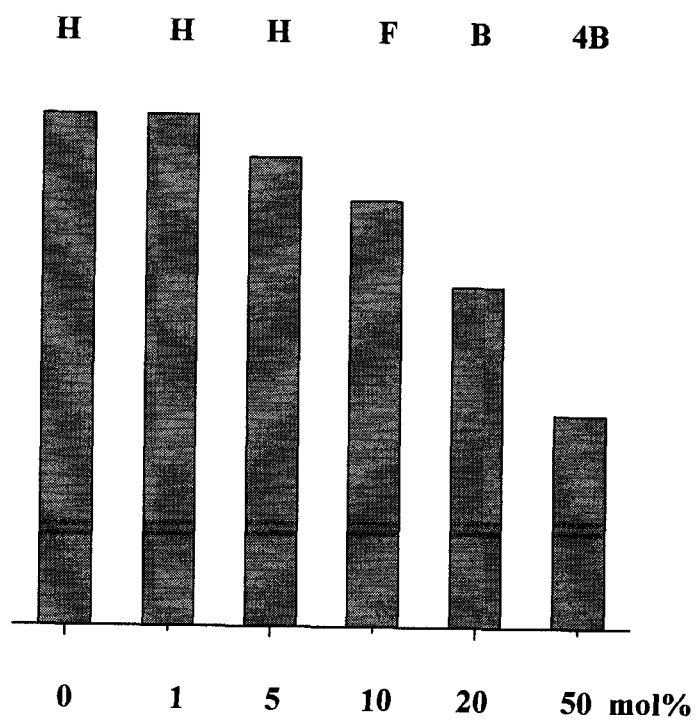
0   1   5   10   20   50 mol%

Figure 16. Diagram of pencil hardness for vPOSS-IOMP/TriThiol-TAE at various concentrations of vPOSS-IOMP.

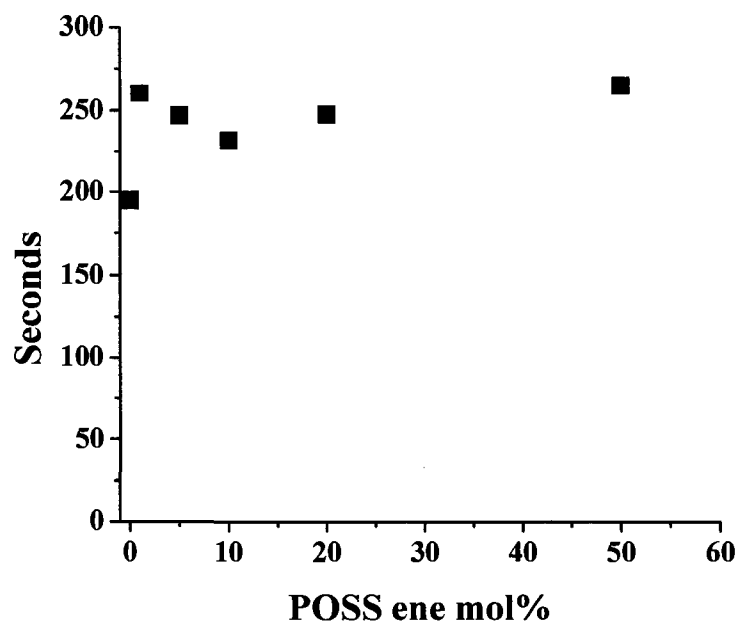**Figure 17.** Plot of Persoz pendulum hardness (Oscillation vs. POSS ene mol%) for vPOSS-IOMP/TriThiol-TAE at various concentrations of vPOSS-IOMP.
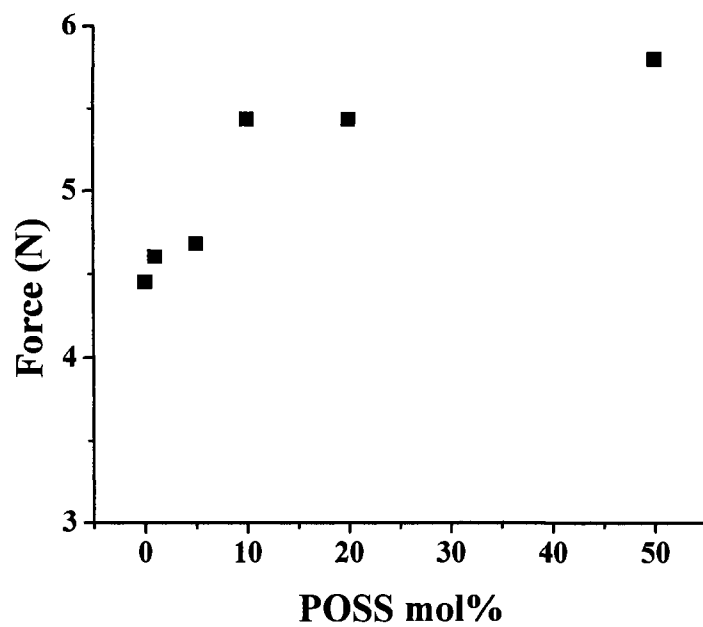
Figure 18. Plot of Shore A durometer hardness (Force vs. POSS mol%) for vPOSS-IOMP/TriThiol-TAE at various concentrations of vPOSS-IOMP.
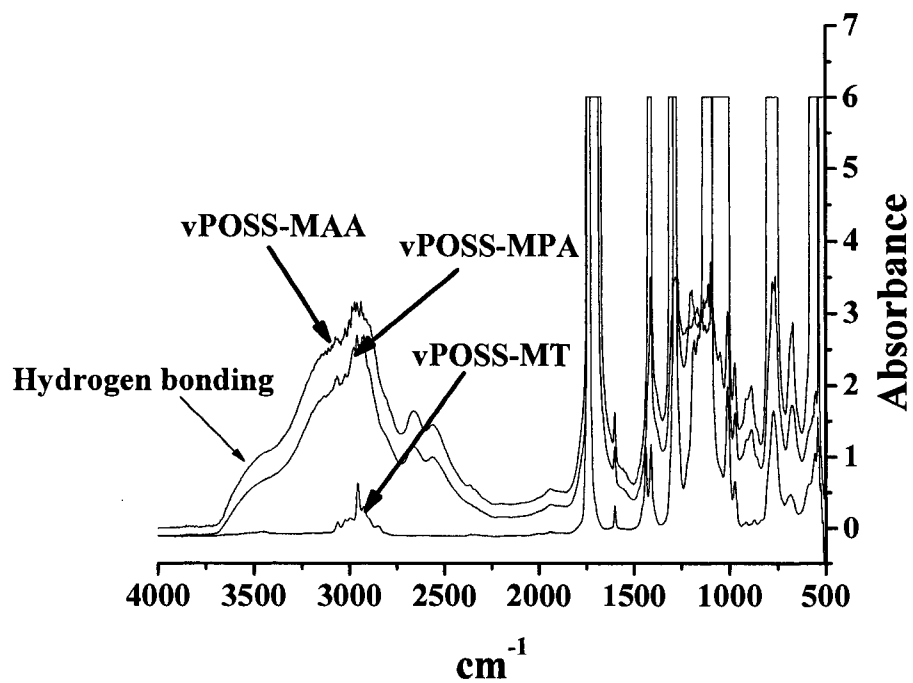
Figure 19. Infrared (IR) spectra of pure a) vPOSS-MAA, b) vPOSS-MPA, and c) vPOSS-MT to show hydrogen bonding of acid groups.
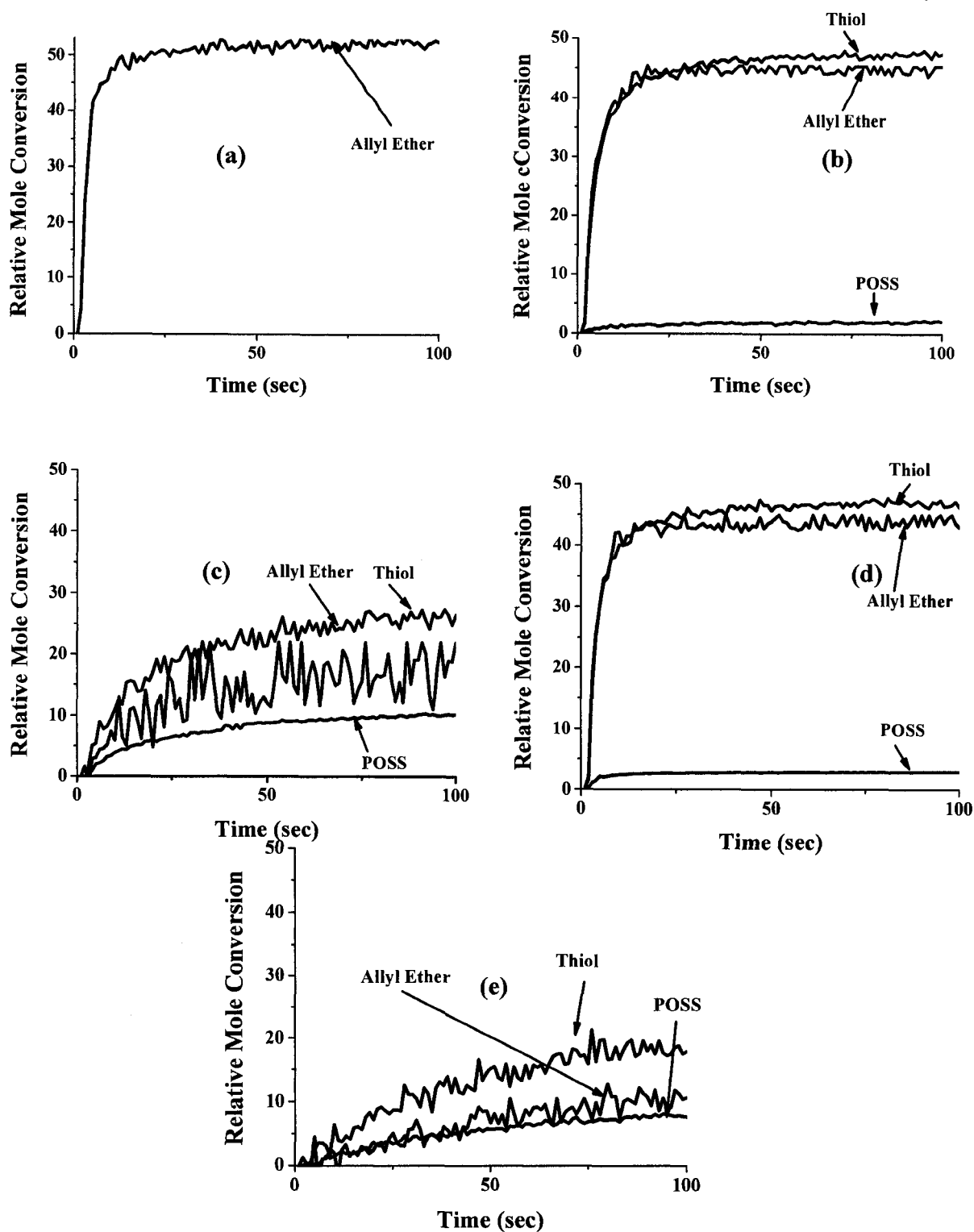
Figure 20. FT-RTIR-based conversion of thiol, vinyl POSS, and allyl ether groups for a) neat TriThiol-TAE (See Appendix C for thiol conversion) , b) 5 mol% vPOSS-MAA c) 50 mol% vPOSS-MAA d) 5 mol% vPOSS-MPA, and e) 50 mol% vPOSS-MPA. Sample thickness was ~20 microns. Light intensity = 19.9 mW/cm^{-2}. Sample thickness was ~20 microns.

Figure 21. DSC curves of a) vPOSS-MPA/TriThiol-TAE at various ene molar concentrations of vPOSS-MPA and b) pure vPOSS-MPA.
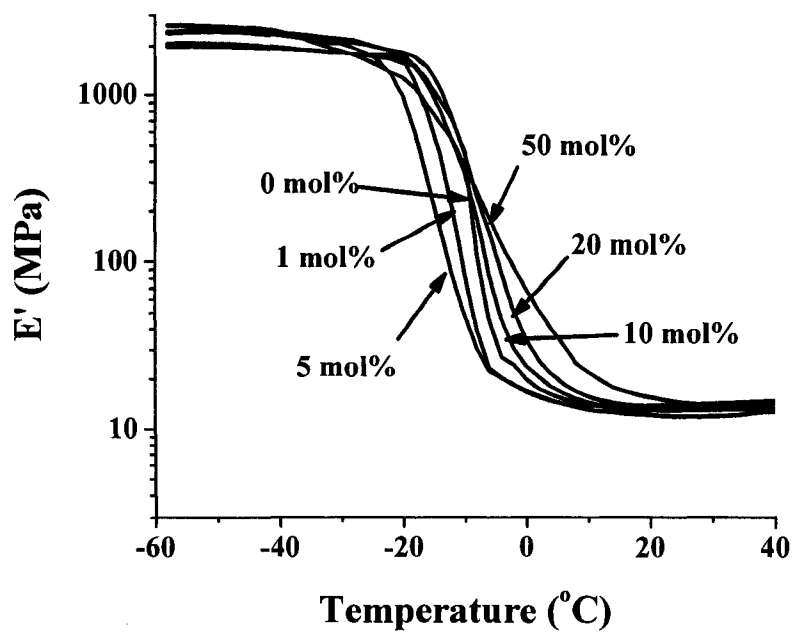
Figure 22. Storage modulus (E') vs. POSS ene mol% for vPOSS-MPA/TriThiol-TAE at various concentrations of vPOSS-MPA.
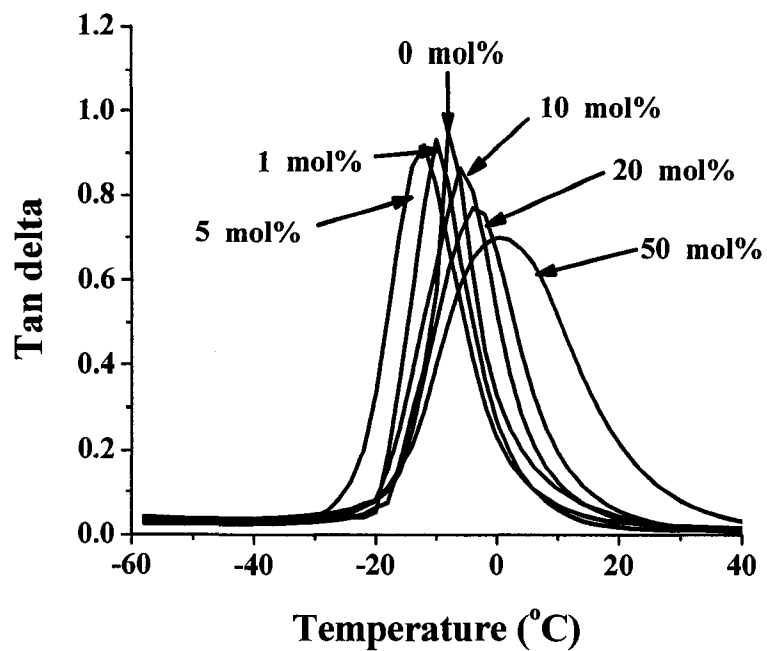
Figure 23. DMA result of loss tangent curves of vPOSS-MPA/TriThiol-TAE at various concentrations of vPOSS-MPA.
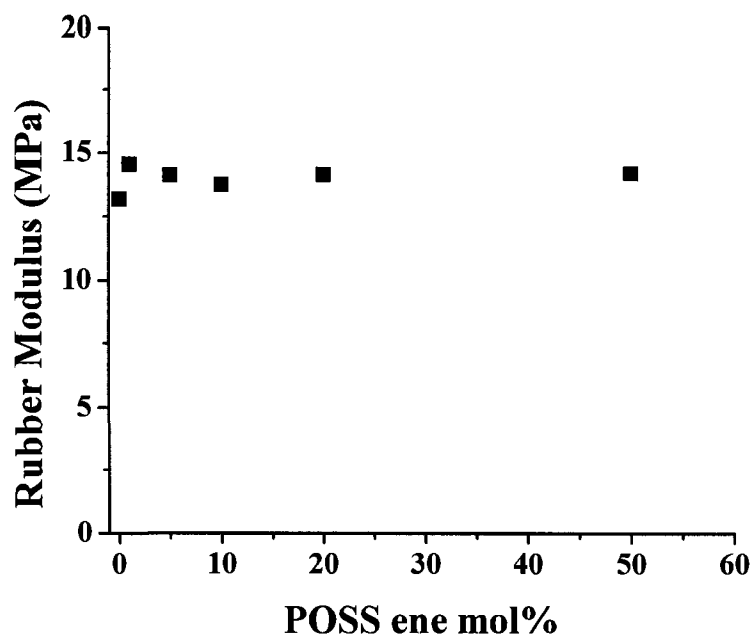
Figure 24. Rubber modulus vs. POSS ene mol% for vPOSS-MPA/TriThiol-TAE at various concentrations of vPOSS-MPA.

(a)

(b)
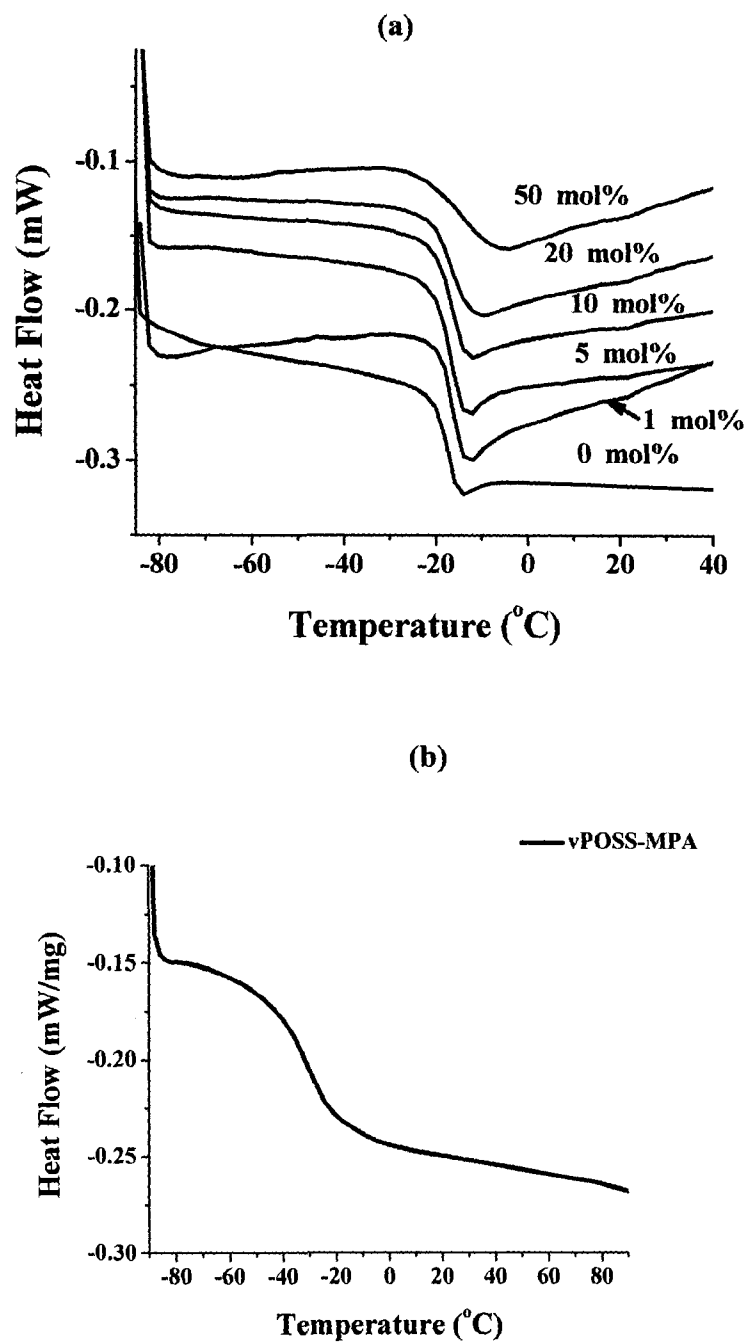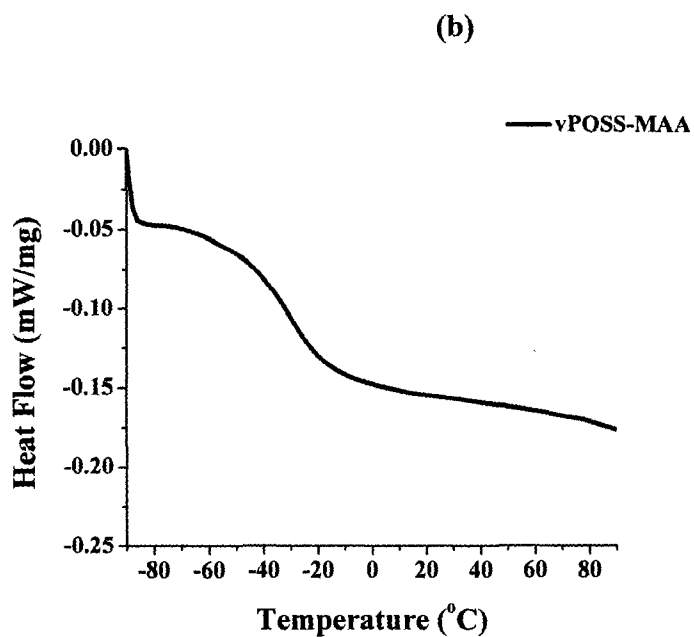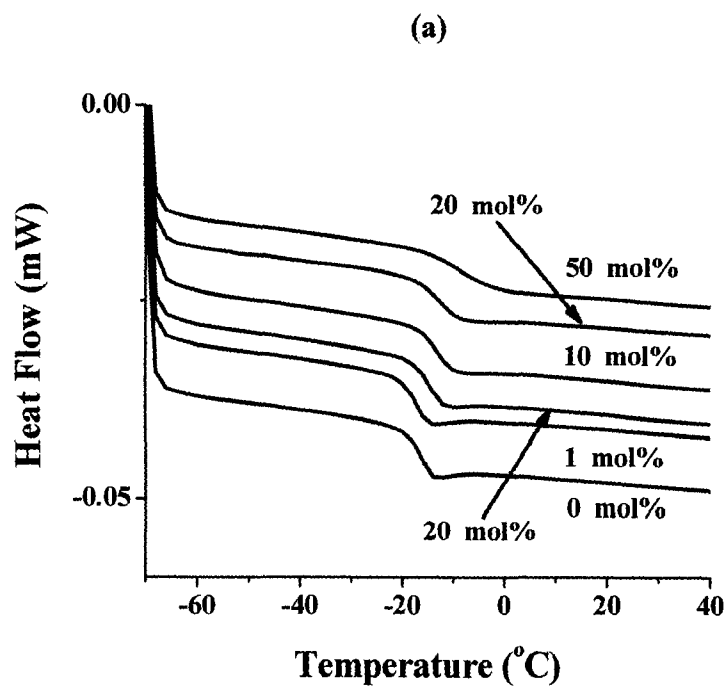

Figure 25. DSC curves of a) vPOSS-MAA/TriThiol-TAE at various ene molar concentrations of vPOSS-MAA and b) pure vPOSS-MAA monomer.
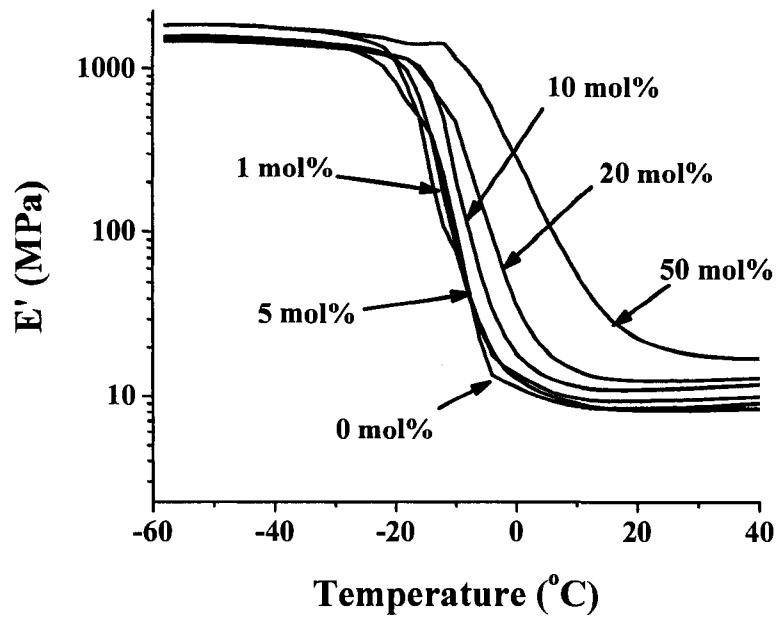
Figure 26. Storage modulus (E') vs. POSS ene mol% for vPOSS- MAA/TriThiol-TAE at various concentrations of vPOSS-MAA.
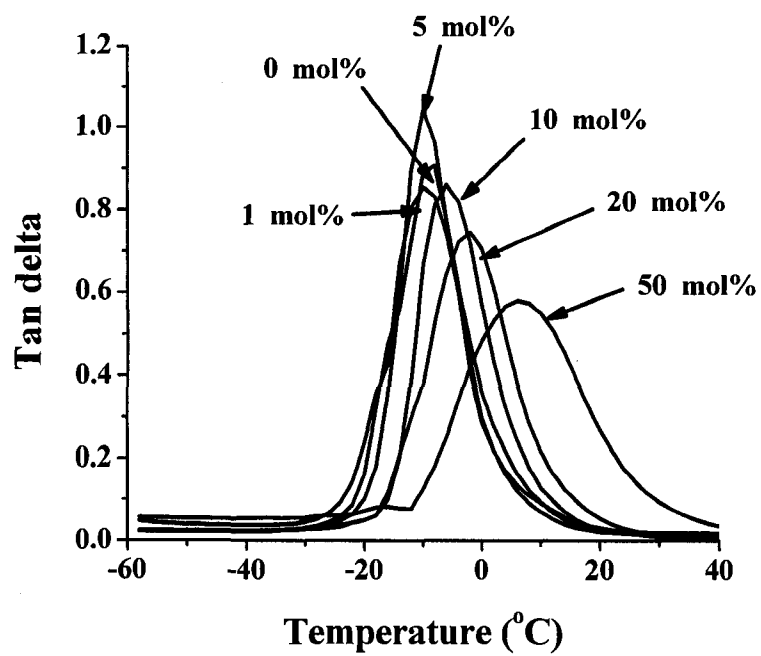
Figure 27. DMA result of loss tangent curves of vPOSS- MAA /TriThiol-TAE at various concentrations of vPOSS-MAA.
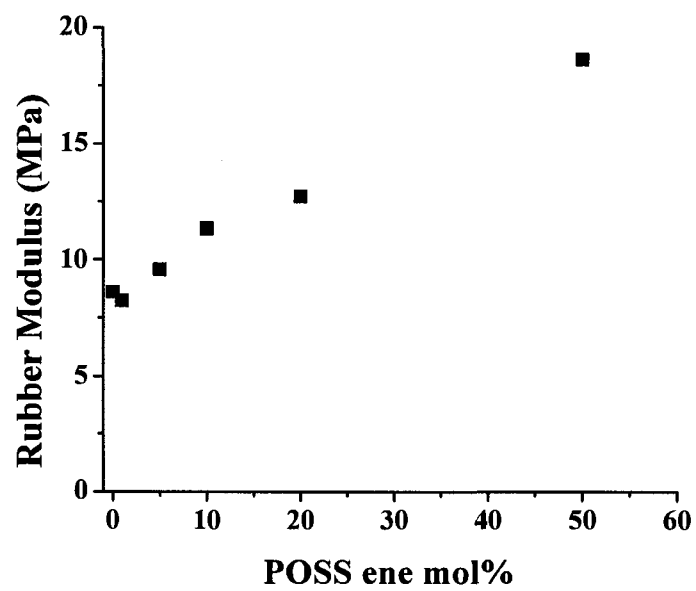
Figure 28. Rubber modulus vs. POSS ene mol% for vPOSS- MAA/TriThiol-TAE at various concentrations of vPOSS-MAA.
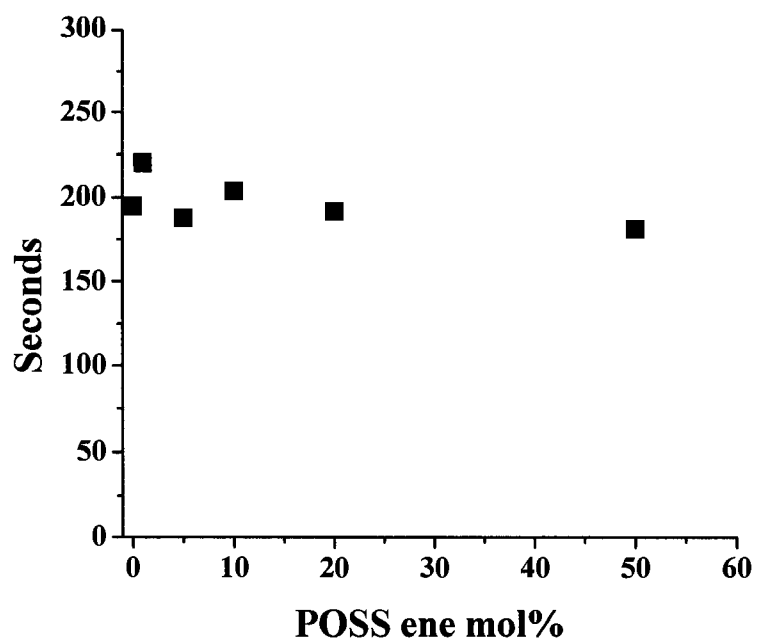
**Figure 29.** Plot of Persoz pendulum hardness (Oscillation (seconds) vs. POSS ene mol%) for vPOSS-MPA/TriThiol-TAE at various concentrations of vPOSS-MPA.
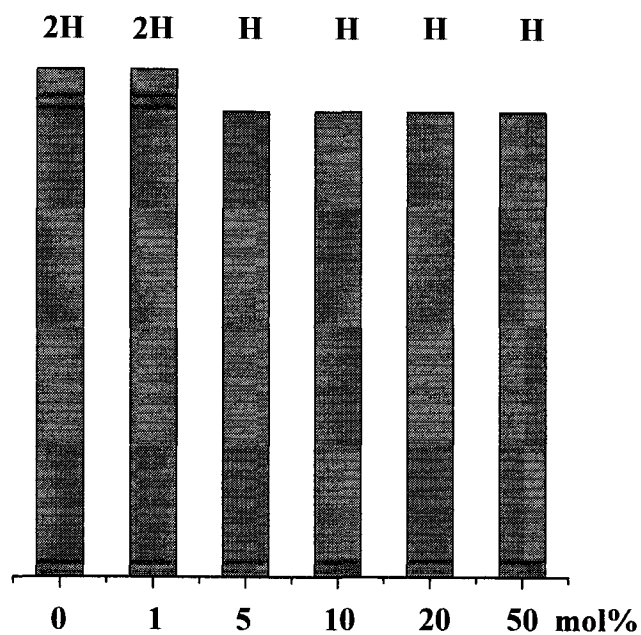
Figure 30a. Diagram of pencil hardness for vPOSS-MPA/TriThiol-TAE at various concentrations of vPOSS-MPA.
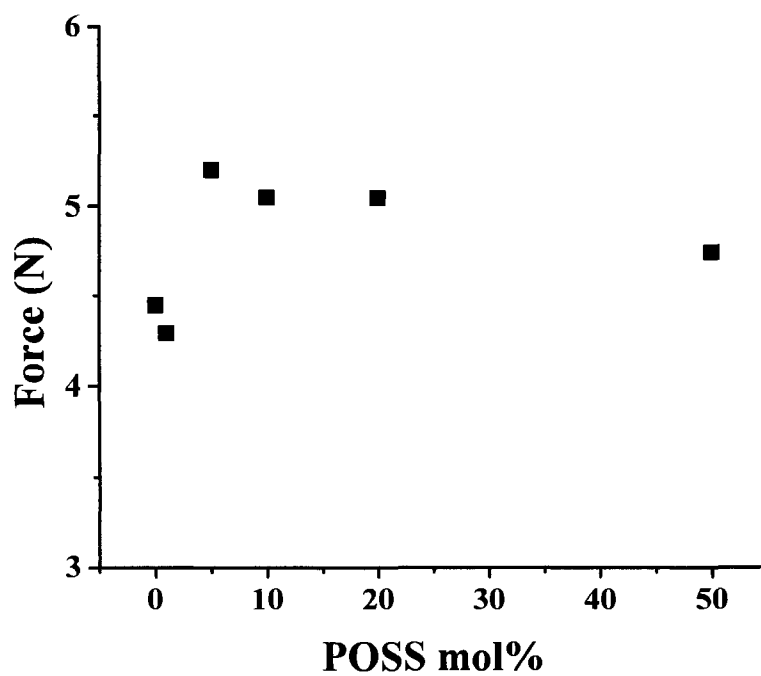
Figure 30b. Plot of Shore A durometer hardness (Force vs. POSS mol%) for vPOSS-MPA/TriThiol-TAE at various concentrations of vPOSS-MPA.
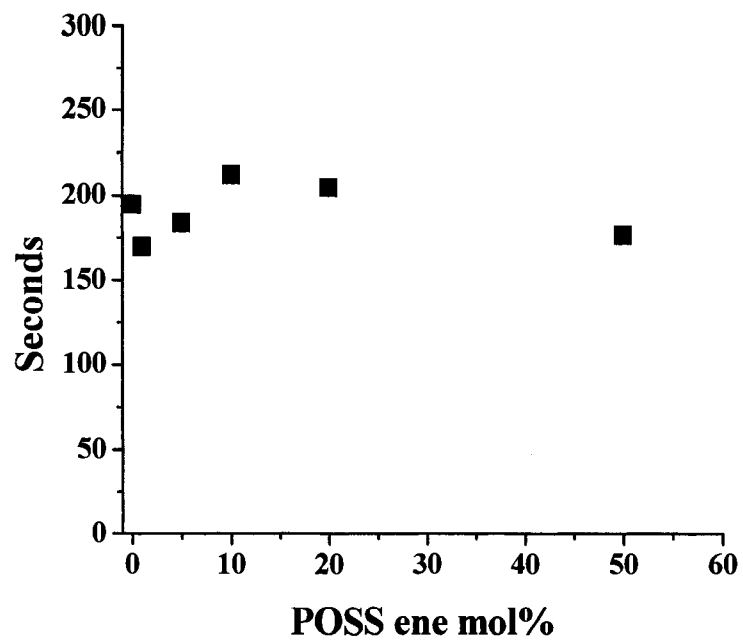
Figure 31. Plot of Persoz pendulum hardness (Oscillation (seconds) vs. POSS ene mol%) for vPOSS- MAA/TriThiol-TAE at various concentrations of vPOSS-MAA.
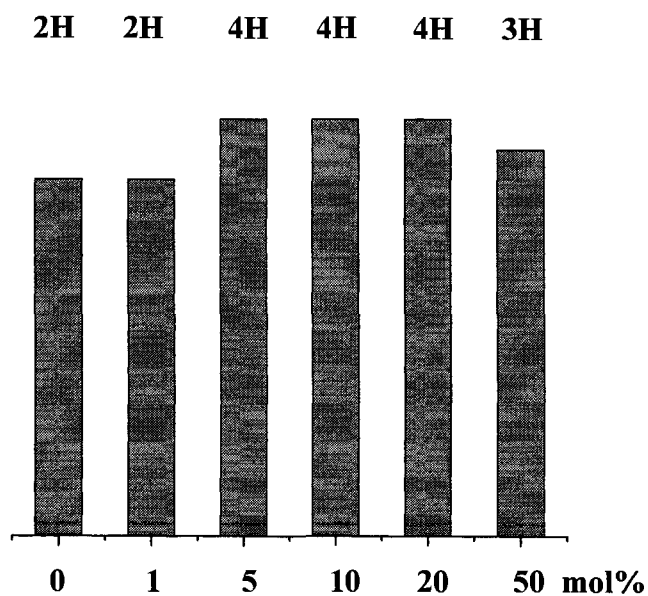
Figure 32a. Diagram of pencil hardness for vPOSS- MAA/TriThiol-TAE at various concentrations of vPOSS-MAA.
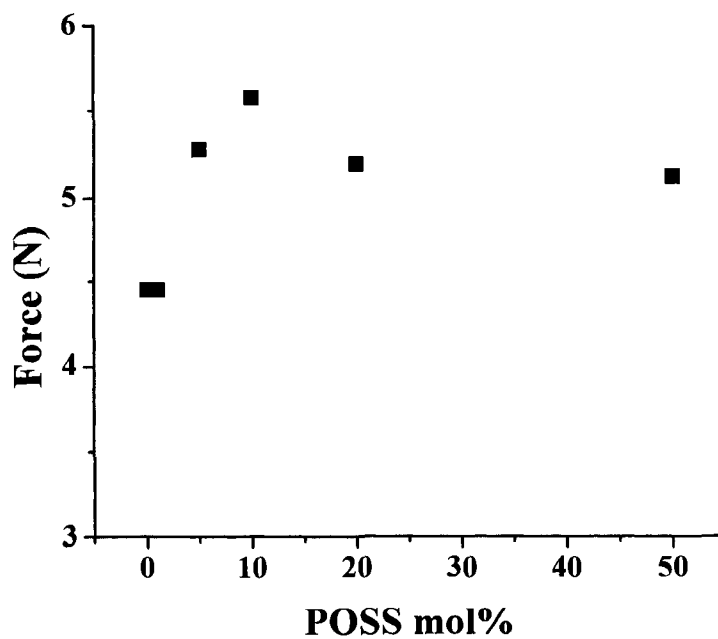
Figure 32b. Plot of shore A durometer hardness (Force vs. POSS ene mol%) for vPOSS-MAA/TriThiol-TAE at various concentrations of vPOSS-MAA.
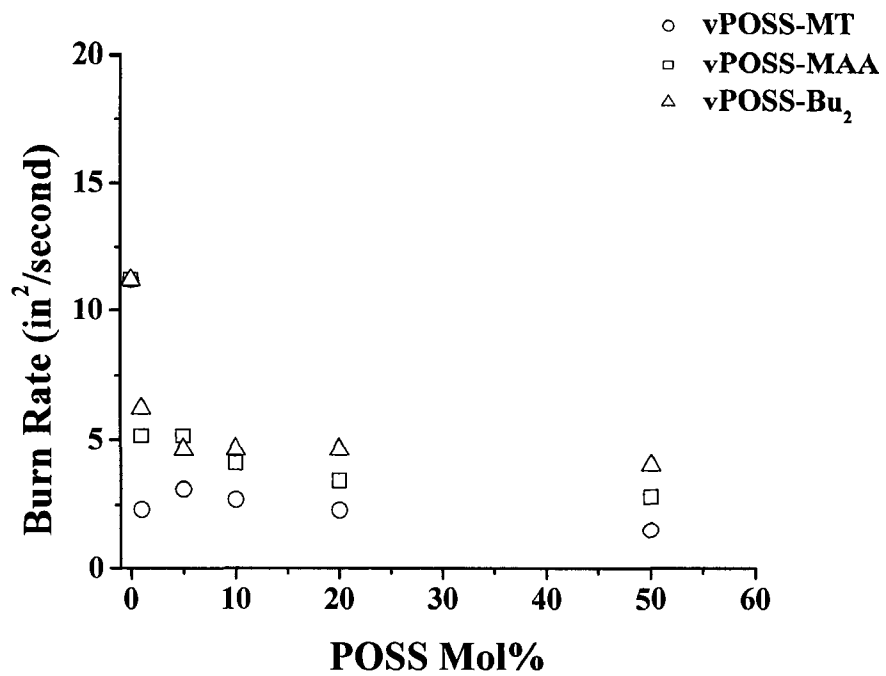
Figure 33. Plot of Burn rates vs. POSS mol% for vPOSS-MT, vPOSS-MAA, and vPOSS-Bu$_2$ at 0, 1, 5, 10, 20, and 50 mol% having a sample thickness of 250 microns.
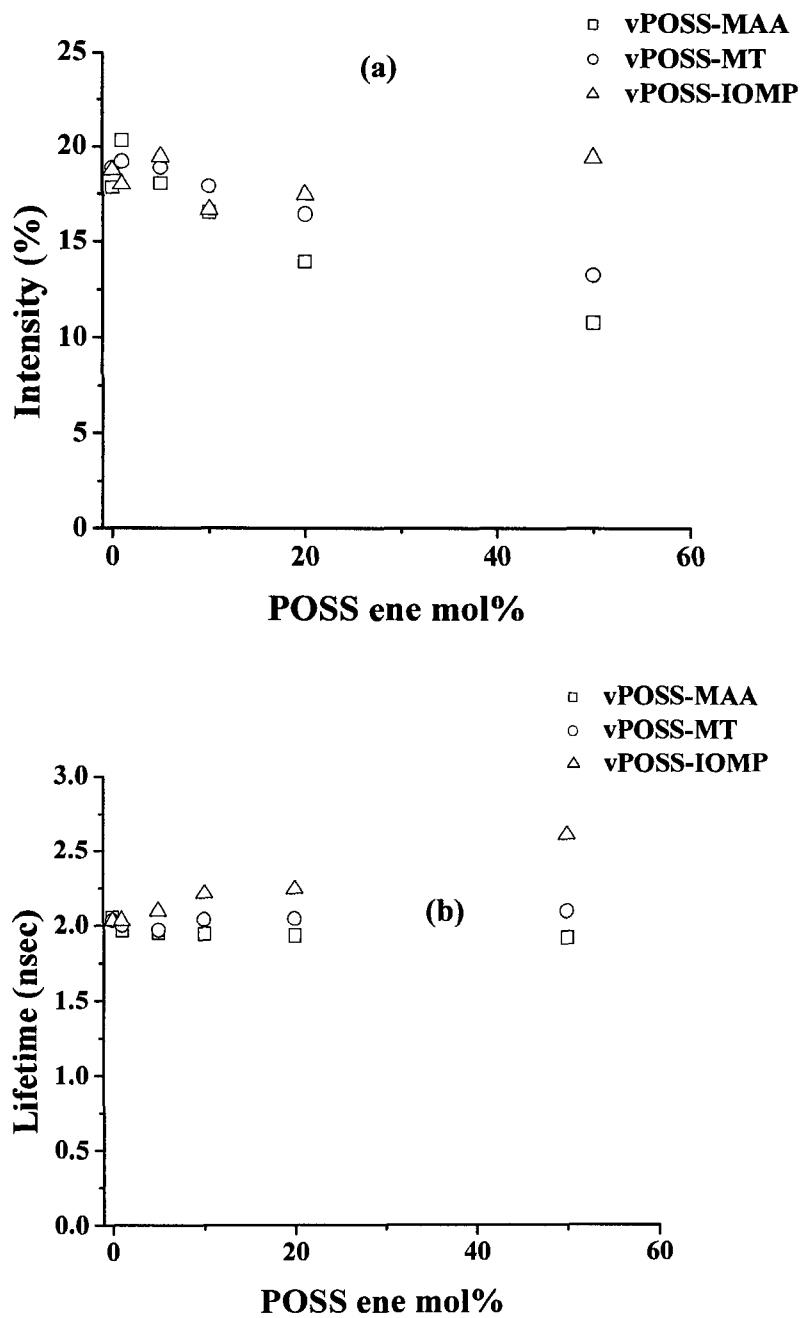
Figure 34. Plot of a) Decay intensity vs. POSS ene mol% and b) Lifetime vs. POSS ene mol% for vPOSS-MAA, vPOSS-MT, and vPOSS-IOMP at various concentrations.
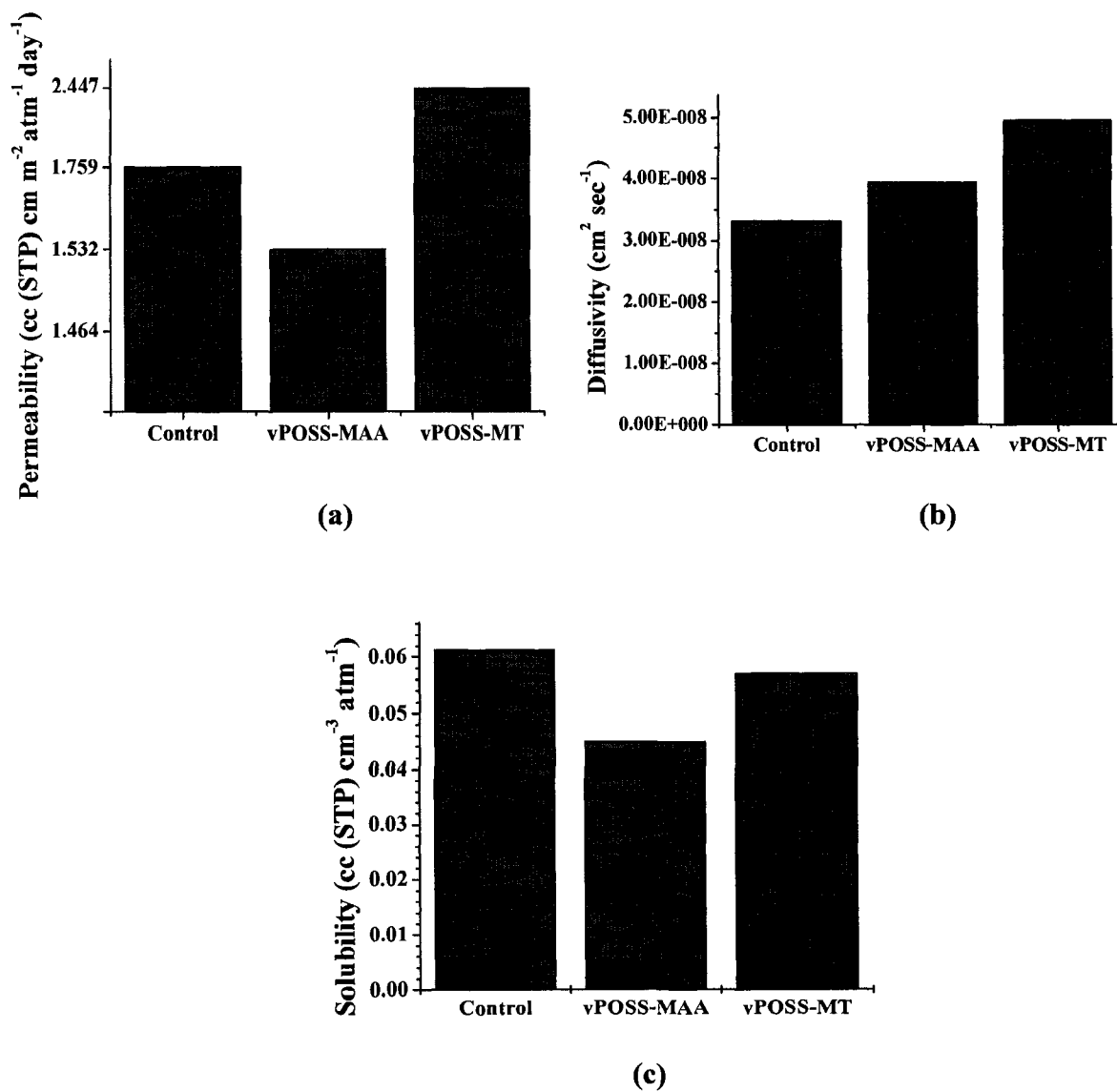
Figure 35. Oxygen flux parameters for a) permeability, b) diffusivity, and c) solubility constants for neat TriThiol-TAE, vPOSS-MAA, and vPOSS-MT.

(a)

(b)

(c)

(d)

(e)

(f)
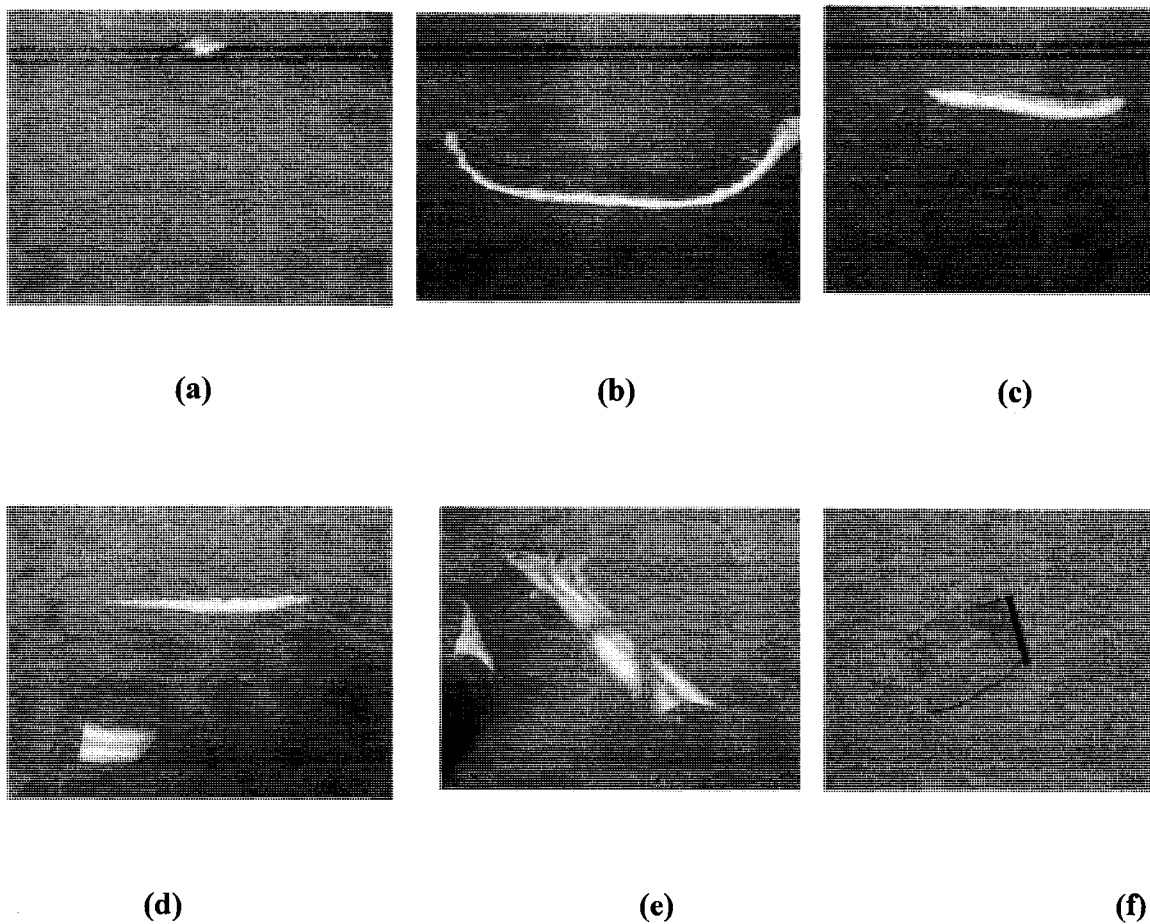
Picture 1. Pictorial illustrations of vPOSS-MT/TriThiol-TAE copolymers. a) neat TriThiol-TAE, b) 1 mol% vPOSS-MT/TriThiol-TAE, c) 5 mol% vPOSS-MT/TriThiol-TAE, d) 10 mol% vPOSS-MT/TriThiol-TAE, e) 20 mol% vPOSS-MT/TriThiol-TAE, and f) 50 mol% vPOSS-MT/TriThiol-TAE. Sample thickness is ~250 microns.

(a) (b) (c)

(d) (e) (f)
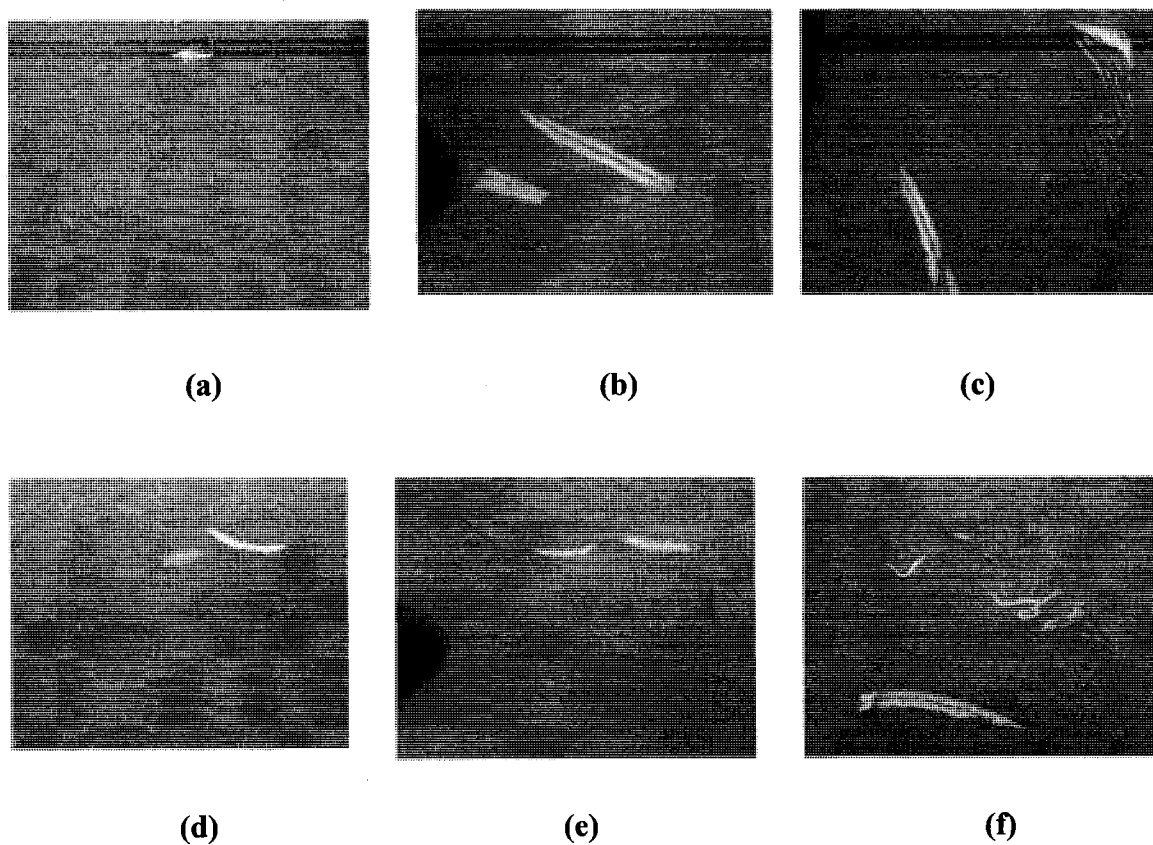
Picture 2. Pictorial illustrations of vPOSS-IOMP/TriThiol-TAE copolymers. a) neat TriThiol-TAE, b) 1 mol% vPOSS-IOMP/TriThiol-TAE, c) 5 mol% vPOSS-IOMP/TriThiol-TAE, d) 10 mol% vPOSS-IOMP/TriThiol-TAE, e) 20 mol% vPOSS-IOMP/TriThiol-TAE, and f) 50 mol% vPOSS-IOMP/TriThiol-TAE. Sample thickness is ~250 microns.

(a)   **(b)**   **(c)**

(d)   **(e)**   **(f)**
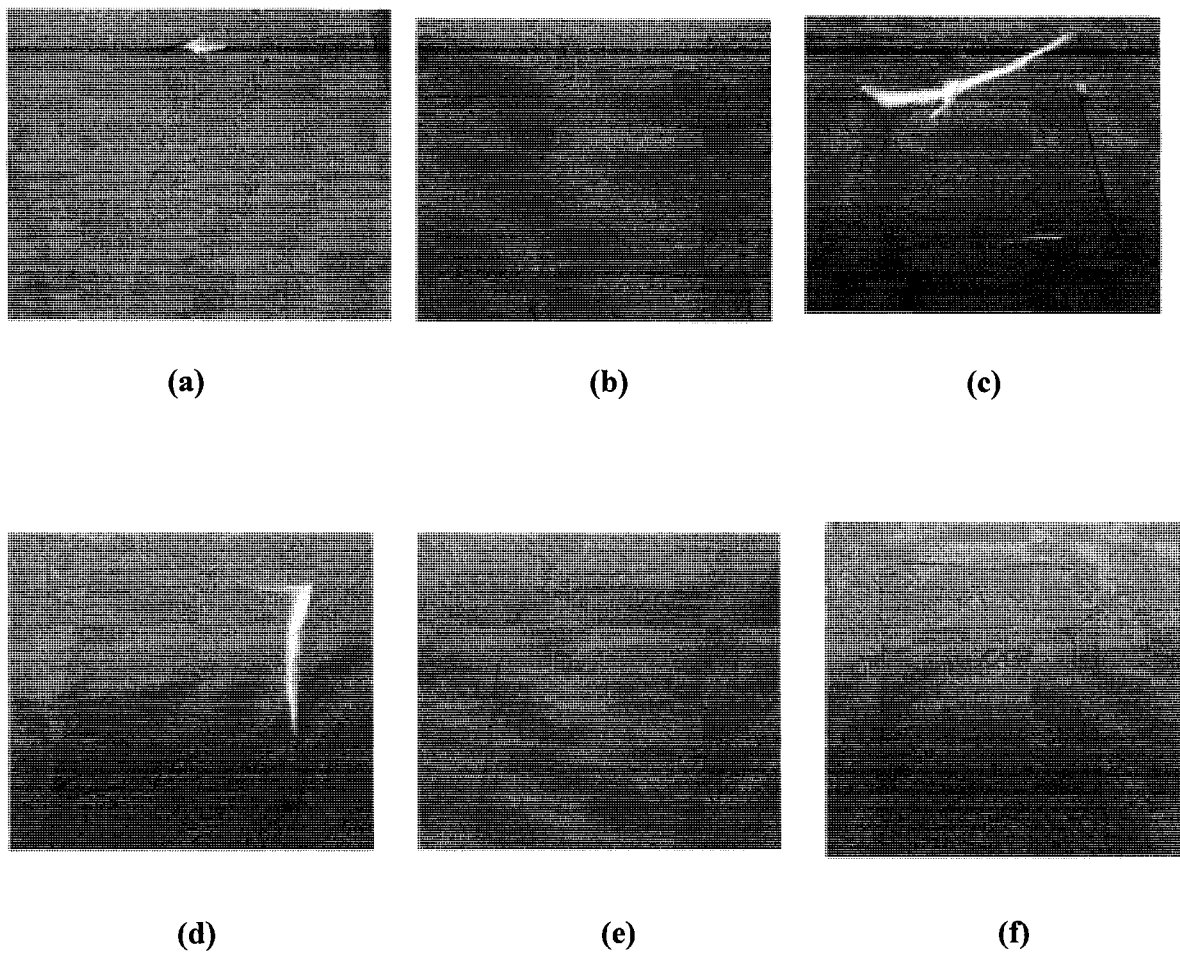
Picture 3. Pictorial illustrations of vPOSS-MPA/TriThiol-TAE copolymers. a) neat TriThiol-TAE, b) 1 mol% vPOSS-MPA/TriThiol-TAE, c) 5 mol% vPOSS-MPA/TriThiol-TAE, d) 10 mol% vPOSS-MPA/TriThiol-TAE, e) 20 mol% vPOSS-MPA/TriThiol-TAE, and f) 50 mol% vPOSS-MPA/TriThiol-TAE. Sample thickness is ~250 microns.

(a) **(b)** **(c)**

(d) **(e)** **(f)**
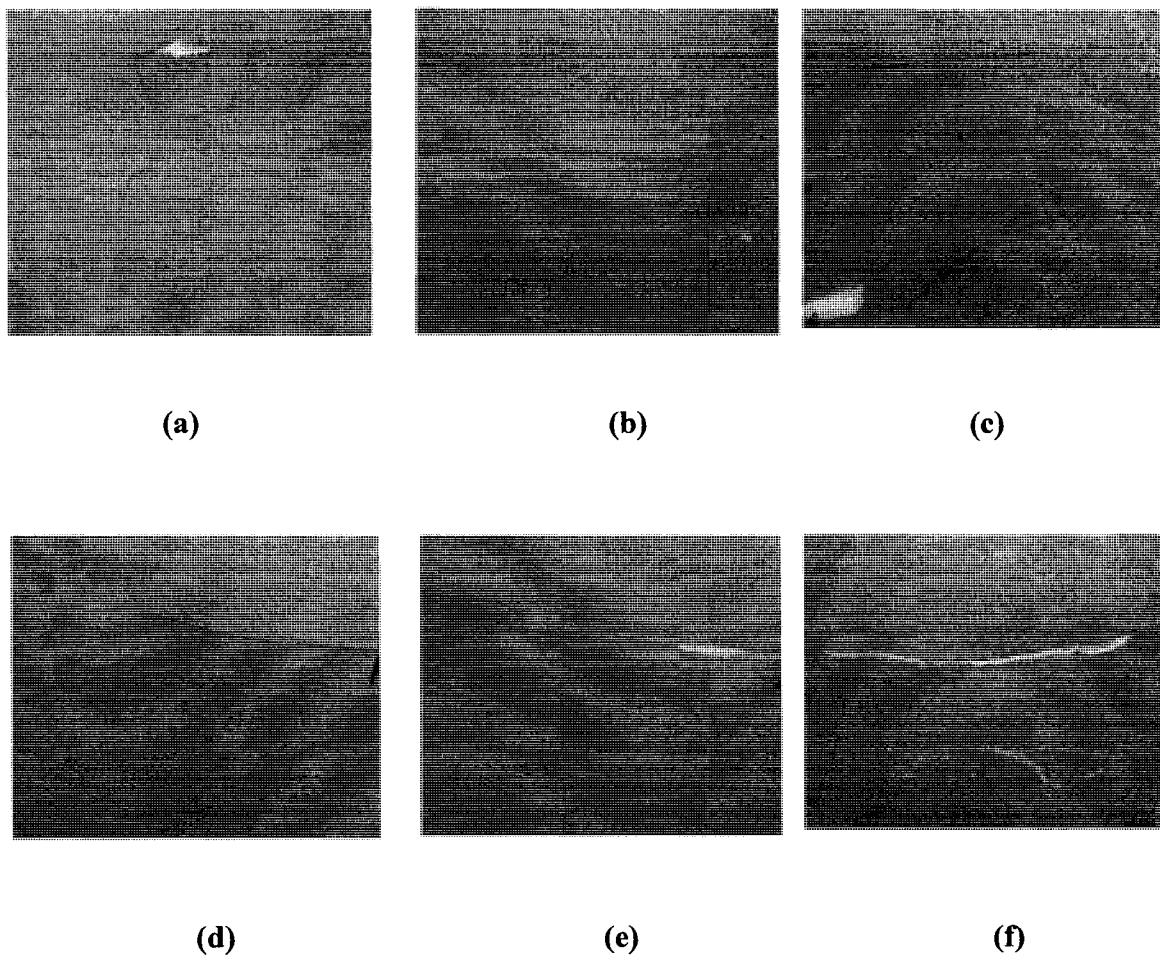
Picture 4. Pictorial illustrations of vPOSS-MAA/TriThiol-TAE copolymers. a) neat TriThiol-TAE, b) 1 mol% vPOSS-MAA/TriThiol-TAE, c) 5 mol% vPOSS-MAA/TriThiol-TAE, d) 10 mol% vPOSS-MAA/TriThiol-TAE, e) 20 mol% vPOSS-MAA/TriThiol-TAE, and f) 50 mol% vPOSS-MAA/TriThiol-TAE. Sample thickness is ~250 microns.

CHAPTER VII

THE STRUCTURAL EFFECTS OF ENE GROUPS ON THE KINETICS OF THE

AMINE-CATALYZED THIOL-MICHAEL REACTION

ABSTRACT

A model study of the amine-catalyzed Michael-type thiol-ene reaction was conducted to determine the structural effects of an ene group (i. e. the electron density) reaction with a monofunctional thiol, ethyl 3-mercaptopropionate. The series of monofunctional ene groups can be classified as electron-rich, electron-poor, and resonance-stabilized double bonds. The amine-catalyzed thio-Michael reaction showed significant reactivity with ethyl acrylate, vinyl acrylate, and vinyl methacrylate, whereas no reactions (under the conditions used) were observed for thiol with butyl vinyl ether and 1-hexene. Limited reaction was observed for ethyl methacrylate, vinyl decanoate, and N-vinyl pyrrolidinone. The reactivity of the amine-catalyzed thio-Michael reaction definitely correlated with the ene electron density.

INTRODUCTION

In general, the order of catalytic reactivity observed for an amine-catalyzed Michael type thiol-ene reaction is based upon the amine type used (1° > 2° > 3°) when a thiol is reacted with an electron-poor ene double bond in a thio-Michael addition reaction.[1] The role of the amine catalyst is not fully understood, although two mechanisms for the proposed role of the amine have been suggested. The amine catalyst may initiate thiol addition to a double bond by either nucleophilic attack of the ene double bond to form a zwitterion (Scheme 1)[2, 3, 4] followed by reaction of the thiol with the zwitterion or by proton transfer from the thiol to the amine via an acid base reaction to form the thiolate anion (Scheme 2).[5, 6] Further study is necessary to elucidate the exact role of the amine catalyst in the thio-Michael reaction: this is not the subject of the present investigation in this chapter. For both proposed chemical processes, the role of the double bond plays a vital role in the reactivity between the ene and the thiol: this is explored in this short chapter. Specifically, the electronic nature and reactivity of the ene was studied by measuring the real-time reaction rate between the thiol and various electron-rich, electron-poor and styrenic enes.

EXPERIMENTAL

Real-time IR analysis was performed on an IFS-88 Bruker spectrometer to obtain the actual conversions of thiol and ene groups versus time. The decrease of peaks

assigned to the thiol (2570 cm^{-1}) and ene groups (1620 cm^{-1} (styrenic), 1640 cm^{-1} (vinyl ether), and 1620 cm^{-1} (acrylate)) was monitored over a specific time period (300 seconds) at a scan rate of 0.5 scans/sec (1 scan/2 sec). For each amine-catalyzed thio-Michael addition reaction, reaction mixtures were prepared containing equal molar amounts of thiol and ene monomers (9 x 10^{-4} mol) along with 0.2 mol% amine diethyl amine catalyst based upon the molarity of the thiol. The components of the reaction mixtures were ethyl 3-mercaptopropionate, vinyl acrylate, vinyl methacrylate, ethyl acrylate, ethyl methacrylate, styrene, 1-methoxy-4-vinyl benzene, butyl vinyl ether, N-vinyl pyrrolidinone, 1-hexene, vinyl decanoate, and diethyl amine and used as received from Aldrich. The reaction rate (R$_{rxn}$) was determined as the slope of the percent versus time plots and final functional group conversions were determined by the maximum of each plot.

Sample preparation

The preparation of the reaction formulation followed a sequence in which the addition of the amine to the thiol monomer was completed prior to mixing the thiol with the ene monomer. After thorough mixing, the thiol/ene/amine reaction mixture was then put between two NaCl plates and placed in the sample holder for 60 sec before time-resolved IR scanning of the reaction began. The sample thickness for each reaction was ~25 microns.

RESULTS AND DISCUSSION

The model systems (monofunctional) for the amine-catalyzed thiol-ene

polymerization involve equal molar concentrations of ethyl 3-mercaptopropionate (EMP)

with ethyl acrylate (EAcr), ethyl methacrylate (EMAcr), vinyl acrylate (VAcr), vinyl

methacrylate (VMAcr), styrene (Sty), 1-methoxy-4-vinyl-benzene (4VA), N-vinyl

pyrrolidinone (NVP), 1-hexene (HEX), vinyl decanoate (VD), and butyl vinyl ether (BE)

catalyzed by 0.2 mol% diethyl amine (DEA). The structures and acronyms of each

component are found in Figure 1. The reactions were monitored in situ using a real-time

IR (RTIR) scanning technique to measure thiol and vinyl group loss simultaneously in

real time. The consumption of thiol and ene groups were measured at 2570 cm^{-1} for the

thiol group and 1620 cm^{-1} (acrylate), 1640 cm^{-1} (BVE, HEX, and VD), and 1630 cm^{-1}

(Sty and 4VA) for the vinyl group.

As previously mentioned, the role of the amine catalyst is not fully understood,

and two mechanisms for the proposed role of the amine have been suggested. Possibly,

the amine catalyst may initiate thiol addition to a double bond by either nucleophilic

attack of the ene double bond by the amine to form a zwitterion (Scheme 1) followed by

proton transfer from the thiol or by an acid base proton transfer from the thiol to form the

thiolate anion (Scheme 2) with subsequent of the thiolate anion with the ene. For this

study, based on other unpublished results we propose that thiol addition is initiated by

nucleophilic attack of the double bond by the amine catalyst followed by proton transfer

of the thiol and subsequent addition of the thiolate anion to the unsubstituted carbon of

the ene group with simultaneous displacement of the amine. In this mechanism, as we have already stated upon attack of the ene group by the nucleophilic amine, an equilibrium is established between the zwitterion and the reactants (amine, thiol). The equilibrium constant should be dependent upon the electron density of the ene double bond. Thus, it would be expected that electron poor enes would result in higher equilibrium constants and ultimately faster rates for addition of the thiol to the ene assuming that the proton transfer rate from the thiol to the zwitterion would be rapid.

Reactions of electron-poor enes, including ethyl acrylate (EAcr), ethyl methacrylate (EMAcr), vinyl acrylate (VAcr), and vinyl methacrylate (VMAcr), with ethyl 3-mercaptopropionate (EMP) showed varying rates (R_{rxn}) and functional group conversions suggesting that the structural differences among the electron-poor enes affects the reactivity of the amine-catalyzed Michael type thiol-ene reaction. Comparatively, R_{rxn} and functional group conversion followed the order: EAcr > VMAcr >> EMAcr as shown in Figure 2, i.e R_{rxn} was 0.58 s^{-1}, 0.63 s^{-1}, and 0. 053 s^{-1} and functional group conversion was 80%, 63%, and 15%, respectively. The reaction of VAcr was so fast that the reaction was completed before measurements could be recorded; and the IR scan of the fully reacted EMP/VAcr mixture showed no absorption at 2570 cm^{-1} and 1620 cm^{-1} on the first scan indicating that both groups were completely consumed (Figure 3). Therefore, the reactivity of electron-poor enes was: VAcr > EAcr > VMAcr >> EMAcr. There is no question that the structure of the ene bond greatly influenced the reactivity of the amine with the acrylate and methacrylate double bonds. For both the acrylate and the methacrylate monomers, the presence of the vinyl group enhanced the rate with the thiol. It is speculated that this is due to the low electron density of the

(meth)acrylate as a result of conjugation with the electron withdrawing vinyl ester group. Also it is noted in general that the methacrylate reactions are much slower than the corresponding acrylates since in each case the methacrylate double bond is more electron dense than the acrylate double attributable to the electron donating methyl group. In Figures 4 and 5, the % conversion vs. time plot of the reaction of EMP with BVE and EMP and HEX showed no reaction between thiol and vinyl groups, respectively, i.e. no loss of vinyl or thiol peaks was measured during the scanning period, thus confirming that the addition of thiol across a double bond by an amine catalyst does not occur with electron rich enes. Conversely, the reaction of EMP with VD and NVP (Figure 6) showed reactivity between the thiol and ene having $R_{rxn} = 0.040$ s^{-1} and 0.05 s^{-1} and functional group conversions of 5% and 15%, respectively. Structurally, VD and NVP are not as electron rich as vinyl ethers and substituted alkenes. Note that R_{rxn} and functional group conversions for NVP and VD were comparable to kinetic parameters for EMAcr suggesting that the vinyl groups have comparable reactivity with EMAcr, an electron-poor ene.

Hitherto, this model study has investigated the reaction of thiol with electron-rich and electron-poor enes adjacent to varying activating and deactivating groups. Reactions of thiol with a styrenic double bond were also examined to observe the effect of resonance stabilization on the kinetics of an amine-catalyzed Michael-type thiol-ene reaction including styrene (Sty) and 1-methoxy-4-vinyl benzene (4VA), which contains an electron-donating group in the para position. For each reaction, the kinetic plots (Figures 7 and 8) showed no reaction between the thiol and the styrenic double bond, i.e,

no consumption of thiol and the corresponding ene was measured. Presumably the intermediate zwitterions are not stable in this case.

CONCLUSION

A time-resolved IR study of the reaction of EMP with various ene groups showed that the rate of thiol addition (R_{rxn}) and functional group conversion were strongly influenced by the ene type and structure. Mechanistically, it was assumed that amine catalysis was initiated by the nucleophilic attack of the double bond subsequent to thiol addition. Overall, the reaction of thiol with an ene via amine catalysis is highly dependent upon the electron density of the double bond. The order of reactivity for acrylate/methacrylate systems was VAcr > EAcr > VMAcr >> EMAcr suggesting that structural effects greatly influences ene reactivity with the amine catalyst. The functional group conversions of VAcr and VMAcr were significantly higher than the ethyl analogs of the reactants. The presence of an sp^2-hybridized bond in VAcr and VMAcr decreased the electron density of the acrylate bond thus rendering the reactants more susceptible to the amine catalyzed thio-Michael addition. Reactions of EMP with electron-rich enes varied with the ene structure. Reaction of EMP with BVE and HEX showed no reactivity between the thiol and vinyl groups as a result of the high electron density of the double bond. However, reaction of EMP and VD and NVP, respectively, showed some reactivity between the thiol and vinyl bond groups. It is spectulated that the presence of an adjacent carbonyl group reduces the electron density of the vinyl group (though the vinyl groups

were analogs of the vinyl ether group in BE) possibly resulting from stabilization of the

dipole moment caused by field effects. Also, no reaction was observed between EMP

and either Sty or 4VA.

REFERENCES

[1] Van Dijk, J. and Theodorus, M., *PCT*, WO 0064959, **2000**.

[2] Klemarczyk, P., *Polym.*, **2001**, *42*, 2837-2848.

[3] Lewandowska, E., *Tetrahedron*, **2006**, 4879-4883.

[4] Gimbert, C.; Lumbierres, M.; Marchi, C.; Moreno-Manas, M.; Sebastian, R. M.; and Vallribera, A. *Tetrahedron*, **2005**, *61*, 8598-8605.

[5] Zienty, F. B.; Vineyard, B. D.; and Schleppnik, A. A.; *J. Org. Chem.*, **1962**, *27*, 3140-3146.

[6] Dmuchovsky, B.; Vineyard, B. D.; and Zienty, F. B.; *J. Org. Chem.*, **1962**, *86*, 2874-2877.
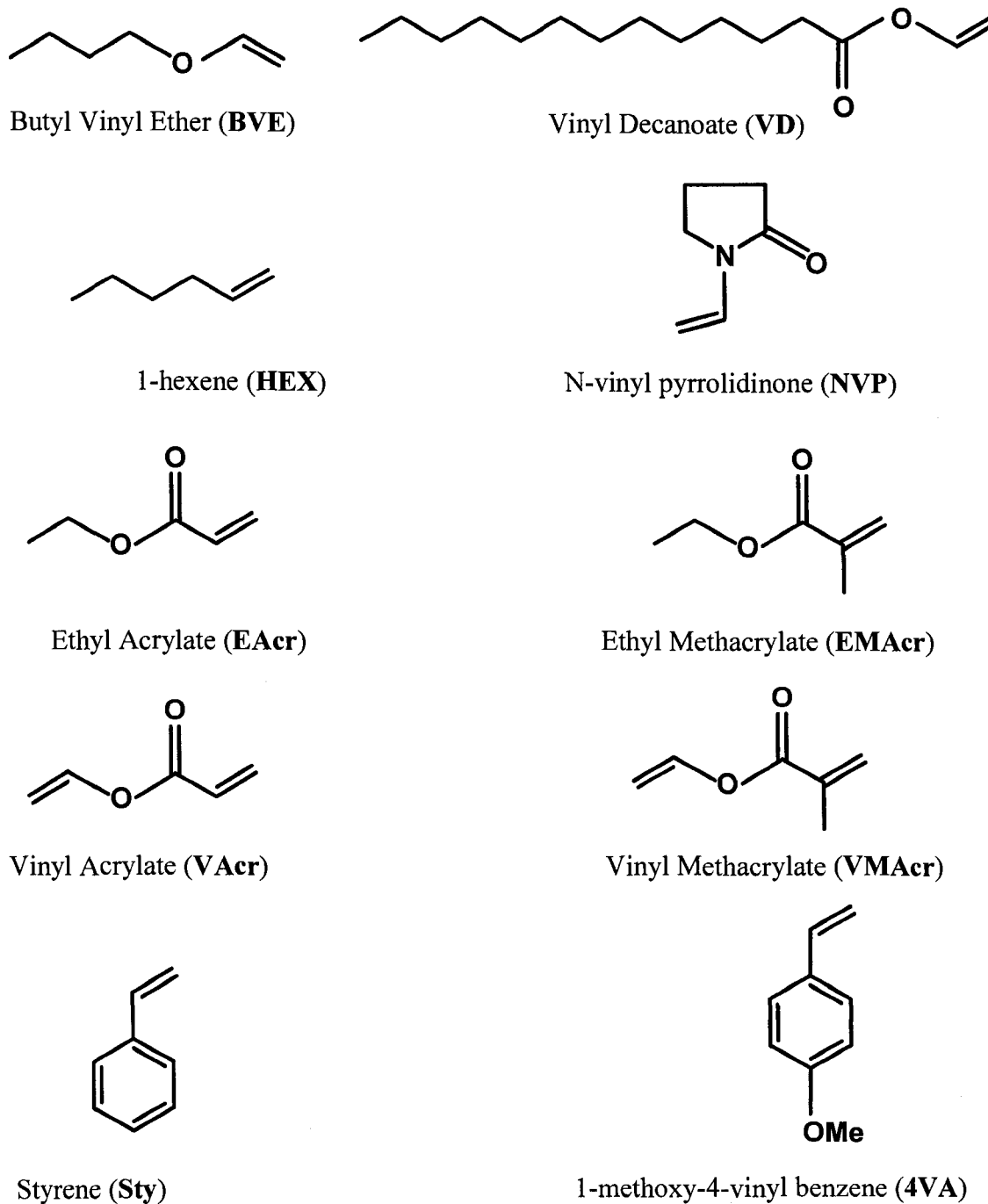
Figure 1. The The chemical structures of the electron-rich, electron-poor, and styrenic ene groups.
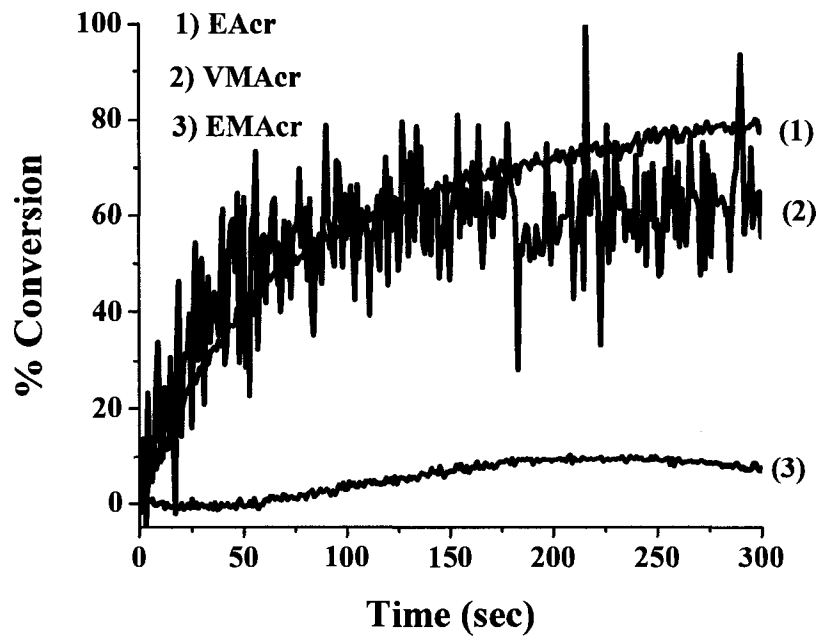
Figure 2. RT-FTIR-based plots of % Conversion vs. Time of the ene group conversions for ethyl acrylate (1620 cm^{-1}), vinyl methacrylate (1620 cm^{-1}), and ethyl methacrylate (1620 cm^{-1}).
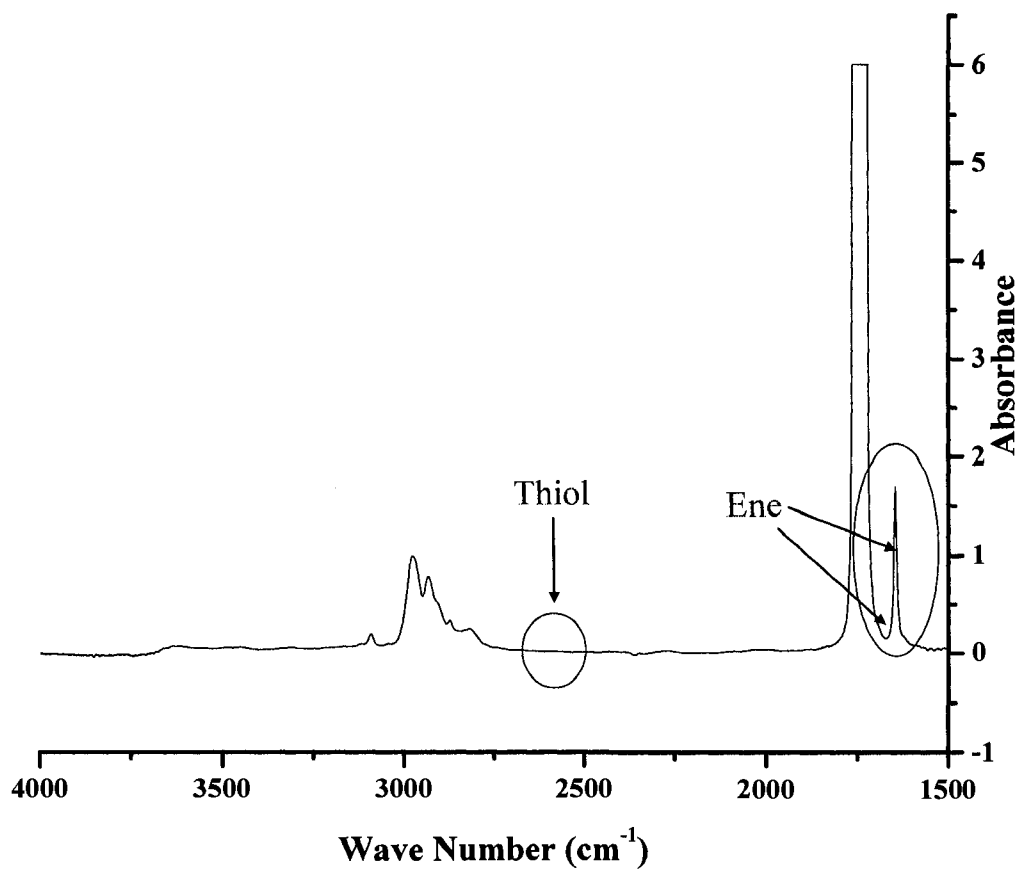
Figure 3. FTIR scan of the fully reacted ethyl 3-mercaptopropionate/vinyl acrylate/diethyl amine reaction mixture with peak depletion occurring at 2570 cm^{-1} for the thiol and 1620 cm^{-1} for the acrylate.
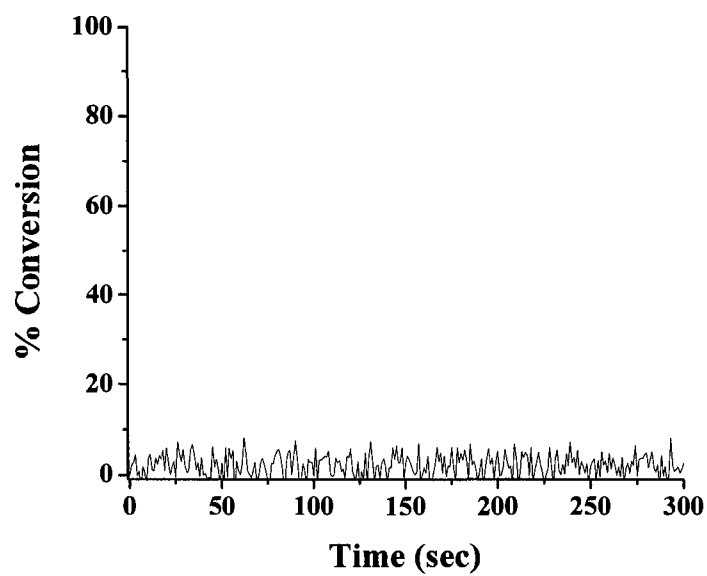
Figure 4. RTIR-based plot of % Conversion vs. Time of the ene group for butyl vinyl ether (1640 cm^{-1}).
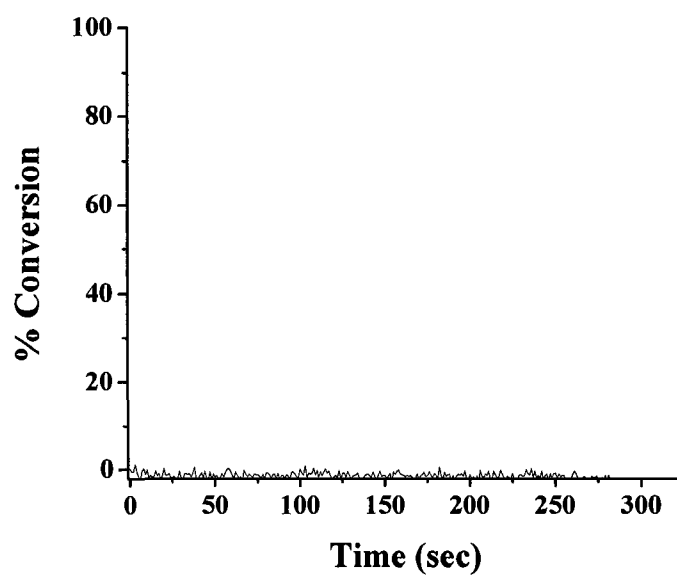
Figure 5. RTIR-based plot of % Conversion vs. Time of the ene group for 1-hexene (1640 cm^{-1}).
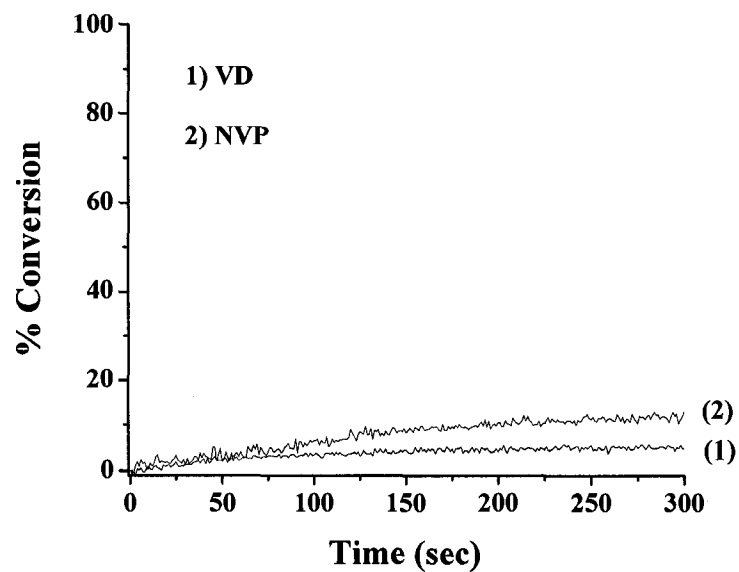
Figure 6. RTIR-based plot of % Conversion vs. Time of the ene group for vinyl decanoate (1640 cm^{-1}) and N-vinyl pyrrolidinone (1640 cm^{-1}).
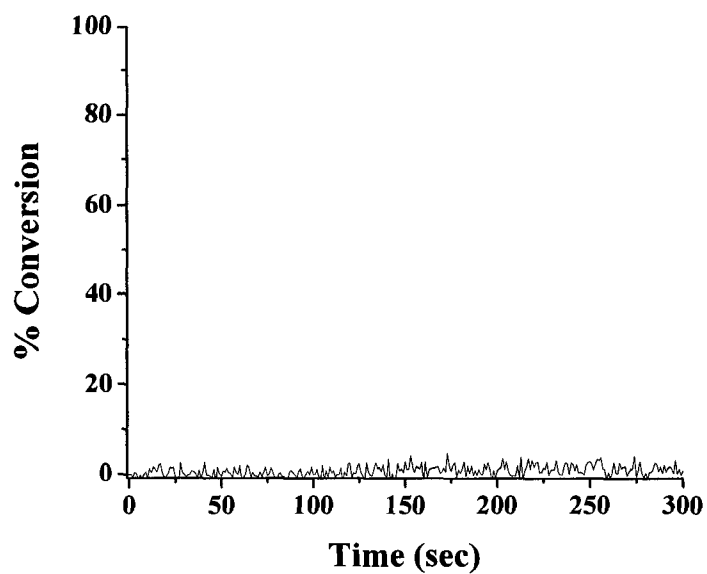
Figure 7. RTIR-based plot of % Conversion vs. Time of the ene group for styrene (1630 cm^{-1}).
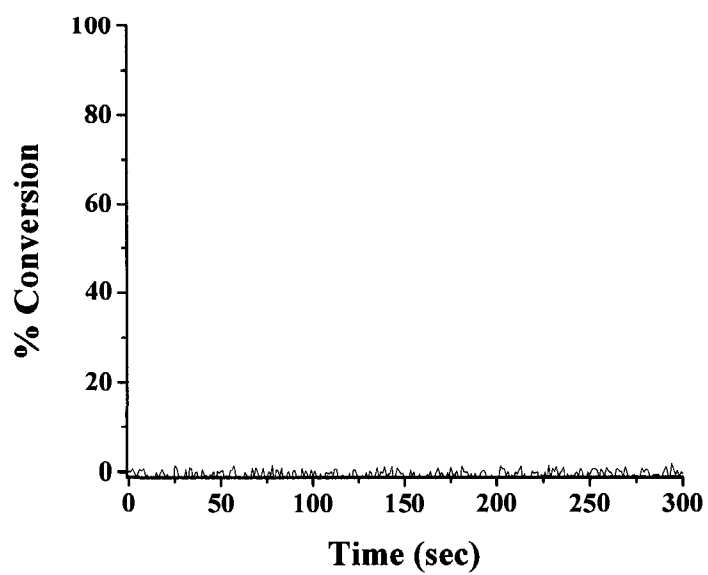
Figure 8. RTIR-based plot of % Conversion vs. Time of the ene group for 1-methoxy-4-vinyl benzene (1630 cm^{-1}).
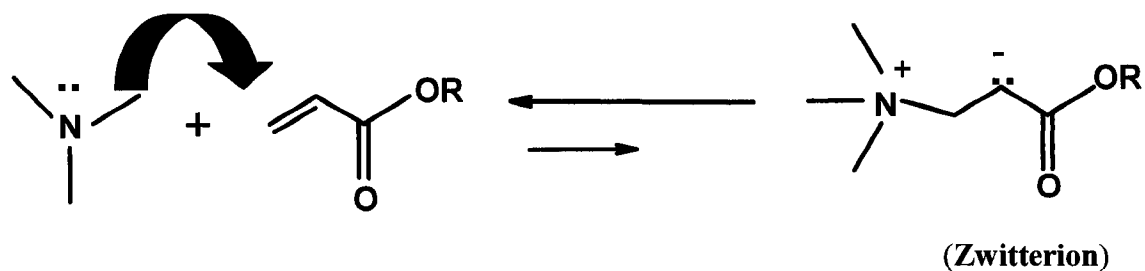
Scheme 1. Proposed mechanism of the nucleophilic attack of the electron-poor double bond by the amine catalyst forming an equilibrium between the reactants and zwitterion.
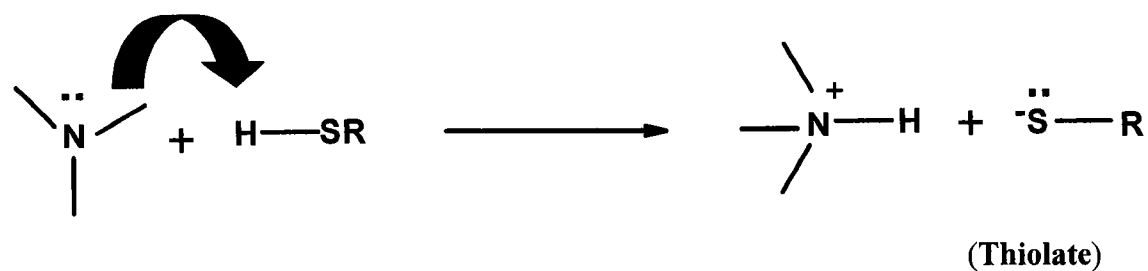
Scheme 2. Proposed mechanism of proton abstraction of the thiol by the amine catalyst forming the thiolate anion.

CHAPTER VIII

CONCLUSIONS

Thiol-ene photopolymers are a unique class of polymers having a highly uniform

crosslinked density and desirable properties such as good adhesion and flexibility.

Advantages of thiol-ene photopolymerizations include fast rates in air conditions,

photoiniatorless polymerizations, low shrinkage, delayed gelation with high monomer

and versatility in ene monomer selection. These advantages can be attributed to the step

growth, free radical, chain transfer mechanism of the thiol-ene polymerization.

Applications of thiol-ene polymers include electronic coatings, adhesives, and optical

lenses. Conversely, thiol-ene polymers are typically soft and thermally unstable materials

that are limited to low temperature applications. The work described in this dissertation

provides information on novel approaches for improving polymer properties while taking

advantage of salient features of the thiol-ene system.

The influence of thiol functionality on network formation was investigated by

observing the polymerization kinetics and thermal and mechanical properties. Kinetic

analysis demonstrated that high conversions ($\geq$ 90%) were attained for highly functional

thiols (f = 2, 3, 4, 5.6, 8.1, and 11) well above the calculated gel points predicted by the

gel point equation. Thermal and mechanical analysis showed that glass transition

temperatures and tensile strength exhibited a linear increase for copolymerization of T2,

T3, and T4 with both multifunctional allyl ether monomers. At higher thiol functionality

($f \geq 5.6$), T_g and tensile strength remain constant with no significant increase in film

properties which, along with high conversions, indicates that formation of the network

structure is effected by the functionality of thiol only for low functional thiols.

Copolymerization of multifunctional thiols resulted in the formation of looped structures and reduced effective network density. Additionally, thiol functionality was shown to have no significant influence on the maximum polymerization rate during polymerization, i.e. the maximum polymerization rate showed marginal differences with respect to increased thiol functionality.

Silicate-based thiol-ene nanocomposites are a novel approach to improving film properties by incorporating organically-modified vinyl POSS within a thiol-ene matrix by physical (blending) or chemical (copolymerization) methods. The physical addition of POSS molecules into the thiol-ene network was proven to be an inefficient method for incorporating POSS into the thiol-ene network. Phase separation was observed for blends containing POSS-iBu (a crystalline solid) and vPOSS-Bu$_1$ (an amorphous liquid) by thermal (DSC) and mechanical (DMA) analysis, i.e. two distinct thermal transitions were observed for POSS-iBu/TriThiol-TAE (T_g = -16 °C and T_m = -60 °C) and vPOSS-Bu$_1$/TriThiol-TAE (T_{g1} = -16 °C and T_{g2} = -75.7 °C) and no observable broadening occurred in the tan delta plots (FWHM) at high concentrations (20 and 50 mo%), thus indicating the incompatibility of POSS-iBu and vPOSS-Bu$_1$ with the TriThiol-TAE network. The glass transitions for pure POSS-iBu and vPOSS-Bu$_2$ occurred at T_m = 60 °C and T_g = -75 °C, respectively. DLS analysis of the prepolymer mixtures demonstrated the strong tendency of POSS toward aggregation, i.e. small particles (~40 nm) were observed for trithiol/triallyl ether solutions containing vPOSS-Bu$_1$, which has substituent groups similar to those found in the TriThiol-TAE backbone, and large particles ($\geq$ 400 nm) were visibly observed for trithiol/triallyl ether solutions containing POSS-iBu. As a result of phase separation for each blended system, small changes in the rubber modulus

(increased for POSS-*i*Bu/TriThiol-TAE and decreased for vPOSS-Bu$_1$/TriThiol-TAE) were observed and scratch resistance and Persoz hardness significantly decreased when POSS concentrations were increased. Also, the polymerization kinetics (polymerization rate and conversions) were unaffected by the presence of solid- or liquid-phase separated POSS. The phase-separated POSS molecules had no apparent effect on the network formation, although the physical properties of the TriThiol-TAE were significantly reduced.

In an effort to prevent phase separation of POSS molecules, chemically modified vinyl POSS molecules (vPOSS-Bu$_2$) were chemically attached to the thiol-ene backbone via polymerizable vinyl groups. The chemical incorporation of vPOSS-Bu$_2$ was confirmed by RTIR through the observation of vinyl group conversion, although the polymerization kinetics (polymerization rates and total conversions) decreased significantly at high concentrations (20 and 50 mol%). DLS analysis showed that aggregates (20-60 nm) formed prior to polymerization, and a reduction of peak maxima of exotherms (photo-DSC) was consistent with RTIR results at high concentrations. A broad thermal transition (T$_g$) was observed for vPOSS-Bu$_2$/TriThiol-TAE copolymers, which decreased in the direction of the glass transition temperature for pure vPOSS-Bu$_2$ (T$_g$ = -69 °C) as concentrations were increased. The observation of a single, broad glass transition indicated that complete phase separation was prevented when POSS molecules were chemically attached to the thiol-ene network. Additionally, broadening in the tan delta plot (20 and 50 mol%) was observed resulting from the incorporation of vPOSS-Bu$_2$ aggregates into the network and possible reduced network linking density caused by decreased vinyl group conversion as well as aggregates attached to the network. Upon the

chemical incorporation of vPOSS-Bu$_2$ into the network, rubber modulus, scratch resistance, and Persoz hardness increased for concentrations up to 10 mol%. Chemical incorporation of POSS molecules was shown to be an effective method for incorporating POSS molecules into the thiol-ene network.

The hydrocarbon content of the organic pendant group was shown to greatly influence compatibilization of POSS and concomitant tendency of POSS molecules toward aggregation. The chemical incorporation of chemically modified vinyl POSS with low (vPOSS-MT) and high (vPOSS-IOMP) hydrocarbon content via polymerizable vinyl groups was confirmed by RTIR. DLS analysis of trithiol/triallyl ether solutions containing vPOSS-MT showed no significant aggregation of POSS molecule, i.e. detected particle sizes (1-2 nm) were equivalent to the size of a single POSS molecule, indicating that vPOSS-MT was highly compatible with thiol and allyl ether comonomers. Further investigation of the thermal and mechanical properties of the copolymers confirmed that vPOSS-MT was truly dispersed throughout the thiol-ene network. The observation of a narrow glass transition with no significant shift in T$_g$ values (DSC) and no width changes of tan delta plots (FWHM) showed the addition of vPOSS-MT, even at high concentrations, had no significant effect on network formation, i.e. the uniformity of the network was maintained. However, good dispersion of the POSS molecules had no significant effect on network properties (rubber modulus, scratch resistance, and Persoz hardness) which changed only marginally. Conversely, network properties decreased significantly upon the inclusion of vPOSS-IOMP, i.e. rubber modulus decreased with respect to increased POSS concentration. DLS analysis confirmed that small vPOSS-IOMP aggregates (10-60 nm) formed prior to polymerization. Lowering T$_g$ values (DSC)

and broadening tan delta plots (FWHM) showed that vPOSS-IOMP aggregates were attached to the thiol-ene network. Additionally, measurable increases in T_g and rubber modulus resulted from the presence of hydrogen bonds between acid groups of vPOSS-MPA and vPOSS-MAA, and changes (increase) were more pronounced for vPOSS-MAA, a short-chain aliphatic group. Viscosity measurements of the each vPOSS monomer showed that each monomer was highly viscous. In all cases of POSS addition, whether physical or chemical, burn rates (flame spread) were significantly reduced. However, the reduction of flame spread was most pronounced for networks containing dispersed vPOSS-MT.

APPENDIX A

TRANSMISSION ELECTRON MICROSCOPY ANALYSIS OF POSS/THIOL-ENE

NANOCOMPOSITES

The changes in network morphology, as observed by transmission electron

microscopy (TEM), were related to POSS compatibility and type of POSS incorporation

into the thiol-ene network. The inclusion of POSS molecules into the TriThiol-TAE

network involved blended (mixed) or chemically bound (via polymerizable vinyl groups)

POSS molecules with various substituent groups and/or functionality. The

POSS/TriThiol-TAE films observed by TEM were networks containing POSS-iBu (solid

blend), vPOSS-Bu$_1$ (liquid blend), vPOSS-Bu$_2$ (copolymer), vPOSS-MT (copolymer),

and vPOSS-IOMP (copolymer) (See POSS structures in Chapters 5 and 6). TEM analysis

was performed on a Zeiss 109-T operating at an accelerating voltage of 50 kV for

observation of size and size distribution of agglomerated silicate particles. Thin film

samples (set in an epoxy medium) containing 50 mol% POSS (copolymers) or its weight

equivalent (57.8 wt% for liquid blend) and 10.2 wt% POSS (solid blend) were

microtomed (-90 °C) into 60-μm sections using a diamond knife. (Microsections for 57.8

wt% solid blend were unattainable due to the high content of POSS-iBu within the

sample.) Each film sample was analyzed at low (7000x) and high (50,000x)

magnification.

For each blended system, phase separation of the POSS molecules (POSS-iBu and

vPOSS-Bu$_1$) and TriThiol-TAE matrix, which is due to the inefficiency of physical

addition of POSS and incompatibility of the POSS molecules, are clearly observed by

TEM imaging. In Picture 1, large, crystalline aggregates (> 500 nm), along with

intermittent regions of dispersed POSS (Picture 1b), are observed in the POSS-

iBu/Trithiol-TAE blend at low and high magnification. Phase separation of vPOSS-Bu$_1$ is

observed as a co-continuous phase of liquid POSS and thiol-ene polymer (Picture 2).

Closer examination of the liquid blended system at high magnification (Picture 2b)

reveals liquid POSS-Bu$_1$ droplets observed as dark, oblong wells (~75 nm diameter)

distributed throughout the TriThiol-TAE matrix.

The chemical addition of POSS molecules with different substituents and

functionality (vPOSS-Bu$_2$, vPOSS-MT, and vPOSS-IOMP) shows the effect of POSS

compatibility on the morphology of the TriThiol-TAE network, i.e. the hydrocarbon

content of the substituent has a strong influence on the network morphology formation.

Clearly, no phase separation (Pictures 3 and 4) is observed for networks containing

vPOSS-Bu$_2$ (50 mol%) and vPOSS-MT (50 mol%) as observed in the solid and liquid

blends demonstrating the efficiency of chemically incorporating POSS into the network.

Observations of each network morpholology show variations of dark and light regions

which correspond to the changes in electron density caused by the presence of POSS.

Observable differences of POSS distribution within these regions at high magnification

(Pictures 3b and 4b) result from the association of chemically attached POSS molecules

or aggregates within the thiol-ene matrix., i.e. dispersed vPOSS-MT particles (3-4 nm)

are observed as an association of individual POSS molecules (darkened region), whereas,

by comparison, dispersed vPOSS-Bu$_2$ aggregates are observed as small, darkened regions

enriched with associated POSS aggregates (40-150 nm) distributed throughout the

network. In Picture 4, a highly-ordered, phase separated morphology observed as

alternating light and dark layers was clearly observed for the thiol-ene network

containing vPOSS-IOMP (50 mol%), a POSS molecule having high hydrocarbon content.

The accumulation of vPOSS-IOMP aggregates (via POSS-POSS associations) into

distinct POSS enriched regions (darkened layers) demonstrates the effects of hydrocarbon

content (i.e. the selection of corner substituents on the cage) on POSS compatibility and

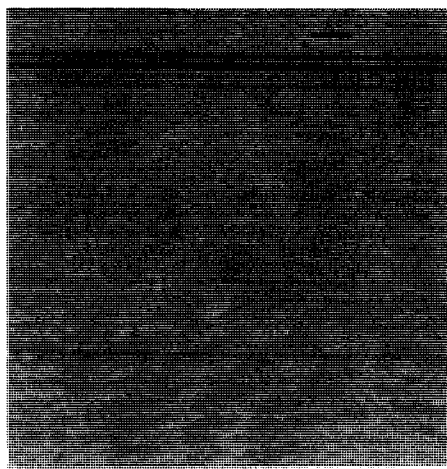the subsequent network morphology of the TriThiol-TAE polymer.
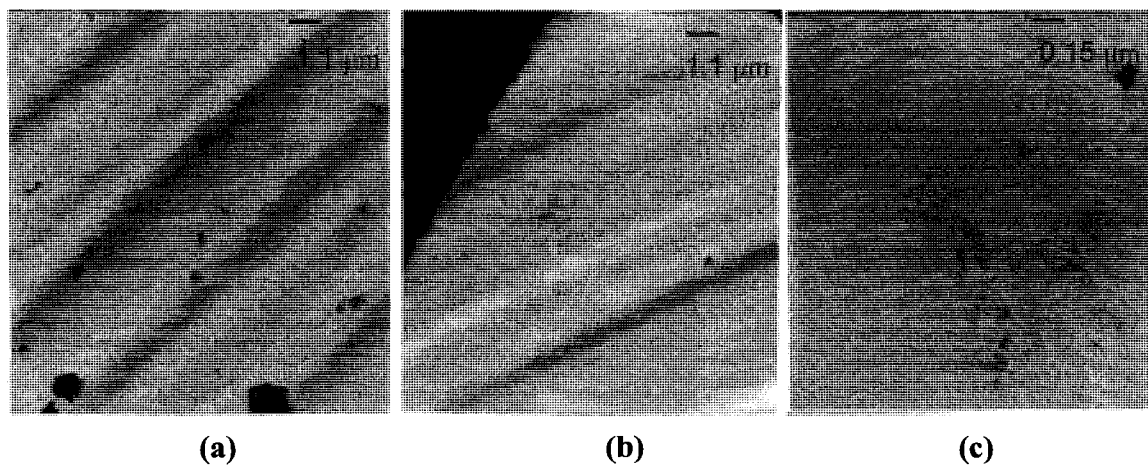
Picture 1. TEM analysis of 10.2 wt% POSS-*i*Bu/TriThiol-TAE blend at a) 7000x, b) 7000x and c) 50,000x magnification.

<div align="center">(a)</div>

<div align="center">(b)</div>
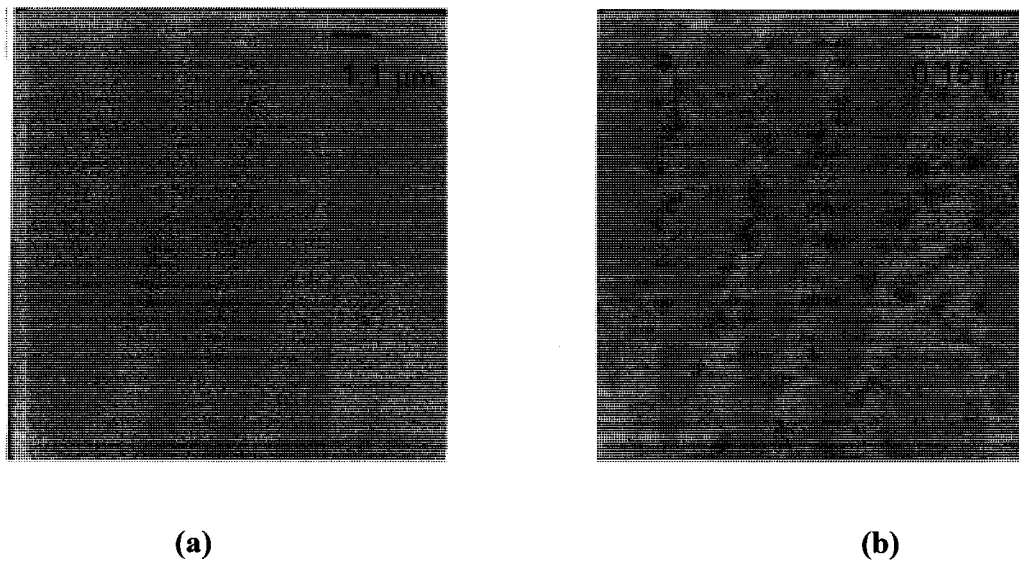
Picture 2. TEM analysis of 57.8 wt% vPOSS-Bu$_1$/TriThiol-TAE blend at a) 7000x and b) 50,000x magnification.
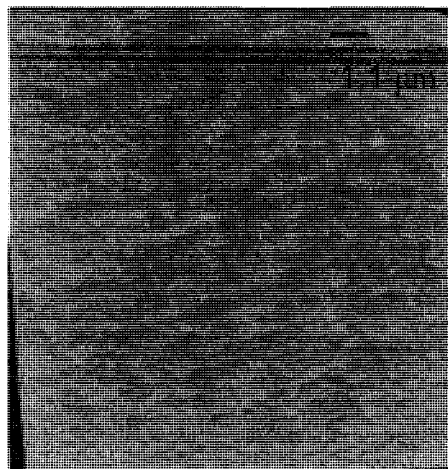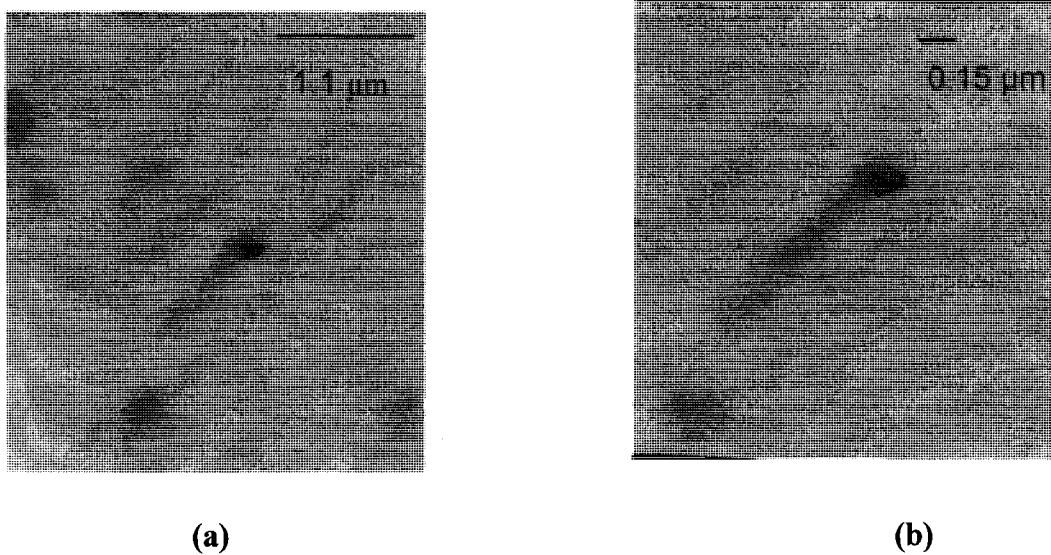
(a)   (b)

Picture 3. TEM analysis of 50 mol% vPOSS-Bu$_2$/TriThiol-TAE copolymer at a) 7000x and b) 50,000x magnification.

(a) (b)

Picture 4. TEM analysis of 50 mol% vPOSS-MT/TriThiol-TAE copolymer at a)7000x and b) 50,000x magnification.
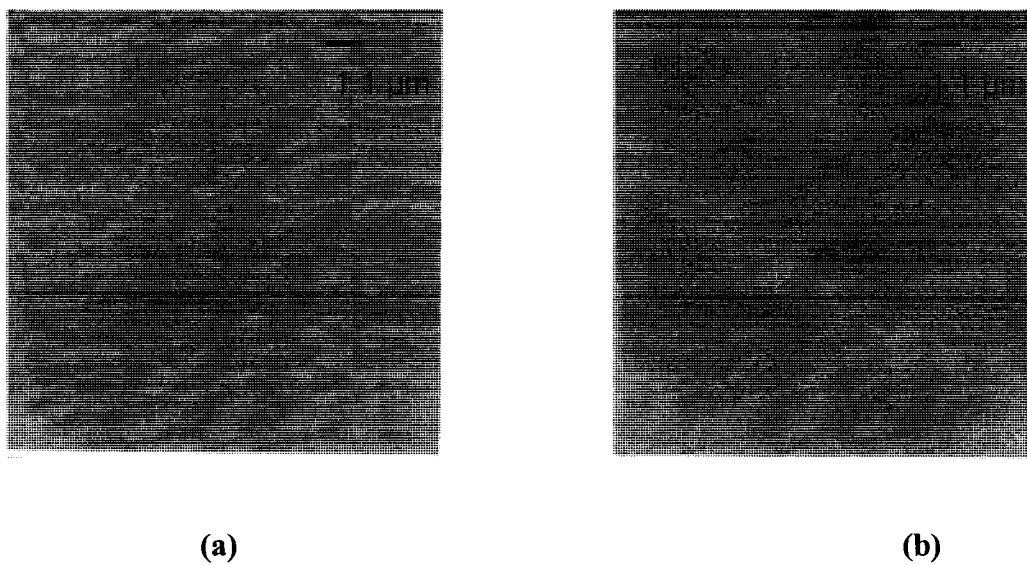
<table>
<tr><td align="center">(a)</td><td align="center">(b)</td></tr>
</table>

Picture 5. TEM analysis of 50 mol% vPOSS-IOMP/TriThiol-TAE copolymer at a) 7000x and b) 50,000x magnification.

APPENDIX B

ATOMIC FORCE MICROSCOPY ANALYSIS OF POSS/THIOL-ENE

NANOCOMPOSITES

The morphological changes of the vPOSS-Bu$_2$ containing thiol-ene network as related to increasing POSS concentration were observed by atomic force microscopy (AFM). AFM was conducted on the surface of the thin film coatings (~250 microns) with MultiMode AFM fromVeeco Instruments, Inc. RTESP silicon tip with nomimal frequency of 275 kHz was used in the tapping mode to obtain height and phase images. The thin film samples contained 0, 5, 10, 20, and 50 mol% vPOSS-Bu$_2$ chemically incorporated into the TriThiol-TAE network via polymerizable vinyl groups. The structures of each thiol and ene component are shown in Chapter 5.

AFM analysis (tapping mode) of the film surface clearly supports differential scanning calorimetry (DSC) results observed in the glass transition region (Figure #, Chapter 5), i.e. increased broadening in the glass transition occurs as the concentration increased from 5 to 50 mol% when compared to the base TriThiol-TAE network. Broadening in the glass transition indicates a loss of the TriThiol-TAE network uniformity that may be observed as a network with a heterogeneous morphology as demonstrated by AFM analysis. In Figure 1 imaging (height) of the base TriThiol-TAE network shows a homogeneous network having no variations in the surface height. Figures 2 and 3 show the height and phase imaging of the thin film samples containing 5 mol% and 10 mol%, respectively. As vPOSS-Bu$_2$ concentration increases from 0 mol%

to 5 mol% to 10 mol%, variation of surface height is clearly observed as high (bright

highlights) and low (dark lowlights) regions within a given area of the film surface

(Figures 2 a and 3 a), and, when the corresponding phase imaging (Figures 2 b and 3 b) is

compared to the height imaging, the phase changes observed show only slight variations

within the network indicating no phase separation of the incorporated vPOSS-Bu$_2$

molecules and the TriThiol-TAE network; therefore, the corresponding height changes

are not directly related to POSS incompatibility. Closer examination of the network

containing 10 mol% in Figure 3 c and d shows no significant change in the phase

although changes in surface height are apparent. Certainly, the phase imaging supports

DSC results (no broadening) showing a TriThiol network that is homogeneous even at

low POSS concentrations. The morphology observed at high POSS concentrations (20

and 50 mol%) in the height and phase imaging is a heterogenous network consisting of

large vPOSS-Bu$_2$ aggregates chemically bound into the TriThiol-TAE network. Clearly,

agglomerated vPOSS-Bu$_2$ particles (10-40 nm) are observed in the height (Figures 4 a

and 5 a) and phase images (Figure 4 a and 5 a), and the presence of the chemically bound

agglomerates contributes to the heterogeneity of the TriThiol-TAE network which is

observed as broadening the glass transition by DSC analysis. The significance of network

heterogeneity is better appreciated when the network morphology is examined at a larger
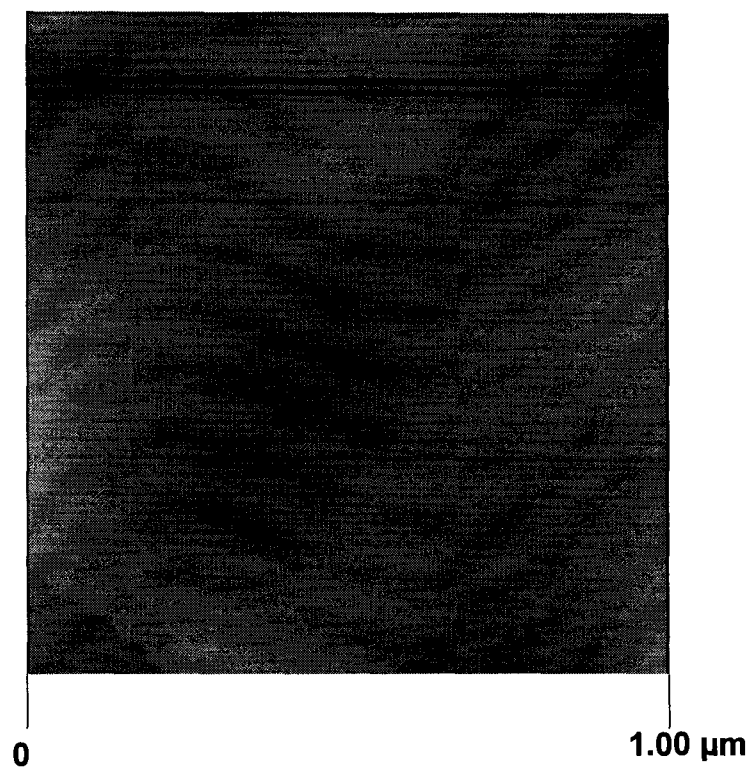
field as shown in Figures 4 c-f and 5 c-f.

0   **1.00 μm**

Figure 1. AFM analysis (height image in tapping mode) of the TriThiol-TAE network at 1.00 μm.
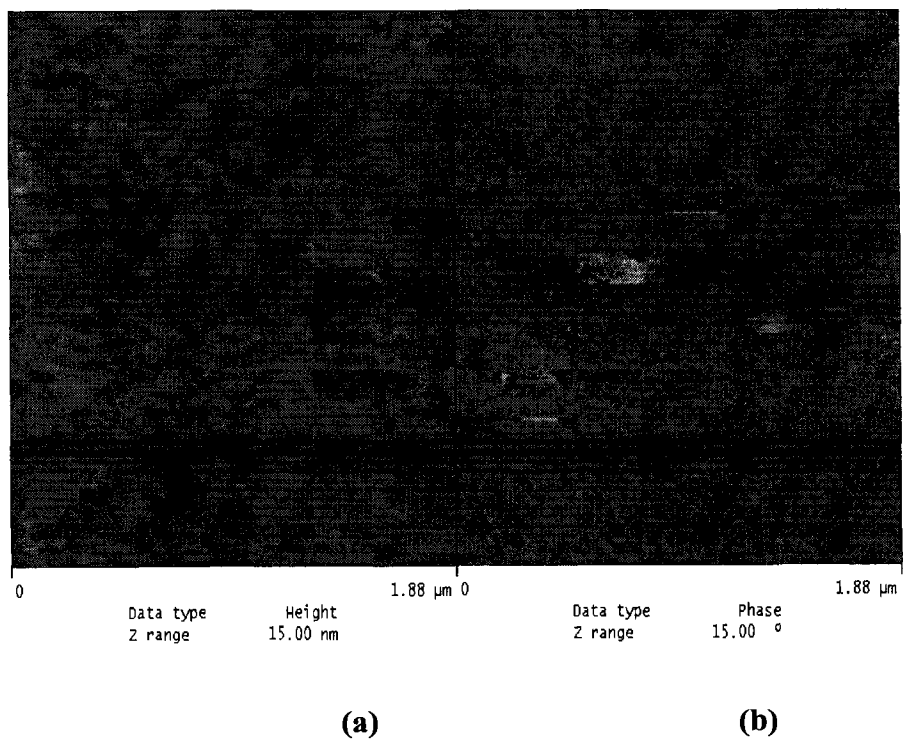
```
0                                    1.88 µm 0                                    1.88 µm
        Data type      Height                    Data type      Phase
        Z range        15.00 nm                  Z range        15.00  °
```

(a)   **(b)**

Figure 2. AFM analyis (tapping mode) of the 5 mol% vPOSS-Bu2/TriThiol-TAE
network as a a) height and b) phase image at 1.88 µm.

Data type   Height   Data type   Phase
Z range   25.00 nm   Z range   30.00 °

(a)   (b)

Data type   Height   Data type   Phase
Z range   10.00 nm   Z range   30.00 °
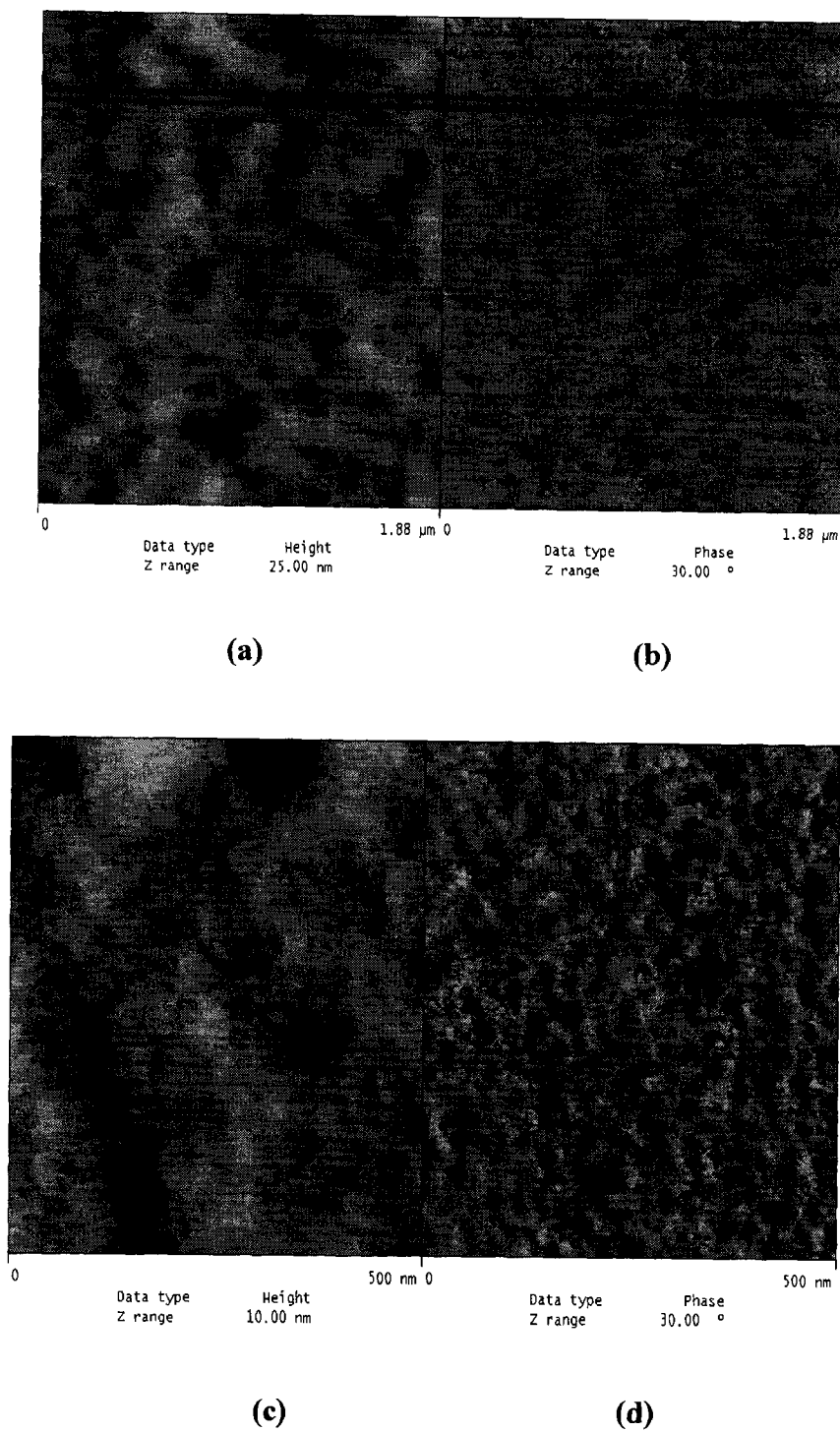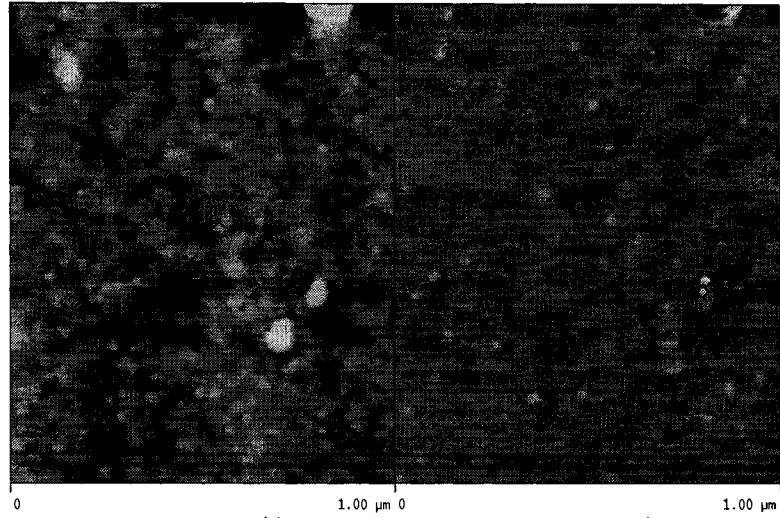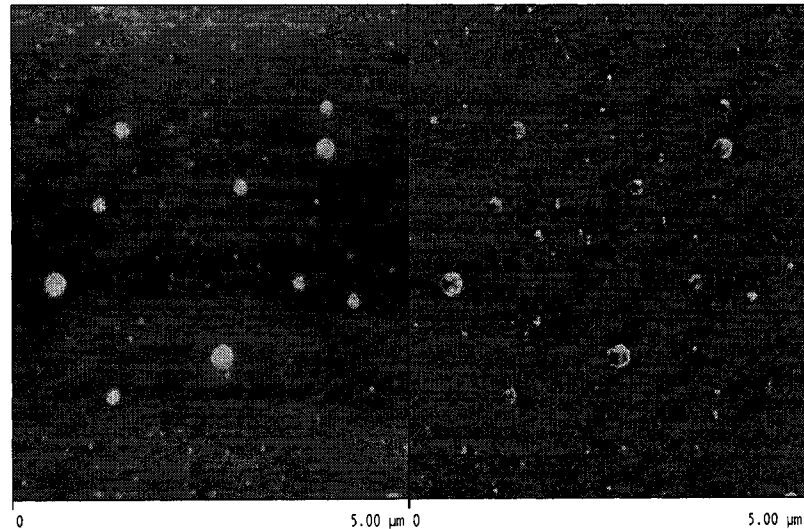
(c)   (d)

Figure 3. AFM analysis (tapping mode) of 10 mol% vPOSS-Bu₂/TriThiol-TAE network as a a) height and b) phase image at 1.88 μm and a c) height and b) phase image at 500 nm.
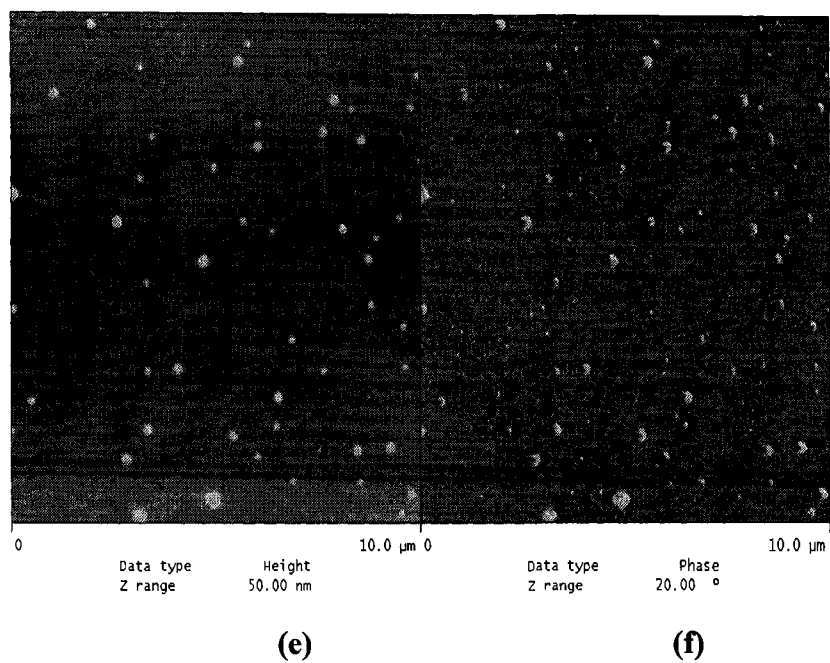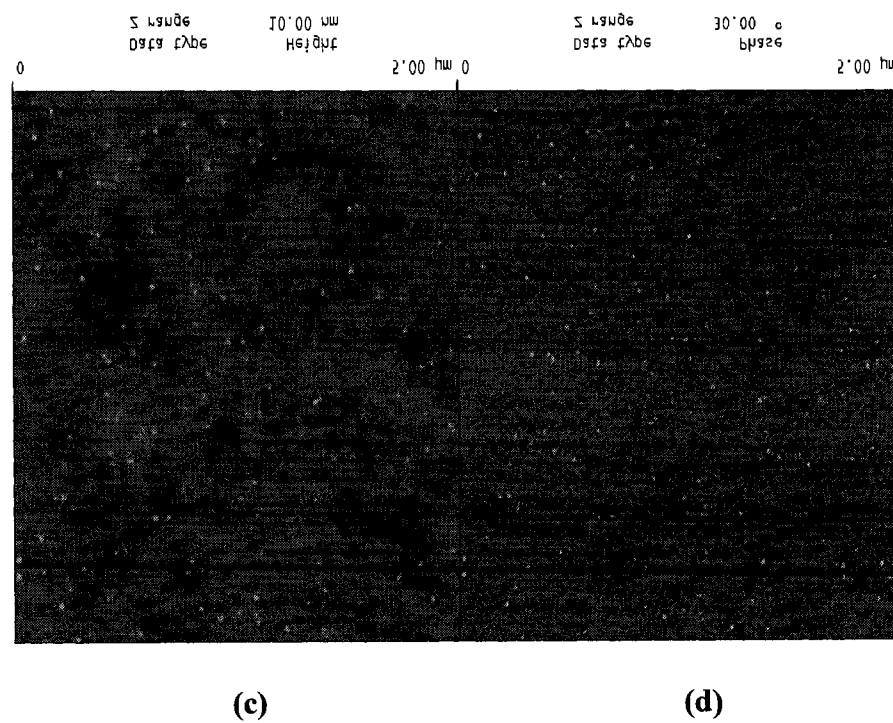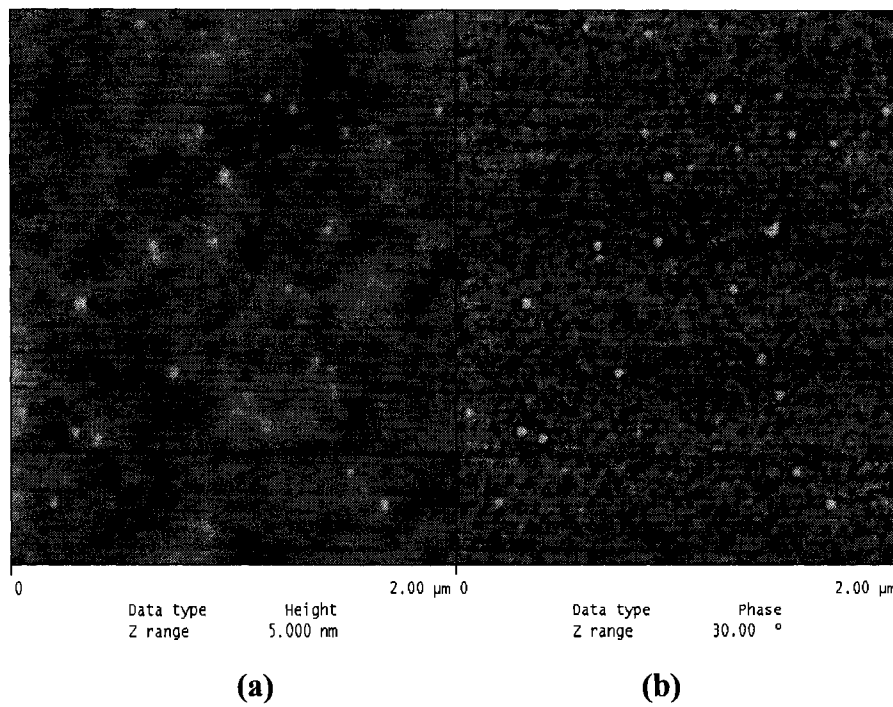
(a)

(b)

(c)

(d)

Data type   Height   Data type   Phase
Z range   50.00 nm   Z range   20.00 °

(e)   **(f)**

Figure 4. AFM analysis (tapping mode) of 20 mol% vPOSS-Bu₂/TriThiol-TAE network as a a) height and b) phase image at 1.00 μm and a c) height and b) phase images at 5 μm, and a e) height and f) phase image at 10 μm.
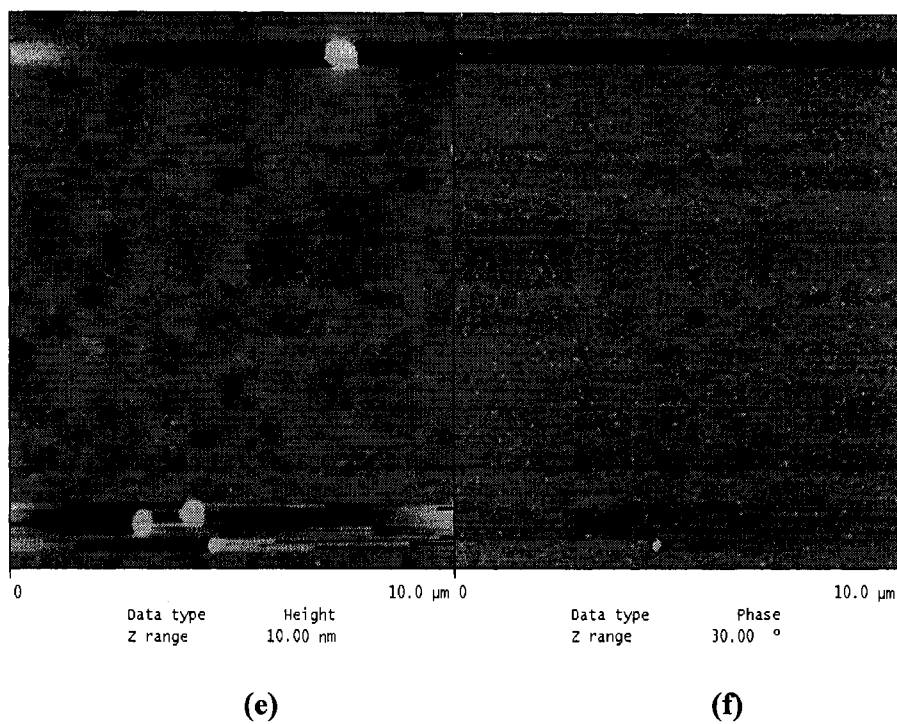
Data type	Height		Data type	Phase
Z range	5.000 nm		Z range	30.00 °

(a)   **(b)**

(c)   **(d)**

Figure 5. AFM analysis (tapping mode) of 10 mol% vPOSS-Bu2/TriThiol-TAE network as a a) height and b) phase image at 2.00 μm and a c) height and b) phase images at 5 μm and a e) height and f) phase image at 10 μm.
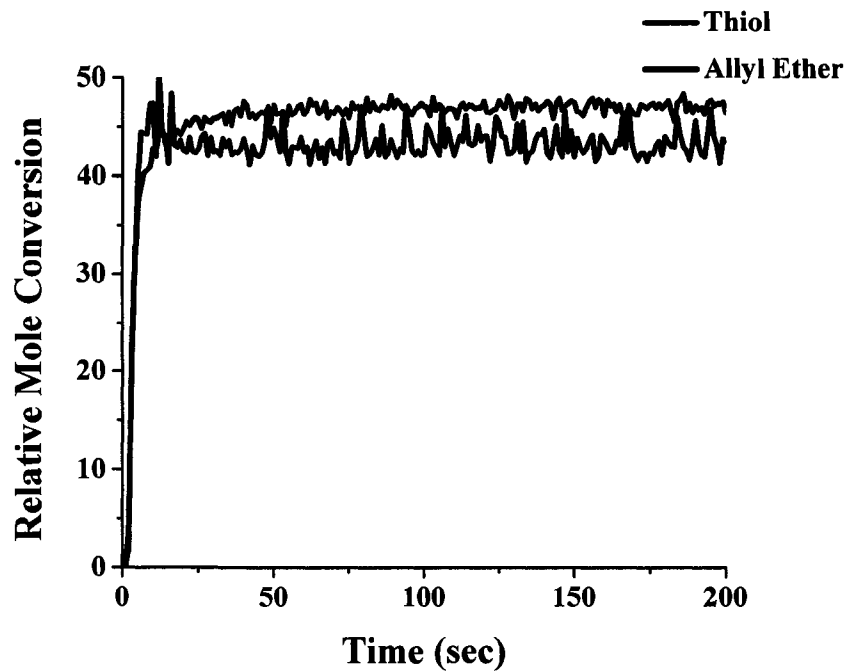
APPENDIX C

Figure 1. RTIR-based plot of an equal molar reaction showing trithiol and triallyl ether conversions. The thiol conversion was not shown for RTIR plots of neat TriThiol-TAE for comparison with RTIR plots of POSS-iBu, vPOSS-Bu$_2$, vPOSS-MT, vPOSS-IOMP, vPOSS-MPA, and vPOSS-MAA at various concentrations.